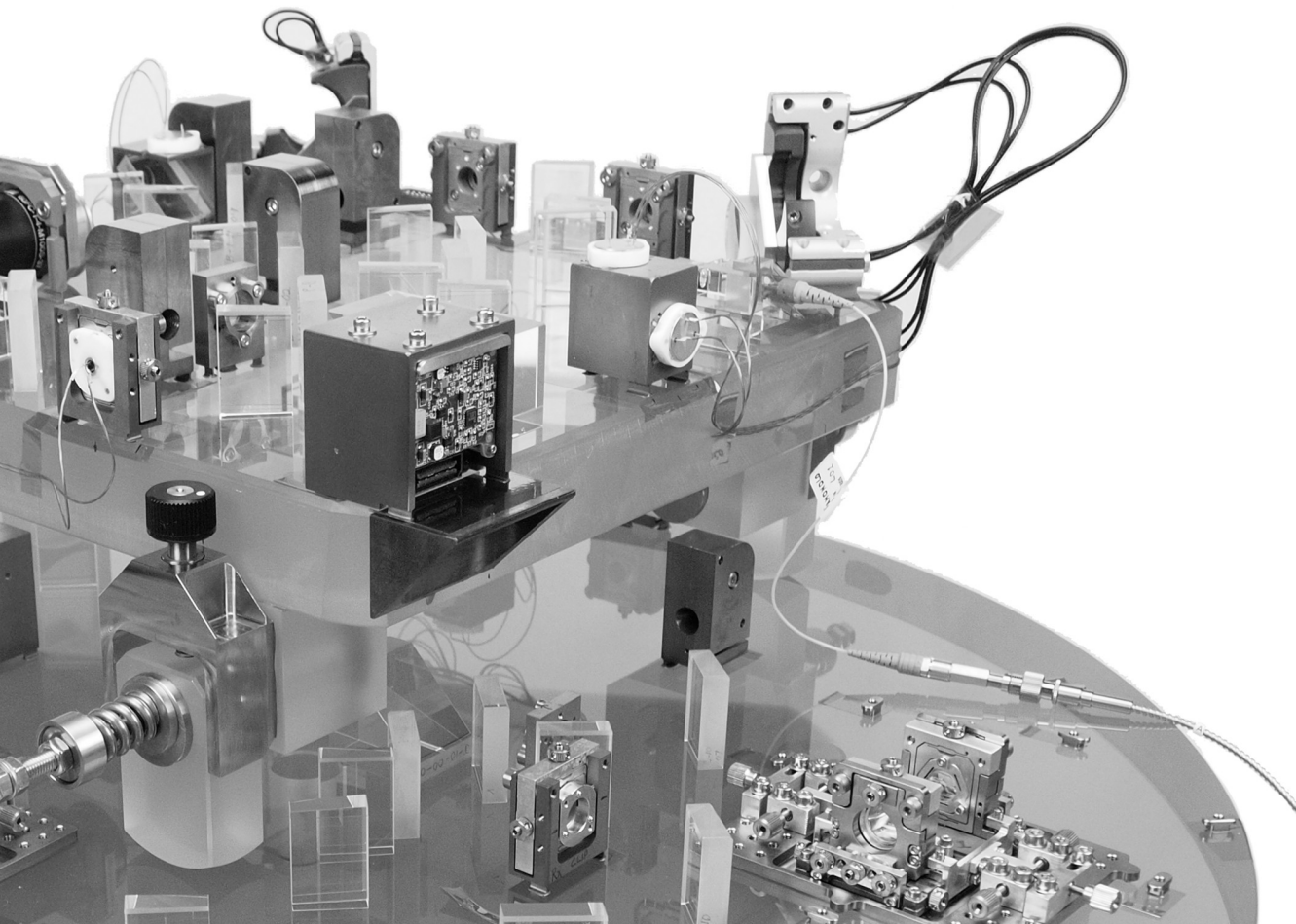


Sönke Schuster
2017



Tilt-to-length coupling and diffraction
aspects in satellite interferometry

Tilt-to-length coupling and diffraction aspects in satellite interferometry

Von der QUEST-Leibniz-Forschungsschule
der Gottfried Wilhelm Leibniz Universität Hannover
zur Erlangung des Grades

Doktor der Naturwissenschaften
— Dr. rer. nat. —

genehmigte Dissertation
von

Sönke Schuster, M. Sc.

2017

Referent: Prof. Dr. Karsten Danzmann
Universität Hannover

Korreferent: Prof. Dr. Gerhard Heinzl
Universität Hannover

Korreferent: Prof. Dr. Guido Müller
University of Florida

Tag der Promotion: 16.02.2017

Abstract

One of the major noise sources in spaceborne optical interferometers like LISA or the laser ranging interferometer in GRACE-FO is expected to be the unintended cross coupling between an angular jitter of the interfering beams and the path length readout, called tilt-to-length coupling. This effect is influenced not only by geometrical effects, like longer propagation distances, but also among others by the wavefront curvatures of the involved beams, the intensity distribution on the detector, and the signal definitions used on quadrant diodes.

One approach to suppress tilt-to-length coupling in the first place is the use of specially designed imaging systems. After the functional principle of these systems were confirmed previously, a dedicated experiment was designed, built and operated in the frame of this thesis. Therein, the imaging systems reduced tilt-to-length coupling below $\pm 25 \mu\text{m}/\text{rad}$ in an environment representative for LISA. Furthermore, by intentionally adding a well measured geometric tilt-to-length coupling contribution, the residual coupling behind the imaging systems could be reduced even more. Two imaging systems were tested, one of which is a pupil plane imaging system, designed using classical optics, the other is a non classical two-lens system that lacks some properties of a classical system in that it neither provides a collimated beam nor does it feature an internal field-stop. During this investigation a correlation between the beam parameters and the performance of the two-lens imaging systems was discovered. To avoid this behavior in the future, an additional requirement for advanced imaging system designs was formulated: to provide nearly collimated output beams. According to simulations, imaging systems that were designed according to the new findings, do not show the previously observed dependency on the beam parameters.

An additional aspect in inter-satellite interferometry is the propagation and interference of expanded beams that are clipped by the receiving spacecraft and propagate with diffraction patterns through the local optics. Different methods to simulate and compute diffraction patterns are known, like the mode expansion method, angular spectrum methods, Gaussian beam decomposition, and analytic solutions of the diffraction integral. However, to the best knowledge of the author, a direct comparison of these methods that meet the required precision for space interferometry cannot be found in literature. Within this thesis, a Gaussian beam decomposition method was implemented in the simulation tool IfoCAD and compared to other, already included methods. A comparison of the free space propagation characteristics lead to the result, that the Gaussian beam decomposition is not only the most precise approach, but also has advantages regarding computational cost.

Keywords: interferometry, tilt-to-length coupling, LISA

Zusammenfassung

Eine der vorraussichtlich bedeutsamsten Rauschquellen von optischen Interferometern im Weltraum wie beispielsweise LISA oder das Laserinterferometer von GRACE-FO ist die unerwünschte Kopplung von Strahlverkipfung in die Längenauslesung, welche als Kipp-zu-Längen-Kopplung (tilt-to-length coupling) bezeichnet wird. Diese Kopplung wird nicht nur durch geometrische Effekte, wie zum Beispiel einer Verlängerung der Wegstrecke, sondern unter anderem auch durch die Wellenfrontkrümmungen der beteiligten Strahlen, die Intensitätsverteilung auf dem Detektor und die genutzten Signaldefinition auf Quadrantendioden hervorgerufen.

Ein Ansatz zur Reduktion dieser Kopplung ist der Einsatz von speziell entworfenen Abbildungssystemen. Nachdem deren Funktionalität in der Vergangenheit gezeigt wurde, wurde im Rahmen dieser Arbeit ein weiterführendes Experiment geplant, konstruiert und betrieben. Mit diesem wurde in einem für LISA repräsentativen Szenario gezeigt, dass Abbildungssysteme die tilt-to-length Kopplung unter $\pm 25 \mu\text{m}/\text{rad}$ reduzieren. Darüber hinaus ist eine weitere Reduktion der verbleibenden Kopplung durch absichtliches Einbringen zusätzlicher geometrischer Kopplung möglich. Eines der beiden getesteten Abbildungssysteme ist ein Pupillenebenen-Abbildungssystem, welches mit Hilfe klassischer Optik entworfen wurde, das Andere ein nichtklassisches System mit zwei Linsen, welches nicht alle Eigenschaften eines klassischen Pupillenebenen-Abbildungssystem aufweist, da es weder einen kollimierten Ausgangsstrahl noch eine interne Pupille aufweist. Da während der Messungen eine Korrelation zwischen den Strahlparametern und der Leistungsfähigkeit der Abbildungssysteme beobachtet werden konnte, sollten zukünftige Abbildungssysteme einen kollimierten Ausgangsstrahl erzeugen. In Simulationen mit entsprechend entworfenen Abbildungssystemen, wurde eine Korrelation zwischen Leistung und Strahlparametern nicht länger beobachtet.

Ein weiterer wichtiger Aspekt in Weltraum-Interferometern ist die Ausbreitung und Überlagerung von ausgedehnten Wellenfronten welche von Satelliten aufgefangen und beschnitten werden, um schließlich unter der Erzeugung von Beugungsmustern durch die lokalen Interferometer zu propagieren. Unterschiedliche Methoden zur Simulation und Berechnung dieser Beugungsmuster sind allgemein bekannt, wie zum Beispiel die Zerlegung in höhere Moden, ebene Wellen oder fundamentale Gauß-Moden und analytische Lösungen des Beugungsintegrals. Jedoch sind nach bestem Wissen des Autors bisher keine Vergleiche publiziert, die den Anforderungen von Interferometern im Weltraum gerecht werden. In dieser Arbeit wurde eine Me-

thode zur Gaußstrahl-Zerlegung in das Simulationsprogramm IfoCAD implementiert und mit den anderen, bereits vorhandenen, Methoden verglichen. Ein Vergleich der Freistahlpropagation ergab, dass die Gaußstrahl-Zerlegung nicht nur die präzisesten Ergebnisse liefert, sondern auch Vorteile beim Rechenaufwand zeigt.

Schlüsselwörter: Interferometrie, Kipp-zu-Längen Kopplung, LISA

Contents

Abstract	i
Zusammenfassung	iii
List of Figures	ix
List of Tables	xiii
1. Introduction	1
Part I General information	5
2. Basics	7
2.1 Satellite interferometry	7
2.1.1 LISA	7
2.1.2 GRACE	11
2.2 Interferometer for high-precision length measurements	12
2.2.1 Homodyne phase readout	12
2.2.2 Heterodyne phase readout	13
2.2.3 Path length definitions	15
2.2.4 Differential power sensing signal	16
2.2.5 Differential wavefront sensing signal	17
2.2.6 Contrast	18
2.3 Optical Simulations with IfoCAD	18
2.3.1 Gaussian beams	19
2.3.2 Ray transfer matrices	20
2.4 Optical pupils	22
3. Tilt-to-length coupling	25
3.1 Geometric tilt-to-length coupling	26
3.1.1 Lever arm tilt-to-length coupling	26
3.1.2 Piston effect	26
3.1.3 Discussion	27
3.2 Non geometric tilt-to-length coupling	29
3.2.1 Beam offset tilt-to-length coupling	30
3.2.2 Beam parameters tilt-to-length coupling	31

3.2.3	Tilt-to-length coupling due to the path length signal definitions	34
3.2.4	Wavefront errors tilt-to-length coupling	35
3.2.5	Detector geometry tilt-to-length coupling	37
3.3	Summary of the different mechanism	37
3.4	How to suppress tilt-to-length coupling	38

Part II LISA optical bench testbed 41

4. LISA testbed – methodology and design 43

4.1	Tilt-to-length coupling in LISA	43
4.2	The LISA optical bench experiment	46
4.2.1	Requirements and goals	46
4.2.2	Representativity of the operation parameters	47
4.3	Methodology and design	48
4.3.1	Calibration principles	49
4.3.2	The properties of an optical copy	50
4.3.3	Optical bench – design	51
4.3.4	Telescope simulator – design	52
4.3.5	RX aperture	57
4.3.6	Flat-top-generator design	67
4.3.7	Electronics, laser preparation and vacuum tank	70
4.3.8	Design properties and noise budget	74
4.3.9	Four-lens imaging system optical design LOB4C	77
4.3.10	Two-lens imaging system optical design LOB2D	79
4.4	Delimitation to other experiments	79
4.4.1	First iteration – large detector heterodyne	80
4.4.2	Second iteration – large detector homodyne	82
4.4.3	Third iteration – LISA testbed	83
4.4.4	Fourth iteration – advanced tilt actuator	83

5. LISA testbed – alignment and measurement campaign 85

5.1	Alignment and calibration	85
5.1.1	Photo diode signal calibration	85
5.1.2	Telescope simulator alignment on optical bench	88
5.1.3	Tilt actuation of the RX beam	89
5.2	Calibration of the telescope simulator	90
5.2.1	Pinhole alignment	90
5.2.2	Alignment test using the flipping procedure	92
5.3	RX clip and temperature drifts	97
5.3.1	Temperature dependencies of the tip-tilt mount	98
5.3.2	Telescope simulator height variation removal	101

5.3.3	The effect of an additional RX-clip	101
5.4	Two-lens imaging system – LOB2D	103
5.4.1	Nominal performance	103
5.4.2	Sensitivity to misalignments	108
5.4.3	Compensation by photo diode alignment	113
5.5	Four-lens imaging system – LOB4C	115
5.5.1	Nominal performance	115
5.5.2	Sensitivity to misalignments	115
5.5.3	Compensation by photo diode alignment	120
5.5.4	The effect of the field stop	120
5.6	Results of the tolerance analysis	122
5.7	Summary LISA optical bench	123

Part III Optical simulations – imaging systems and diffraction 125

6.	Parameter sensitivity of imaging systems	127
6.1	Beam parameter sensitivity simulator	128
6.1.1	Results for the two-lens imaging system	129
6.1.2	Results for the LOB4C imaging system	134
6.1.3	Consequences from the beam parameter investigations	135
6.2	Two-lens imaging system – GIS2C	136
6.2.1	Second generation design algorithm	136
6.2.2	Imaging system design	139
6.2.3	Results of the GIS2C imaging system investigation	141
6.3	Three-lens imaging system – GIS3C	142
6.4	Misalignment sensitivity comparison to old imaging systems	144
7.	Diffraction	147
7.1	Reasons for diffraction	148
7.2	Simulation of diffraction	149
7.2.1	Angular spectrum decomposition	150
7.2.2	Mode expansion method	150
7.2.3	Gaussian beam decomposition	151
7.3	Comparison of diffraction model techniques in free space	155
7.3.1	Large Gaussian behind a circular aperture	155
7.3.2	Small Gaussian behind a circular aperture out of waist	158
7.3.3	Summary of the free space propagation comparison	160
8.	Summary	165

Appendix	167
A. Vanishing tilt-to-length coupling	169
A.1 Plane waves	169
A.2 Gaussian beams	171
B. Proof-of-principle experiment	177
B.1 Mechanisms of tilt-to-length coupling	178
B.1.1 Parasitic longitudinal movement of the tilt actuator	180
B.1.2 Wavefront curvature mismatch	180
B.1.3 Higher order Gaussian modes	180
B.2 Experimental setup	180
B.3 Photo diode calibration	183
B.4 Coherent filtering	184
B.5 Post-processing	184
B.6 Measurement results	185
C. Miscellaneous information	187
C.1 The difference between intensity and irradiance	187
C.2 Phase extraction	188
C.3 Propagation characteristic of a pivot	191
C.4 Auxiliary information regarding the LISA OB TS testbed	192
C.5 Numerical trouble spot in IfoCAD: GA_GBeam	194
D. Auxiliary optical simulations	197
D.1 Beam parameter sensitivity simulations	197
D.2 Alignment test	207
D.2.1 GIS2C system	207
D.2.2 GIS3C system	209
Glossary	213
Bibliography	217
Project Documents	223
Complete list of publications	225
Acknowledgements	227
Curriculum Vitae	229

List of Figures

2.1	Heliocentric orbits and concept of the LISA	8
2.2	Gravitational wave alters space.	8
2.3	Single LISA arm concept	9
2.4	LISA: Moving Optical Subassembly	10
2.5	Sketch of a simplified test mass interferometer.	10
2.6	Quadrant photo diode with four segments;	15
2.7	Entrance and exit pupil plane definition via the aperture stop	23
2.8	Sketch of a classical pupil imaging system.	23
3.1	Geometric path length change explained in a simplified scenario. .	26
3.2	Illustration of piston tilt-to-length coupling	27
3.3	Geometric TTL coupling vanishes in real application.	28
3.4	Vanishing TTL coupling with equal beams	29
3.5	Illustration of the superposition of two wavefronts.	30
3.6	Tilt-to-length coupling due to beam offset.	31
3.7	Phase cancellation with overlap function.	32
3.8	Phase cancellation with overlap function and offset.	32
3.9	TTL coupling generated by a wavefront curvature mismatch.	34
3.10	Path length definitions and wavefront curvature	36
3.11	Higher order modes asymmetry	37
4.1	Tilted wavefront in a LISA telescope	45
4.2	Sketch of a test mass imaging system.	45
4.3	Space restrictions for imaging systems	46
4.4	Schematic of the telescope simulator test bed concept.	49
4.5	Schematic of the OB layout and labeling of the key components. . .	53
4.6	Schematic of the TS layout.	55
4.7	Schematic of the TS's degrees of freedom.	56
4.8	Schematic of the TS orientation with respect to the OB.	58
4.9	Telescope simulator mounting system	59
4.10	Photography of TS	60
4.11	Photograph of TS and OB	60
4.12	Relative power change behind a circular aperture	61
4.13	Photograph of different apertures	62
4.14	Differences between small and a point-like photo diodes.	64
4.15	Heterodyne efficiency for small photo diodes of different radii . . .	64

4.16	Visualization of the parameters: r_{ap} and d_{ap}	65
4.17	Diffraction pattern behind a four-hole aperture	66
4.18	QPD four-hole aperture diffraction simulation.	68
4.19	DPS signal for a lateral shift of $3\ \mu\text{m}$ for a $5\ \text{mm}$ diameter QPD.	69
4.20	Photograph of the apodized aperture in aluminum mount.	69
4.21	Schematic of the laser preparation and electronic setup.	70
4.22	Screenshot of the user interface of the measurement program.	72
4.23	Optical model of the four-lens imaging system LOB4C.	78
4.24	Optical model of the two-lens imaging system LOB2D.	80
4.25	Schematic setup of the first TTL experiment	81
4.26	Schematic setup of the second TTL experiment	82
4.27	Advanced tilt actuator setup.	84
5.1	Calibration of the DWS signals for the Gaussian RX beam.	86
5.2	DPS and DWS calibration for the RX flat-top beam.	87
5.3	Beam angle vs. DWS signal for the RX flat-top beam	88
5.4	Schematic of the RX beam actuation.	89
5.5	Reference pinhole alignment using the RX Gaussian	93
5.6	Reference pinhole alignment using the RX flat-top	94
5.7	Path length signal of the temporary pinhole, after flip, RX Gaussian	96
5.8	Path length signal of the temporary pinhole, after flipping	96
5.9	Path length signal before and after flipping	97
5.10	Longterm measurement of the adjustment screw stability	99
5.11	Clamping spring of the TS mounting feet	100
5.12	Path length vs. temperature, with adjustment screws.	100
5.13	Path length vs. temperature, without adjustment screws.	101
5.14	A phase and A+B phase comparison.	102
5.15	Comparison of a scenario with and without RX clip	103
5.16	LOB2D imaging system: best possible performance	104
5.17	Simulation of additional TTL coupling due to beam parameters	105
5.18	LOB2D imaging system: performance with lens 1	106
5.19	LOB2D imaging system: performance with lens 2	107
5.20	LOB2D imaging systems: best possible performance	108
5.21	LOB2D: sensitivity to lateral QPD displacement	109
5.22	LOB2D: lateral displacement of the imaging system	110
5.23	LOB2D: sensitivity to longitudinal displacement of the QPD	111
5.24	LOB2D: sensitivity to displacement of lens 1	112
5.25	LOB2D: sensitivity to displacement of lens 2	113
5.26	Misalignment of lens 2 and realignment of the QPD	114
5.27	Performance with optimized QPD position	114
5.28	LOB4C: nominal performance	116
5.29	LOB4C: lateral QPD displacement	117

5.30	LOB4C: lateral displacement of lens 1	118
5.31	LOB4C: lateral displacement of lens 2	118
5.32	LOB4C: lateral displacement of lens 3	119
5.33	LOB4C: lateral displacement of lens 4	120
5.34	Misalignment of lens 1 and realigning of the QPD	121
5.35	Diffraction pattern behind field stop.	122
5.36	Comparison of a scenario with field stop and a scenario without. . .	122
5.37	Response to misalignment for both imaging systems	123
6.1	Beam parameter sensitivity of the two-lens system – TTL coupling	130
6.2	Beam parameter sensitivity of the LOB2D system – beam curvature	131
6.3	Beam parameter sensitivity of the LOB2D system – QPD position .	132
6.4	Beam parameter sensitivity of the LOB2D system – comparison . .	133
6.5	Beam parameter sensitivity of the LOB4C system – comparison . .	135
6.6	Optical model of the GIS2C imaging system.	140
6.7	GIS2C: nominal performance	140
6.8	Beam parameter sensitivity of the GIS2C system – comparison . . .	141
6.9	Optical model of the GIS3C imaging system.	142
6.10	Beam parameter sensitivity of the GIS3C system – comparison . . .	143
6.11	Sensitivity of the different misalignment parameters	146
7.1	Grid of fundamental Gaussian beams	153
7.2	Exemplary Gaussian beam decomposition	154
7.3	Demonstration of the Gaussian beam decomposition.	156
7.4	Diffraction pattern after propagation	157
7.5	Method comparison in the Fresnel regime scenario 1	159
7.6	Method comparison in the Fraunhofer regime scenario 1	160
7.7	Method comparison in the Fresnel regime scenario 2	161
7.8	Method comparison in the Fraunhofer regime scenario 2	162
A.1	Numerically/Analytically computed path length signal	173
A.2	Waist position dependency of the path length signal	174
B.1	Doo3 imaging system design.	179
B.2	Simulated TTL coupling in the LISA TM interferometer	179
B.3	Working principle of a test mass interferometer.	181
B.4	Draft of the experimental setup.	181
B.5	Calibration of the path length signal	183
B.6	Path length signals compared to a numerical simulation	185
C.1	Propagation of a pivot.	191
D.1	Beam parameter sensitivity of the LOB4C system – TTL coupling .	198

List of Figures

D.2	Beam parameter sensitivity of the LOB4C system – beam curvature	199
D.3	Beam parameter sensitivity of the LOB4C system – QPD position . .	200
D.4	Beam parameter sensitivity of the GIS2C system – TTL coupling . .	201
D.5	Beam parameter sensitivity of the GIS2C system – beam curvature	202
D.6	Beam parameter sensitivity of the GIS2C system – QPD position . .	203
D.7	Beam parameter sensitivity of the GIS3C system – TTL coupling . .	204
D.8	Beam parameter sensitivity of the GIS3C system – beam curvature	205
D.9	Beam parameter sensitivity of the GIS3C system – QPD position . .	206
D.10	GIS2C: lateral QPD displacement	207
D.11	GIS2C: longitudinal QPD displacement	208
D.12	GIS2C: lateral displacement of lens 1	208
D.13	GIS2C: lateral displacement of lens 2	209
D.14	GIS3C: lateral QPD displacement	210
D.15	GIS3C: longitudinal QPD displacement	210
D.16	GIS3C: lateral displacement of lens 1	211
D.17	GIS3C: lateral displacement of lens 2	211
D.18	GIS3C: lateral displacement of lens 3	212

List of Tables

2.1	The different fundamental ray transfer matrices.	21
3.1	TTL mechanism overview	39
4.1	Simulated main performance figures for the flat-top generator.	69
4.2	Path length performance budget.	74
4.3	Number of transmissions in silica	76
4.4	Tilt-to-length coupling budget	76
4.5	Estimated actual tilt-to-length coupling contributions	77
4.6	Specifications of the four-lens imaging system LOB4C	78
4.7	Specifications of the two-lens imaging system LOB2D	81
6.1	Requirements for the new imaging system design.	137
6.2	Fit parameters of the new imaging system design algorithm.	137
6.3	Specifications of the second generation imaging system GIS2C.	139
6.4	Specifications of the three lens imaging system.	143
6.5	Comparison of the different imaging systems	145
B.1	Specifications of the Doo3 imaging system.	178
C.1	Fit parameters: before and after flipping	192
C.3	Fit parameters: nominal performance two-lens imaging system	193
C.5	Fit parameters for the two-lens system, RX flat-top.	193
C.7	Fit parameters: nominal performance four-lens imaging system	194

1

Introduction

In September 2015 the two detectors of the Laser Interferometer Gravitational-Wave Observatory (LIGO) witnessed a signal that was conform with a merger of two black holes around 1.3 billion years ago [1, 2]. The merging process generated gravitational waves that traveled trough the universe and finally reached Earth to allow for the first direct measurement of gravitational waves. LIGO is essentially a Michelson interferometer, which monitors the relative length variations of two perpendicular laser arms. The gravitational wave from September 2015 was propagating through the LIGO arms, periodically compressing the length of on arm while simultaneously stretching the other. After half a period of the gravitational wave, the formerly stretched arm was compressed and vice versa. Being able to measure distance variations accurately enough to detect the tiny variations generated by the gravitational wave, LIGO started a new era in astronomy. LIGO was the first step in the observation of the gravitational universe but the potential of LIGO is limited. Earth curvature limits the arm length to a few kilometers while seismic noise and the gravity gradient limit the sensitivity at lower frequencies. The limited low frequency performance decreases the number of possible sources that can be observed with LIGO. The most massive objects in the cosmos, e.g. super massive black hole binaries emit gravitational waves at lower frequencies which cannot be detected by LIGO. To get a better impression of the gravitational wave spectrum and therefore deeper knowledge about the cosmos, the insight provided by LIGO needs to be enhanced by an additional detector that features performance in lower frequencies with a higher accuracy. The name of this detector is LISA.

LISA, the Laser Interferometer Space Antenna [3, 4], is a generic class of missions, featuring a space base gravitational wave observatory. The limitations of LIGO, mainly the limited arm length and the environmental noise are overcome with LISA. LISA will be an inter-satellite interferometer with millions of kilometers arm length, this arm length enhances the effect of a gravitational wave strain tremendously. LISA will be operating on a heliocentric orbit, without seismic noise. With the enhanced performance of LISA especially in the low frequency regime, another door to the universe will be open to discover new science [5].

Even with an arm length of millions of kilometers, the required precision in the distance measurement is demanding. The required overall noise is in the range of $\text{pm}/\sqrt{\text{Hz}}$. This overall noise budget contains any imaginable noise source that can disturb the measurement. The second largest noise sources is originating from angular misalignments in the different interferometers [TD1]. On board a LISA satellite, the position of a free floating test mass is read out by an interferometer. Therefore, the reflection of a laser beam that hits the test mass is superimposed with another laser beam, forming the test mass interferometer. Since the test mass is free floating and the satellite follows the movement of the test mass, tiny misalignments between test mass and satellite are inevitable. While offsets between satellite and test mass interferometer in the laser axis are the primary measurement value of the test mass interferometer, other misalignments are undesirable. Especially angular alignment errors are a crucial source of noise. If a test mass has an angular misalignment to its surrounding satellite, twice the relative angle is imprinted on the beam that is reflected from this test mass. This angular misalignment of the beam will couple into the readout of the test mass interferometer and will look like a longitudinal movement of the test mass itself. The coupling from angular misalignment of an interferometric beam into the length readout of an interferometer is called tilt-to-length (TTL) coupling.

TTL coupling is a nuisance, not only in LISA but also in other high precision interferometers. Especially in the GRACE-FO mission, which is the successor of the gravitational recovery and climate experiment (GRACE). GRACE is a satellite mission to monitor Earth's gravity field by tracking the distance between two satellites flying behind each other. Since the measurement principles in GRACE and LISA are very similar – tracking the distance variations between satellites – it was decided to enhance GRACE-FO with respect to GRACE by adding a LISA like inter satellite interferometer to the existing microwave ranging system. Future geodesy mission beyond GRACE-FO might use even more of LISA technology like testmass gradiometers featuring optical readout.

With regard to LISA and the future of laser interferometer based geodesy, it is of utmost importance to analyze, understand, and subsequently suppress tilt-to-length coupling in interferometric applications. To solve this challenge for the space missions named above, a solution has to be found and experimentally verified. Furthermore, sophisticated models and tolerance analysis are required to adapt the found solutions to according flight hardware and estimate the expected performance in space.

In previous experiments imaging systems were successfully tested due to their capability of reducing tilt-to-length coupling. However, these results are more a proof of principle than a performance estimation for real applications. In [TD2] it was not possible to rule out that the underlying concept which was used to stabilize the experiment is affecting the residual TTL coupling. Therefore, the result of this pre-experiment cannot be used to quantitatively describe the performance of imaging systems but only to test for certain properties. In the next iteration [6, P1], TTL

coupling behind an imaging system is measured in a simplified scenario with ideal beams. This was required to successfully stabilize the tilt actuator without removing TTL coupling contributions. However, in a realistic implementation additional contributions from imperfections and non optimal beams are expected which were not considered in this experiment. Within this thesis, a more sophisticated experiment is shown. A testbed is designed, built, and operated to proof that imaging systems can reduce tilt-to-length coupling below the required level in a scenario as representative as possible for LISA. This testbed consists of a LISA like optical bench and a telescope simulating device which provides a tiltable beam, either top-hat oder Gaussian shaped, which simulates the behavior of a LISA telescope or a test mass, respectively. The same testbed is used for a tolerance analysis of the tested imaging systems which provides information of the required alignment accuracy in future manufacturing. Based on the measured performance and the observed behavior of the old imaging system designs, the development of a new type of imaging system is presented which features the same performance as the old designs but is more robust against beam parameter variations.

Among others, the tilt-to-length coupling investigations in this thesis serve the purpose of testing the numerical simulation tool IfoCAD. The experimental measurements and analytic results are compared to respective simulations. On the one hand, this serves as a sanity check to eliminate systematic errors, and on the other hand, with a working and trusted simulation tool, the performance of future optical designs can be estimated. In this context, a diffraction simulation method (Gaussian beam decomposition) was implemented in IfoCAD. It uses a decomposition into spatially divided fundamental Gaussian beams to model the propagation and diffraction of an initial wavefront, which is demonstrated in a comparison between different diffraction simulation methods.

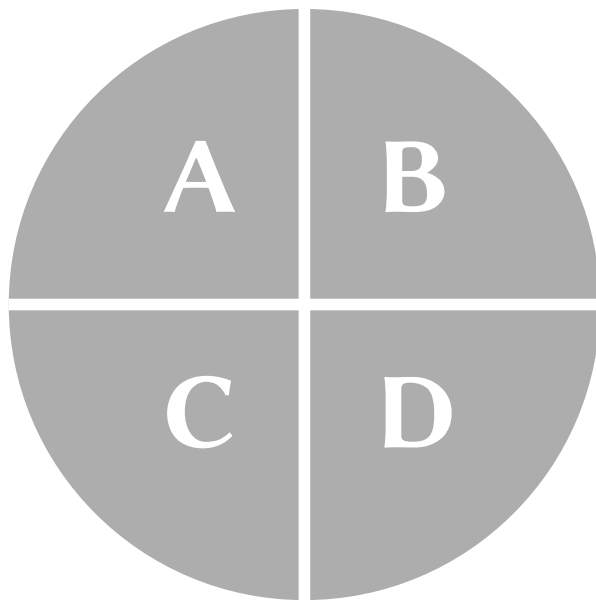
This thesis comprises three parts. The first part contains general information: basic knowledge about laser interferometry and an overview of different TTL coupling mechanisms. In Chapter 2 the fundamental methodology of LISA and GRACE-FO is explained. Further, basic knowledge concerning laser interferometry, including phase extraction and the definition of different signals are presented. IfoCAD, together with its underlying methods and algorithms is introduced and the classical concept of optical pupils is explained. In Chapter 3 TTL coupling is discussed. The basic concept is explained and an overview over the different TTL coupling sources is shown. Furthermore, different approaches to suppress TTL coupling are shown and imaging systems as a suppression concept is introduced.

The second part covers the LISA optical bench telescope simulator testbed. In Chapter 4 the concept and the methodology of the LISA testbed is explained. In Chapter 5 the results of the LISA testbed experiment are shown; starting with the alignment and calibration of the experimental setup and followed by the measurement results, including a tolerance analysis of two imaging systems.

The third part contains further investigations of optical noise sources. In Chapter 6 numerical simulations are used to investigate the beam parameter dependencies of the two imaging systems tested before. As a result, additional requirements are formulated, which enhance the robustness of future imaging systems. With the new requirements a new imaging system design algorithm is developed and two exemplary imaging systems are designed and compared to the two previous. In Chapter 7 a Gaussian beam decomposition method is developed and implemented into IfoCAD. This implementation is compared to other diffraction propagation methods and analytic solutions.

Part I

General information



2

Basics

This chapter describes the fundamental methodology of LISA and GRACE-FO. Further, basic knowledge concerning laser interferometry, including phase extraction and the definition of different signals are presented. IfoCAD, together with its underlying methods and algorithms is introduced. Parts of this chapter were previously shown in [6, 7].

2.1. Satellite interferometry

All investigations in this thesis were performed in the context of the space missions LISA and GRACE-FO. In the following sections the basic methodology of these missions is explained. Furthermore, the technical components which are relevant in the context of this thesis are introduced.

2.1.1. LISA

The Laser Interferometer Space Antenna (LISA) is a generic mission class for a space born gravitational wave observatory. LISA will consist of three spacecraft that form an equilateral triangle with an arm length in the range of millions of kilometers that follow Earth in a heliocentric orbit, as shown in Figure 2.1a.

The working principle of LISA is that the distance variations between free floating test masses are measured. The test masses act a gravitational reference sensors that follow the local gravity without external disturbances. A gravitational wave traveling trough the LISA constellation will alter the distance between the test masses as illustrated in Figure 2.2. The space in between two test masses (red and blue point) is compressed and stretched periodically. By monitoring the test masses the gravitational wave can be measured. The test masses are guarded by satellites in the corners of the triangle, following the movement of the test masses (Figure 2.1b). The purpose of the satellite is to protect the test masses from external forces, track the movement and orientation of the test masses and measure the distance to the other satellites.

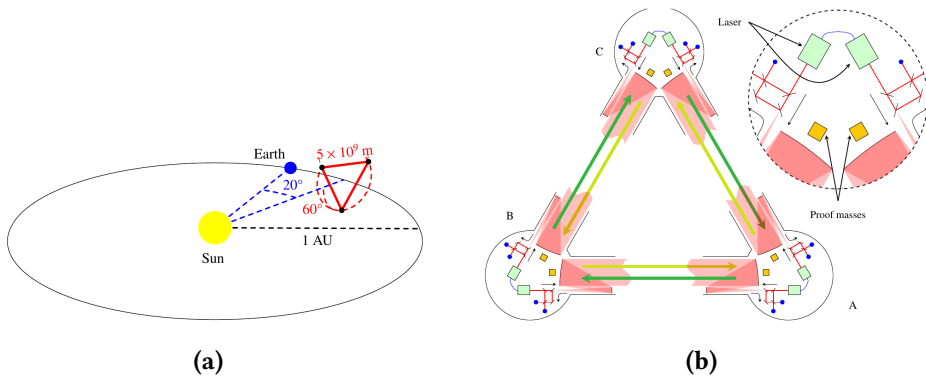


Figure 2.1.: Figure (a) shows the heliocentric orbits of LISA: the three satellites of LISA will form an equilateral triangle that follows Earth’s path around Sun, with a radial angle of $\approx 20^\circ$. Figure (b) shows the simplified concept of LISA, three spacecrafts (A,B and C) with each two test masses (one per axis) exchange laser light (green arrows) to track the distance between the satellites. Credit: [4]

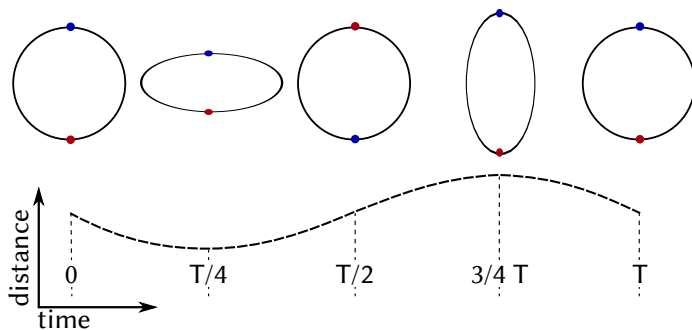


Figure 2.2.: A gravitational wave alters the distance between two sample points (red and blue). The circle indicates the actual deformation of space due to the gravitational wave. Without gravitational wave or at time zero, the space is not altered and the distance between the two points is “nominal” for times $\frac{1}{4}T$ and $\frac{3}{4}T$ the deformation is maximal and the distance between the two points is minimal and maximal. In between and after the gravitational wave has passed, the distance is “nominal”.

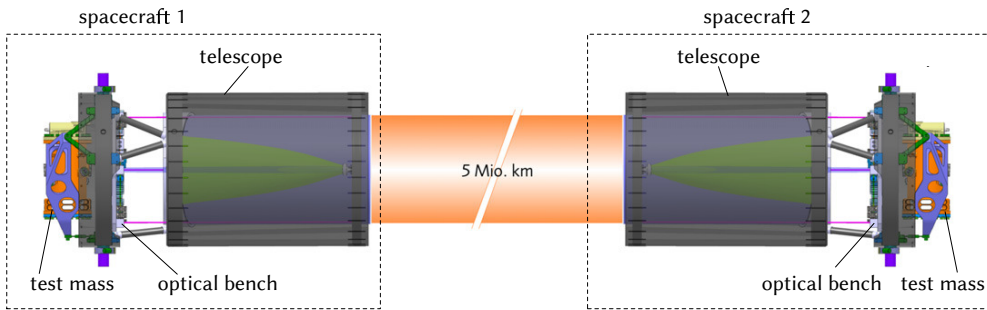


Figure 2.3.: Overview of one inter-satellite link of LISA. The distance measurement between two test masses is divided into three parts, the measurement between test mass one and the optical bench of spacecraft one (left), between spacecraft one and spacecraft two (center) and between test mass two and the optical bench of spacecraft two (right). Credit: [3]

In order to measure the distance between two test masses, multiple independent measurements are required (Figure 2.3): distance between satellite 1 and test mass 1, distance between satellite 1 and satellite 2 and distance between satellite 2 and test mass 2. To track all these length changes and establish a laser link, each satellite requires multiple interferometers. One to track the test mass (TM interferometer), one to track the distance to the remote spacecraft (science interferometer) and a reference interferometer to provide a stable reference for the heterodyne readout. All these interferometers are implemented on the optical bench, one of the key components of the LISA payload, which consists of two moving optical subassemblies (MOSA) per satellite, as shown in Figure 2.4. For each laser link to a remote satellite one MOSA is required, which consists of the telescope in the “front”, that gathers light coming from the distant spacecraft and sends light back. Located on the back side of the MOSA is the gravitational reference sensor, formed by the free floating test mass in its housing. In between test mass and telescope, the formerly mentioned optical bench (OB) is situated, that consists of a large Zerodur[®] plate with all interferometric components attached to it. All interferometers, optical readout diodes, and laser couplers are located on the OB.

The following section addresses the basics principles and functions of the different interferometers of LISA.

Test mass interferometer

The heart of a LISA satellite is the test mass, which is gold-coated cubic block made of a gold-platinum alloy, that act as a gravitational reference sensor. They follow the local gravity and are shielded from any external forces. The exact purpose of the TM interferometer is to measure the longitudinal movement of the TM as well as its tilt angles. A sketch of a TM interferometer is shown in Figure 2.5. A test mass is read out by reflecting one of two interferometric beams from it, with all required

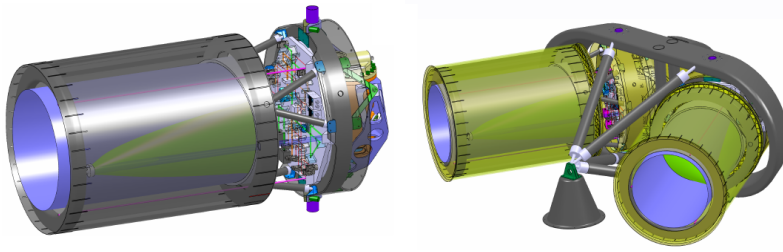


Figure 2.4.: LISA: Moving Optical Subassembly (MOSA). Left: single MOSA with telescope in the front, test mass in the back (inside the orange vacuum tank), and the optical bench in between. Right: two MOSA together (one for each arm) fixed in the support structure forming the default angle between two LISA arms of 60°. Credit: [4]

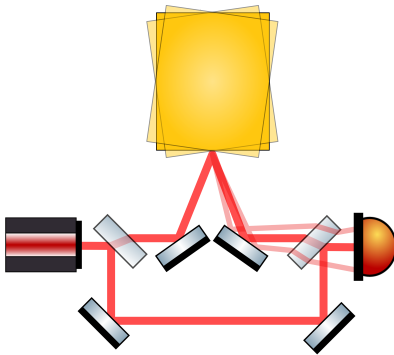


Figure 2.5: Sketch of a simplified test mass interferometer. One of the interferometric beams is reflected from the test mass and is therefore affected with the longitudinal position and the tilt angle of the TM, while the other beams is not. After the recombination of the two beams, the detector can readout the longitudinal position and the tilt angles. In contrast to the sketch shown here, most test mass interferometer are much more complex and feature a heterodyne readout.

information being imprinted on this beam. The longitudinal movement of the TM is imprinted on the phase relation between the two interferometric beams while the orientation is imprinted in the propagation direction of the reflected beam. The phase relation is read out using the longitudinal path length signal (Section 2.2.3) while simultaneously the TM angles are monitored, using the differential wavefront sensing signals (Section 2.2.5). Since both beams are generated within the test mass interferometer, they are very similar, in that they both feature a Gaussian profile with a waist radius of around one millimeter at a specified position within or near the core interferometer optics.

Science interferometer

The purpose of the science interferometer is to track the distance variation to a spacecraft on the other side of one LISA arm. The light, coming from the other side, is received via a large telescope to gather as much light as possible. The light from the telescope is delivered to the interface between telescope and science interferometer, which is an aperture, called RX-clip. The science interferometer measures the phase relation between this received laser beam (RX) and a locally generated beam (TX) while simultaneously sending the TX back to the distant spacecraft through the

telescope. Here, one locally generated beam is interfered with a beam that traveled millions of kilometers and was imaged to the interferometer through a telescope. Therefore, one beam is a Gaussian fundamental mode with e.g. a waist radius of 1 mm at a specified position, while the other is a small piece of a flat wavefront that was cut out by the telescope from a gigantic Gaussian fundamental mode. In the science interferometer it looks like a flat-top beam with the perturbations from the telescope. The science interferometer measures the received laser beam from the distant spacecraft delivered by the telescope and is therefore tracking the distance-change to the remote spacecraft.

2.1.2. GRACE

The technology developed for LISA in the past, is capable of tracking distance variations of satellites and test masses with an accuracy never reached before. In LISA this technology is used to measure space curvature induced by gravitational waves. However, it can also be used to measure space curvature originating from other sources, for example Earth.

With GRACE-FO (described in the subsequent section) LISA technology is used in a geodesy satellite mission for the first time. Since the technical requirements of LISA and laser interferometer based geodesy missions is similar, the results obtained within this thesis are applicable to these missions, too.

Gravity Recovery and Climate Experiment (GRACE)

The Gravity Recovery And Climate Experiment (GRACE) [8, 9] is a satellite mission measuring and monitoring Earth's gravity potential, launched in 2002. GRACE consists of two satellites trailing each other in a distance around 200 km in a low earth orbit. Both satellites follow the Earth's gravity potential, which alters the distance between the two satellites, and by monitoring distance variations between the satellites, the actual gravity field can be computed. Besides the gravity field itself, temporal changes in the gravity potential are very interesting. Changes in the gravity potential of Earth are caused by mass variations generated for example by decreasing ground water level [10], melting glaciers [11] or massive seismic events (Sumatra-Andaman earthquake 2004 [12]). With the help of GRACE, large scale variations in the mass distribution can be observed, which gives insight into mechanisms difficult to monitor using Earth-bound technology.

GRACE is flying in a low earth orbit and is experiencing a significant atmospheric drag, which has to be counteracted in order to keep the orbit stable, which in return consumes fuel. Upon fuel depletion, the orbit of GRACE will decay, and GRACE will burn up in the atmosphere. Since the lifetime of GRACE is expected to end in 2018, a successor mission is planned with the launch scheduled in 2018. In this successor mission, called GRACE-FO [13] the microwave ranging is still in place, but

an additional laser ranging system was added [14]. This laser ranging tool features a technique very similar to the inter-satellite ranging of LISA, promising a much higher accuracy than the microwave ranging system. Besides the enhanced data quality, the laser ranging interferometer on board GRACE-FO will demonstrate the first inter-satellite laser interferometer in space.

Beyond GRACE Follow-On

Specific missions beyond GRACE-FO are not designed yet, but the investigation and planning for possible mission concepts has already started. The overlap in required technology between gravitational observatories and gravity-based geodesy missions is quite large. The inter-satellite ranging on GRACE-FO is already based on LISA technology and further technology transfer is possible. This leads to advanced versions of previous missions, which are enhanced using techniques capable of improving the sensitivity of former designs and provides a link between gravitational observatories like LISA and the mentioned geodesy missions.

For the next generation, a laser link similar to the one implemented in GRACE-FO could provide an even higher accuracy than in GRACE-FO. A multi-axis gravity gradient sensor consisting of multiple LISA-like test masses with optical readout, could add a detailed measurement of the gravity gradient. Together, a state-of-the-art concept with enhanced sensitivity that features multiple measurements at the same time, can be sketched. However, a detailed design that can be realized with available technology has not been established yet. The different topics discussed in this thesis are work towards understanding and solving the challenges which stand between today and the future of satellite geodesy.

2.2. Interferometer for high-precision length measurements

Both the mission concept LISA and GRACE-FO are using laser interferometer technology to track the movement of satellites and test masses. In this section, the basic principles of high precision interferometry as used in these space based interferometers are explained.

2.2.1. Homodyne phase readout

Optical interferometry is a well known technique to track length variations. In a homodyne interferometer, a laser beam is split up into two secondary beams. Both secondary beams travel an individual path in an interferometer and are recombined later. This recombination generates an interference pattern which contains information about the distinct travel distances of the two beam parts. Assuming the optical

path length difference between the two beam parts is Δs , the interference pattern monitored by a photo diode would be

$$P = \bar{P} \left[1 + c \cdot \cos \left(\frac{2\pi}{\lambda} \Delta s \right) \right]. \quad (2.1)$$

Here, P is the power detected on the diode, \bar{P} is the mean power, c the contrast and λ the wavelength of the light used. This detectable power oscillates with the path length difference; the spacial frequency of this oscillation $2\pi/\lambda = k$ is called wavenumber and depends only on the wavelength. For $\Delta s = \lambda \cdot i$, $i \in \mathbb{Z}$ the power P is maximal, the two beams interfere constructively, this situation is called bright fringe. For $\Delta s = \lambda \cdot (i + 0.5)$, $i \in \mathbb{Z}$ the two beams interfere destructively and form the dark fringe with minimal detected power. In between at $\Delta s = \lambda \cdot (0.5 \cdot i + 0.25)$, $i \in \mathbb{Z}$, at the mid fringe point, the power detected is the average power. By choosing the operation point carefully, one can find the best trade-off between signal strength and noise, like the dark fringe detection in gravitational wave observatories [15] or the mid fringe detection in Appendix B.

The contrast c indicates the relation between the oscillating part and the DC part of the detectable power. With a perfect contrast of $c = 1$ the interference pattern oscillates between zero power and twice the mean power, at dark fringe and bright fringe. In this scenario the readout of the actual path length difference is optimal. With a bad contrast $c = 0.01$ only 1% of the detected power actually oscillates. In such scenarios the noise is usually very high.

2.2.2. Heterodyne phase readout

Besides the homodyne approach shown above, a more complex interferometric system is the heterodyne approach which will be used in LISA and GRACE-FO. In a heterodyne interferometer the frequencies of the two interfering beams are not equal, therefore the interference pattern is not stable in time but oscillates with the heterodyne frequency, which is the frequency difference between the two beams. The path length difference is now encoded in the phase change of the oscillation which can be seen in the following equations [6, 16, P2]. In a conventional heterodyne interferometer, two beams b_i with different phases ϕ_i , amplitudes A_i and frequencies Ω_i are superimposed. With the two beams represented as plane waves

$$b_n = A_n \cdot \exp(-i\phi_n) \cdot \exp(i\Omega_n t), \quad (2.2)$$

the intensity¹ J of the superposition of two beams becomes

$$\begin{aligned} J(r, z, t) &= \|A_1 \cdot \exp(-i\phi_1) \cdot \exp(i\Omega_1 t) + A_2 \cdot \exp(-i\phi_2) \cdot \exp(i\Omega_2 t)\|^2 \\ &= A_1^2 + A_2^2 + 2 \cdot A_1 A_2 \cdot \cos \left(-(\phi_1 - \phi_2) + (\Omega_1 - \Omega_2) \cdot t \right). \end{aligned} \quad (2.3)$$

¹The definition of intensity used within this thesis can be found in Appendix C.1.

With the frequency difference of the two beams $\Omega_{\text{het}} := \Omega_1 - \Omega_2$, the phase difference $\phi_1 - \phi_2 =: \Delta\phi$ and the average intensity $\bar{J} := A_1^2 + A_2^2$, this intensity J can be written as

$$\begin{aligned}
 J &= A_1^2 + A_2^2 + 2 \cdot A_1 A_2 \cdot \cos \left(\underbrace{(\Omega_1 - \Omega_2)}_{\Omega_{\text{het}}} \cdot t - \underbrace{(\phi_1 - \phi_2)}_{\Delta\phi} \right) \\
 &= (A_1^2 + A_2^2) \cdot \left[1 + \frac{2 \cdot A_1 A_2}{\underbrace{A_1^2 + A_2^2}_{c_J}} \cdot \cos \left(\Omega_{\text{het}} \cdot t - \Delta\phi \right) \right] \\
 &= \bar{J} \cdot \left[1 + c_J \cdot \cos \left(\Omega_{\text{het}} \cdot t - \Delta\phi \right) \right].
 \end{aligned} \tag{2.4}$$

By using a suitable detector, it is possible to measure the power fluctuation on its surface. The intensity is therefore integrated over the detectors surface S , to generate a power signal. The power is defined as a function of the contrast c , mean power \bar{P} , the frequency difference Ω_{het} and the phase difference $\Delta\phi$, by

$$\begin{aligned}
 P &= \int_S dx dy J \\
 &= \bar{P} \cdot \left[1 + c \cdot \cos \left(\Omega_{\text{het}} \cdot t - \Delta\phi \right) \right].
 \end{aligned} \tag{2.5}$$

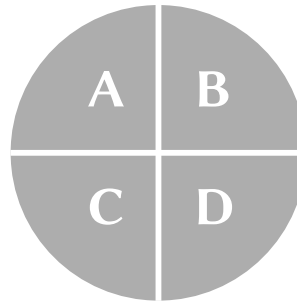
This measured power contains the phase $\Delta\phi$, which depends on the path length difference between the two interfering beams. To extract the phase from the measured power, it must be monitored over a period of $T_{\text{min}} = 1/\Omega_{\text{het}}$. The resulting pattern is then multiplied by an electronic oscillator of the same frequency. After an integration, the phase can be extracted. The detailed procedure to extract the phase $\Delta\phi$ from the detected power in Equation (2.5) is explained in Appendix C.2. In numerical simulations and analytical calculations this phase extraction can be simplified. Instead of simulating the power over an entire period and computing the phase from the results, it is possible to compute the phase via the complex amplitude a of the cos term, which can be computed via the overlap between the two beams

$$a = \int_S d^2 r b_1 b_2^* \tag{2.6}$$

$$\Delta\phi = \arg(a). \tag{2.7}$$

Here, b_2^* is the complex conjugated of b_2 . By handling the integration in the complex regime, the integration and phase estimation is much simpler. Furthermore, from the complex amplitude also the contrast can be computed, as shown in Section 2.2.6. A more detailed explanation and further information on this topic can be found in [6, 16, P2].

Figure 2.6: Illustration of a quadrant photo diode (QPD) with four segments that are separated by an insensitive slit. Standard labeling when seen from front (looking with the incident beam).



2.2.3. Path length definitions

In the previous section it was shown how the phase signal can be extracted from a detector in a heterodyne interferometer using a single element photo diode (SEPD). The relation between phase signal and path length change is given by

$$\frac{2\pi}{\lambda}\Delta s = \Delta\varphi. \quad (2.8)$$

Therefore, the longitudinal path length signal (s_{LPS}) can be defined as

$$s_{\text{LPS}} = \frac{1}{k}\Delta\varphi, \quad (2.9)$$

using the wavenumber $k = 2\pi/\lambda$, which translates a phase change of 2π into a path length change of λ . By using the complex amplitude a , the resulting SEPD path length signal becomes

$$s_{\text{LPS}} = \frac{1}{k}\arg(a). \quad (2.10)$$

However, in most interferometers more complicated split-detectors with multiple independent segments are used. In the scenarios described in this thesis, mostly quadrant photo diodes (QPD) are used. These diodes consist of four active segments, separated by an insensitive slit. An illustration of a QPD with labeling of the segments is shown in Figure 2.6.

In an experiment each of these segments provides an individual photo current from which an individual phase can be extracted. Analogously, a complex amplitude for each segment of such a QPD can be computed (cf. Section 2.2.2). In order to combine the complex amplitudes of the different segments to get an overall phase signal of the entire QPD, one has multiple options. The two most common QPD path length definitions are shown below [P3].

Averaged phase longitudinal signal

The first signal definition of the QPD phase is called averaged phase (AP). Here, the complex argument of each complex amplitude is computed and the resulting phases of each segment are summed up and divided by the number of segments

$$s_{\text{LPS}}^{\text{AP}} = \frac{\arg(a_A) + \arg(a_B) + \arg(a_C) + \arg(a_D)}{4k} = \frac{\varphi_A + \varphi_B + \varphi_C + \varphi_D}{4k}. \quad (2.11)$$

This path length definition is the most straightforward way of computing an overall signal, but it has some disadvantages. If the beam is not centered on the QPD, for example, it is located completely on one segment only, the phases on the other segments are completely meaningless but still used to compute the QPD path length signal. Another problem is, that this signal definition does not become the SEPD path length signal (s_{LPS}) for a QPD with slits of zero diameter, which would be an intuitive behavior of a proper QPD signal definition.

LISA Pathfinder longitudinal signal

The second signal definition is the most ‘‘SEPD’’ like way to compute a QPD path length signal. It is called LISA Pathfinder (LPF) signal definition because it is used in the LISA Pathfinder phase meter [17, 18]. To get the phase of the entire QPD, the complex amplitudes of each segment are summed up and the complex argument of this sum is computed

$$s_{\text{LPS}}^{\text{LPF}} = \frac{1}{k} \arg(a_A + a_B + a_C + a_D). \quad (2.12)$$

For a QPD with slits of zero diameter, the sum of the complex amplitudes of the single quadrants, corresponding to a sum of the integrals of the single segments, is equal to the complex amplitude of the entire diode (SEPD like). Therefore, for a slit diameter of zero the LISA Pathfinder QPD path length definition ($s_{\text{LPS}}^{\text{LPF}}$) becomes equal to the SEPD path length definition (s_{LPS}) [P3].

2.2.4. The differential power sensing signal

By comparing the time averaged power \bar{P} of the different segments, it is possible to determine the position of the beam centroid. If the beam is not centered on the QPD, single segments will sense a larger power than others. These power differences are used in the Differential Power Sensing (DPS) signal

$$\text{DPS}_h = \frac{\bar{P}_{\text{right}} - \bar{P}_{\text{left}}}{\bar{P}_{\text{total}}} = \frac{\bar{P}_{\text{right}} - \bar{P}_{\text{left}}}{\bar{P}_{\text{right}} + \bar{P}_{\text{left}}} \quad (2.13)$$

$$\text{DPS}_v = \frac{\bar{P}_{\text{up}} - \bar{P}_{\text{down}}}{\bar{P}_{\text{total}}} = \frac{\bar{P}_{\text{up}} - \bar{P}_{\text{down}}}{\bar{P}_{\text{up}} + \bar{P}_{\text{down}}}. \quad (2.14)$$

With respect to the different segments of a QPD, the horizontal and vertical DPS signals are computed by

$$\text{DPS}_h = \frac{\bar{P}_B + \bar{P}_D - \bar{P}_A - \bar{P}_C}{\bar{P}_A + \bar{P}_B + \bar{P}_C + \bar{P}_D} \quad (2.15)$$

$$\text{DPS}_v = \frac{\bar{P}_A + \bar{P}_B - \bar{P}_C - \bar{P}_D}{\bar{P}_A + \bar{P}_B + \bar{P}_C + \bar{P}_D}. \quad (2.16)$$

More information about the DPS signals can be found in [16, 19].

2.2.5. The differential wavefront sensing signal

By comparing the phases on different segments, it is possible to compute the angle between the incoming wavefronts (η_h and η_v for the horizontal and vertical angle). Therefore, the phases on different segments of the photo diode are compared. The phase relation between different sides of the QPD is for small angles proportional to the relative angle between the wavefronts with the constants of proportionality k_v^{DWS} and k_h^{DWS} respectively. This comparison is called differential wave front sensing signal (DWS) [16, 18, 20, 21]. The horizontal and vertical DWS signals are defined by

$$\text{DWS}_h = \varphi_{\text{left}} - \varphi_{\text{right}} \approx k_h^{\text{DWS}} \eta_h \quad (2.17)$$

$$\text{DWS}_v = \varphi_{\text{top}} - \varphi_{\text{bottom}} \approx k_v^{\text{DWS}} \eta_v. \quad (2.18)$$

The exact values of k_v^{DWS} and k_h^{DWS} depend on the beam parameters and on the geometry of the detector. With exact knowledge of these parameters, k_v^{DWS} and k_h^{DWS} can be computed analytically as shown in [22]. However, in experimental setups the DWS calibration parameters are usually measured.

Using the quadrant labeling shown in Figure 2.6, the horizontal and vertical DWS signals are computed by

$$\text{DWS}_h^{\text{AP}} = \frac{\varphi_A + \varphi_C}{2} - \frac{\varphi_B + \varphi_D}{2} \quad (2.19)$$

$$\text{DWS}_v^{\text{AP}} = \frac{\varphi_A + \varphi_B}{2} - \frac{\varphi_C + \varphi_D}{2}. \quad (2.20)$$

Here, φ_i is the phase on the segment i . This definition of DWS^{AP} means that the average phase of the left/right (Equation (2.19)) or upper/lower (Equation (2.20)) quadrants are being compared. This is just one option to define an AP DWS signal. Another way would be to neglect the divisions by 2, thus comparing the sum of the phases. This would lead to identical performance and identical results because the factor of 2 would simply end in the calibration of the angular readout (k_ϕ and k_η). Similar to the LPF path length signal definition also an SEPD like DWS signal can be defined.

$$\text{DWS}_h^{\text{LPPF}} = \frac{1}{2} \arg(a_A a_C) - \frac{1}{2} \arg(a_B a_D) = \frac{1}{2} \arg\left(\frac{a_A a_C}{a_B a_D}\right) \quad (2.21)$$

$$\text{DWS}_v^{\text{LPPF}} = \frac{1}{2} \arg(a_A a_B) - \frac{1}{2} \arg(a_C a_D) = \frac{1}{2} \arg\left(\frac{a_A a_B}{a_C a_D}\right) \quad (2.22)$$

This definition is less vulnerable to phase jumps and leads to the same result shown before. Therefore, this implementation is preferred.

2.2.6. The contrast

The power on a photo diode of a heterodyne interferometer oscillates in time with the difference of the field frequencies, as shown in Equation (2.5). The phase modulates this oscillation. To measure the phase, the oscillation has to be measured, too. To measure an oscillation with high accuracy, a big difference between the minimum and maximum in relation to the total power is necessary. This difference between the maximum power P_{\max} and the minimum power P_{\min} on the photo diode, is described by the contrast (compare to Section 2.2.2)

$$c = \frac{P_{\max} - P_{\min}}{P_{\max} + P_{\min}}. \quad (2.23)$$

In a heterodyne interferometer, the contrast is also related with the complex amplitude of Equation (2.6) as shown in [P2]

$$c = \frac{|a|}{\bar{P}}. \quad (2.24)$$

If the difference between maximum and minimum power is too low, an accurate measurement of the oscillation is difficult, or nearly impossible. The phase and also the DWS signals, which depend on the phases of the various segments, can be measured the more accurate the better the contrast is.

2.3. Optical Simulations with IfoCAD

IfoCAD [P2, 23, P4] is a framework of subroutines to model and simulate laser interferometers, which is developed at the Albert Einstein institute and used extensively within this thesis. Furthermore, in the context of this thesis new methods were implemented in IfoCAD, which is shown in Chapter 7. With IfoCAD it is possible to define arbitrary interferometric setups, use different beam types, propagate beams through the interferometer and compute the interferometers signals (path length, DWS, DPS, contrast, etc.) as they would be measured by a photo diode and processed by a phase meter. Together with powerful optimization routines [24, 25],

IfoCAD simplifies the planning and debugging of experiments significantly. Usual applications for IfoCAD are: signal prediction of experimental setups, optimization of optical designs (e.g. ghost-beam suppression), and computing of exact component positions for bonding [26, 27] or other permanent mounting methods. IfoCAD is able to trace and compute different laser beam models, like fundamental and higher order simple astigmatic Gaussian beams [28] and fundamental general astigmatic Gaussian beams [29, 30]. Furthermore, diffraction simulation methods are implemented in IfoCAD, as described later on in Chapter 7.

In the following sections, fundamental mechanisms and models used in IfoCAD are explained. This is not a complete list of the content of IfoCAD, but covers the core functionality of the software.

In the context of this thesis, the terms “mode” and “beam” describe different objects. A “mode” defines a particular fundamental solution of the wave equation. A “beam” is a more pragmatic closed object, like a laser in the lab. Such a beam can be represented by different modes, for example a certain beam can either be represented by a single Gaussian fundamental mode or by a superposition of many higher order modes.

2.3.1. Gaussian beams

The best option to describe a laser beam in an interferometer of the kind used in this thesis is the Gaussian beam [31, 32]. It is also the smallest of all solutions of the paraxial Helmholtz equation, and close to many practical beams.

Without polarization, higher order modes, and astigmatism, the fundamental Gaussian beam is often the best trade-off between simplicity and representativity. Assuming an interferometer with accurately built and aligned fiber couplers, thoughtful use of polarizers and wave plates, and the absence of clipping and diffraction the fundamental Gaussian beam represents the real laser beams very well and in a simulation it can easily be traced through the setup. In the end, the interferometric signals can be computed numerically and in special cases even analytically [P5] [22, 33].

The analytic expression of a fundamental Gaussian beam is commonly known

$$E(r, z, t) = E_0 \frac{\omega_0}{\omega(z)} \exp\left(\frac{-r^2}{\omega^2(z)}\right) \exp\left(-ik(z-z_0) - ik\frac{r^2}{2R(z)} + i\zeta(z)\right) \exp(i\Omega t). \quad (2.25)$$

E_0 is the amplitude of the electric field

$$E_0 = \sqrt{\frac{2P}{\pi\omega_0^2}}, \quad (2.26)$$

ω_0 is the waist radius, $\omega(z)$ is the spot size at the longitudinal position z , given by

$$\omega(z) = \omega_0 \sqrt{1 + \left(\frac{z - z_0}{z_R}\right)^2}, \quad (2.27)$$

with the position of the waist z_0 and the Rayleigh length z_R which is related to the waist radius and the wavelength λ

$$z_R = \frac{\pi \omega_0^2}{\lambda}. \quad (2.28)$$

$k = \lambda/(2\pi)$ is the wave number, $R(z)$ is the radius of curvature at the longitudinal position z

$$R(z) = (z - z_0) \left[1 + \left(\frac{z_R}{z - z_0} \right)^2 \right], \quad (2.29)$$

$\zeta(z)$ is the Gouy phase at the longitudinal position z

$$\zeta(z) = \arctan \left(\frac{z - z_0}{z_0} \right), \quad (2.30)$$

$\Omega = 2\pi c/\lambda$ is the angular frequency with the speed of light c and $r = \sqrt{x^2 + y^2}$ is the transversal distance to the beam axis. With the complex q parameter

$$q(z) = z - z_0 + iz_r \quad (2.31)$$

$$\frac{1}{q(z)} = \frac{1}{R(z)} - i \frac{\lambda}{\pi \omega^2(z)}, \quad (2.32)$$

Equation (2.25) can be simplified to

$$E_{\text{Gauss}}(x, y, z) = E_0 \exp \left(-ik \frac{x^2 + y^2}{2q} - ik(z - z_0) + i\zeta(z) \right) \exp(i\Omega t). \quad (2.33)$$

The electric field of the Gaussian beam can be computed at any point in space. The only parameters necessary are the beam axis, the waist position z_0 , the beam power P , and either two of the three parameters: waist ω_0 , Rayleigh length z_R , wavelength λ .

2.3.2. Ray transfer matrices

In IfoCAD, the beam tracing is realized using transfer matrices [32, 34–37]. Therefore, each ray (e.g. representing the axis of a Gaussian beam) is represented as a vector

$$\vec{b} = \begin{pmatrix} r \\ \alpha \end{pmatrix}, \quad (2.34)$$

with r representing the offset of the ray with respect to the optical axis and α showing the angle between ray and optical axis. A ray in this representation can be traced through a setup represented by the transfer matrix \hat{M} by simply multiplying the vector \vec{b} with the matrix to compute the propagated ray \vec{b}^*

$$\vec{b}^* = \hat{M} \cdot \vec{b}. \quad (2.35)$$

Table 2.1.: The different fundamental ray transfer matrices.

Description	Matrix
Propagation in constant refractive index – distance d	$\hat{P} = \begin{pmatrix} 1 & d \\ 0 & 1 \end{pmatrix}$
Refraction at a surface – refractive index from n_1 to n_2 , curvature ρ	$\hat{S} = \begin{pmatrix} 1 & 0 \\ \left(\frac{n_1}{n_2} - 1\right)\rho & \frac{n_1}{n_2} \end{pmatrix}$
Reflection at a surface – curvature ρ	$\hat{R} = \begin{pmatrix} 1 & 0 \\ -2\rho & 1 \end{pmatrix}$
Refraction at a thin lens – focal length f	$\hat{L} = \begin{pmatrix} 1 & 0 \\ -\frac{1}{f} & 1 \end{pmatrix}$

This propagation method is also called ABCD matrix analysis according to the naming convention of the matrix elements

$$\hat{M} = \begin{pmatrix} A & B \\ C & D \end{pmatrix}. \quad (2.36)$$

For a generic optical setup, the overall transfer matrix can be compiled by a simple sequences of fundamental transfer matrices. A list of the mostly used fundamental transfer matrices can be found in Table 2.1. A more complete list can be found in [34, Table 15.1].

An example for a more complex matrix is the refraction at a thick lens. With the primary and secondary curvatures ρ_1 and ρ_2 , the thickness t and refractive indices n_{lens} and n_{env} , the overall transfer matrix becomes

$$\hat{M}_{\text{thick lens}} = \hat{S}_2 \hat{P} \hat{S}_1 = \begin{pmatrix} 1 & 0 \\ \left(\frac{n_2}{n_1} - 1\right)\rho_2 & \frac{n_2}{n_1} \end{pmatrix} \begin{pmatrix} 1 & t \\ 0 & 1 \end{pmatrix} \begin{pmatrix} 1 & 0 \\ \left(\frac{n_1}{n_2} - 1\right)\rho_1 & \frac{n_1}{n_2} \end{pmatrix}. \quad (2.37)$$

Besides simple rays, more complex beams can be propagated using transfer matrices too. A Gaussian beam can be characterized by its base ray (beam axis) and the q parameter as shown in the previous section. In an optical setup the base ray can be propagated by ABCD matrices and the q parameter can be propagated too. According to the convention in Equation 2.36, the propagated q parameter becomes

$$q^* = \frac{Aq + B}{Cq + D}. \quad (2.38)$$

2.4. Optical pupils

In classical optics, a pupil is an aperture. Related to the human eye, the pupil is the central transparent area which allows light to enter the eye and reach the retina where the actual detection happens. In this optical system, the pupil limits the amount of light that can enter the system and therefore defines the brightness of the captured image. Besides the human eye, optical systems have one or more pupils, too. One of these pupils in an arbitrary optical system is a real aperture or an optical element of finite size. This real pupil is the narrowest part of the optical system and limits the allowed angle and offsets of beams passing through. Any image of this pupil that is produced by the surrounding optical elements, e.g. lenses, is a virtual pupil. That means, any ray passing through a virtual pupil can pass the entire system, and any ray that does not fit through the virtual pupil will be blocked later, or was blocked before by the real aperture. It does not matter which of the pupils in an optical system is real, if either of the virtual pupil would become real, the properties of the system would not change.

Out of the many pupils of an optical system, two are especially important. These are the entrance and the exit pupil. The entrance pupil is the image of the real aperture through the optics in front of the aperture (if there are no optics in front, the aperture itself is defined as the entrance pupil). The exit pupil is the image of the aperture stop through the optics that follows the aperture stop (if there are no optics behind the aperture, the aperture itself is the exit pupil). Figure 2.7 shows an exemplary lens with focal length f and an aperture in front of the lens. The real aperture defines the entrance pupil, the projection of the aperture through the lens defines the exit pupil. The entrance pupil defines under which angle an object can send light through the system. The exit pupil defines under which angle the light leaves the system (bottom half of Figure 2.7).

By aligning the exit pupil (position, orientation and size) of one system with the entrance pupil of another system, optical systems can be combined. For example if the exit pupil of a telescope is matched with the entrance pupil of a human eye (the original pupil), the two system act together and the human can see a sharp image through the telescope.

Of special interest within this thesis is the concept of a classical pupil plane imaging system. A classical pupil plane imaging system is a lens setup with some special attributes: Parallel rays, that enter the entrance pupil will leave the exit pupil also parallel (example in Figure 2.8 top). Rays with different angles to the optical axis, that cross the entrance pupil plane in the same point, will also cross the exit pupil in the same point (example in Figure 2.8 bottom).

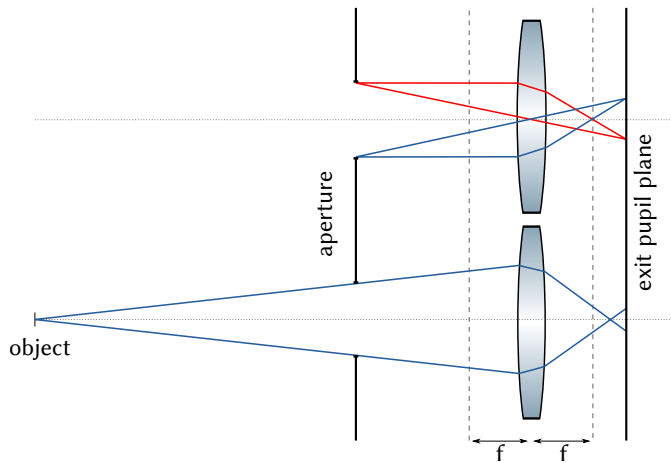


Figure 2.7.: Top: the pupil planes are defined via the aperture stop. The aperture in front of the lens defines the entrance pupil, the image of the aperture behind the lens defines the exit pupil. Bottom: the entrance pupil defines under which angle a ray from an object can propagate through the system, the exit pupil defines under which angle a ray can leave the system.

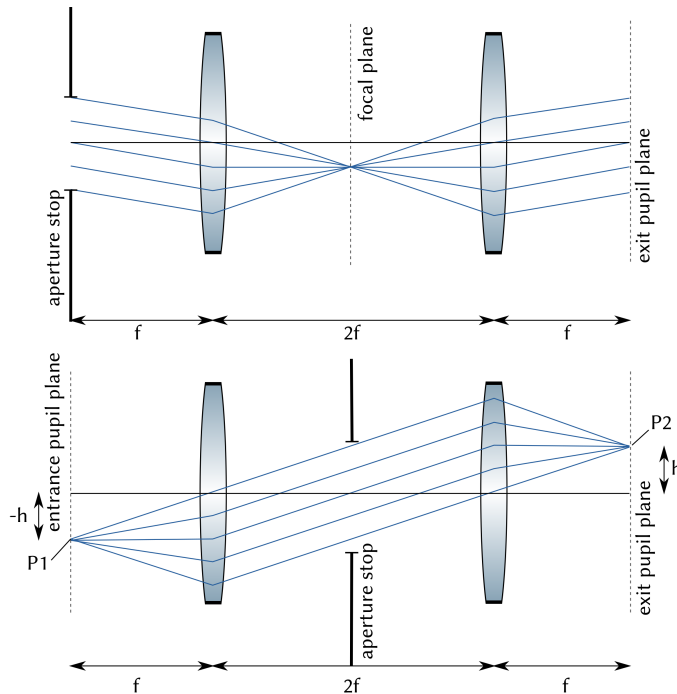


Figure 2.8.: Classical pupil imaging system. (a) Each ray of a parallel ray-package, that enters the pupil imaging system under an arbitrary angle, will cross the focal plane between the lenses in the same point, and the outgoing rays are again a parallel package. (b) Independent of the angle at the start point P_1 , all rays will cross at the same point P_2 . Credit: [38]

Tilt-to-length coupling

This chapter introduces tilt-to-length (TTL) coupling as an optical noise source. The basic concept is explained and an overview over the different TTL coupling sources is given. Furthermore, different approaches to suppress TTL coupling are shown and imaging systems as a suppression concept are introduced. Parts of this chapter were previously published in [6, P1, P5].

One of the major noise sources in satellite interferometry is originating from angular misalignments between the interferometric beams, as might result by an angular mismatch between a LISA satellite and the free floating test mass in the center of the spacecraft. The purpose of the test-mass interferometer is to monitor position and orientation of the TM. Therefore, the DWS signal is measured in order to track the angular alignment of the TM and the path length signal is measured to observe its longitudinal position. If the TM happens to be tilted, the measurement beam reflected at the TM becomes tilted, too. This tilt of one of the interferometric beams couples into the path length readout. In Figure 3.1, a tilted measurement beam is compared to a non tilted reference beam. The tilt increases the distance that the measurement beam has to propagate until it reaches the detector. Thus, the path length signal will measure this longer distance and the pure tilt of the beam will look like a longitudinal movement. This cross correlation between tilt and path length readout is called tilt-to-length (TTL) coupling. Besides geometric TTL coupling mechanisms, like a longer propagation distance, also non geometric TTL sources are known (e.g. wavefront related). In certain scenarios it is sufficient to describe TTL coupling with pure geometry, but in general, the non geometric aspects have to be considered as well. Within this chapter, the fundamental mechanisms behind TTL coupling are explained, both geometric and non-geometric. This is not a quantitative computation of the strength of the different effects, but more a qualitative explanation of the different mechanisms. Furthermore, examples are shown in which the TTL coupling is dominated by wavefront related mechanisms and the geometric effects are not visible anymore.

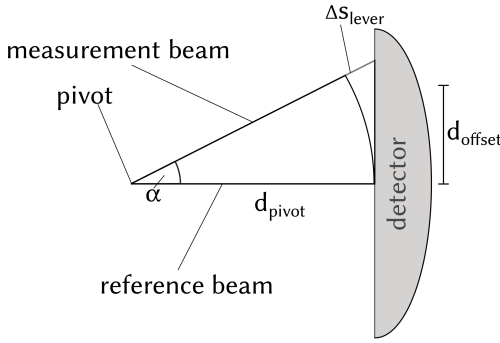


Figure 3.1: Geometric (lever arm) TTL coupling explained in a simplified scenario. The reference beam is centered on the detector and the measurement beam is tilted by the angle α around the pivot. The geometric path length change Δs is the additional distance the measurement beam has to propagate until it reaches the detector.

3.1. Geometric tilt-to-length coupling

3.1.1. Lever arm tilt-to-length coupling

Assuming a tilting TM where the center of rotation coincides with the beam reflection point, the lever arm TTL coupling can be observed. To understand the lever arm TTL coupling caused by a tilted beam, only a simplified interferometer reduced to its essential components is required, considering just the reference beam, the (tilted) measurement beam, and the photo diode as shown in Figure 3.1.

Since the point of rotation has a longitudinal offset with respect to the detector (lever arm), a measurement beam tilt results in a longer distance that the measurement beam has to travel from the pivot to the photo diode. Using straightforward geometry, this geometric path length change Δs_{lever} can be computed analytically,

$$\Delta s_{\text{lever}} = \left(\frac{1}{\cos(\alpha)} - 1 \right) d_{\text{pivot}} \approx \frac{\alpha^2}{2} d_{\text{pivot}} + O(\alpha^4). \quad (3.1)$$

Here, α is the beam angle and d_{pivot} the distance between the pivot and photo diode (as shown in Figure 3.1).

3.1.2. Piston effect

In reality, it is unlikely that a tilting object will rotate around the point of reflection. For example a TM in LISA will rotate around its center of mass rather than a point on its surface. Thus besides the lever arm TTL coupling, also the piston effect has to be taken into account.

Figure 3.2 illustrates this piston effect, which is produced by an offset between pivot and the reflective surface of a component. A rotation will lead to movement of the reflective surface, which will be imprinted on the beam that is reflected at it. The coupling between tilt and twice the longitudinal movement of the surface (the beam has to propagate the distance twice) is called piston effect. For a longitudinal/lateral offset between point of rotation and point of reflection $d_{\text{long}}/d_{\text{lat}}$, the longitudinal

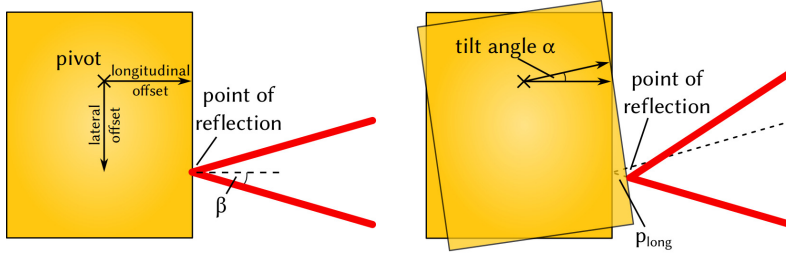


Figure 3.2.: Piston tilt-to-length coupling is produced by an offset between pivot and reflecting surface. A tilt of a TM leads to a longitudinal movement of the reflective surface.

movement p_{long} of the surface can be computed

$$p_{\text{long}} = d_{\text{lat}} \sin \alpha + d_{\text{long}}(1 - \cos \alpha) \quad (3.2)$$

$$\approx d_{\text{lat}} \alpha + d_{\text{long}} \alpha^2. \quad (3.3)$$

Depending on the angle of incidence β , the resulting path length change of a reflected beam Δs_{piston} is given by

$$\Delta s_{\text{piston}} = 2 \cos(\beta) p_{\text{long}} \approx 2 \cos(\beta) (d_{\text{lat}} \alpha + d_{\text{long}} \alpha^2). \quad (3.4)$$

3.1.3. Discussion

The TTL coupling mechanisms explained so far originate from pure geometry, longer propagation distances and real movements of surfaces. In order to treat these effects as simple as they were introduced, we must assume that our laser beams are either classical rays or infinite plane waves. Unfortunately, both is not realizable in an experimental setup. In the best scenario, the beams that are used in real interferometers can be described as Gaussian beams, while in LISA and similar missions, we have to deal with diffracting and wavefront error affected flat-top like beams. In these situations the previously introduced mechanisms are still active, however, depending on the system details, they might be covered by other effects that might be even stronger. The following two examples demonstrate that the geometric effects shown before are not sufficient to describe TTL coupling in real interferometers.

Rotation around the radius of curvature The first example is a rotation of a Gaussian beam (measurement beam) around a pivot that has a longitudinal distance to the detector that is equal to the radius of curvature of the wavefront on the detector, as shown in Figure 3.3a. In this scenario, a tilt of the measurement beam does not change the phase distribution on the detector. If the reference beam features the same

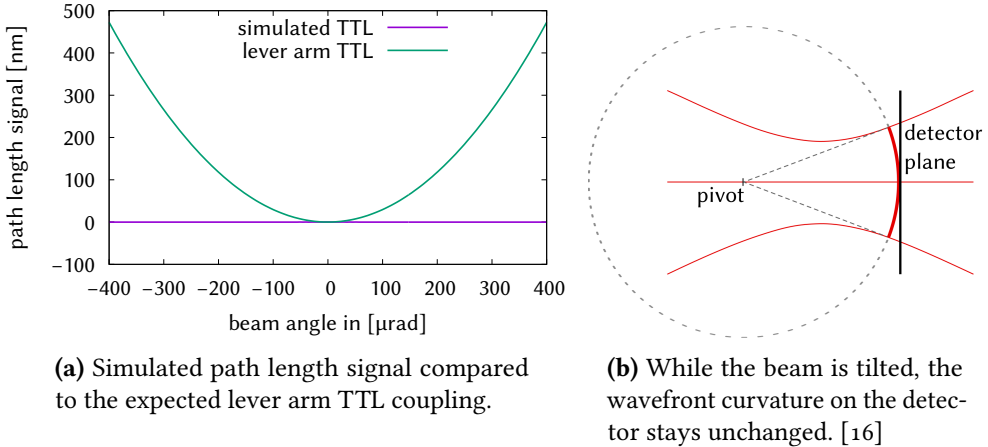


Figure 3.3.: A Gaussian beam is tilted around a pivot that coincides with the center of the wavefront curvature at the detector position. The expected lever arm TTL coupling can not be observed in the simulation. Due to the special conditions of this scenario (rotation without change of the wavefront), the system behaves differently than expected. The simulation parameters are: waist radius 1 mm, waist position 0, pivot -1 times Rayleigh length, lever arm two times Rayleigh length, SEPD radius 5 mm.

wavefront curvature, each point on the detector will see the same phase relation between the two beams, independently of the tilt angle. Thus, the TTL coupling should vanish in this situation, since a tilt is not affecting the phase distribution on the detector. However, in this setup a lever arm between point of rotation and detector should lead to TTL coupling, according to the previously introduced lever arm TTL coupling. To verify that in fact no TTL coupling is present in this scenario, a simulation is shown in Figure 3.3b. The path length signal is compared to the analytic expression of the lever arm TTL coupling. The simulated data show no TTL coupling, thus the pure geometric description of this scenario is not sufficient. Due to the fact, that the used beams are neither plane waves nor geometric rays, but Gaussian beams, the lever arm is invalid. The sole factor that defines the amount of TTL coupling in this special case is the shape of the wave fronts alone.

Vanishing tilt-to-length coupling In the second example, two perfectly equal beams, i.e. with the same intensity distribution and phase fronts, are superimposed to form an interferometer. If one of the two beams is tilted with respect to the other around a pivot that only has a longitudinal offset, but no lateral offset to a detector (cf. Figure 3.1), which is infinitely large, no TTL coupling occurs. A comparison between the expected lever arm TTL coupling and the simulated path length signal in this scenario is shown in Figure 3.4. The lever arm TTL coupling that should be present here cannot be measured, even if the phase on the detector changes while tilting. In

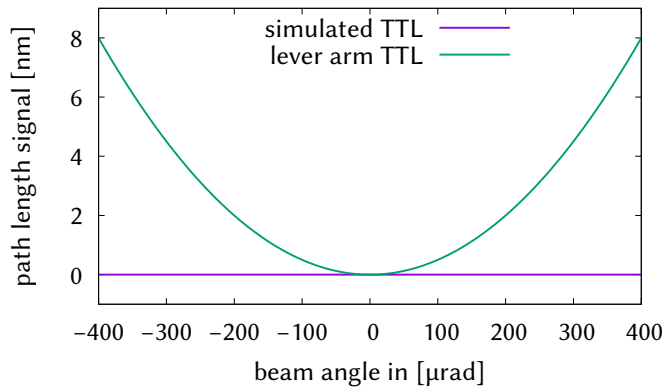


Figure 3.4.: Vanishing TTL coupling in a scenario with two equal Gaussian beams and an infinitely large detector – Simulation parameters: waist radius 1 mm, waist position 0 mm, pivot 0 mm, lever arm 100 mm, SEPD radius 100 mm.

this case, another TTL coupling mechanism that is caused by the tilt dependent beam walk on the detector, happens to generate the exact same amount of TTL coupling, but with a different sign. The two effects cancel each other out, such that no TTL coupling can be measured. A detailed investigation and explanation of this effect can be found in Appendix A.

3.2. Non geometric tilt-to-length coupling

The two previous examples show that TTL coupling with Gaussian beams is more than pure geometry of the beam axis. The shape of the beam, especially the phase front has a large influence on the expected TTL coupling. When two wavefronts are superimposed on a detector, the phase differences at individual positions are integrated over the detector surface. A tilt of one of the wavefronts will induce additional phase differences that depend on the tilt angle and the lateral distance to the rotation axis, as demonstrated in Figure 3.5. Here, a reference beam (blue wavefront) and a measurement beam (red wavefront) are interfered. The local phase difference between the two wavefronts at different positions (Φ_i) are symbolized by small arrows (phasor). Assuming the photo diode and the phase extraction is simplified by a summation over all Φ_i , the resulting total phase is shown as a green arrow. The angle of the green arrow contains the phase, while its length is the local amplitude. It can be observed that the angle-induced phase variations cancel and no TTL coupling occurs. However, many mechanisms disturb this balance and thus generate TTL coupling. As an addition to the previously introduced geometric effects, the following section lists and explains different wavefront and beam property related TTL coupling mechanisms.

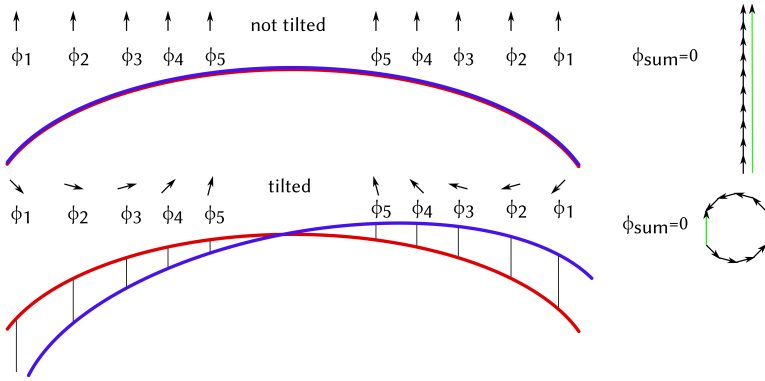


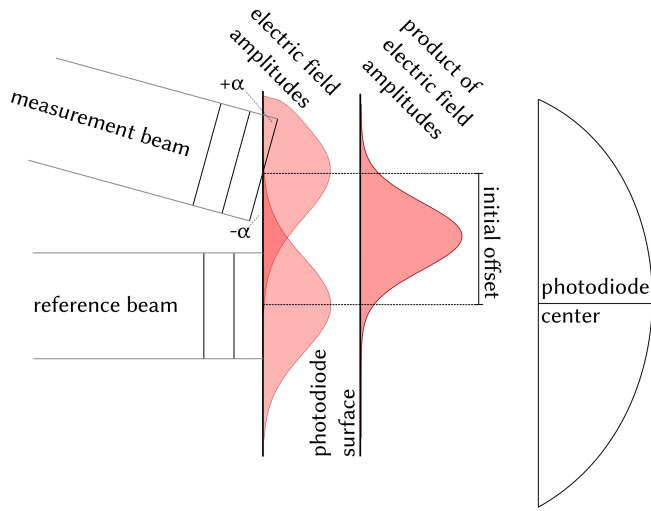
Figure 3.5.: Two wavefronts are superimposed. Here, the Φ_i indicate the local phase difference between the two wavefronts at different points on the detector. Φ_{sum} is the integrated phase of the entire detector, indicated by the green arrows on the left. If one wavefront is tilted around its center on the detector, the phase differences between the two wavefronts change. The lateral distance between the individual points and the center of rotation determine how large the phase change is, while the side (left or right with respect to the rotation point) defines the sign of the phase change. The phase changes are point symmetric with respect to the rotation axis. Therefore, by integrating over the entire detector, the phase changes cancel each other and the total phase stays the same.

3.2.1. Beam offset tilt-to-length coupling

The additional offset on the detector leads to a shift of the overlap between the two interfering beams, as shown in Figure 3.6. Without beam offsets, the overlap is symmetric with respect to the wavefronts and the weighting will not disturb the cancellation of the additional phases on each side, as shown in Figure 3.7. An offset of one beam and the resulting imbalance of the overlap will favor one side and therefore generate TTL coupling, as demonstrated in Figure 3.8. The amount of TTL coupling generated by a beam offset depends strongly on the beam and detector geometry. Additionally, besides dynamic offsets that vary over the beam angle (compare to the previous Section 3.1.1), also initial offsets that are constant over the beam angle are possible. The difference between a dynamic and a constant offset shows in the expected TTL coupling shape. A constant offset discriminates different sides of a detector and therefore produces TTL coupling $\Delta s_{\text{const. offset}}$ that can be expressed by an odd polynomial (asymmetric towards the tilt angle)

$$\Delta s_{\text{const. offset}} \propto \sum_n a_n \alpha^{2n+1}. \quad (3.5)$$

Figure 3.6: The reference beam is centered on the SEPD, the measurement beam has an offset and is tilted around its center. This offset results in a different weighting of the phase differences; the negative phase part has a higher weighting and the resulting coupling shows a negative phase.



In contrast, a dynamic offset, which leads to perfect alignment at angle zero, is a circular symmetric problem. Thus, a dynamic offset produces TTL coupling $\Delta s_{\text{dyn. offset}}$ that is symmetric towards the tilt angle (even polynomial)

$$\Delta s_{\text{dyn. offset}} \propto \sum_n a_n \alpha^{2n}. \quad (3.6)$$

The parameters a_n describe the contribution in different polynomial orders. In principle they can have any value, however most of the time the TTL coupling is dominated by lower orders. The exact value for a specific situation depend on the involved beams, the offsets of the rotation point, and the detector geometry.

In general, the real movement of a beam in an experiment is a combination of both, a constant offset (misalignment) of the beam and additional beam walk on the detector, which depends on the angle. Thus the symmetric and the asymmetric contributions add up and the resulting TTL coupling can take any shape.

3.2.2. Beam parameters tilt-to-length coupling

In the previous examples, measurement and reference beam had the same intensity and phase profile on the detector. However, this is not representative for interferometers like LISA, GRACE-FO or future geodesy missions that use heterodyne interferometers with beams that are generated from different components and therefore have differences in their parameters. Furthermore, in the science interferometer a flat-top beam is superimposed with a Gaussian beam, which means that the beam parameters are significantly different and it is impossible to match them. Unfortunately, beam parameters have a strong influence on the TTL coupling, and mismatches in the beam parameters generate additional TTL coupling [P1]. The main reason for this is a discrepancy between the wavefront curvatures of the beams in the detector plane.

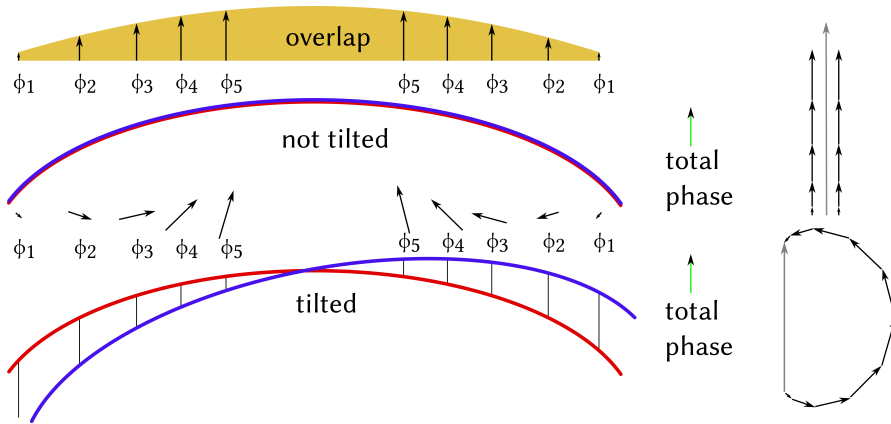


Figure 3.7.: The phase informations at different positions on the detector are weighted with the overlap (product of the electric field amplitudes) between the two interfering beams. The overall phase (green) does not change via tilting.

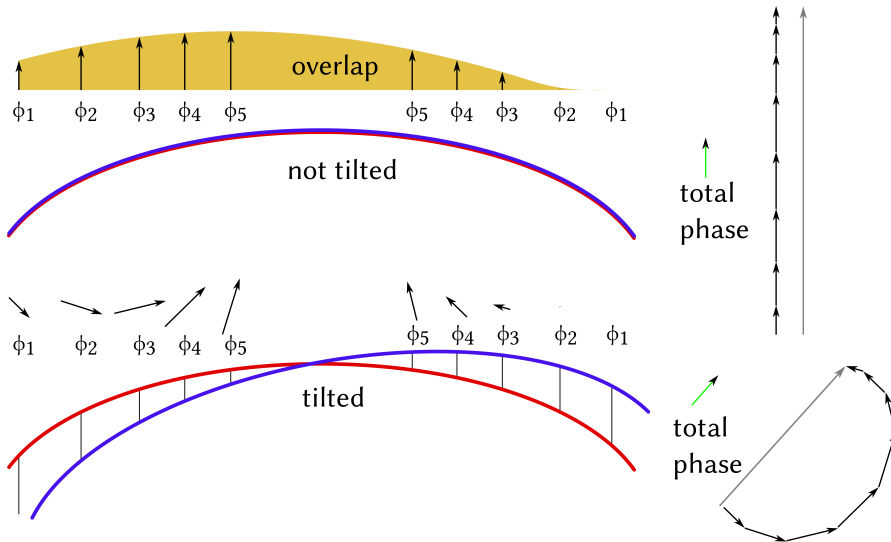


Figure 3.8.: The phase information at different positions on the detector are weighted with the overlap (product of the electric field amplitudes) between the two interfering beams. This overlap is asymmetric because an initial offset shifted the amplitude profile of one beam. The overall phase (green) changes via tilting, because the different sides are weighted differently.

Figure 3.9 shows a qualitative explanation of the effect. If the wavefronts and the pivot are well aligned as shown in the upper part of Figure 3.9, the phase difference is equal for all Φ_i . The averaged total phase will be equal to each single phase of the Φ_i . By tilting two beams against each other, an additional-phase-difference will appear between the measured wavefronts. This additional-phase-difference increases with the lateral distance to the pivot. The same phase difference will appear on both sides of the pivot, but in opposite directions. By measuring the entire interference pattern, the additional-phase-differences cancel each other and the resulting total phase will stay constant (compare the angle of the two green arrows in the upper part of Figure 3.9).

If the wavefront curvatures happen to be unequal (lower part of Figure 3.9), the values of the Φ_i will vary, depending on the curvature mismatch. Therefore, the averaged total phase will be different from the single Φ_i phases. If the wavefronts with different curvatures are tilted they see the same additional-phase-difference which appears on both sides with different sign and increases with lateral distance. By measuring the entire interference pattern these additional-phase-differences still cancel each other, but will result in a loss of contrast in the interferometric signal. This loss of contrast as well as the additional-phase-difference depends on the lateral distance to the pivot. Therefore, a wavefront tilt will discriminate the Φ_i in the outer areas of the photo detector. For equal wavefronts this is uncritical since every point on the detector gives the same signal. However, for unequal wavefronts, each point generates a different phase signal. By tilting the wavefronts, the balance between the different phases changes and thus the resulting total phase signal (the average of the Φ_i) changes, too. This can be seen in the two green arrows in the bottom half of Figure 3.9. The total phase in the titled scenario is shorter (loss of contrast) and has a different angle (the phase has changed).

Beam parameter variations generate (at least for fundamental Gaussian beams) circular symmetric variations in the geometry of the beam. Without initial offsets and misalignments between reference-, measurement-beam, and detector, the entire scenario is symmetric with respect to the tilt angle. Therefore, the resulting beam parameter related TTL coupling $\Delta s_{\text{beam parameter}}$ must be symmetric, too.

$$\Delta s_{\text{beam parameter}} \propto \sum_n a_n \alpha^{2n} \quad (3.7)$$

The TTL coupling $\Delta s_{\text{beam parameter}}$ can be expressed as an even order polynomial. However, usually this effect is dominated by the second order term. The exact values of the constants a_n depend on beam parameters, the detector, and the geometric setup.

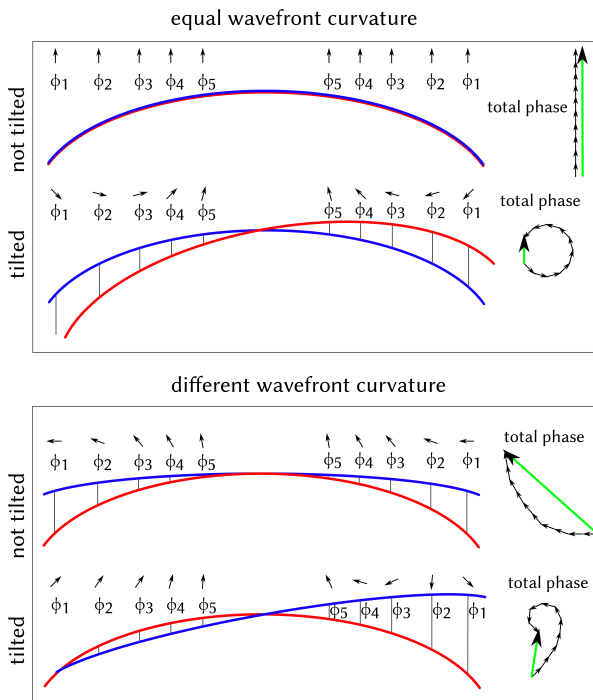


Figure 3.9: Demonstrative explanation of the TTL coupling generated by a wavefront curvature mismatch. For simplicity, the electric field amplitudes are considered to be constant over the detector’s surface.

3.2.3. Tilt-to-length coupling due to the path length definitions

As shown in Section 2.2.3, many different ways of combining the signals from different QPD segments to compute a longitudinal path length signal are known. The two mostly used definitions were explicitly shown in Section 2.2.3, however many more definitions are possible. All these different definitions have distinct properties and in this section, an explanation is given why the averaged path length signal (AP) generates less TTL coupling than the LPF signal in certain situations.

Figure 3.10 intuitively depicts the effect of different wavefront curvatures on the TTL coupling with different path length definitions. In the center, two interfering wavefronts are shown, with equal curvatures in Figure 3.10a, and with unequal curvature in Figure 3.10b. The local phase difference between the two wavefronts is indicated by a small phasor. The overall phase is a combination of these small vectors. Depending on the phase signal definition, the phasors are recombined in different ways. On the right, the LPF definition sums up all phasors coherently. On the left, the AP definition computes a coherent average phase per side (left and right) and adds the averaged side phases incoherently. In case of equal wavefront

curvatures, Figure 3.10a, the overall phase (green phasor) is independent of the tilt angle for both phase definitions. In contrast, in case of unequal wavefront curvatures in Figure 3.10b, the overall LPS phase changes via tilting while the overall AP phase is unaffected by tilts.

For the LPS signal, the path length change can be explained by an inhomogeneous contrast loss over the QPD area, the outer parts lose more contrast than the inner parts, the resulting path length is different because the phases of the different points are unequally weighted. For the AP signal, this loss of contrast is less important, because the left and the right parts are not added directly. The left phase and the right phase are added incoherently and therefore, the conjugated points cannot balance each other and no point loses any contrast. The phase does not change even for unequal wavefront curvatures. If the AP signal is used in an interferometer where no beam walk occurs, it could be a possible way to minimize the TTL coupling produced by unequal wavefront curvatures.

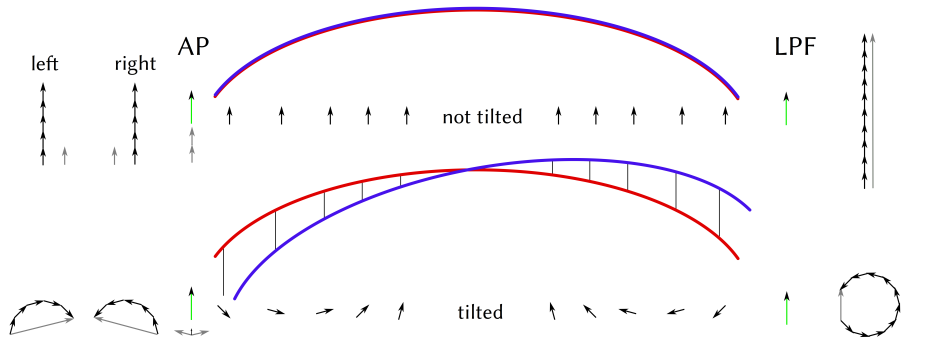
Without initial misalignments in the interferometer and assuming a path length definition that is symmetric with respect to the QPD segments, the TTL coupling due to the path length signal Δs_{LPS} is a circular symmetric problem. Therefore, this TTL coupling must be symmetric with respect to the beam angle and can be expressed as an even order polynomial, similar to the beam parameter TTL coupling

$$\Delta s_{LPS} \propto \sum_n a_n \alpha^{2n}. \quad (3.8)$$

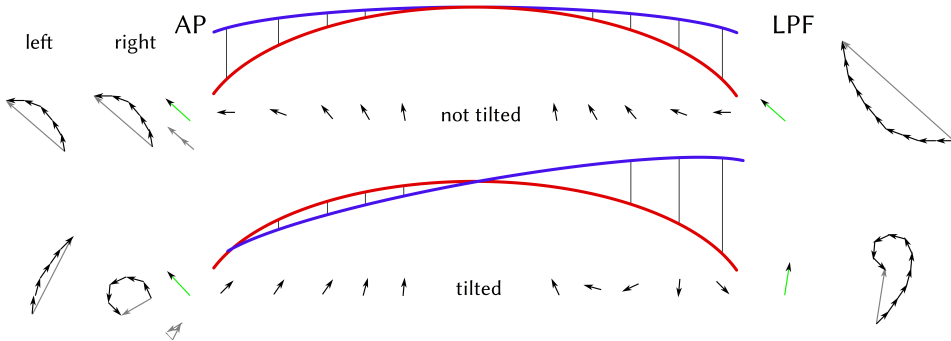
3.2.4. Wavefront errors tilt-to-length coupling

The cancellation of the different phase changes from the two sides as shown in Figure 3.10, only works if the amplitude of the different phases is uniform or at least symmetric to the axis of rotation. If the two interfering beams are not fundamental Gaussian modes without disturbances like clipping or wavefront errors of any kind, it happens that the amplitude profile is not symmetric anymore. In this case additional TTL coupling appears because the tilted wavefront is weighted differently on the two sides as shown in Figure 3.11, which disturbs the cancellation shown in Figure 3.5 [6]. In general, a higher order Gaussian beam or a clipped wavefront is not symmetric with respect to its beam axis. Therefore, the resulting imbalance on the detector shows no specific symmetry, thus the resulting wavefront error related TTL coupling Δs_{WFE} is expected to be arbitrary

$$\Delta s_{WFE} \propto \sum_n a_n \alpha^n. \quad (3.9)$$



(a) equal wavefront curvatures



(b) unequal wavefront curvatures

Figure 3.10.: The effect of different wavefront curvatures with different path length definitions on the overall phase. On the right, the LPF definition sums up all phasors coherently. On the left, the AP definition computes a coherent average phase per side (left and right) and adds the averaged side phases incoherently. In case of equal wavefront curvatures, Figure (a), the overall phase (green phasor) is independent of the tilt angle for both phase definitions. In contrast, in case of unequal wavefront curvatures in Figure (b), the overall LPF phase changes via tilting while the overall AP phase is unaffected by tilts.

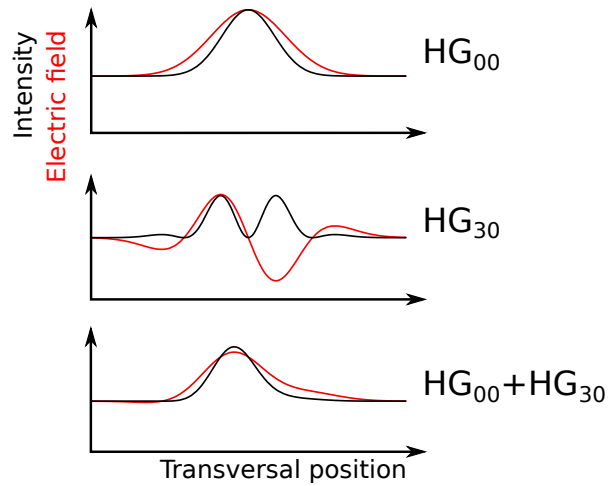


Figure 3.11: A fundamental mode is mixed with a HG_{30} mode, the resulting beam is asymmetric.

3.2.5. Detector geometry tilt-to-length coupling

The same effect can be achieved with a change of the detectors geometry. If the segments have different efficiencies or different shapes due to defects or additional features like bonding wires, the balance is disturbed and a tilting wavefront, even with perfect parameters, will induce additional TTL coupling. A detailed investigation about the spatial response pattern, additional features (bonding wires), and crosstalk between segments of photo diodes can be found in [39]. Similar to wavefront errors, the exact aberration to an ideal detector can take any form. Therefore, the TTL coupling generated by such a detector $\Delta s_{\text{detector}}$ can take any form, too

$$\Delta s_{\text{detector}} \propto \sum_n a_n \alpha^n. \quad (3.10)$$

3.3. Summary of the different mechanism

While the pure geometric effects that generate TTL coupling can be computed analytically, it is not possible to give a simple general expression that describes the other, wavefront related, effects. However, the principle behavior can be described. For the TTL coupling effects, shown in the previous sections, an overview with the basic behavior and the expected TTL coupling is shown in Table 3.1.

In a real scenario, multiple of these effects act together and generate only one measurable overall TTL coupling. To decompose this into contributions from different effects is not trivial. However, in certain special cases it is possible to analytically compute the overall TTL coupling, as well as identifying the contributions of different effects. One example is the previously mentioned scenario with two perfectly equal beams, where the TTL coupling vanishes because two mechanisms cancel each other perfectly (further details in Appendix A).

Furthermore, it is possible to compute the overall path length signal analytically for systems consisting of misaligned fundamental Gaussian beams as shown in [33]. From the path length signal it is trivial to compute the derivative with respect to the tilt angle to obtain the present TTL coupling in the given system. However, dividing an analytic expression of an overall tilt-to-length coupling into different contributions is not straightforward and from the authors state of knowledge often impossible.

3.4. How to suppress tilt-to-length coupling

Besides describing and estimating the amount of TTL coupling that is produced by different effects, the main challenge is to remove or suppress TTL coupling in future measurements. By now, we have three main approaches which serve the purpose of reducing TTL coupling:

1. Measure and characterize the TTL coupling well enough in order to remove it in post processing.
2. Remove the cause that produced the coupling in the first place.
3. Intentionally add more TTL coupling that cancels out the previous.

Point 1. was the approach used in LISA pathfinder (LPF) [40], a technology demonstrator for LISA. In the LPF mission, it was shown that a drag-free TM interferometer can be operated in space under LISA conditions. To suppress the TTL coupling below the required level, it was measured and characterized by intentionally tilting the TM and measuring the output. The result was used to estimate the TTL coupling in the performance measurement and subtracting it from the measured data. This is possible if the correlation between tilt angle and resulting path length change does not change and the actual tilt angle can be measured accurately enough. Furthermore, the subtraction of TTL coupling requires a good signal to noise ratio and the range in which subtraction is successful is limited. Subtracting TTL coupling that is a factor of 10 above the actual measurement signal should lead to good results, while anything far above this ratio bears the danger of affecting the actual signal in the subtraction process.

Table 3.1.: Overview of the different TTL coupling mechanisms with a short description and the mathematical expression (approximated). For some mechanisms only a general behavior can be described, like symmetric or asymmetric with respect to the tilt angle. The mathematical expressions of these mechanisms is given as a polynomial with either even or odd orders. TTL coupling due to wavefront errors and detector geometry can have any form – the corresponding mathematical expression is given as a general polynomial without specific form. Here, α is the tilt angle, d_{long} and d_{lat} the longitudinal and lateral offset, d_{pivot} the distance to the pivot, β the angle of incidence, and the a_n are parameters with arbitrary values.

TTL coupling mechanism	General form	Description
piston – longitudinal	$2 \cos(\beta) d_{\text{long}} \alpha^2$	Offsets between point of rotation and reflective surface of a component generate movement of the surface.
piston – lateral	$2 \cos(\beta) d_{\text{lat}} \alpha$	Offsets between point of rotation and reflective surface of a component generate movement of the surface.
lever arm	$\frac{\alpha^2}{2} d_{\text{pivot}}$	Longitudinal offsets between rotation point and detector will lead to variations in the propagation distance to the detector.
beam offset – constant	$\sum_n a_n \alpha^{2n+1}$	Initial misalignment on the detector generate disparity.
beam offset – dynamic	$\sum_n a_n \alpha^{2n}$	Offsets between rotation point and detector lead to angle dependent beam walk.
beam parameters	$\sum_n a_n \alpha^{2n}$	Tilting wavefronts with a curvature mismatch generate coupling.
path length signal	$\sum_n a_n \alpha^{2n}$	The way of combining QPD segments to an overall signal influences the outcome.
wavefront errors	$\sum_n a_n \alpha^n$	Aberrations in the wavefronts disturb the balance between different detector sides.
detector geometry	$\sum_n a_n \alpha^n$	Errors and additional detector features alter the measured results.

The idea behind option 2. is to understand all mechanisms that generate a noteworthy amount of TTL coupling and remove all contributions individually. This means for example: align the interferometer well enough to remove initial offsets, match the involved beam parameters, use a suited path length definition, avoid wavefront errors (e.g. use a modecleaner), chose the detectors carefully (sufficiently large, no clipping), etc. While this is the “good scientific practice” approach, it is not possible to remove the entire TTL coupling. The main reason for this is the fact that most of the TTL coupling contributions are not well understood yet. Often, it is only possible to estimate the principle shape of the coupling (symmetric or asymmetric). To improve the success of this approach is one of the core topics of this thesis – investigate different TTL coupling contributions and find solutions to suppress these aspects. Either by carefully designing the optical systems, adding additional components, or finding new measurement concepts that avoid TTL coupling.

Option 3. is a good supplement to option 2. The idea is to add additionally TTL coupling that is well understood and well controlled (e.g. additional misalignment of the detector) to counteract the residual coupling that cannot be removed with option 2. An exemplary scenario, where this method is used can be found in Section 5.4.3.

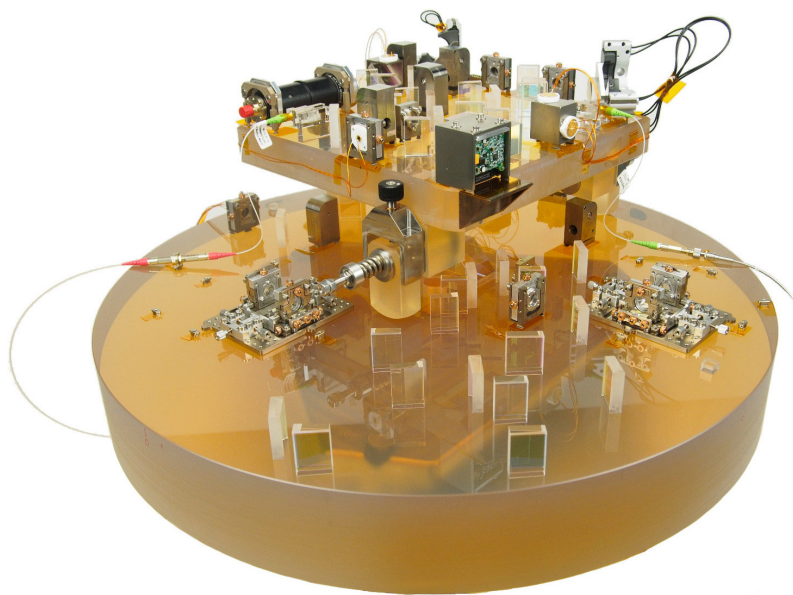
In the end a combination of all three methods might lead to the best result. Starting with option 2., removing as much TTL coupling as possible, followed by option 3., compensate the residual TTL coupling by carefully misaligning the detector, and finally characterize the remaining TTL coupling to subtract it afterwards (option 1.).

Imaging systems to suppress tilt-to-length coupling To suppress geometric TTL coupling and the effect of beam walk and offsets on the detector, imaging systems can be used [TD2, 16, 41]. The idea is to image the point of rotation onto the detector. Still, one beam in the interferometer is tilted, but the detector senses no beam walk, since the point of rotation coincides with the center of the detector. Furthermore, no geometric TTL coupling remains, since the rotation point is imaged to the center of the detector and according to Fermat’s principle the propagation length between point of rotation (object plane) and the detector (image plane) is equal, independently of the actual angle. Combined with the AP signal definition (Section 2.2.3) which is relatively robust against beam parameter variations, this should lead to zero or at least significantly reduced TTL coupling.

In optical simulations and dedicated proof-of-principle experiments, it could be demonstrated, that imaging systems can reduce the TTL coupling way below the required level, c.f. Appendix B.

Part II

LISA optical bench testbed



4

LISA testbed – methodology and design

For the most part, this and the following chapter describe the results of the LISA optical bench telescope simulator experiment. Within this project, the majority of the content has already been published in the project documents [TD3–TD5]. Furthermore, the concept and the design has been published in [P6] and further details are published in [P7, P8].

I claim the optical design of the telescope simulator, the optical design of the two-lens imaging system, the control and alignment software, as well as all simulations presented in this chapter to be my work. Besides minor assistance from my side, the rest of the project was done by others. Particular attention shall be paid to Maike Lieser and Michael Tröbs who did the largest contribution to construction and operation of the testbed. Further information on these topics can be found in [42].

4.1. Tilt-to-length coupling in LISA

In the previous chapter TTL coupling as an optical noise source was introduced and multiple different mechanisms that lead to TTL coupling were explained.

In this chapter, TTL coupling in LISA is investigated. In the original LISA noise budget, TTL coupling was the second largest entry ($5.3 \text{ pm}/\sqrt{\text{Hz}}$), after shot noise ($7.7 \text{ pm}/\sqrt{\text{Hz}}$) [TD1]. The exact values of these noise contributions are not determined yet and depend on the detailed mission parameters and design choices. Thus, the final budget will probably contain different numbers. However, TTL coupling is expected to be a dominant noise source and will contribute on a similar scale as shot noise. This large TTL noise consists of two major contributions. The first originates from the LISA TM interferometer (see Section 2.1.1). Here, a free-floating test mass is read out by a laser beam. Since the test mass is free-floating inside the satellite, angular misalignments between the satellite that follows the movement of the TM, and the TM itself are unavoidable. From the point of view of the spacecraft, the test

mass is tilted and the beam, reflecting from it becomes tilted, too. In the simplified TM interferometer, shown in Figure 2.5, a tilted TM is indicated together with the tilted beam (semitransparent), which generates TTL coupling that will make a tilt of the TM look like a longitudinal movement.

The second major TTL contribution is originating from the science interferometer (c.f. Section 2.1.1). When the spacecraft becomes tilted with respect to the line of sight to the distant spacecraft, the wavefront gathered by the telescope becomes tilted as well. Since the telescope has the optical properties of an imaging system, the tilted wavefront is imaged to the optical bench and therefore one of the beams in the science interferometer is tilted with magnified angles. An illustration of a tilted wavefront that is propagated through a telescope is shown in Figure 4.1. A tilted beam from the telescope is superimposed with a non-tilted local beam and TTL coupling occurs.

Without further action, this TTL coupling would limit the LISA performance and disturb all measurements. Thus, it is of utmost importance to reduce the TTL coupling in the science and the TM interferometer.

One approach to achieve this is the use of imaging systems. Therefore, e.g. the TM is placed in the first pupil plane of a classical pupil plane imaging system (introduced in Section 2.4). Independently of the angle of the TM, each ray starting on the TM will hit the same point in the second pupil plane where the detector is placed, as illustrated in Figure 4.2. The same applies to the science interferometer, where the entrance pupil of the imaging system coincides with the exit pupil of the telescope, with the detector being placed in the exit pupil of the imaging system. Therefore, telescope and imaging system act together and the wavefront entering the telescope is directly imaged to the final detector.

However, this type of imaging system requires positioning of two lenses in the middle between the point of rotation and the detector, while the distance between pivot and first lens and second lens and detector is equal to the respective focal lengths, and the distance between the two lenses is equal to the sum of the two focal lengths. While this was possible to implement on the laser ranging interferometer of GRACE-FO, the geometrical constraints on LISA do not allow the use of two lenses placed directly in the middle between for example the TM (point of rotation) and the QPD (as shown in Section 4.3.3). Only a small area in front of the QPD can be used for an imaging system. This limitation for the lens positions form an additional requirement for the imaging system (Figure 4.3). With this requirements it is not possible to design a classical pupil plane imaging system with just two lenses, but a more complex design with more lenses is necessary.

In LPF, it was sufficient to measure the TTL coupling and subtracting it from the measured signal in post processing. In the LISA TM interferometer this might be sufficient, too. However, reducing the TTL coupling before subtracting it is likely to increase the accuracy. For the science interferometer on the other hand, subtracting the TTL coupling is not sufficient and an imaging system is required for other reason,

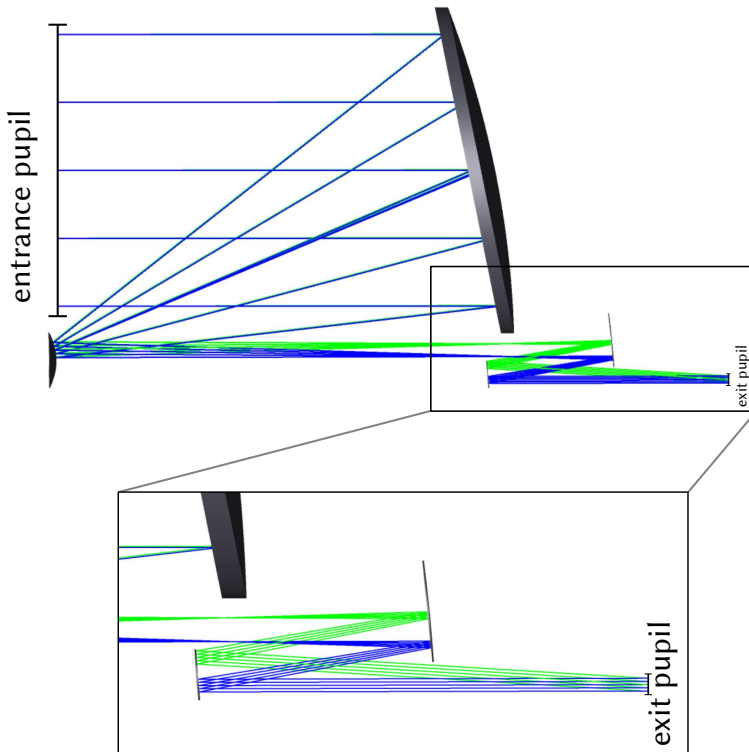
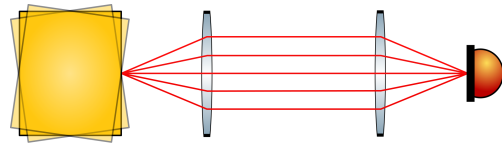


Figure 4.1.: Schematic of a LISA telescope. The incoming nominal light (blue rays) are propagated through the telescope and at the exit pupil, the compressed beam is delivered to the optical bench. The green rays indicate an angular misalignment between telescope and wavefront. Due to the imaging properties of the telescope, the tilted beams are imaged to the exit pupil and delivered to the optical bench, however the tilt angle is magnified with the inverse of the telescopes magnification. For illustration purposes, the tilt of the green beam is magnified – the expected tilts in a LISA satellite are much smaller. Credit: telescope design by Jeffrey Livas, illustration by Yong Ho Lee.

Figure 4.2: Sketch of a test mass imaging system. The TM is placed in the entrance pupil plane, the photo diode is placed in the exit pupil plane. All rays hit the photo diode in the center, independently of the TM tilt angle.



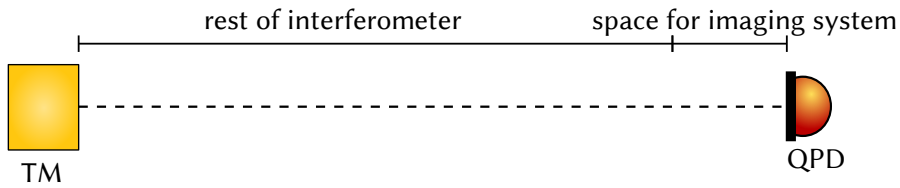


Figure 4.3.: The space between TM and QPD is used for other optical components and it is impossible to place an imaging system directly in the middle between QPD and TM.

too. The telescope clips a fraction of a large incident wavefront and images this top-hat wavefront to the science interferometer. At the interface between telescope and optical bench (RX-clip), the received wavefront is still flat in intensity and phase. Without an imaging system in the science interferometer, the wavefront would diffract while propagating through the science interferometer and at the detector, a high spatial frequency diffraction pattern instead of a flat wavefront would be observed. This would lead to a significant loss in contrast and accuracy. Therefore, besides the reduction of TTL and other properties which are not in the focus of this thesis (magnification, beam walk, etc.), the imaging system needs to image the flat wavefront from the RX-clip onto the detector to suppress diffraction effects.

4.2. The LISA optical bench experiment

In the past, imaging systems were tested in optical simulations as well as in a proof of principle experiment (cf. Appendix B). Dedicated optical simulations suggest that imaging systems are a possible option to reduce TTL coupling in LISA. However, TTL coupling has never before successfully been tested in a system as complex as LISA. The alignment accuracy of an imaging system under the conditions of a bonded interferometer might be insufficient. Furthermore, the use of interfering beams with unmatched parameters, up to the use of highly divergent top-hat beams, might prevent the imaging systems from successfully reducing TTL coupling. In order to confirm that imaging systems are a solution for LISA we need to experimentally validate that the TTL coupling can be sufficiently reduced under LISA like conditions.

4.2.1. Requirements and goals

The primary goal of the investigation is to demonstrate, in a representative way, that suitably designed imaging systems can be used to suppress TTL coupling for LISA. The suppression is considered successful for coupling coefficients below $\pm 25 \mu\text{m}/\text{rad}$. This value was derived from the eLISA noise budget [TD6]. The required suppression and the allowed TTL coupling depend on the detailed mission parameters. Thus, the limit of $\pm 25 \mu\text{m}/\text{rad}$ is not a strict threshold but rather a guidance level indicating good performance within this project.

To achieve representativity we need the testbed to have the following features:

- Use a LISA like optical bench (OB), that could be exchanged by real flight hardware.
- This OB must be operational at MHz heterodyne frequencies with a few $\text{pm}/\sqrt{\text{Hz}}$ performance.
- The measurement and alignment procedure must be applicable to real flight hardware in order to develop and test an OGSE concept. An OGSE (optical ground support equipment) comprises additional hardware that is used to test the functionality and alignment of flight hardware before and during implementation. In the scenario here, the OGSE allows to measure TTL coupling of a LISA OB on ground.
- The testbed must be capable of measuring TTL coupling of imaging systems to an accuracy below $\pm 25 \mu\text{m}/\text{rad}$.
- It must be possible to exchange the imaging systems to measure and test different designs.
- The system must feature different beam types to simulate science interferometer and TM interferometer scenarios.

The imaging system performance tests comprises the following:

- Measuring the TTL coupling and showing that they can reach the requirement of $\pm 25 \mu\text{m}/\text{rad}$ within $\pm 300 \mu\text{rad}$.
- Investigating the effect of imaging system alignment on the measured TTL coupling.
- Investigating the effect of photo-receiver misalignment on the measured TTL coupling.
- Testing different imaging system designs.

4.2.2. Representativity of the operation parameters

To simplify the testbed, some of the requirements mentioned above were eased without loss of representativity. The different requirements that were rejected are explained in the following list:

- The OB features only the science interferometer, all other optical components that would be present on a real LISA OB are not required for TTL coupling tests.
- Due to space constrains on the OGSE, the OB features a calibrated photo diode pair (CQP) that would not be present on LISA. For a real LISA OB, the CQP would be placed on the OGSE.

- The test is operated with kHz and not MHz heterodyne frequencies. Since the TTL coupling is independent of the frequency, the results are not affected by the change of the heterodyne frequencies. With additional effort, the test bed can be operated with MHz.
- The testbed is operated in air to reduce the experimental effort. This prevents $\text{pm}/\sqrt{\text{Hz}}$ performance. However, we intend to measure coupling factors. Here, pm sensitivity is not required. With additional effort, the testbed can be operated in vacuum and perform on a pm level. A detailed noise budget of the estimated performance in vacuum can be found in Section 4.3.8.
- For the tolerance analysis, the imaging systems are mounted with multiple degrees of freedom. This is not required for LISA, where the mounting system would be less flexible but more stable.

4.3. Methodology and design

To have a system that is representable for LISA, the experimental setup is divided into two parts. The first is the optical bench (OB), which is a part replica of an optical bench of LISA, providing all interferometric parts that are crucial for the planned measurements. The second part (the OGSE) is the telescope simulator (TS), a device that can be attached to the OB and from the OB's point of view looks like a telescope. The TS provides either a flat top or a Gaussian beam (to simulate the science/TM interferometer) to the OB that can be rotated around a specific aperture on the OB, the RX-clip. This resembles the optical interface between optical bench and telescope in LISA. When the spacecraft rotates, the incoming wavefront will rotate around the center of the RX-clip. By rotating the flat-top beam around the RX-clip, the science interferometer can be simulated. By rotating the Gaussian around this point, the TM interferometer can be simulated, imitating a TM being placed in the RX-clip. Important in this configuration is that the TTL coupling generated by the tilting actuators, the TS, or the misalignment between OB and TS does not couple into the measurement. Only the TTL coupling that is generated after the RX-clip should be measured. With the built setup, this disentanglement is possible.

A draft of the measurement principle is shown in Figure 4.4. On the right is the OB with the science interferometer. On the LISA OB the fixed red TX beam is used as a reference in the science interferometer and it is transmitted through the telescope to the distant spacecraft. The interface to the telescope is the RX-clip in the center of the OB. The telescope will deliver the received wavefront (green RX beam) to this point. From here, the imaging system will image the wavefront to the science interferometer detectors. On the left is the OGSE, here called telescope simulator (TS). The purpose of the TS is to simulate the behavior of the telescope, that comprises two major tasks: the first is to deliver an RX beam (green) to the OB that looks like it came from a telescope – flat in phase and intensity – and it must be tiltable around

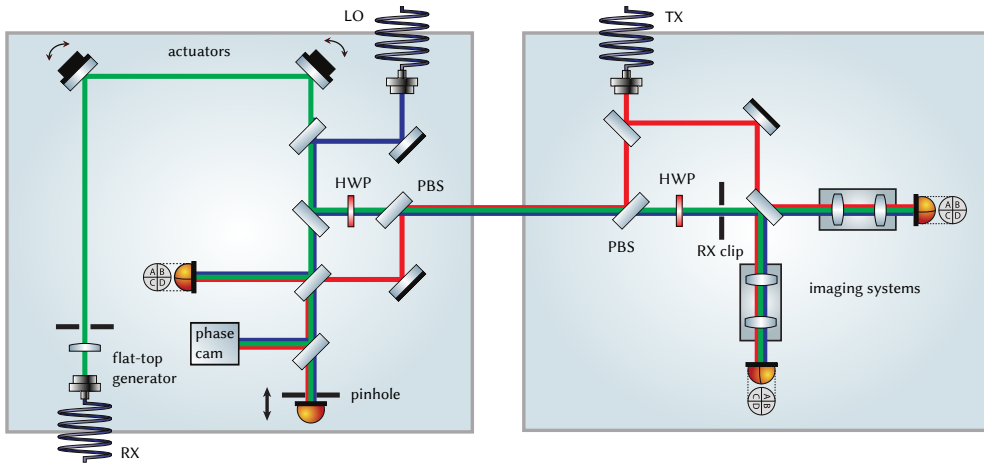


Figure 4.4.: Schematic of the test bed concept. The Telescope Simulator (left) and Optical Bench (right) are shown with the key components to illustrate the measurement concept. The RX beam is shown in green, the LO beam in blue and the TX beam in red. The RX beam is tilted around the middle of the RX clip with the two actuators and the reference photo diode is placed at the same optical distance as the RX clip. The beams between the two baseplates have a different polarization and are separated by polarization beam splitters (PBS). On the optical bench the imaging systems are placed in the science interferometer in front of the photo diodes in both output ports. Credit: [42]

the RX-clip. The second task is to receive the TX beam from the OB and keep a stable phase relation between RX and TX beam. The RX beam is tilted via two actuators in the top of the TS. The phase relation between TX and RX beam is kept constant via the reference interferometer and the stable local oscillator (LO in blue) on the TS. The transmitted and received beams at the interface between OB and TS are separated by polarizers and wave-plates: the TX beam from the OB to the TS propagates in p -polarization. The LO and RX beam travel in s -polarization from the TS to the OB.

4.3.1. Calibration principles

The main challenge in this experiment was to disentangle the different TTL coupling contributions to ensure that only the TTL coupling that would be present in LISA will be considered in the measurement. For example, the residual movement of the tilt actuator must be kept out of the measurement in order to provide useful results, like in the proof-of-principle experiment. Therefore, a phaselock between LO and RX as well as LO and TX ensures that the phase relation between RX and TX beam in the RX-clip is zero. Crucial for this method is to set up a reference diode in a position that is equivalent to the RX-clip. Ideally, the phase relation between TX, LO and RX would be measured in the RX-clip, however this would block the beams in the science interferometer. Instead, the reference diode is placed in an optical copy of

the RX-clip (explained in Section 4.3.2). Thus, compared to the proof-of-principle experiment in Appendix B, the actuators are not in the measurement path anymore and therefore their TTL coupling is removed. Measuring the path length signal at the science interferometer diodes behind the imaging systems will only show the TTL coupling reduced by the imaging system. Crucial to this strategy is that the reference diode is perfectly aligned in the optical copy of the RX-clip, within μm accuracy. To ensure that, the reference diode is aligned with a temporary diode. This temporary diode is placed in the center of the RX-clip with the help of suited apertures. By measuring the TTL coupling between temporary diode and reference diode, the residual misalignment between the two can be measured. If this TTL coupling becomes zero or drops below the required level, the reference diode is aligned well enough.

Besides the geometric equivalence of the RX-clip position and the reference diode position, it is also important that the reference diode measures only geometric TTL coupling. If the reference diode would measure TTL contributions that are related to the present beam parameters or the diodes geometry, this contributions could not be measured in the science interferometer and the results would be distorted. As explained in Chapter 3, the geometric TTL coupling contributions are only applicable to plane waves or rays. Therefore, the reference diode was chosen to be a $150\ \mu\text{m}$ pinhole diode. Thus the wavefront curvature and intensity profile of the involved beams are large with respect to the diode and the beams can be approximated by plane waves. In the end, the reference diode only measured the geometric TTL coupling.

4.3.2. The properties of an optical copy

In the context of this experiment optical copy means, that the geometric relation between the two points is equal with respect to the RX beam. If the RX beam rotates around the center of the RX-clip, it will also rotate around all optical copies of this point. Thus, the RX beam has the same phase change, geometry, and movement in all RX aperture copies and at the original RX aperture. All photo diodes on the TS experience the same movement of the RX beams as the RX-clip.

The distance to a pivot can be computed similarly to the distance of a Gaussian waist position, as described in Appendix C.3. In contrast to the phase of a Gaussian beam, it computes not as $n \cdot d$, but as $1/n \cdot d$, where n is the refractive index and d the propagated physical distance [23]. Therefore, the optical path length between tilting actuators and all RX copies and the RX aperture is different, related to the number of transmitted components, to achieve the claimed geometry. Instead of the path length, the real part of the Gaussian q-parameter is matched, since it is related to the position of the waist and therefore follows the same propagation scheme as the pivot.

4.3.3. Optical bench – design

The optical bench is the interferometric heart of a LISA satellite and due to its planned location behind the circular telescope laid out on a circular baseplate. This baseplate has a diameter of 580 mm, thickness of 80 mm and a mass of 55 kg. These dimensions originate from the classic LISA mission, where a higher number of components required more space on the optical bench [43]. The baseplate was originally purchased to build an engineering model of the classical LISA optical bench. After classic LISA was down sized, the original OB project was redefined with the purpose of investigating TTL coupling. Thus, the existing large baseplate was used here.

The optical bench needs to carry all interferometric components that are necessary to read out the different interferometers: science interferometer, test mass interferometer and reference interferometer, as well as all auxiliary optical equipment: star camera, acquisition sensor, all photo detectors (QPDs, SEPDs, power monitors) and fiber couplers.

Features

To reduce design and construction efforts, a minimal optical bench was designed and built that only provides those features that are essential to operate the science interferometer. All other interferometers and optical components were left out. Furthermore, a few additional alignment tools are added to the optical bench, which are not necessary for LISA, but simplify the alignment and operation of the telescope simulator. To allow the planned measurements and the required alignment and calibration, the optical bench needs to provide the following features:

- Provide a stable TX beam, launched from a quasi-monolithic fibre injector optical subassembly (FIOS) [TD7, 44, 45].
- The measurement interferometer provides a flexible space for the DUT¹, and the DUT is removable and replaceable.
- The ratio of the entrance-to-exit pupil distance is representative for a LISA science interferometer as well as a generic test mass interferometer.
- The RX aperture – the pupil interface between the telescope and science interferometer – is in an accessible location on the optical bench. The aperture is removable and replaceable with an accuracy of a few μm to allow investigations of aperture sizes, aperture position and effects of overlap with other apertures in the system. Furthermore, all of this is required for the calibration procedure.

¹Since multiple imaging systems were tested with this setup, and it is possible to test more imaging system designs with this experiment, a generic imaging system design is called device under test (DUT).

- The OB facilitates mounting of the TS directly on its surface in two orientations, rotated by 180° around the vertical axis (z axis – compare to Figure 4.7) with respect to one another, to enable verification of the residual coupling in the TS and OB (described in Section 5.2.2).
- The OB provides a dedicated alignment aid, in the form of two spatially separated QPDs, which are pre-aligned to a beam which is perfectly aligned to the science interferometer. This facilitates the precision alignment between OB and TS.

Layout

The optical layout is shown in Figure 4.5. The key features – the photo diodes, RX-clip, TX FIOS, TS interface, TS outline and the beam combiner (BS₂₁) – of the measurement interferometer are indicated. The red beam is the locally generated, static TX beam launched from a FIOS on the OB. The green beam is the RX beam produced on the telescope simulator. It represents the actual telescope beam that rotates around the RX-clip. Also present is the blue, static, local oscillator beam. It facilitates alignment and follows the same path on the OB as the RX beam. Both imaging systems are shown: the four-lens (LOB4C) system in front of SCI QPD₁ and the two-lens (LOB2D) system located in front of SCI QPD₂. The slots in which the individual systems are present are chosen arbitrarily. The stable 2 mm diameter TX beam launched from a monolithic fused silica FIOS is combined with the RX beam and LO beam at the beam combiner of the measurement interferometer, BS₂₁, then directed through each imaging system and read-out at their respective photo diode. Additional QPDs are placed on the left and in the top of the OB. The position of the RX and the LO beam from the TS can be monitored on these two diodes, which makes them function like a calibrated quadrant diode pair (CQP) [46]. This CQP was aligned during manufacture such that any beam from the TS intersecting at the center of both QPDs would then be optimally aligned in the measurement interferometer. The optical distance the red TX has to travel until reaching BS₂₁, appears to be unnecessarily long, but is required for the path length matching between reference and measurement interferometer (compare to Section 4.3.8).

4.3.4. Telescope simulator – design

The TS, like the OB, has been designed to utilize as many as possible of the components that were designed and purchased for the classical LISA elegant bread board (EBB) [43] in order to maximize efficiency in cost and time. It consists of a 280 mm x 280 mm Zerodur[®] baseplate purchased for the previous TS design. This baseplate has two holes, one for the telescope interface and one for the test mass interface, of which only one is needed here. The location of the holes, which was dictated by the old EBB design, is now necessarily a design driver for the new TS, as they cannot be

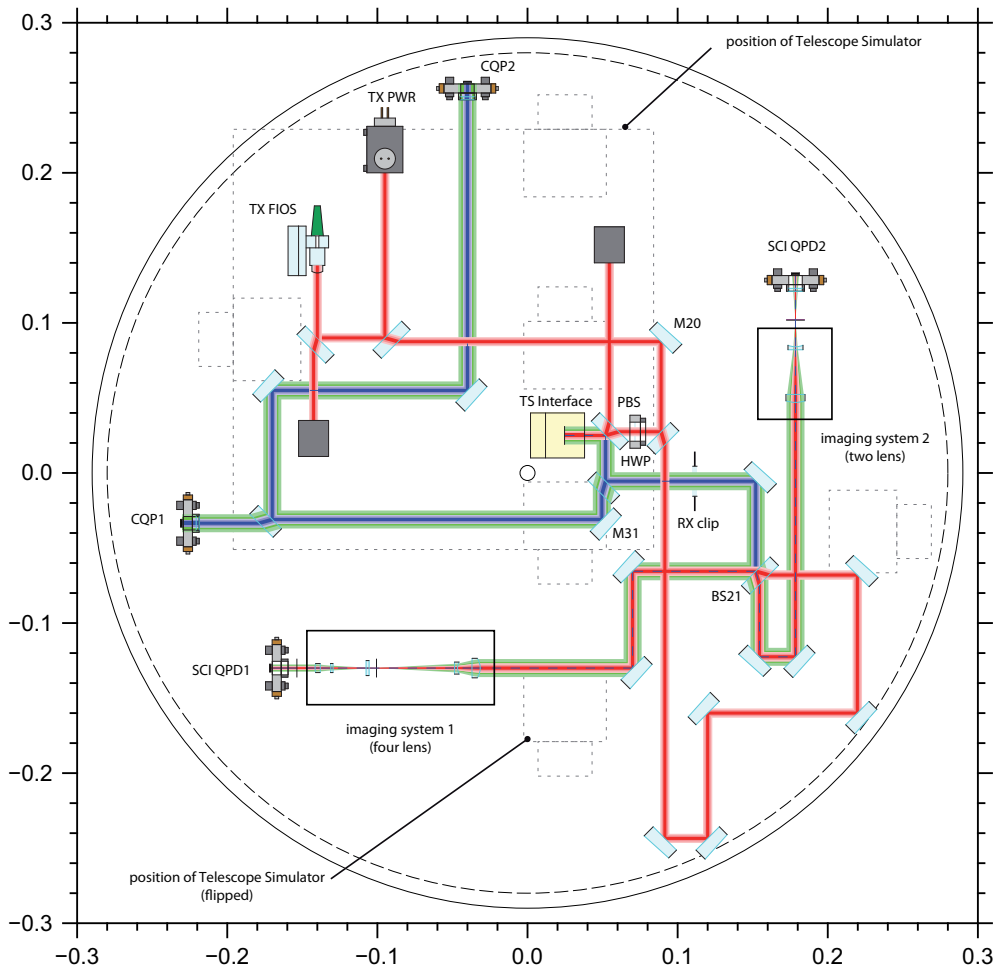


Figure 4.5.: Schematic of the OB layout and labeling of the key components. The imaging systems (DUT) in front of the science interferometer (SCI) QPDs are on separate base plates and can be exchanged. Here one four-lens (LOB4C) and one two-lens (LOB2D) imaging system are shown. The RX (green) and the LO (blue) beam are produced on the telescope simulator and interfered with the TX (red) beam from the TX FIOS. The calibrated quadrant photo diode pair (CQP1 and CQP2) is used for the alignment. The dashed outline indicates the position of the telescope simulator in the nominal and the flipped position.

changed. This means, that the OB-TS out of plane interface is fixed at the position of the larger hole and the area around the smaller hole cannot be populated by optical components that require good stability or alignment. In the final design, the smaller hole is underneath a beam dump, which does not need to be well aligned.

Features

In order to successfully perform all required measurements, the TS has to facilitate the following features:

- Two actuated mirrors to facilitate tilting of the RX beam around the RX-clip
- An RX flat-top generator, to produce a flat-top beam (to represent the LISA telescope beam)
- An RX Gaussian beam from a FIOS to allow representative testing of the test mass interferometer
- An LO Gaussian beam from a FIOS, as a stable alignment and phase reference
- At the reference interferometer, all outputs are optical copies of the RX-clip– this ensures that the phase and coupling measured at the reference interferometer is identical to the phase and coupling present at the entrance pupil to the device under test, allowing unambiguous determination of the effect of the device under test.
- There are four output ports from the reference interferometer – to maximize the design flexibility – consisting of:
 - A pinhole SEPD photo diode to stabilize the RX beam
 - A QPD photo diode for monitoring alignment and controlling the actuators
 - A phase camera and a trigger-detector for diagnostics – in particular spatially resolved intensity and phase measurements
- The distance between the actuators is as large as possible to achieve a wide tilting range (more than $\pm 500 \mu\text{rad}$).
- The telescope simulator has a mounting system to interface between the TS and the OB which offers precision adjustment of the TS in 5 degrees of freedom with μm and μrad accuracy.
- The beam which would be optimally aligned to the reference interferometer can be aligned to the out-going LO beam to within $20 \mu\text{m}$ and $50 \mu\text{rad}$ at the (virtual) location of the RX aperture.

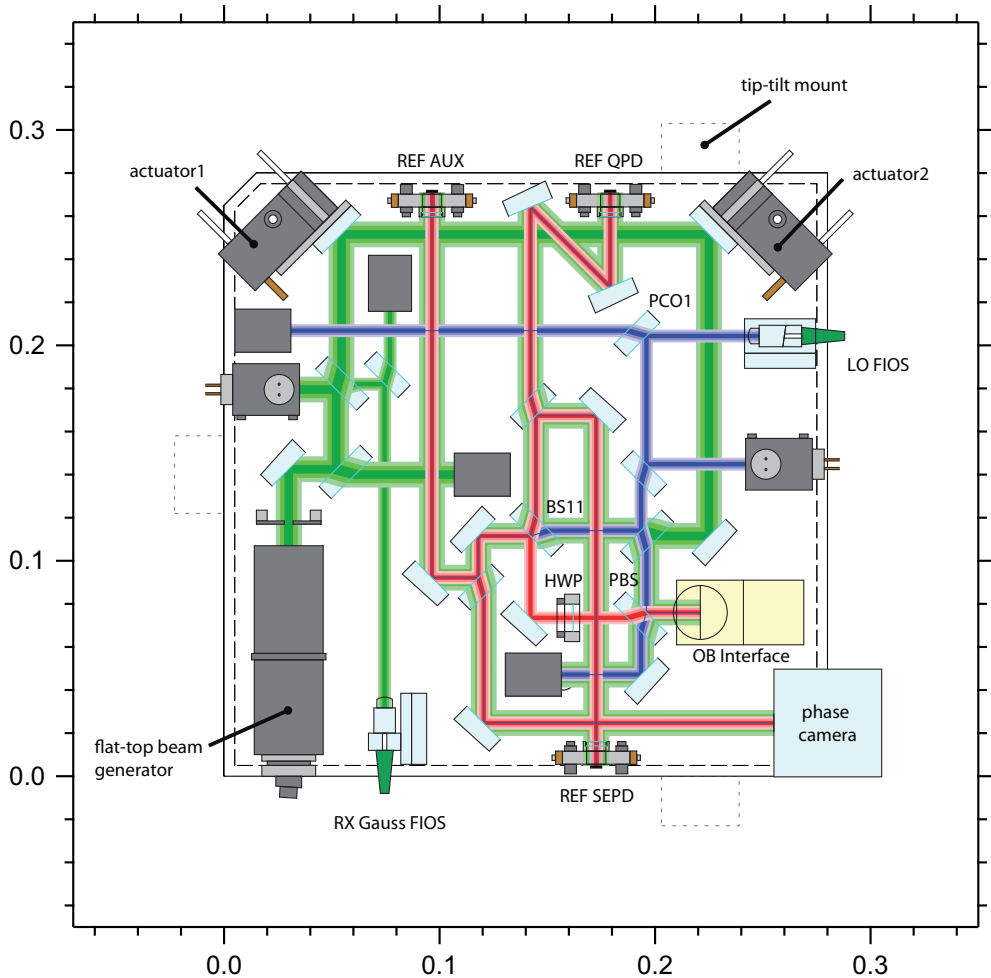


Figure 4.6.: Schematic of the TS layout and labeling of the key components. Either the RX flat top from the flat-top generator or the RX Gauss from the RX FIOS can be used. The RX beam (green) is tilted by two piezo driven actuators and combined with the stable reference LO beam (blue). The reference interferometer has four readout ports with three different photo diodes and a phase camera. The REF SEPD is a $150\ \mu\text{m}$ pinhole photo diode, the REF QPD a quadrant photo diode and the AUX-SEPD a 5 mm single element photo diode. The dashed outlines are the positions of the feet for the tip-tilt mount to align the telescope simulator.

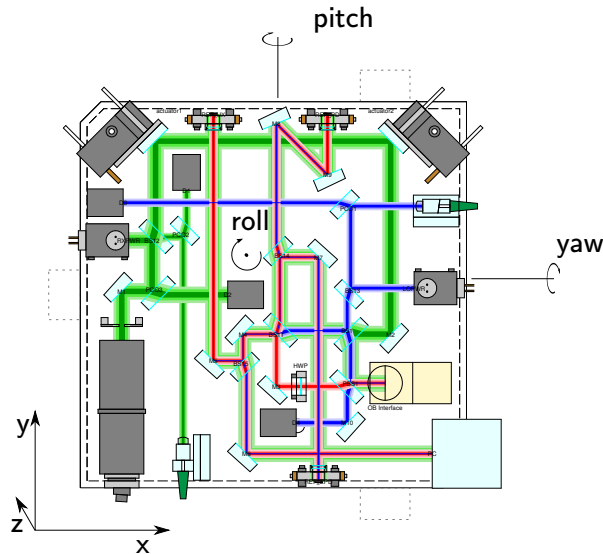


Figure 4.7.: Schematic of the TS's degrees of freedom.

Layout

Figure 4.6 shows the schematic of the telescope simulator layout and labeling of the components. The key features - the RX generators, the LO FIOS, the reference detectors and the actuators are highlighted, as is the outline of the TS interface mount. The telescope simulator has a quad-readout of the reference interferometer (each port is split once) to maximize the system's flexibility. Nominally, these would consist of a reference QPD, and reference SEPD, a phase camera and a trigger for the phase camera. Each port is path-matched to the RX Aperture as per the design requirements (optical copy). Furthermore, the TS features a twin RX Beam source – one Gaussian (from a FIOS) and one flat-top – both can be actuated via the on-bench actuators.

The flat-top generator consists of a large fiber coupler producing a 9 mm-radius beam that is clipped by an apodized aperture. The aperture is optimized to minimize diffraction and result in a flat phase and flat intensity in the inner three millimeter at the plane of the RX beam clip on the optical bench, more details can be found in Section 4.3.6.

The LO beam from a FIOS provides the required ultra-stable reference for the TS. It can be aligned to the CQP on the OB to ensure a perfect alignment between OB and TS. A polarizing beams splitter and half-wave plate facilitate the required polarization multiplexing between the OB and the TS. LO and RX beam traveling from the TS to the OB are *s*-polarized. The TX is propagating from the OB to the TS in *p*-polarization.

Figure 4.7 shows the TS with a coordinate system and the alignment degrees of freedom (lateral *x*, lateral *y*, height *z*, yaw, pitch, roll).

The xy plane of the TS coordinate system lies in the plane of the TS baseplate and the z axis points into the paper plane. Lateral shifts of the TS and roll adjustments can be made by tapping the TS (micro-hammering). Adjustments in height, pitch and yaw can be performed by the tip-tilt mount of the TS (shown in the following section).

Mounting

The TS can be mounted on top of the OB in two different orientations as shown in Figure 4.8. The two orientations representing a 180° rotation around the vertical beam axis of the interface between TS and OB. Switching between these two orientations is called flipping. The purpose of the flipping procedure is to distinguish the TTL coupling contributions of TS and OB, as explained in Section 5.2.2.

The path length stability between OB and TS is an important factor in this testbed. The vertical path couples twice into the result. In the reference interferometer on the TS, the TX has traveled the vertical path, while in the science interferometer on the OB, the RX and the LO have traveled from the TS to the OB. Thus, in the resulting difference between reference and science interferometer, any path length change between OB and TS will appear twice.

To have a stable connection (a few $\text{pm}/\sqrt{\text{Hz}}$), an all Zerodur[®] mount was designed. This system, illustrated in Figure 4.9, consists of two pieces of Zerodur[®] – a foot and a mounting block – clamped together with a spring. By decreasing the clamping force, the foot can be moved (by means of a micrometer screw) in a metal guide to provide adjustment in one degree of freedom (up-down). Increasing the clamping force increases the force of friction between the foot and the mount, allowing the load of the TS to be transferred through the foot via the Zerodur[®] interface alone. After the clamping force is applied, the micrometer screw is backed off.

The entire optical setup of the telescope simulator can be seen in Figure 4.10. A combination of the telescope simulator and the optical bench is shown in Figure 4.11.

4.3.5. RX aperture

On the LISA optical bench, the RX aperture (RX-clip) is the interface to the telescope. In the experiment, the RX beam will be rotated around the RX aperture and the resulting length change in the science interferometer will be measured. The two tilt actuators on the telescope simulator, which perform the rotation of the RX beam will cause a longitudinal shift (compare to Section B.1.1). Hence, a reference interferometer that measures only this longitudinal shift is required. A small photo diode (pinhole) will serve as reference interferometer detector. It will be placed in a

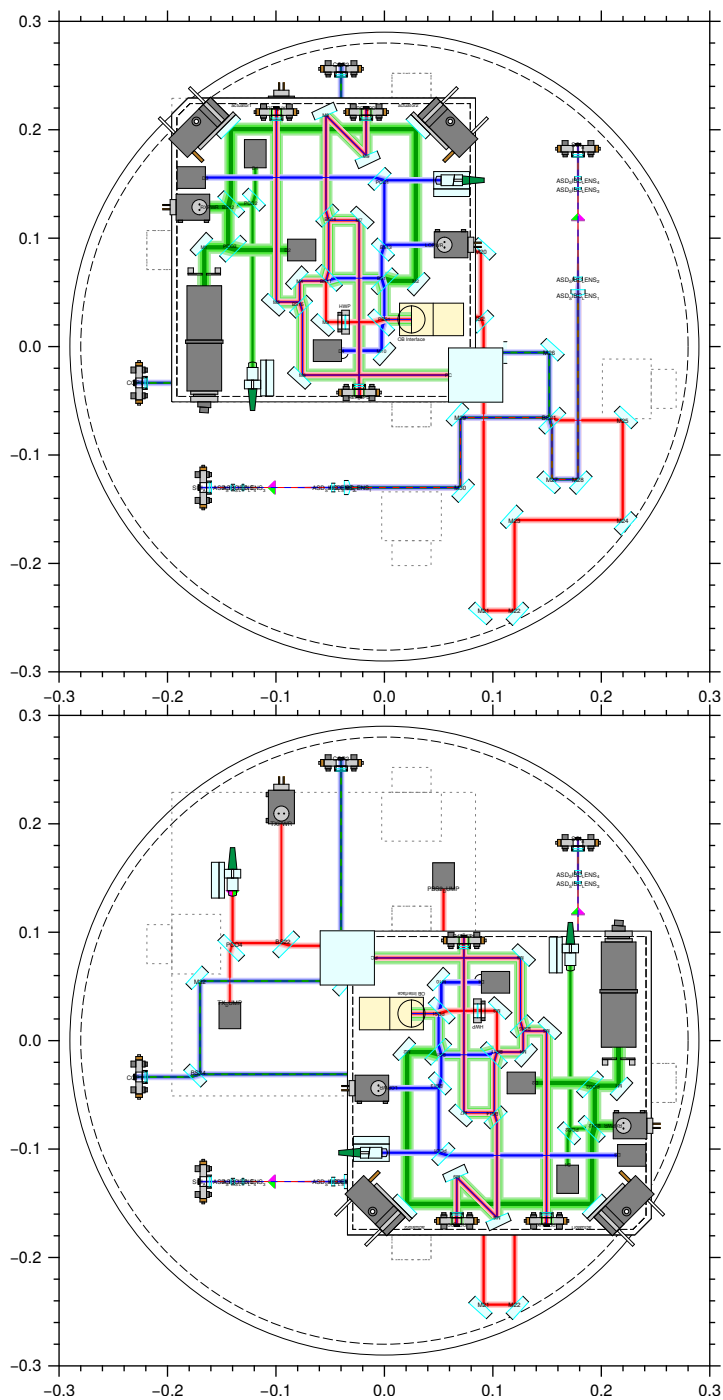


Figure 4.8.: Schematic of the TS orientations with respect to the OB. The upper image represents orientation 1 and the lower image represents orientation 2.

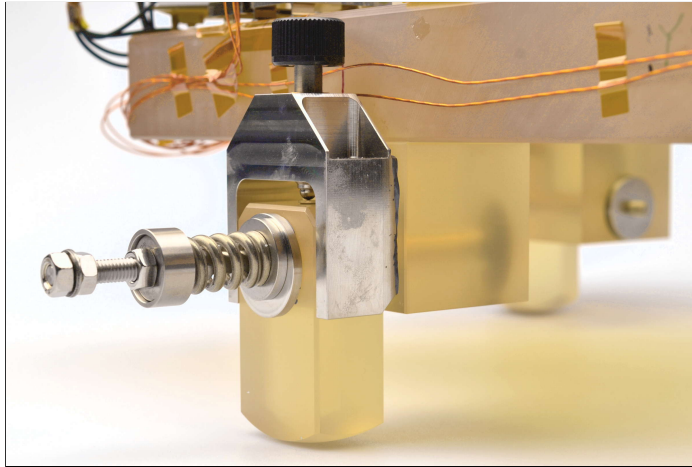


Figure 4.9.: Telescope simulator mounting system – two pieces of Zerodur® are clamped together. Due to friction, an all-Zerodur® path between OB and TS can be realized. By reducing the friction (clamping force) the mounting system can be adapted with micrometer screws.

position equivalent to the RX aperture (optical copy, cf. Section 4.3.2). If the RX beam is rotated around the RX aperture, a precisely centered small photo diode will only sense the longitudinal shift of the actuators but none of the additional TTL coupling. In the following the design of this RX-clip is described.

Requirements

In order to place the reference pinhole accurately we need to align the RX aperture to the LO beam and place a temporary pinhole in the center of the RX aperture. The optimal position of the RX-clip is laterally defined by the science interferometer. The center of the TX beam defines the axis of the science interferometer. However, since the TX beam is not present in the RX-clip (compare to Figure 4.5), the center of the LO beam defines the optimal position of the RX-clip.

By measuring the TTL coupling between the reference pinhole and the temporary pinhole, we can adjust the reference pinhole to match the optical positions of the two pinholes. If the temporary pinhole and the RX aperture are perfectly aligned, the reference pinhole can be aligned as well. Therefore, we can formulate requirements for the RX aperture and the temporary pinhole.

- Measurements with OB and TS shall be possible with and without RX-clip (2.24 mm diameter).
- The RX-clip shall be centered on the LO beam that is aligned to the science interferometer laterally to within a few micrometer using the CQP on the OB.

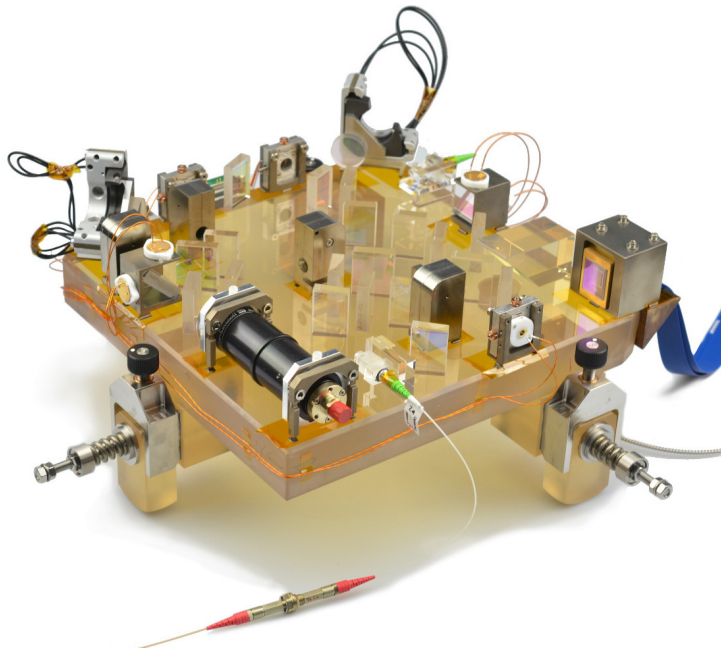


Figure 4.10.: Photography of the telescope simulator

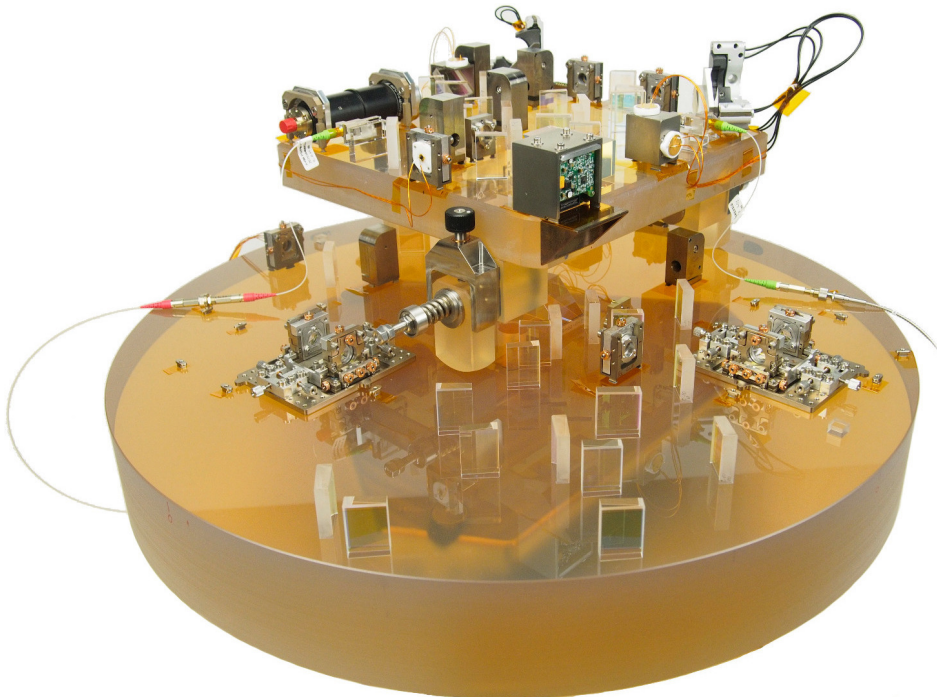


Figure 4.11.: Photography of the telescope simulator on top of the optical bench in nominal position

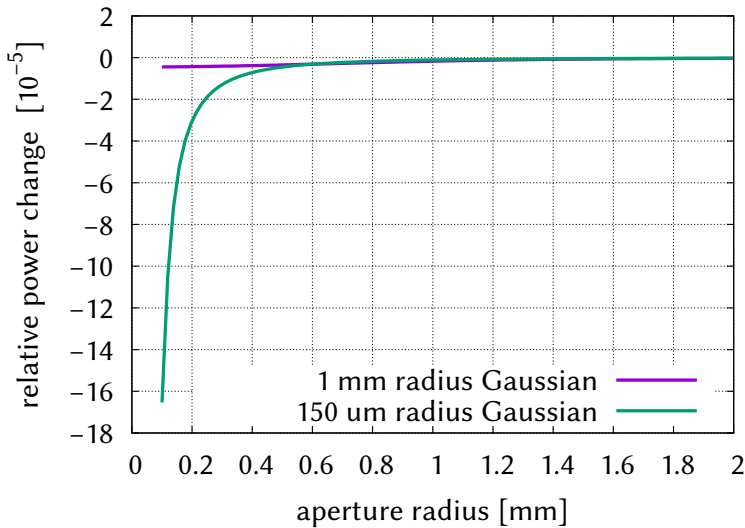


Figure 4.12.: Relative power change for the transmitted power through a circular aperture for a lateral shift of $3\ \mu\text{m}$ between beam and aperture as function of aperture radius.

- It should be possible to remove and reinsert the RX-clip into its mount without changing its alignment by more than the alignment tolerance (i.e. a few μm)
- It should be possible to replace the RX-clip by a pinhole and a single-element photo diode closely behind it. If the pinhole is laterally centered on the LO beam that is aligned to the science interferometer, then the photo diode behind it does not sense TTL coupling when the beam is rotated around the center of the pinhole. Only the longitudinal movement of the actuators are measured.
- It shall be possible to remove and reinsert the RX-clip, pinhole and four-hole aperture into the same mount repeatedly without changing its alignment by more than the alignment tolerance (i.e. a few μm).

Concept

The temporary pinhole aperture needs to be aligned to the center of the LO. The standard approach to align a diode to a beam is to shift the diode until the sensed power is maximized. Unfortunately, this is not sufficient here. Figure 4.12 shows the results of a simulation where a pinhole diode is shifted over Gaussian beams. One Gaussian beam is in the size of the LO beam while the other one is much smaller. For the large beam, the pinhole diode senses nearly no change in the measured power. Thus, centering the pinhole diode to the nominal LO is not sufficient. Therefore, either a smaller reference beam or a different approach to center the pinhole is required.

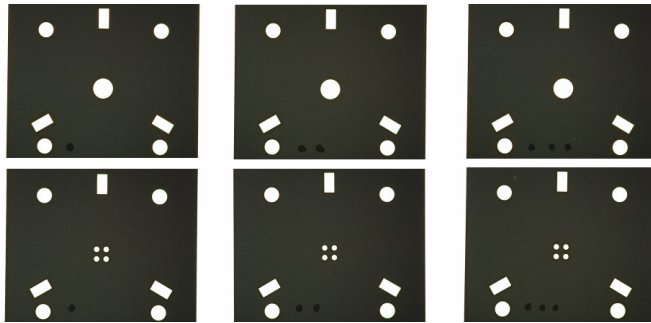


Figure 4.13.: Photograph of different apertures used in the experiment. Top row is the default RX-clip, bottom row is the QPD four-hole aperture. The pinhole aperture is not shown.

Centering the RX-clip and pinhole is performed by a different aperture with four holes and a QPD behind it. Figure 4.13 shows two different RX-clip apertures. They were manufactured with precision laser cutting which allows for micrometer accuracy when processing metal foils. In the corners of each aperture are four large holes which can be used to align the apertures among themselves. The rectangular holes which are arranged in a triangle are used to attach the aperture to three spherical magnets which are the connection points between the RX-clip mount and the actual apertures. By design, the three magnets can be attached to the three holes in only one specific position. Therefore, it is possible to align different apertures repeatedly to the RX-clip mount with the required accuracy.

In the test bed, two different photo diodes need to be repeatedly and accurately placed behind these apertures:

- a quadrant photo diode with the four-hole aperture
- a single-element photo diode with a small single-hole aperture

Pinhole aperture design

The goal that the RX-clip pinhole senses no additional TTL coupling can only be fulfilled if the pinhole is infinitely small. A real pinhole has a certain finite size due to manufacturing and the required amount of light that is necessary to determine the phase on a photo diode behind it. In the following, the results of a simulation are shown that were used to find an optimal pinhole size (trade-off between TTL coupling and noise).

The main requirement towards the pinhole size is the difference to an ideal pinhole in terms of TTL coupling. Furthermore, it is required that the signal quality (heterodyne efficiency) does not change via tilting. Additionally, the signal power needs to be high enough to achieve a good signal to noise ratio. In detail the requirements are:

- TTL coupling difference to an ideal pinhole must be significantly smaller than $25 \mu\text{m}/\text{rad}$ within a range of $\pm 300 \mu\text{rad}$.
- The detected power and amplitude must allow a path length noise of less than $1 \text{ pm}/\sqrt{\text{Hz}}$.

To compare different sized pinholes, the TTL coupling on different diodes was simulated. Figure 4.14 shows path length slope differences versus beam angle between small single-element photo diodes of different radii and a point-like photo diode (1 nm radius) for a scenario with arbitrary misalignments. The parameters for this simulation are: Reference beam – 1 mm waist at 2.5 m in front of the SEPD, measurement beam – 100 mm waist at the SEPD (top hat), pivot – 100 μm transversal offset (both directions) and 200 mm longitudinal offset. For the same simulation, the heterodyne efficiency over beam angle is shown in Figure 4.15. It can be observed, that the larger the diode is, the bigger is the difference to the ideal pinhole diode, as expected. Furthermore, on a larger diode the heterodyne efficiency drops faster with the tilt angle than on a smaller diode.

Besides the 10 μm diode, which is too small to achieve the requested path length stability, all tested diodes fulfill the requirements. Finally, a photo diode radius of 75 μm was chosen. The difference in coupling coefficient to an imaginary perfect 1 nm radius photo diode is below 0.1 $\text{pm}/\mu\text{rad}$ for the beam angle range from -500 μrad to +500 μrad (even more than the required $\pm 300 \mu\text{rad}$). The heterodyne efficiency is above 99% in the same angular range. With the actual beam power, this results in a path length noise on the pinhole of less than 0.5 $\text{pm}/\sqrt{\text{Hz}}$. However, from the requirements, it is also possible to use larger photo diodes but the 75 μm was the one with the best TTL coupling performance that can be easily manufactured.

Four-hole aperture design

To determine the optimal geometry for the four-hole aperture an IfoCAD simulation was computed. There are three parameters of the four-hole aperture that need to be defined: the distance between aperture and the QPD (d_{QPD}), the radius of the four holes (r_{ap}) and the distance between their centers (d_{ap}), Figure 4.16 demonstrates the different parameters.

The QPD will not be attached directly to the aperture. Due to manufacturing, there will be a gap (d_{QPD}) between the back surface of the aperture and the active surface of the QPD. The gap size is at least 1 mm but it would ease the manufacturing if the allowed gap size would be larger. Due to the gap, the electric field will show some diffraction and thus the area where the field can be detected is larger than the actual aperture holes. Furthermore, the QPD will not be aligned perfectly to the aperture due to manufacturing tolerances single μm lateral misalignment will be unavoidable. The two effects combined, diffraction and misalignment of the QPD, will lead to increased cross-coupling between the QPD segments when the distance

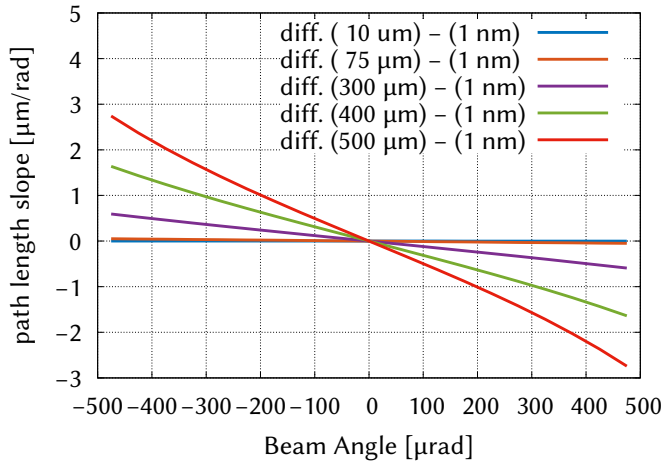


Figure 4.14.: Path length slope differences versus beam angle between small single-element photo diodes and a point-like photo diode (1 nm radius).

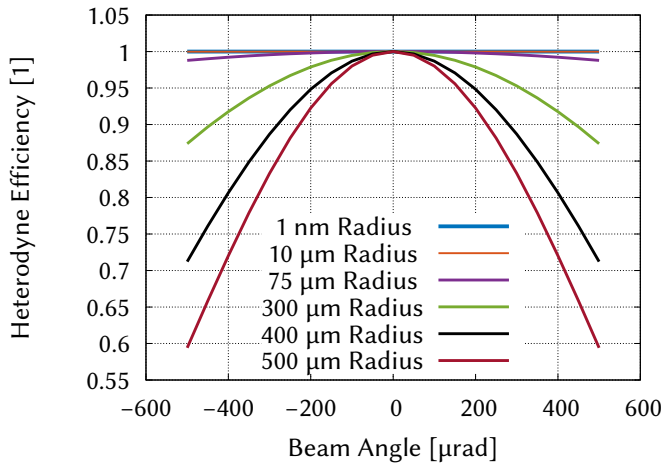


Figure 4.15.: Heterodyne efficiency over beam angle for small photo diodes of different radii. For the 75 μm radius photo diode it is above 98% for beam angles ranging from -500 μrad to +500 μrad .

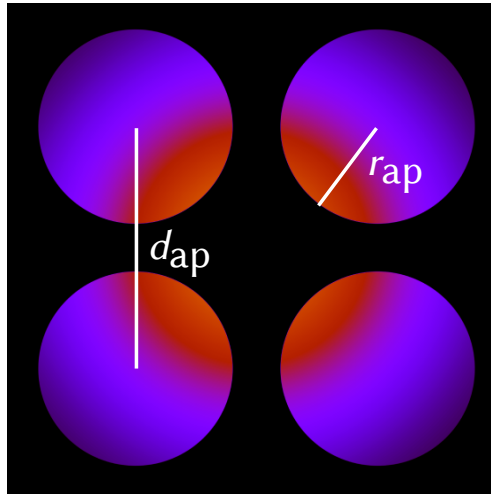


Figure 4.16.: Visualization of the parameters: r_{ap} and d_{ap} in a four-hole aperture. The third parameter is the longitudinal distance between aperture and QPD.

between aperture and QPD is increased and might lead to intolerable errors in the DPS signals. Depending on the distance between QPD and aperture, the holes of the aperture have to be small enough, that the diffraction pattern do not overlap with neighboring quadrants, even if the QPD is misaligned to the aperture.

To estimate this effect the following simulation was computed. The electric field of a 1 mm radius Gaussian beam (LO beam with 4.3 mW), clipped by a four-hole-aperture (with variable d_{ap} and r_{ap}), is computed using FFT optics (compare to Section 7.2.1). The diffraction pattern in various distances for one exemplary combination of d_{ap} and r_{ap} is shown in Figure 4.17. The DPS signal is computed on a QPD, for various distances between QPD and aperture. The QPD is transversally misaligned (with various offsets) to the aperture. Accordingly, the initial beam in front of the aperture is transversally misaligned until the resulting DPS signal becomes zero. The required beam misalignment is plotted against the QPD misalignment to acquire zero DPS. The result is a measure of how large the resulting offset of a QPD will be, which measures to be perfectly aligned. The results of this simulation are shown in Figure 4.18. The distance between aperture and photo diode d_{QPD} was varied between 0 and 11 mm, to cover the area between a perfect system without gap and a scenario where QPD and aperture can be fixed in different mounts.

We assumed that it is possible to align the QPD laterally to 0.1 mm with respect to the four hole aperture with the use of an optical coordinate measurement machine (CMM). For aperture radii up to 0.3 mm and 0.1 mm QPD misalignment, the beam position must be shifted by less than 1 μm to achieve zero DPS signal for a gap of 2.5 mm. Larger radii lead to an increased shift and hence are not beneficial. The resulting offset for a gap of 1 mm will be even smaller than 1 μm .

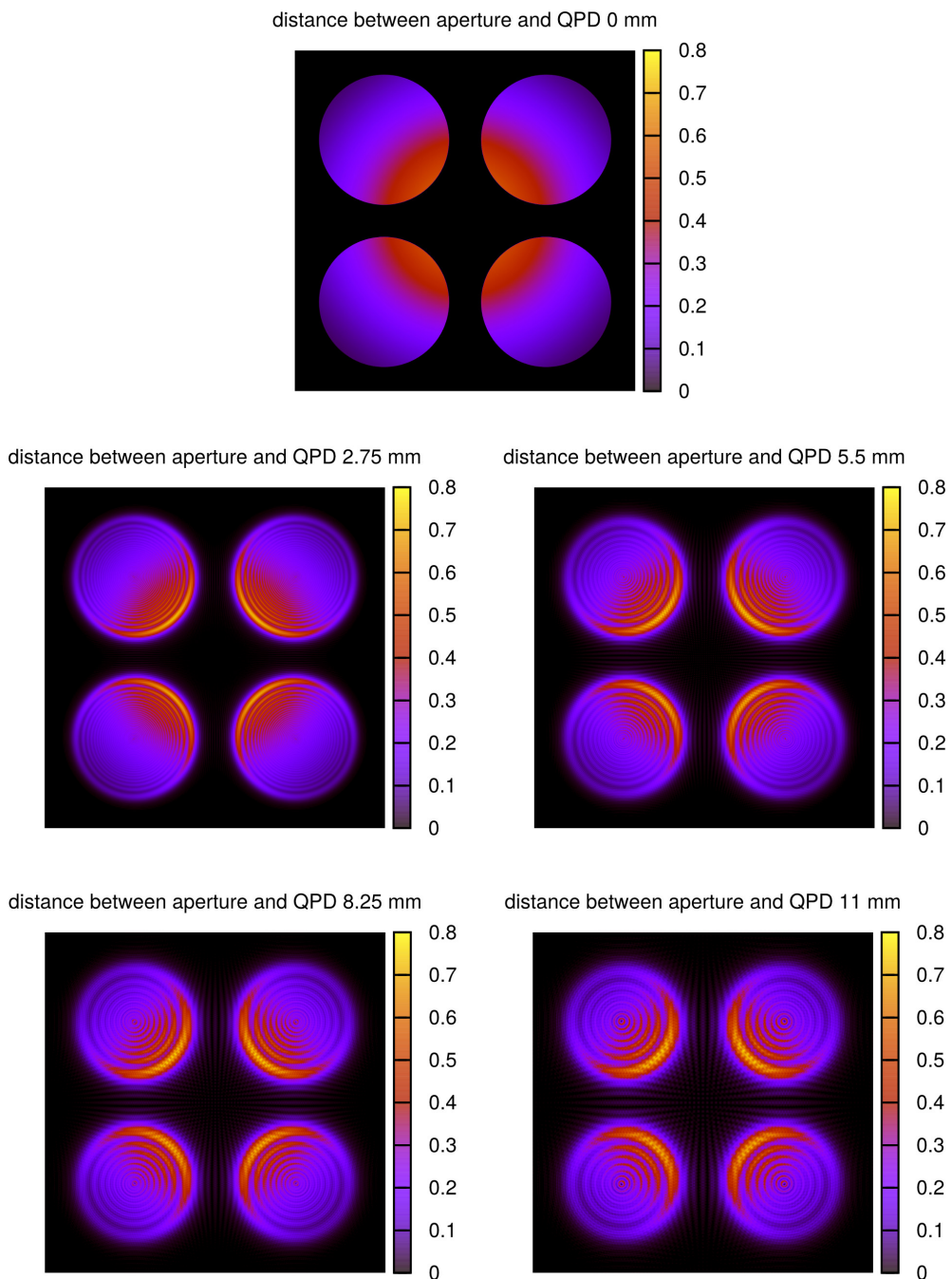


Figure 4.17.: Diffraction pattern behind a four-hole aperture for various distances between aperture and QPD.

An additional requirement was, the DPS signal should be as large as possible. Therefore, the simulated DPS signal for different aperture designs and a lateral shift of $3\ \mu\text{m}$ is shown in Figure 4.19. To simplify the simulation, instead of a four hole aperture, a QPD with suited parameters is simulated. The four hole aperture parameters, d_{ap} and r_{ap} , are approximated by a large QPD (5 mm) with a slit size of $d_{\text{ap}} - 2r_{\text{ap}}$. On the horizontal axis, the slit width between QPD segments was varied. The simulation shows that the DPS signal is fairly constant for slit widths between $1\ \mu\text{m}$ to 0.1 mm and then decreases for larger slit widths.

In the actual design the d_{QPD} was made as small as possible. The final distance is approximately 1 mm. From both simulations we chose 0.5 mm slit widths which corresponds to $r_{\text{ap}} = 0.25\ \text{mm}$ and $d_{\text{ap}} = 1\ \text{mm}$.

4.3.6. Flat-top-generator design

The idea and the design of the flat-top-generator was developed by Ewan Fitzsimons for Airbus Defence and Space. To fully replicate the science interferometer, the telescope simulator must produce a representative flat-top beam which simulates the far-field beam from a LISA spacecraft as it would be delivered by a LISA telescope.

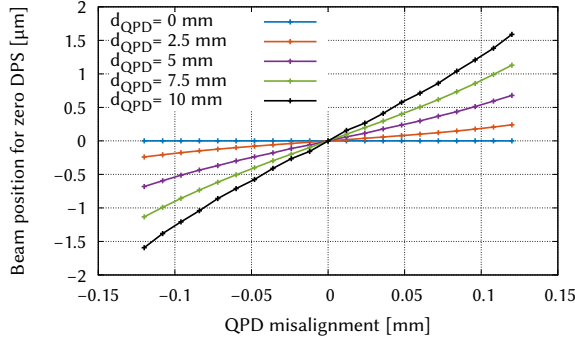
The first approach to produce such a flat-top beam was to use the beam from a naked fibre end. After a reasonable propagation distance, a very large Gaussian beam would be generated whose inner part can be cut out by an aperture and used as a top-hat beam. The top-hat beam afterwards needs to be imaged to the RX-clip to suppress diffraction from the aperture. The main reasons to discard this idea was the required amount of money and space. To generate a beam that is sufficiently large to produce a decent flat-top beam, a long distance between fiber end and aperture is required which is not available on the TS. Furthermore, imaging of the flat-top beam from its aperture to the RX-clip requires high quality imaging systems with requirements much more stringent than the DUT, which leads to large and expensive optical designs.

The flat-top design used within this project is based on a different approach. Instead of producing an excellent flat-top beam in the beginning and imaging it to the RX-clip, a wavefront is generated that becomes a reasonably shaped flat-top at the position of the RX-clip. Therefore, the beam from a large fiber coupler² is clipped at an apodized aperture, previously mentioned in Section 4.3.4. This specially designed aperture has a clear area in the center region and a Gaussian transmission drop off on the edges, which is realized by hyper Gaussian shaped pedals that form a star like structure. A photography of the aperture used is shown in Figure 4.20.

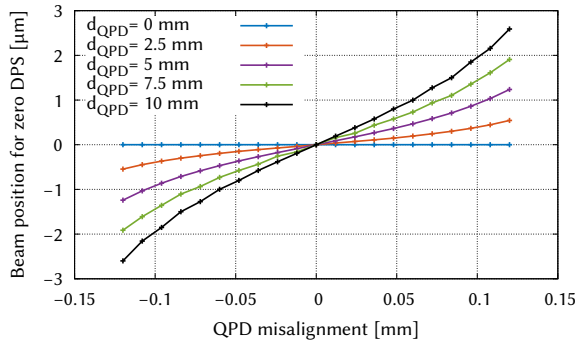
The Gaussian intensity transition in radial direction when averaged over all angles from the clear aperture to the edge suppresses diffraction and allows for a wavefront that keeps the plane phase and intensity profile in its center while propagating.

The design of the aperture (e.g. number and shape of the pedals, size of the clear aperture etc.) were optimized by a Monte-Carlo simulation to achieve the best performance at the RX-clip. The predicted performance of the system is shown in Table 4.1.

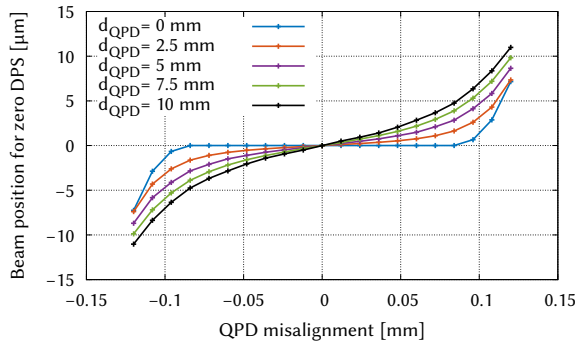
²Schäfer & Kirchhoff model 60FC-T-4-M100S-37



(a) $d_{\text{ap}}=1 \text{ mm}$, $r_{\text{ap}}=0.2 \text{ mm}$



(b) $d_{\text{ap}}=1 \text{ mm}$, $r_{\text{ap}}=0.3 \text{ mm}$



(c) $d_{\text{ap}}=1 \text{ mm}$, $r_{\text{ap}}=0.4 \text{ mm}$

Figure 4.18.: QPD four-hole aperture simulation. For different four-hole aperture parameters the beam position, at which the DPS signal becomes zero is plotted over the lateral offset of the QPD for various distances between QPD and aperture. E.g. in (a), for 10 mm distance between aperture and QPD, a QPD misalignment of 0.1 mm will result in a required beam offset of $1.2 \mu\text{m}$ to achieve zero DPS signal. This means: if the beam will be aligned using the DPS signal it ends up in a position, where the DPS signal indicates perfect alignment, but the beam will have a residual offset of $1.2 \mu\text{m}$.

Figure 4.19: Differential power sensing signal for a lateral shift of $3\ \mu\text{m}$ for a 5 mm diameter QPD; on the horizontal axis, the slit width between QPD segments was varied.

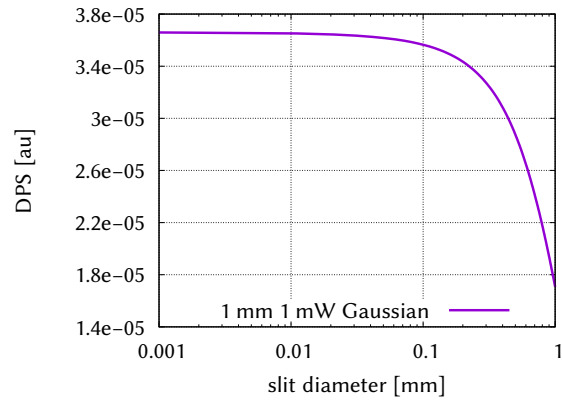


Figure 4.20: Photograph of the apodized aperture in aluminum mount. The bore in the aluminum mount has a diameter of 8 mm. This aperture is used for the flat-top generator of the TS as explained in Section 4.3.4.



Table 4.1.: Simulated main performance figures for the flat-top generator.

Property	Nominal	Including Tolerance
Intensity Flatness ($\varnothing\ 3\ \text{mm}$)	5.4%	11%
Phase Flatness ($\varnothing\ 3\ \text{mm}$)	$\lambda/100\ \text{PV}$	$\lambda/25\ \text{PV}$
Power Transmission ($\varnothing\ 2.2\ \text{mm}$)	3.1%	2.9%
Power loss ($> \varnothing\ 10\ \text{mm}$)	3.5%	3.6%

4.3.7. Electronics, laser preparation and vacuum tank

An overview of the entire setup with TS, OB and modulation bench is shown in Figure 4.21. The modulation bench provides three laser beams with different frequencies to allow a simultaneous measurement of all phase differences between the three beams (LO, RX and TX). The different heterodyne signals are called A, B and C in the following. Where A is the interference between TX and RX, B is the interference between LO and TX and C the interference between RX and LO. The three beams are

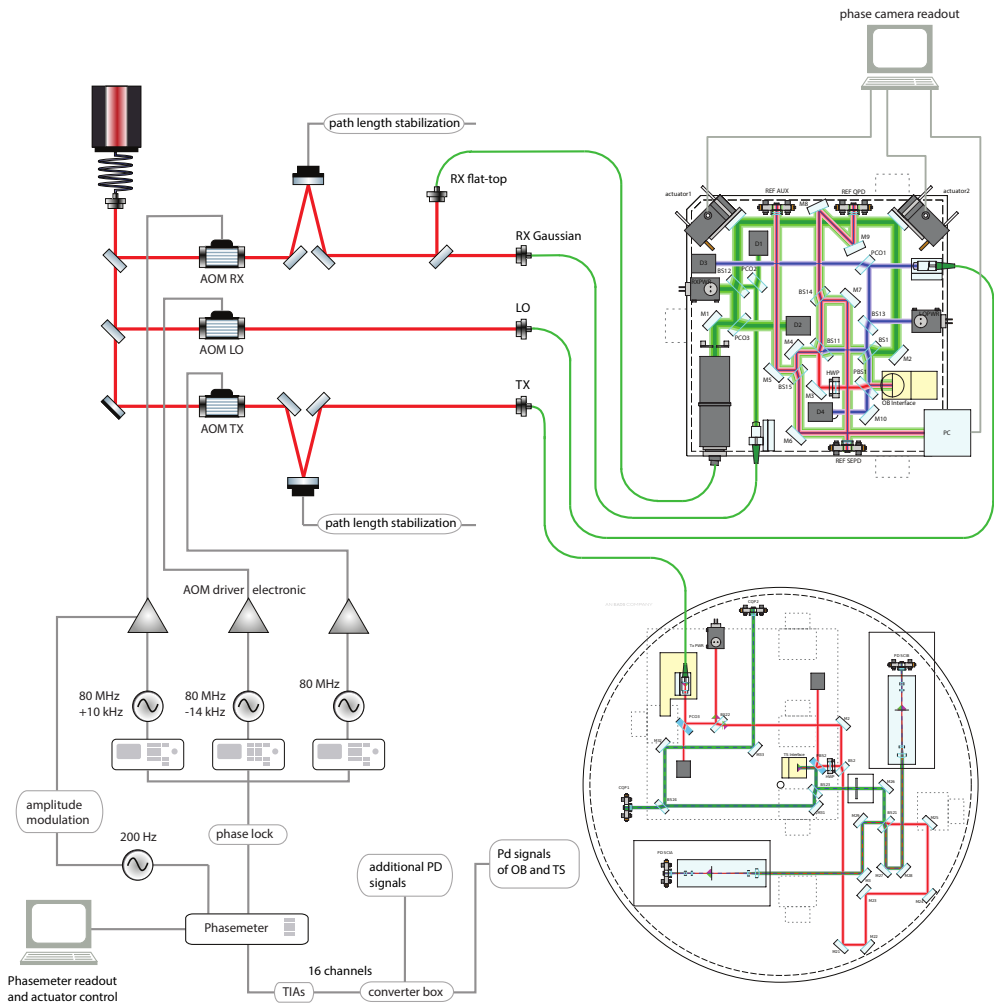


Figure 4.21.: Schematic of the laser preparation and electronic setup for the heterodyne frequency generation and the phase readout. The initial laser is split in three parts, to provide light for RX, TX, and LO. Each path has its own acousto-optical modulator (AOM) which generate the required heterodyne frequencies. Piezo mirror mounts on the modulation bench are used for an offset phase lock between the interferometer beams.

delivered to the setup by optical fibers and the RX beam is split again and coupled into two different fibers to allow an easy switching between the RX Gaussian and RX flat-top beam. One of the two is always blocked in front of the fiber coupler on the modulation bench.

In the beam path of the TX and the RX beam are additional linear piezo actuators after the AOMs. They are used for OPDs (optical pathlength difference stabilization) implemented in the phase meter. The phase difference between LO-TX (B) and LO-RX (C) is stabilized on the reference pinhole on the telescope simulator by actuating the path length with the piezo mounted mirrors. Therefore, the phase relation between all beams is constant on the reference pinhole and also in all optically equivalent points (RX-clip and all diodes on the TS).

Furthermore, an amplitude modulation, implemented in the AOM driver electronic, modulates the RX beam with ≈ 200 Hz. In the phase meter the photo diode signals are demodulated with this frequency and used to read out the position of the RX beam on the reference QPD independently of the other beams.

Signal readout

The signal readout and overall organization is performed with a single-bin discrete Fourier transform phasemeter [47] and a “readout and control” software. The phasemeter has 16 input channels for reading out the photo diode signals. The photo diode signals are connected to 25 D-Sub feed-through in the vacuum tank and divided into signals going to the phasemeter and additional signals in a converter box. The signals going to the phase meter are amplified with trans-impedance amplifiers (TIA) and connected to the analog-to-digital converter of the phase meter. More details and circuit layouts of the converter box and the TIAs can be found in [TD3].

Not all photo diodes can be read out simultaneously with the 16 channels. The CQP and the temporary four-hole aperture QPD are connected to separate TIAs and the signals are displayed with an oscilloscope for the alignment. However, the converter box can be used to feed different signals to the phase meter temporarily like the CQP diodes or the power monitor diodes for debugging.

Control software

The actuation of the tilt mirrors on the TS is controlled via a PC and piezo driven mirror mounts³. An automated measurement procedure performing a tilt measurement with all the necessary actuation and alignment of the tilt mirrors is implemented in a measurement program. The 16 channels of the phase meter are recorded with the DC value, phase and amplitude of all three heterodyne signals and the amplitude modulated signal. In addition error signals and actuation signals of the two optical

³Newport Agilis™ AG-M100LV6

```

lob_khz_pm      Freq A: 9765.625000 |   Freq B: 14648.437500 |   Freq C: 24414.062500 |
Package counter: 118 |Missing packages: 1

Signals         CH01:      CH02:      CH03:      CH04:      CH05:      CH06:      CH07:      CH08:
DC              :+0.382      +0.973      +0.252      +0.260      +0.256      +0.267      +0.194      +0.059
A:Amp           :+0.000036   +0.000001   +0.000009   +0.000012   +0.000014   +0.000013   +0.000030   +0.000012
A:Phase         :+41.996361   +31.278860   +16.513461   +61.378273   +61.290500   +55.252966   +44.997982   +40.918958
B:Amp           :+0.000018   +0.000002   +0.000056   +0.000030   +0.000028   +0.000035   +0.000079   +0.000128
B:Phase         :-45.434957   -40.754397   -54.760145   -60.134653   -53.313354   -53.896588   -44.093116   -36.606916
C:Amp           :+0.160737   +0.000007   +0.097172   +0.096540   +0.093878   +0.099346   +0.072253   +0.025744
C:Phase         :-2.925382   -2.640138   -2.897313   -2.818474   -2.987472   -3.031109   -0.019556   -3.140261
AM:Amp          :+0.022658   +0.000000   +0.013166   +0.013050   +0.012830   +0.013085   +0.010034   +0.004375

Signals         CH09:      CH10:      CH11:      CH12:      CH13:      CH14:      CH15:      CH16:
DC              :+0.088      +0.088      +0.091      +0.082      +0.069      +0.083      +0.071      +0.091
A:Amp           :+0.000008   +0.000006   +0.000013   +0.000010   +0.000011   +0.000011   +0.000006   +0.000014
A:Phase         :+45.305271   +53.165830   +46.591479   +49.310459   +38.052031   +50.200625   +37.829114   +43.772668
B:Amp           :+0.000036   +0.000055   +0.000099   +0.000059   +0.000094   +0.000074   +0.000051   +0.000093
B:Phase         :-48.448627   -42.455584   -49.022286   -41.428725   -47.948953   -41.238092   -41.570598   -40.277950
C:Amp           :+0.001004   +0.000880   +0.000912   +0.001056   +0.000083   +0.000078   +0.000057   +0.000083
C:Phase         :+0.440226   +0.458830   +0.502341   +0.424478   +0.121826   +0.108529   +0.167541   +0.278696
AM:Amp          :+0.000101   +0.000079   +0.000081   +0.000107   +0.000002   +0.000002   +0.000001   +0.000010

OPD1:          OPD2:
ERR            : -0.000032   ERR            : -0.000000
ACT            : +0.257      ACT            : -0.001
CH|FREQ:       08 | c   CH|FREQ:       02 | a

---- Ref QPD ----      ---- Sci QPD 1 ----      ---- Sci QPD 2 ----
DPS 1:         +0.000301   DPS 1:         +0.004694   DPS 1:         -0.030946
DPS 2:         +0.000374   DPS 2:         -0.024483   DPS 2:         +0.021003
DWS 1:         +0.302791
DWS 2:         -0.122472
    
```

Figure 4.22.: Screenshot of the user interface of the measurement program. For each phasemeter channel the DC value, phase, and amplitude for all three heterodyne frequencies and the amplitude modulated (AM) signal is displayed. In addition error signals and actuator signals for the OPD locks, DPS, and DWS signals are displayed.

path difference (OPD) locks are recorded. For the TTL measurement averaged values for every step are recorded as well as a log file for checking alignment and measurement steps. A screen shot of the terminal output of the measurement program is shown in Figure 4.22.

The program has a watch-mode where it is run without the tilt actuation for alignments and system checks. For this mode it is displaying the DPS signals of the science QPDs.

Complete measurement procedure In the following, the automated measurement procedure is described. It contains the control software, which is controlling the different components of the experiment. The phasemeter is responsible for the signal readout, the OPDs and the amplitude modulation of the RX, the actuators are tilting and shifting the RX beam, the temperature board is responsible for the temperature readout, and the phase cam program is operating the phase camera. Before the measurement, the total angular range, and the tilt steps are defined (e.g. $\pm 500 \mu\text{rad}$ in 75 steps).

Measurement procedure

1. Control software is started and initializes the phasemeter and the temperature board in additional separate threads.
2. Control software establishes connection to the tilt actuators (RS232) and the phase cam (TCP).
3. Control software aligns the RX beam using the tilt actuators.
 - a) Tilt actuators go to optimal position using an actuation to an absolute position (rough).
 - b) Tilt actuators center the RX beam on the Ref QPD using the amplitude modulated DPS signals.
 - c) Tilt actuators maximize the C-amplitude on the Ref QPD.
 - i. Actuator 1 moves in one axis in one direction.
 - ii. Actuator 2 centers the RX beam on the Ref QPD using the amplitude modulated DPS signals.
 - iii. If the amplitude becomes better, repeat. Otherwise go in other direction.
 - iv. Repeat for both axis.
 - d) Tilt actuator minimizes the C-phase DWS signal on the Ref QPD.
 - i. Actuator 1 moves in one axis in one direction.
 - ii. Actuator 2 centers the RX beam on the Ref QPD using the amplitude modulated DPS signals.
 - iii. If the DWS signal becomes better, repeat. Otherwise go in other direction.
 - iv. Repeat for both axis.
 - e) Start measurement at angle zero, actuate step by step from zero to the minimal angle, next to the maximal angle and back to zero. For each step use the tilt actuators to center the RX beam on the Ref QPD and perform a measurement:
 - i. Control software informs the phasemeter to start a measurement step.
 - ii. Phasemeter averages the next 900 sample points and saves the averaged data to a dedicated output file and tells the control software to proceed.
 - iii. Control software disables the amplitude modulation and tells the phase camera to record a picture.

- iv. Phase camera records a picture, saves it and tells the control software to proceed.
 - v. Control software enables amplitude modulation.
 - vi. Control software commands tilt actuator to go to the next angle.
- f) After all angle steps are measured, the program has finished.

Step 3(e)iii and 3(e)iv can only be done with two active beams (no TX beam).

4.3.8. Design properties and noise budget

This section summarizes the design properties of the test bed including the optical power budget, path-length performance budget and the tilt-to-length coupling budget.

Path length performance budget

The path length noise budget has been estimated, taking into account all noise sources that are currently known. For some noise sources – like shot noise and electronic noise – the expected noise varies with beam power, and so is different at each detector. Here, we take the worst case value computed to create a single worst-case estimate of the system noise performance. Note that tilt-to-piston coupling is explicitly excluded from the performance budget as it is the measurement target. The budget is detailed in Table 4.2.

Table 4.2.: Path length performance budget.

Noise Source	Expected Value [pm/ $\sqrt{\text{Hz}}$]
Laser frequency noise	0.01
Residual CTE (Zerodur [®])	0.1
Non-common mode silica noise	0.5
Shot noise	0.03
RIN	0.62
Electronic noise	1
Phasemeter quantization noise	0.2
Total (RSS)	1.29

Path length and fused silica matching

Mismatches in path length between adjacent interferometer arms cause coupling of laser frequency noise into displacement noise. In order to minimize this coupling, the test bed was designed to have a nominal path-matching error between the adjacent arms of zero. In addition, the testing program makes use of a frequency stabilized laser (locked to an Iodine standard), with a frequency noise in the range of $300 \text{ Hz}/\sqrt{\text{Hz}}$. Combined with a cm-scale path length mismatch this will reduce the impact of laser frequency noise in the measurement band to ca. $10 \text{ fm}/\sqrt{\text{Hz}}$ and is thus negligible in the performance budget.

The other requirement is on the differential number of fused silica transmissions between the reference and measurement interferometer. Each transmission of a beam through a fused silica substrate will induce phase (displacement) noise to the beam due to coupling of temperature noise via the thermal expansion of the substrate and the change of refractive indices. It is necessary to ensure this noise is not dominant [48].

There are two requirements here:

1. For each frequency combination in an interferometer, the differential number of silica transmissions should be identical between the measurement and reference interferometers. This ensures that the induced temperature noise is common mode between measurement and reference and will cancel out - under the assumption of homogeneous and isotropic temperature fluctuations. In reality, manufacturing and alignment tolerances will leave some residual, but this should be small and in any case cannot be corrected for.
2. To minimize coupling through non-common mode temperature noise (which can exist e.g. due to thermal delays), the absolute difference in transmissions should be as small as possible - in practice this means zero or one.

The number of silica transmissions on the test bed is summarized in Table 4.3, and is compliant with both of the requirements outlined above. Assuming a temperature stability of $10 \text{ K}/\sqrt{\text{Hz}}$, a non-common mode contribution of around 1 mm per arm (due to manufacturing and alignment tolerances of the optics) and a de-coherence of temperature noise of 50% across the OB at low frequency, this would lead to a displacement noise contribution from this effect of around $0.5 \text{ pm}/\sqrt{\text{Hz}}$.

TTL coupling budget

The goal of the OB-TS experiment is to measure and analyze imaging systems regarding their property of suppressing TTL coupling. As shown previously Section 3, the overall TTL coupling is a superposition of multiple contributions, which are indistinguishable if only the overall TTL coupling is measured. Most of these sources

Table 4.3.: Number of transmissions in silica for the measurement interferometer on the OB and the reference interferometer on the TS. Since the thickness of all transmissive components is equal, it is sufficient to only match the number of them.

Beam	Reference	Measurement
TX	3	3
LO	2	2
RX (flat-top)	3	3
RX (Gaussian)	2	2

Table 4.4.: Tilt-to-length coupling budget, derived from system level bottom-up estimation.

Contributor	Comment	Requirement [$\mu\text{m}/\text{rad}$]
Imaging Systems	Including all alignment and manufacturing tolerances	25
Non-common mode WFE	Required $\lambda/20$ RMS WFE	10
RX Aperture Alignment	Requires RX Aperture alignment to $\pm 20 \mu\text{m}$	20
QPD Alignment	Requires QPD alignment to $\pm 10 \mu\text{m}$	20
TS Residual	Requires alignment of the TS at $\pm 20 \mu\text{m}$	20
Longitudinal Offsets	Requires control of longitudinal offsets to $\pm 1 \text{ mm}$	2
Total	(RSS)	44

can be significantly suppressed, (e.g. alignment of the setup or the longitudinal movement of the actuators). However, none of these sources can be removed completely. Therefore, requirements for TTL coupling contributions have to be set to ensure that the residual TTL coupling behind the imaging systems is not dominated by effects that are not related to the imaging systems themselves.

The TTL coupling budget for the OB-TS experiment is derived from the analysis developed in [TD6, TD8], and assumes that the coupling is dominated by the linear component. A list of requirements derived from the system level budget is shown in Table 4.4. The actual residual TTL coupling is much better than the required level. In Table 4.5 the estimated TTL coupling contributions of the present testbed are listed.

Table 4.5.: Estimated tilt-to-length coupling contributions of the test bed.

Contributor	Comment	Goal [$\mu\text{m}/\text{rad}$]
Imaging Systems	Including all alignment and manufacturing tolerances - maintain from requirements.	25
Non-common mode WFE	Measured differential WFE of LTP FIOS is $< \lambda/100$ RMS and test bed does not feature the telescope which is expected to dominate the WFE.	3
RX Aperture Alignment	Utilize repeat measurement and adjust capability to try and achieve $< 5 \mu\text{m}$ alignment, combined with ca. $5 \mu\text{m}$ manufacturing accuracy.	10
QPD Alignment	Utilize ability to re-adjust QPD to achieve $< 2 \mu\text{m}$ alignment	4
TS Residual	Utilise CQP to ensure sub $2 \mu\text{m}$ alignment	2
Longitudinal Offsets	Requires control of longitudinal offsets to $\pm 1 \text{ mm}$	2
Total	(RSS)	27.6

4.3.9. Four-lens imaging system optical design LOB4C

The imaging system shown in this section was designed by Airbus Defence and Space and is part of the LISA optical bench telescope simulator project [TD3, TD5, P6].

The four lens imaging system is designed using a classical optics approach. The resulting on-axis design utilizes spherical fused silica lenses with curvature radii that were selected from the list of standard tools from Zeiss. The design includes a $150 \mu\text{m}$ field stop between lens two and three to block stray beams reaching the photo diode. Figure 4.23 shows the four-lens imaging system. In the coordinates of the given x-axis, the point of rotation is placed at zero, the imaging system is placed in the range from 0.35 m to 0.46 m right in front of the QPD. A list of specifications are shown in Table 4.6. This specific four-lens design is named LOB4C- LISA optical bench four-lens imaging system providing a collimated beam.

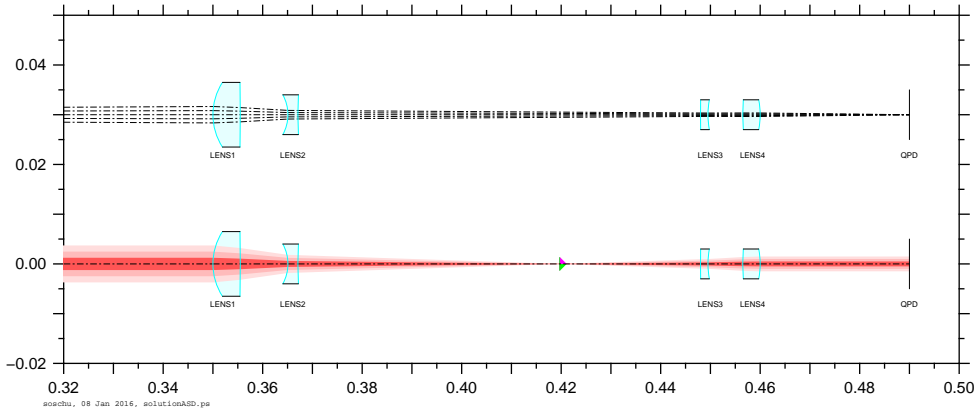


Figure 4.23.: Optical model of the four-lens imaging system LOB4C. The point of rotation (RX clip) is located at position 0 mm. The first plot shows the propagation of different base rays, which start under different angles at the point of rotation and end up in the center of the QPD (demonstrating zero beam walk). The second plot is showing the propagation of a Gaussian beam. The triangles indicate the waist position (tangential and sagittal plane). Furthermore, the magnification factor can be seen. The large 1 mm waist Gaussian beam is compressed and becomes 0.4 mm on the QPD.

Table 4.6.: Specifications of the four-lens classical pupil plane imaging system LOB4C.

		Lens 1	Lens 2	Lens 3	Lens 4	QPD
Radius of Curvature 1	mm	12.009	-8.289	220.27	40.115	
Radius of Curvature 2	mm	376.3	-72.758	-16.295	15.609	
Position	mm	350	365.079	419.745	456.499	490
Thickness	mm	5.5	2.0	1.5	3.5	
Diameter	mm	13	8	6	6	
Refraction index	1	1.44963	1.44963	1.44963	1.44963	
QPD Aperture Diameter	mm					0.9
QPD Slit Diameter	μm					20

4.3.10. Two-lens imaging system optical design LOB2D

The imaging system presented in this section was designed by myself and formerly published in [TD3, TD5, P6].

The two-lens imaging system was designed using a design algorithm developed by Gerhard Heinzel [TD2, 49]. The central idea is to neglect all requirements that appeared to be unimportant. The main requirements discarded here are the property to provide a collimated exit beam and the need of an internal pupil, thus only vanishing beam walk, vanishing TTL coupling, and a suitable beam size on the QPD are required. However, one result of this project is that a collimated output beam is necessary in order to be robust against beam parameter variations. Further details can be found later on in Chapter 6.

The reduced set of requirements allows a reduction in the number of lenses. The two-lens imaging system was designed by using the framework IfoCAD. A list of off-the-shelf spherical fused silica lenses was used as starting point. For each combination of two lenses, the distance between both lenses as well as the distance between the second lens and QPD was varied until a measurement beam tilted by $100\ \mu\text{rad}$ hit the center of the QPD at an angle of $250\ \mu\text{rad}$ (0.4 magnification). For any solution found, the path length signal and its slope (tilt-to-length coupling) were computed. The solution with the best performance was chosen. The resulting set of lenses and parameters can be found in Table 4.7. A sketch of the setup can be found in Figure 4.24. This specific design is named LOB2D– LISA optical bench imaging system, providing a divergent output beam.

The functional principle of a two-lens imaging system was successfully tested in a previous experiment – in a special scenario with perfectly equal beams it could be demonstrated that the TTL coupling can be reduced below $2\ \mu\text{m}/\text{rad}$ in an angular range of $\pm 100\ \mu\text{rad}$. Technical details and the measurement results can be found in Appendix B as well as in [6] and [P1].

4.4. Delimitation to other experiments

The LISA optical bench testbed is not the first experiment dedicated to measure TTL coupling and will not be the last. Since TTL coupling is the relation between a beam tilt and the longitudinal path length signal, an actuator is required that does not move longitudinally. Thus, any TTL coupling experiment needs to readout and stabilize the longitudinal position of the actuator by using methods that are unaffected by TTL coupling. The reliable stabilization of the tilt actuator is usually the main challenge in measuring TTL coupling.

Within this section the different iterations of TTL coupling experiments are shown and the different mechanisms that were used to stabilize the actuators are compared to explain the advantages of the LISA testbed with respect to previous work and give an outlook of what might be improved in future experiments.

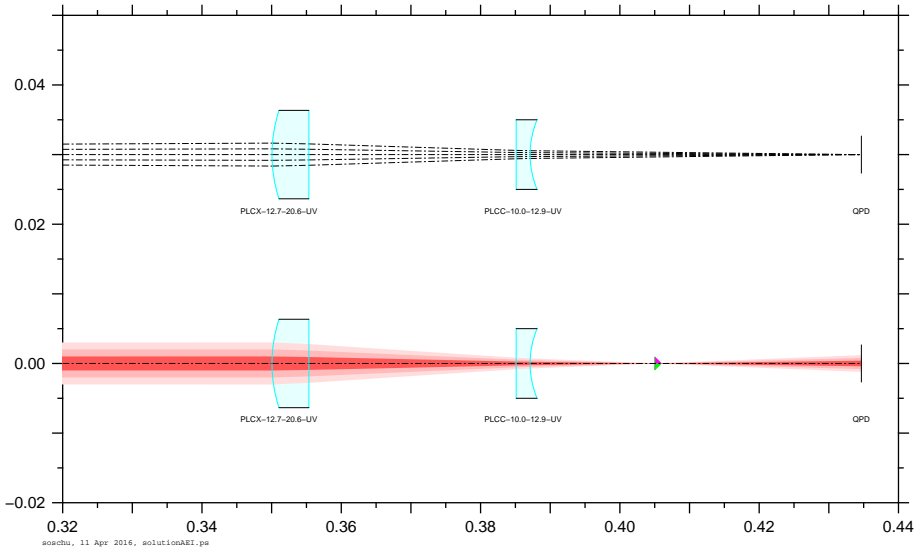


Figure 4.24.: Optical model of the two-lens imaging system LOB2D. The point of rotation (RX clip) is located at position 0 mm. The first plot shows the propagation of different base rays, which start under different angles at the point of rotation and end up in the center of the QPD (demonstrating zero beam walk). The second plot is showing the propagation of a Gaussian beam. The triangles indicate the waist position (tangential and sagittal plane). Furthermore, the magnification factor can be seen. The 1 mm waist Gaussian beam is compressed and becomes 0.4 mm on the QPD.

4.4.1. First iteration – large detector heterodyne

In the first TTL coupling experiment the longitudinal movement of the tilt actuator was measured on a large SEPD. In case of equal beam parameters of the two interfering beams, a large detector and no lateral offset of the point of rotation, no TTL coupling is expected, as explained in Section 3.1.3 and Appendix A. Thus, the longitudinal signal measured on the large detector must be the movement of the actuator. This measured movement can either be used to actively stabilize the tilt actuator, or it can simply be subtracted from the measured signal behind the tested imaging system. A simplified setup of the first experiment is shown in Figure 4.25. The design and results of this experiment are shown in [TD2].

In summary, in this experiment it could be shown that imaging systems can reduce the TTL coupling significantly. However, one major problem with the tilt actuator stabilization was discovered. A large diode senses no TTL coupling only in a scenario with two perfectly equal beams. In this experiment, the reference and the measurement beam came from two individual fibre injectors. Thus, the beam parameters of the two beams could not be matched perfectly (variations in the spot

Table 4.7.: Specifications of the AEI two-lens imaging system LOB2D.

		Lens 1	Lens 2	QPD
Name		PLCX-12.7- 20.6- UV-1064	PLCC-10.0- 12.9- UV-1064	
Position	mm	350.051	385.109	434.673
Primary Curvature	mm ⁻¹	0.0485601	0.0	
Secondary Curvature	mm ⁻¹	0.0	-0.0774931	
Center Thickness	mm	5.3	2.0	
Substrate Radius	mm	6.35	5.0	
Refraction Index	1	1.44963	1.44963	
QPD Aperture Diameter	mm			0.9
QPD Slit Diameter	μm			20
Minimum Ghost Power Suppression	1			$1.36 \cdot 10^{-7}$

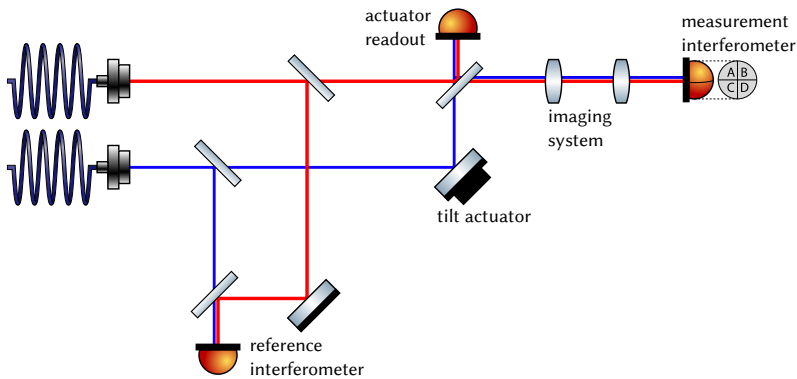


Figure 4.25.: Schematic setup of the first TTL experiment. In a heterodyne interferometer, the tilt actuator is stabilized on a large single element photo diode. In the measurement interferometer an imaging system can be placed to measure the TTL coupling suppression.

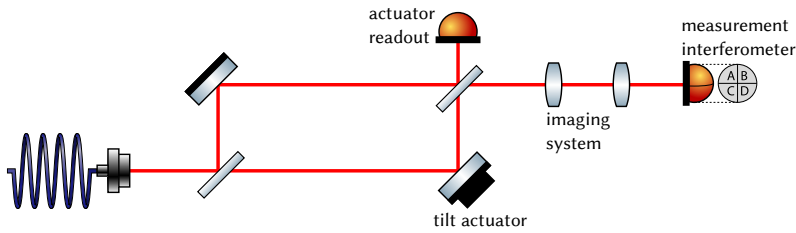


Figure 4.26.: Schematic setup of the second TTL experiment. A homodyne interferometer ensures equal beam parameters of the two superimposed beams.

size on the detector in the scale of 30% between the nominally equal beams were observed). Therefore, the large diode sensed TTL coupling coming from the beam parameter mismatch between the two beams. This TTL coupling was subtracted from the actual measurement, because it was not possible to distinguish between a movement of the actuator and TTL coupling on the large detector.

Concluding, the result from this experiment is that imaging system can reduce TTL coupling, but additional TTL contributions due to the beam geometry were neglected here, since they were probably removed by the tilt actuator stabilization method.

4.4.2. Second iteration – large detector homodyne

The second iteration of TTL experiments is an improved version of the heterodyne setup shown above. To overcome the uncertainty in the beam parameters and avoid subtraction of unintended TTL contributions, additional measures were taken to match the beam parameters perfectly. Instead of a heterodyne interferometer with two fibre injectors, a homodyne setup with only one initial beam was set up. By matching the arm length in the interferometer it was ensured that the two interfering beams are perfectly equal. A simplified setup is shown in Figure 4.26. Further details about this experiment can be found in Appendix B.

With this experiment it was confirmed that imaging systems can reduce the TTL coupling significantly. However, this result was achieved in an interferometer with perfectly equal beams. In space applications like LISA, the interferometers feature unequal beams (e.g. flat-top vs. Gaussian beam). Thus, additional TTL contributions that were not covered with this experiment will be present. In order to show that imaging systems can perform sufficiently in LISA, an experiment featuring unequal beams and heterodyne readout must be performed. These two requirements are contradictory with the method to stabilize the tilt actuator used so far.

4.4.3. Third iteration – LISA testbed

The LISA optical bench testbed uses a different approach to stabilize the tilt actuator. The tilt actuator is not in the measurement path anymore. As explained in Section 4.3.1 and shown in Figure 4.4, the measurement beam is tilted before the reference interferometer. The longitudinal movement of the actuator is read out with a pinhole diode in an optical copy of the intended point of rotation. The pinhole senses only the longitudinal movement of the actuator, since it is placed directly at the point of rotation and the wavefront curvatures of the interfered beams are small with respect to the pinhole (cf. Chapter 3). With this approach it is not required to use beams with equal beam parameters, even a superposition between a Gaussian and a flat-top is possible. Thus, in this testbed TTL coupling can be measured under realistic conditions.

The main disadvantage of this setup is its complexity. The alignment between the optical bench and the telescope simulator is crucial and it is impossible to exchange several components (FIOS, mirrors, etc. are bonded permanently to the base plates). The chosen design and working principle of the LISA testbed is optimal to test imaging systems in a LISA like scenario, but for more universal tests of varying interferometric designs and beam parameters, this approach might be too complicated.

4.4.4. Fourth iteration – advanced tilt actuator

The advanced tilt actuator (ATA) is a concept for the next generation of TTL coupling experiments. Here, a different approach was chosen. Since the main challenge in TTL coupling experiments so far was the suppression of the longitudinal movement of the tilt actuator, the new testbed will cover only this problem. The idea is to build an actuator without longitudinal movement. With this device future TTL coupling experiments will be simplified significantly. Instead of including a tilt actuator stabilization mechanism in each experiment, the ATA can be used. In a test mass scenario the optical layout of the TM interferometer can be used as it is, just the TM is replaced with the ATA. Similar for any imaging system test, the ATA is placed in the intended point of rotation and the setup is ready to test imaging systems.

The ATA is a closed system, featuring a tilt mirror and a control and stabilization concept. The only interface to future experiments is the mirrors surface (e.g. as a TM simulator). Multiple corner cubes (retro-reflector or cats eye) are attached on the backside of this mirror. For each corner cube one interferometer is set up on a baseplate. Corner cubes have the special features, that a laser beam which is sent into the cube comes out of the cube under the exact same angle and the round trip path length does not change when the retro reflector is rotated around its vertex. Therefore, corner cubes sense no TTL coupling. A rotation of the corner cube around its vertex, does not change the phase and orientation of a laser beam that is reflected from this corner cube.

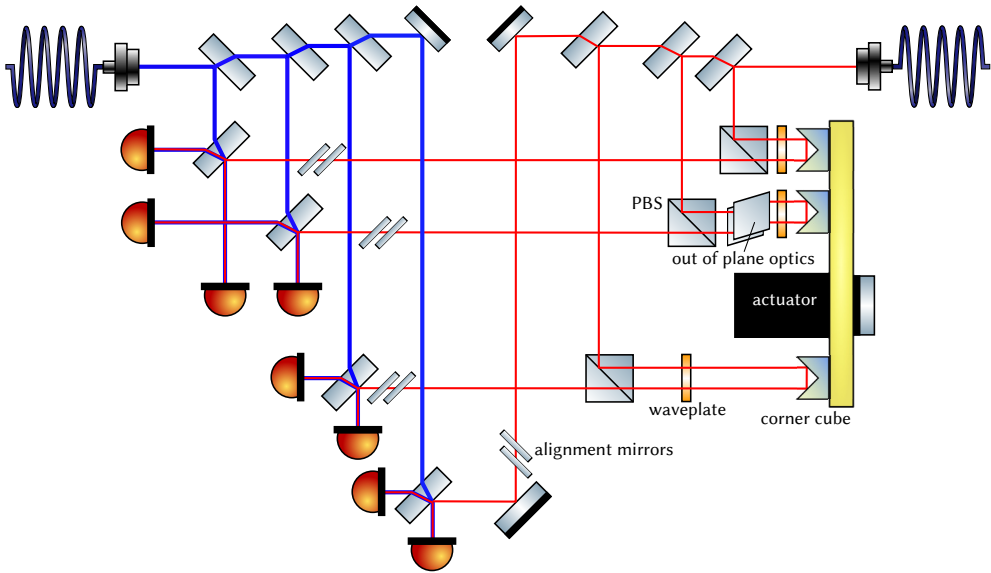


Figure 4.27.: Advanced tilt actuator (ATA) setup; the ATA tilt mirror provides an optical readout of four corner cubes that are attached to the backside of the mirror plane. With multiple interferometers the entire mirror plane can be monitored and with sophisticated control electronics, the longitudinal movement can be suppressed.

With the simultaneous readout of the vertex movement of the four corner cubes, the exact position and orientation of the mirrors surface can be computed and stabilized to zero longitudinal movement. A sketch of the ATA optical layout is shown in Figure 4.27.

5

LISA testbed – alignment and measurement campaign

Within this chapter, the measurement campaign of the LISA testbed is shown. Including the calibration and alignment of the TS as well as the performance measurement of the two imaging systems and the corresponding tolerance analysis.

5.1. Alignment and calibration

The following sections report on the different calibration measurements necessary to operate TS and OB. One aim of the DUT investigation is to compare the simulated and the measured performance, in order to verify that the predictions obtained by simulations are valid. Therefore, a match between simulations and experiment in the calibration is desirable. Wherever possible, the measurements were repeated in IfoCAD and the results are compared.

5.1.1. Photo diode signal calibration

Quadrant photo diodes (QPD) can be used to readout position and angle of incident beams. On the TS especially the reference QPD is used to monitor the RX beam. The DPS signals are used for aligning the RX beam, suppressing beam walk on the reference QPD. The DWS signal of the reference QPD is used for measuring the actual angle of the RX beam. The information from the tip-tilt actuators cannot be used because the step size is varying too much.

The DPS and the DWS signals were calibrated. They depend – besides the beam parameters – on the photo diode geometry and therefore each diode has to be calibrated for every beam that needs to be monitored.

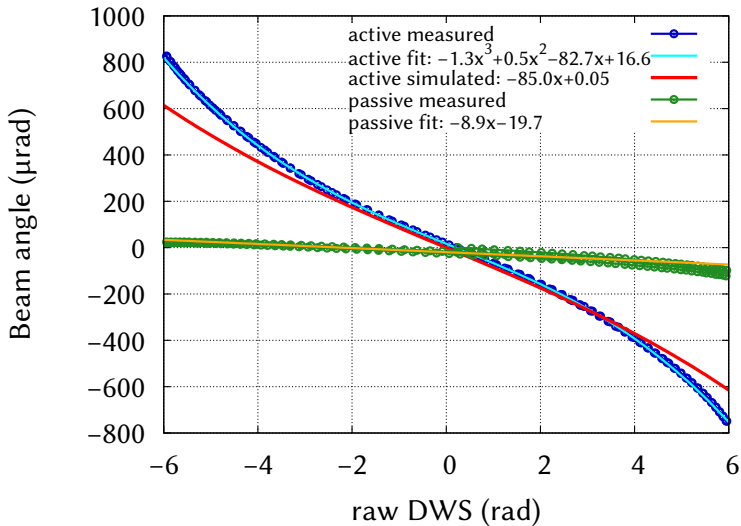


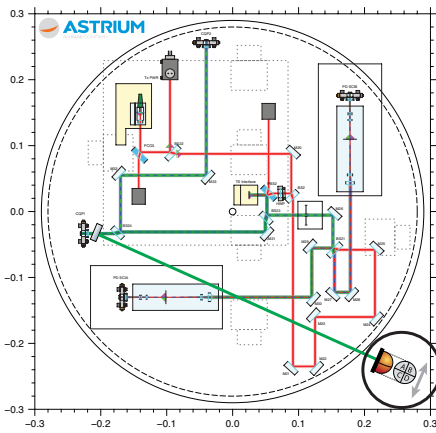
Figure 5.1.: Calibration of the DWS signals for the Gaussian RX beam on the reference QPD. The beam angles from calibrated DPS signals are plotted versus DWS signals for the active axis (vertical) and the passive axis (horizontal). Polynomials are fitted to the measured data. The IfoCad simulation fits well to the measured data.

Calibration for the Gaussian beams

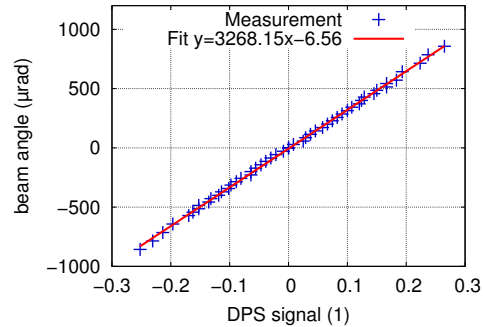
For the LO beam and the RX Gaussian beam with a Gaussian beam profile the DPS signals can be calculated analytically using the measured beam size and the QPD geometry as shown in [16] on page 44. The beam radii are 1.11 mm for the LO beam and 1.35 mm for the RX Gaussian beam measured with a beam profiler (WinCam) at the distance of the RX-clip from the FIOS.

With the beam position on two QPDs (calibrated DPS signal) and the known distance between them the beam angle can be calculated. Here the Ref QPD on the Telescope Simulator and the QPD₂ from the CQP on the Optical Bench are used for measuring the angle of the RX Gaussian beam. The beam angle is then used to calibrate the DWS signal as shown in Figure 5.1. For a comparison, the DWS signal was calculated with IfoCAD, too. The result is plotted in Figure 5.1 and shows a good match with the measured calibration. IfoCAD simulates a calibration coefficient of $-85.0 \mu\text{rad}/\text{radDWS}$ compared to the measured value of $-82.9 \mu\text{rad}/\text{radDWS}$. The difference between the two values is $\approx 2.5\%$. Considering the inaccuracies in the beam parameter determination and the variations in the QPD geometry, the match in the DWS calibration is adequate.

This calibration of the DWS signal for the RX Gaussian beam on the reference QPD is used in the subsequent measurements.



(a) Position of the temporary QPD for the DWS calibration of the RX flat-top beam.



(b) DPS signal vs. beam angle. The beam angle is calculated from the distance to the rotation point and the lateral position of the QPD.

Figure 5.2.: DPS and DWS calibration for the RX flat-top beam with an additional QPD on a translation stage next to the OB.

Calibration for the RX flat-top beam

For the flat-top beam the DPS signals cannot be calculated analytically with sufficient precision, since the intensity and phase profile of the real “flat-top” beam is not easily characterized. At the position of the RX-clip and therefore also at the position of the reference QPD, the flat-top is supposed to be flat in phase and intensity, but even small deviations to a flat profile will alter DPS and DWS signals.

Thus, before calibrating the DWS signal the DPS signal has to be calibrated to get well calibrated signals. This is done by laterally shifting an additional QPD by a known distance and reading out the DPS signal. The relation between DPS signal and corresponding shift of the QPD is used as calibration. The additional QPD is required because the CQP diodes cannot be shifted, hence their alignment is defining the alignment of the Telescope Simulator and needs to be fixed in a certain position. The additional QPD was installed next to the OB on an x-y translation stage with micrometer screws as shown in Figure 5.2a. The result of the DPS calibration for this temporary QPD is shown in Figure 5.2b.

With the distance of this additional QPD from the rotation point in the RX aperture the angle is calculated and the DWS signal is calibrated. The result is shown in Figure 5.3. The coefficient for the flat-top beam is $-84.2 \mu\text{rad}/\text{radDWS}$, corresponding to a DWS gain of $\approx 12000 \text{ rad}/\text{rad}$.

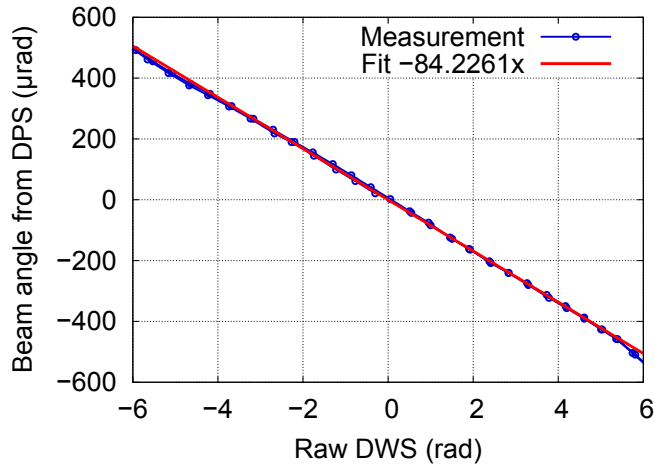


Figure 5.3.: DWS calibration with the RX flat-top. The resulting beam angle is shown vs. the raw DWS signal. The resulting beam angle is calculated from the calibrated DPS signal.

5.1.2. Telescope simulator alignment on optical bench

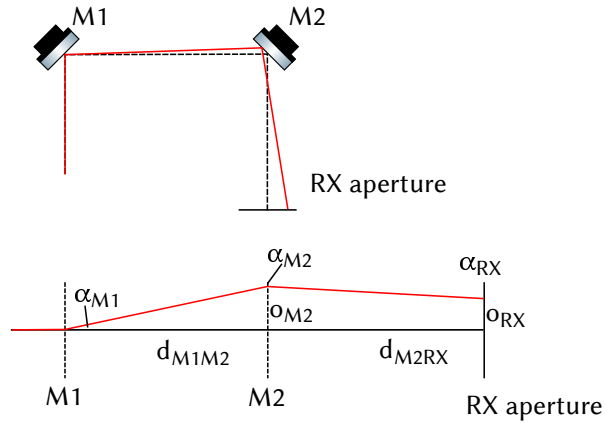
The TS needs to be aligned to the OB. Therefore, the TS position and orientation can be adjusted in all degrees of freedom using the mounting feet described in [TD3]. The target for the alignment are the two CQP diodes on the optical bench which are aligned to the nominal beam position of the LO in a way, that any beam, centered on both CQP diodes, is perfectly completing the science interferometer (good alignment and contrast with respect to the TX).

To align the TS to the OB, the following steps are required (more details in [TD4]):

1. Place the TS on top of the OB, roughly in the right position for one of the two possible orientations.
2. Turn all lasers except the LO off.
3. Adjust the TS by eye until the LO is detected by the CQP and centered.
4. Use the CQP DPS signals to fine align the TS (lateral x, lateral y, yaw, pitch).
5. Optional: Use the signal of an auxiliary photo diode to align the roll degree of freedom (align the polarization of the LO to PBS₂). The auxiliary photo diode measures the LO light power in the wrong polarization between BS₂ and M₂₀.
6. Optional: The height degree of freedom is not critical and can be aligned with an external measurement of the distance between OB and TS.

With this procedure an alignment of less than 2 µm (limited by air movement) was possible.

Figure 5.4: Schematic of the RX beam actuation. The upper part shows the two tilting mirrors (here called M1 and M2) with the optical axis and a test beam. In the lower part, the actuation process is projected onto one direction, the two mirrors are simulated with two planes where the test beam is tilted.



5.1.3. Tilt actuation of the RX beam

The RX beam is tilted around the pivot in the RX aperture with the two piezo actuators on the Telescope Simulator, placed at a distance of ≈ 460 mm and ≈ 630 mm in front of the aperture. By coordinated movement of both actuators a tilt around a pivot in the RX aperture can be achieved.

Figure 5.4 shows a draft of the actuation process. For the computation of the required angles of the two tilt mirrors, the consideration of a simplified situation is sufficient. The two mirrors are replaced by two planes where a beam is tilted by twice the mirror angle. The distance between the two mirrors (M1 and M2) is called d_{M1M2} , the distance between M2 and the RX aperture is called d_{M2RX} , the tilt angle of M1 from its nominal orientation is α_{M1} , the corresponding angle of M2 is α_{M2} and the resulting angle at the aperture is α_{RX} . The resulting offset of the beam at M2 is named o_{M2} and the optional offset of the pivot to the center of the RX-clip is called o_{RX} .

With straight forward algebra, the required mirror angles (α_{M2} and α_{M1}) can be computed for an arbitrary combination of α_{RX} and o_{RX} .

$$\alpha_{M1} = \frac{1}{2} \arcsin \left(\frac{o_{RX} + d_{M2RX} \sin(\alpha_{RX})}{d_{M1M2}} \right) \quad (5.1)$$

$$\alpha_{M2} = \frac{1}{2} \left[\alpha_{RX} + \arcsin \left(\frac{o_{RX} + d_{M2RX} \sin(\alpha_{RX})}{d_{M1M2}} \right) \right] \quad (5.2)$$

The design values are $d_{M1M2} = 170$ mm and $d_{M2RX} = 460$ mm. The beam angle at the RX aperture α_{RX} shall take values from $-500 \mu\text{rad}$ to $500 \mu\text{rad}$, the offset o_{RX} shall be zero. Unfortunately, the actuation precision of the actuators used is not sufficient to reach the required alignment, the deviation of the step size can reach up to 10% [50], which is not sufficient here. Therefore, the results shown above, when applied to the

actuators only lead to a roughly aligned state. For the measurement steps and the fine alignment an automatic procedure was implemented in the readout program. The procedure aligns the RX beam to the LO beam before starting a measurement and realigns the beam after every angle step.

For the pre-alignment, first the beam position on the ref QPD is optimized using the heterodyne amplitude between the RX and the LO beam. Afterwards the DWS signal on the reference QPD is aligned to zero.

During the measurement only the position is optimized to make sure the RX beam is tilted around the center of the RX aperture. The DWS signal of the reference QPD is used for measuring the actual angle. The realignment after every angle step means, that the two actuators are commanded to rotate the RX beam around the center of the reference QPD. But, due to the variation of the step sizes, a realignment is required to remove the remaining offset between RX beam and reference QPD after every step. The resulting angle is then slightly different from the commanded angle but this is not critical since the actual angle is measured with the DWS signal (see Section 5.1.1).

Before starting the fine alignment (amplitude and DWS based), the rough alignment between the beams has to be sufficiently good to have enough heterodyne amplitude for the optimization. In this scenario it is important to align the interferometer to the right amplitude maximum. The optimal amplitude is in a scenario with perfectly aligned beams. If one of the two beams becomes tilted, the amplitude decreases until it reaches zero. If beams are misaligned further, the amplitude rises to a second amplitude maximum (much smaller than the first one). If the fine alignment starts in the area of a second amplitude maximum it will optimize towards its center and therefore never reach the optimal aligned case. Setting the actuators to a default position is enough to have roughly half of the maximal amplitude (0.12 V), which is a sufficient starting point. A lower limit for the amplitude, from which the automatic alignment can sufficiently start was not measured.

Without loss of generality the actuation axis is z (compare to Figure 4.7).

5.2. Calibration of the telescope simulator

In the combined setup of OB and TS the TTL coupling has a contribution from the OB but also from the TS. To characterize only the OB contribution, the one from the TS needs to be removed. Within this section, the different steps that are required to distinguish the TTL coupling contributions are explained.

5.2.1. Pinhole alignment

The reference pinhole SEPDP should be optically equivalent to the temporary pinhole placed in the center of the RX aperture, as described in Section 4.3.1. This requires two alignment steps:

1. Align the temporary pinhole to the center of the LO beam in the RX-clip.
2. Align the reference pinhole to the temporary pinhole.

Starting with the first step, the temporary pinhole SEPD is mounted in the RX aperture with a magnetic kinematic mount and aligned as described in [TD3] using an additional aperture with four holes and a QPD as described in Section 4.3.5. The alignment procedure shall be as followed:

- Align the Telescope Simulator to the OB using the LO beam and the CQP.
- Place the temporary QPD with the four hole aperture in the RX-clip and align it to the LO beam using DPS signals.
- Exchange the four hole aperture by the temporary pinhole aperture with an SEPD. The temporary pinhole is in the center of the four hole aperture.

The critical part of this procedure is to be able to place the apertures repeatedly on the RX aperture mount within a few microns. The manufacturing tolerances of the apertures and the repeatability of their placement were checked before [TD5].

In the next step, the reference pinhole SEPD on the Telescope Simulator is aligned to the temporary pinhole. The longitudinal alignment is less critical, a few mm is sufficient, since the longitudinal offset of the point of rotation corresponds to a longitudinal piston effect, which is proportional to the tilt angle squared, cf. Table 3.1. The RX aperture mount and the mount of the reference pinhole were longitudinally positioned with with the CMM (accurate to a few μm) and the distance between TS and OB is adjusted to the default height with the tip-tilt mount (cf. Section 4.3.4). The lateral alignment – corresponding to a lateral piston effect, which is linear in beam angle – has to be accurate to micrometer and can be aligned by measuring the TTL coupling difference between the two pinhole SEPDs. The coupling should be the same on both pinhole diodes if they are in similar positions.

The following alignment procedure is used to align the reference pinhole:

- Perform a TTL measurement and look at the difference of the two pinhole SEPDs.
- Move the reference pinhole laterally according to the linear TTL contribution measured.
- Perform another TTL measurement.
- Repeat until the difference between the two pinhole SEPDs is minimized.

Alignment using the Gaussian RX This alignment procedure was performed with the Gaussian RX and the flat-top RX. The results of the two alignment procedures are shown in here, starting with the Gaussian RX.

An intermediate step in the alignment procedure is shown in the upper half of Figure 5.5, a and b. The reference pinhole is not aligned to the temporary pinhole, which leads to a linear coupling – corresponds to a lateral piston effect in Table 3.1.

The lower half of Figure 5.5 (c and d) shows the resulting situation after completion of the alignment procedure for the RX Gaussian beam. The linear coupling could be reduced to be well below the requirement of $25 \mu\text{m}/\text{rad}$ by aligning the reference pinhole laterally. A small amount of quadratic coupling – longitudinal piston effect, cf. Table 3.1 – is still visible after the alignment. A longitudinal shift of the reference pinhole is assumed to reduce this residual quadratic coupling, but this degree of freedom was not foreseen and cannot be realized with the photo diode mounts used. However, the residual quadratic coupling is sufficiently small to fulfill the requirement, as expected.

Alignment using the flat-top RX Figure 5.6a shows the path length difference between temporary pinhole and reference pinhole for the RX flat-top beam at an intermediate step during alignment. The reference pinhole is laterally not aligned to the temporary pinhole. This leads to the linear coupling shown in Figure 5.6b.

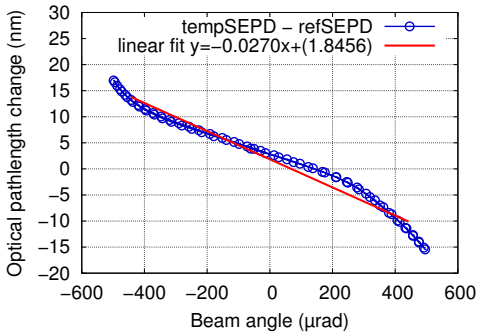
The bottom half of Figure 5.6 shows the resulting situation after completion of the alignment procedure for the RX flat-top beam. Here, the linear part of the coupling could also be removed by a lateral alignment of the reference pinhole. However, the quadratic part of the coupling is larger than for the Gaussian beam and the requirement could not be fulfilled. The quadratic contribution cannot be removed with the foreseen procedure of lateral alignment of the reference pinhole.

In principle it is not necessary to repeat the alignment of the reference pinhole with the flat-top RX beam. Since the alignment of the diode with respect to the LO beam is a pure geometric problem, a pinhole, aligned using the Gaussian RX beam, must be aligned for the flat-top as well.

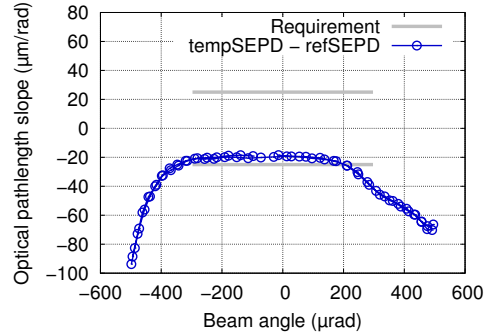
In later measurements it was shown that the flat-top beam meets all requirements in the science interferometer, therefore the problems in the alignment of the pinhole are assumed to be a special behavior connected with the temporary pinhole. The cause of the high quadratic term in the coupling is not known yet and needs further investigation at a later stage.

5.2.2. Alignment test using the flipping procedure

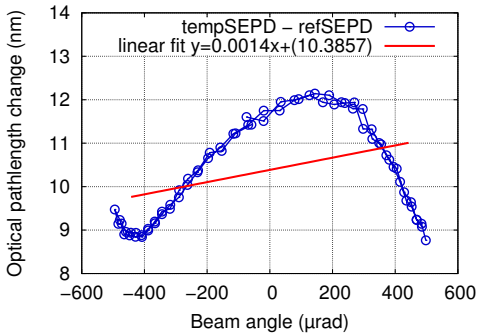
The entire performance of the testbed based on a proper alignment of the reference pinhole diode. In this section, the flipping procedure is explained and demonstrated, which is used to validate the proper alignment for the reference pinhole and can be used to distinguish the TTL contribution from the OB and the TS. The fundamental idea behind flipping is, to change the orientation between OB and TS. Therefore, the TS is rotated by 180° (as shown in Figure 4.8) around the axis the LO beam goes down from the TS to the OB. The flipping causes the angle of the RX beam to switch sign



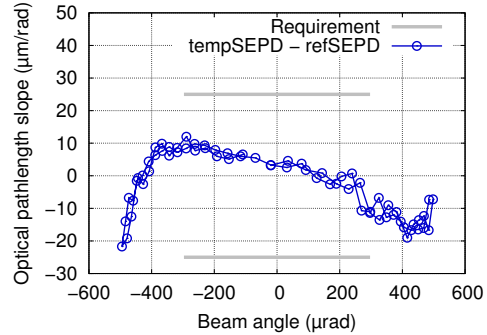
(a) Path length change vs. beam angle – misaligned Gaussian RX.



(b) Slope of path length change vs. beam angle. – misaligned Gaussian Rx.

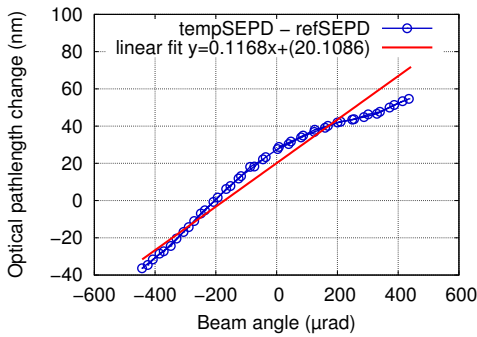


(c) Pathlength change vs. beam angle. – aligned Gaussian Rx.

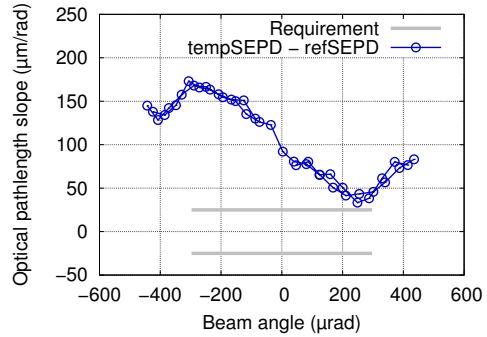


(d) Slope of path length change vs. beam angle. – aligned Gaussian Rx.

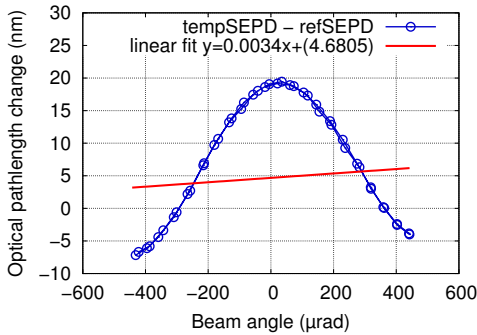
Figure 5.5.: Process of the reference pinhole alignment using the RX Gaussian – The path length difference between reference pinhole and temporary pinhole is shown for two scenarios. The first (upper half) is an intermediate step, still a linear TTL coupling between the two pinholes can be measured. The second scenario (bottom half) is after the alignment of the reference pinhole. The relative TTL coupling is not linear anymore – within the requirements no linear TTL coupling contribution remains. The remaining nonlinear TTL coupling fulfills the requirement.



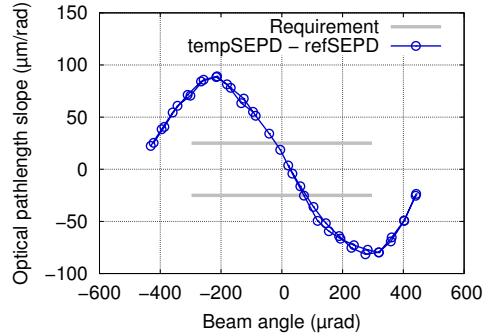
(a) Pathlength change vs. beam angle – misaligned flat-top RX.



(b) Slope of path length change vs. beam angle – misaligned flat-top RX.



(c) Pathlength change vs. beam angle – aligned flat-top RX.



(d) Slope of path length change vs. beam angle – aligned flat-top RX.

Figure 5.6.: Process of the reference pinhole alignment using the RX flat-top – The path length difference between reference pinhole and temporary pinhole is shown for two scenarios. The first (upper half) is an intermediate step, still a linear TTL coupling between the two pinholes can be measured. The second scenario (bottom half) is after the alignment of the reference pinhole. No linear TTL coupling contribution remains. However, the remaining nonlinear TTL coupling does not fulfill the requirement.

between the orientations, but only on the optical bench – an angle α of the RX beam is defined with respect to the coordinate system of the TS, by flipping the TS, the previous angle α on the OB becomes $-\alpha$. Since the angle of the RX beam is measured on the TS, the angle on the reference pinhole is not affected by the flipping. However, for the temporary pinhole the angle changes between the orientation. Since the TTL coupling is assumed to be dominant in the first order [TD3], the TTL coupling contribution from the OB switches sign, according to the angle. Therefore, the total TTL coupling measured in orientation 1 is the sum of the contributions from the TS (c_{TS}) and from the OB (c_{OB}) and in orientation 2 the TTL coupling (t_2) is the difference between them

$$\begin{aligned} t_1 &= c_{TS} + c_{OB} \\ t_2 &= c_{TS} - c_{OB}. \end{aligned} \quad (5.3)$$

Thus, only simple math is required to determine the different components

$$\begin{aligned} c_{TS} &= (t_1 + t_2)/2 \\ c_{OB} &= (t_1 - t_2)/2. \end{aligned} \quad (5.4)$$

By disentangling the first order contributions of the TTL coupling from the OB and the TS it is possible to remove the residual lateral misalignment between the temporary and the reference pinhole – a longitudinal mismatch produces a quadratic TTL coupling that is symmetric towards the beam angle and therefore cannot be measured here. The flipping procedure is described in more detail in [TD4].

The flipping procedure can be adapted to measure the TTL coupling of an entire LISA satellite. By illuminating the telescope with a large external light source, the TTL coupling in orientation 1 can be measured. By turning the entire satellite upside down, the TTL coupling in orientation 2 can be measured. Thus, with one external light source, that is capable of delivering a tilting beam to a LISA telescope, the entire science interferometer with all participating components can be tested. More details about the flipping procedure as an OGSE for LISA can be found in [TD9].

Measurement results The resulting TTL coupling in orientation 1 was shown in the previous section in Figure 5.5 and Figure 5.6 for the Gaussian and the flat-top RX beam, respectively. The total TTL coupling after flipping in orientation 2 is shown in Figure 5.7 for both, Gaussian and flat-top RX. In orientation 1 the total TTL coupling was close to zero. After flipping a significant linear component was measured. The measured TTL coupling is a result of an initial offset of the temporary pinhole in the RX-clip. The reference pinhole was later aligned to the same offset by minimizing the difference of the coupling between the two pinholes. According to the flipping procedure, both pinholes have to be adapted in different directions. By using the equations above, the required shifts of the individual pinholes can be estimated. To

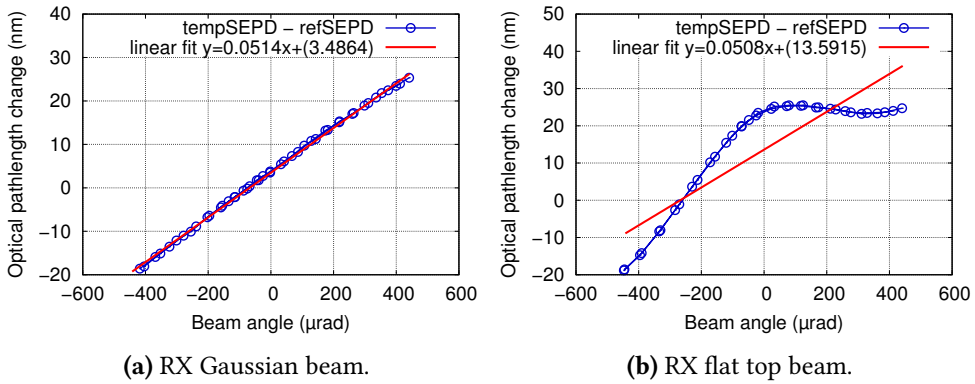


Figure 5.7.: After flipping and before adjusting the temporary pinhole, a large linear TTL coupling can be measured between reference and temporary pinhole, for the RX Gaussian and the RX flat-top. Additionally, the RX flat-top shows a quadratic contribution that was already present before flipping.

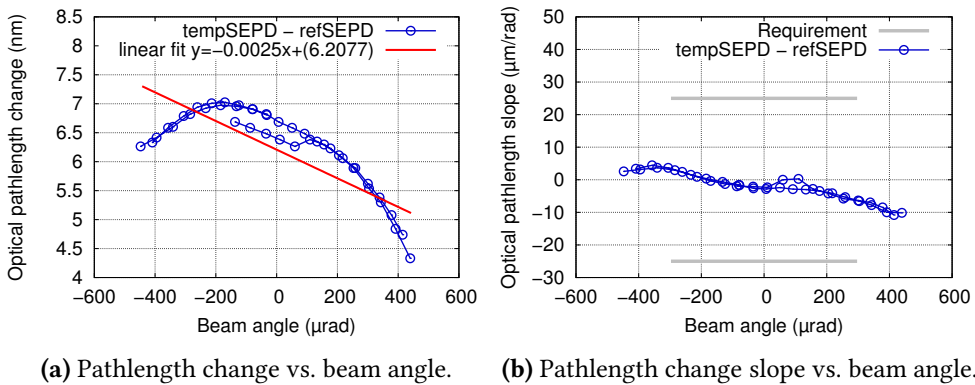


Figure 5.8.: After realigning both pinholes according to the flipping procedure the required TTL coupling can be achieved with the RX Gaussian.

align both pinholes to the center of the rotation axis (beam axis of the LO) they are shifted half of the total offset in different directions. The measured TTL coupling after the flipping was $51 \mu\text{m}/\text{rad}$ for both RX beams (see fits in Figure 5.7a and Figure 5.7b). That means both pinholes had to be shifted by $25 \mu\text{m}$.

In Figure 5.8 the result after the realignment of the pinholes is shown for the Gaussian RX beam. The procedure was successful and the remaining TTL coupling of the aligned TS and OB setup is well inside the requirement using the RX Gaussian beam. The TTL coupling using the RX flat-top beam does not meet the requirement, not even before flipping as shown in Figure 5.6. The reason of the additional quadratic

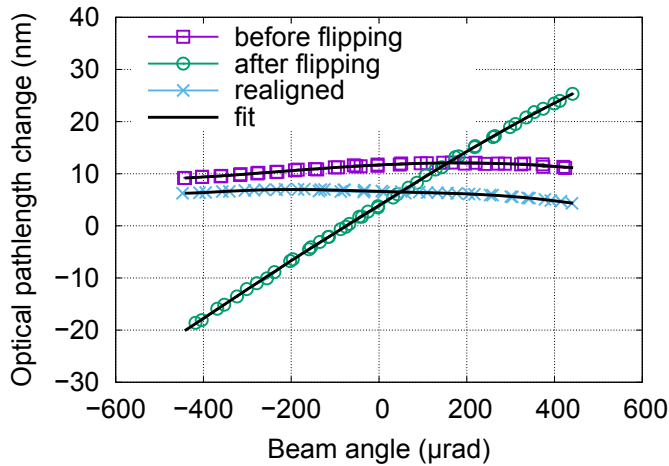


Figure 5.9.: Difference of the path length signal between reference pinhole and temporary pinhole with the RX Gaussian before and after flipping, as well as after realignment of the reference pinhole, is shown. Furthermore, a sixth order polynomial is fitted to each measurement.

coupling is not yet understood. However, it was shown with the RX Gaussian beam that the TS and the reference pinhole are aligned. The RX Gaussian and the RX flat-top are both aligned in the same way with respect to the LO beam, therefore the alignment of the TS and the reference pinhole is valid for both beams.

As additional information, the path length measurements before flipping, after flipping and after realignment of the reference pinhole are shown in Figure 5.9, together with sixth order polynomial fits. The fitted parameters can be found in Appendix C.4 in Table C.1. The reason for the sixth order fit is the previously assumed first order dominance of the TTL coupling. With the results shown here – higher order polynomial – it can be reviewed if the TTL coupling is really dominated by the first order.

5.3. Effect of RX clip and mitigation of temperature effects

During the calibration campaign, hysteresis within the tilt measurements were observed. The start point and the end point showed significant differences in the total phase. Since the alignment signals (DPS, DWS) showed the same result between the two points, a systematic error was assumed. The strength of the hysteresis was not constant but varied over time and seemed to correlate with outside temperature changes.

In the first part of this section, measurements of the temperature dependencies of the tip-tilt mounts (introduced in Section 4.3.4) are shown which happen to cause the hysteresis mentioned above.

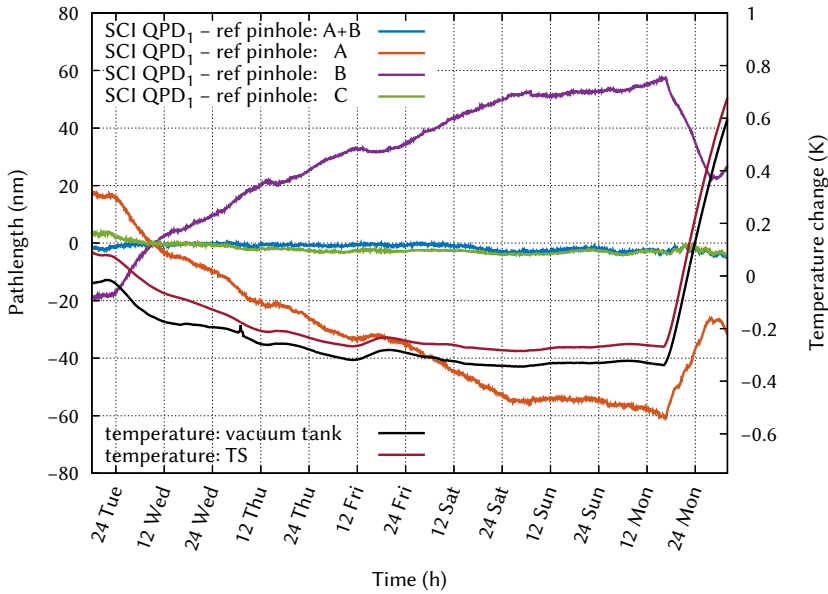
The second part of this section concerns, whether it makes a difference if the RX-clip contains a real aperture or is just a fictive plane which do not affect the beam.

5.3.1. Temperature dependencies of the tip-tilt mount

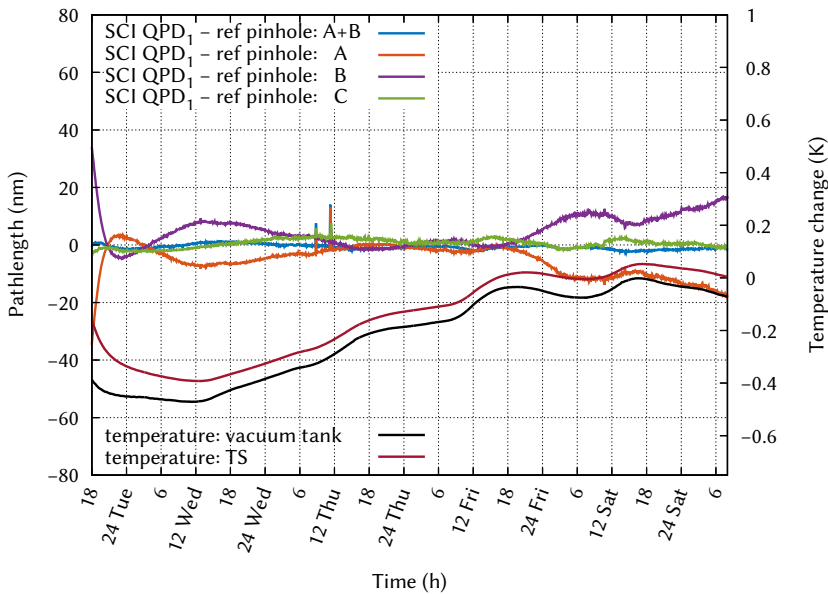
The interferometric signals on all photo diodes were measured while the tilt actuators were standing still. Furthermore, temperature sensors were placed within the vacuum tank to monitor the temperatures of the tank, the OB, and the TS. This measurement was performed twice, once with the adjustment screws in contact to the mounting feet and once with the adjustment screws retracted, which means there was no contact between adjustment screws and mounting feet. Only with retracted adjustment screws there is an all-Zerodur[®] connection between the two baseplates as intended in the design – further details of the mounting system can be found in [TD3]. Figure 5.10a shows the variation of the path length signals between science interferometer and reference pinhole for the scenario with the adjustment screws attached to the mounting feet. Figure 5.10b shows the measurement setup with the adjustment screws retracted from the mounting feet. Both figures show additional temperature data for the vacuum chamber and the telescope simulator. In Figure 5.10a the temperature was increased in the end in order to investigate the experiment's response.

In the measurement with the adjustment screws a strong relation between temperature and path length change in A and B phase can be observed. Presumably the temperature driven length change of the adjustment screws is responsible for this behavior. This cannot be observed in the measurement with the adjustment screws retracted. In this situation the all Zerodur[®] path between OB and TS provides a connection with no temperature driven expansion. However, a strong variation in the A and B phase can still be observed. The clamping mechanism seems not strong enough in order to provide a stable connection between the two Zerodur[®] parts. By increasing the clamping force we could observe an improvement in the mounting feet stability. The measurement in Figure 5.10a was performed with the maximal possible clamping force that can be obtained by the given mechanical design, see Figure 5.11.

Figure 5.12 and Figure 5.13 show the relation between path length change and temperature with adjustment screws attached and retracted, respectively. When the adjustment screws are attached a linear correlation between temperature and path length can be observed, with a slope of ≈ 130 nm/K. The TS displacement amounts



(a) adjustment screws attached



(b) adjustment screws retracted

Figure 5.10.: Longterm measurement with adjustment screws attached/retracted from the mounting feet. The total change in path length on the individual diodes is below 20 nm for retracted screws and up to 80 nm with the screws attached. The temperature curves of the vacuum tank and the TS are related to the temperature axis on the right. The time axis shows days of the week together with an indication of the hour.

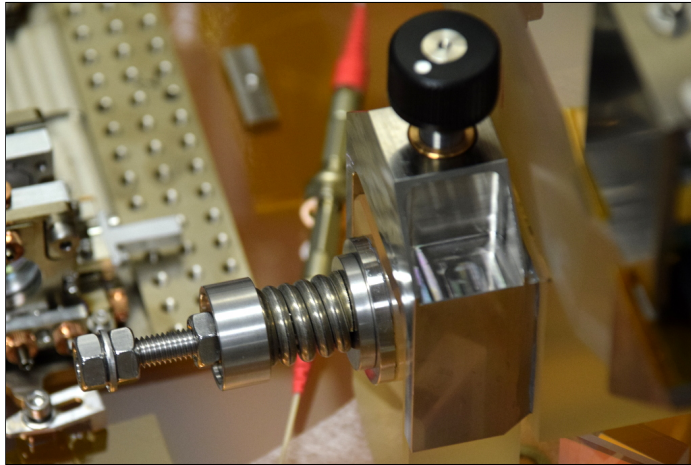


Figure 5.11.: Clamping spring of the mounting feet in the position with the maximal possible clamping force.

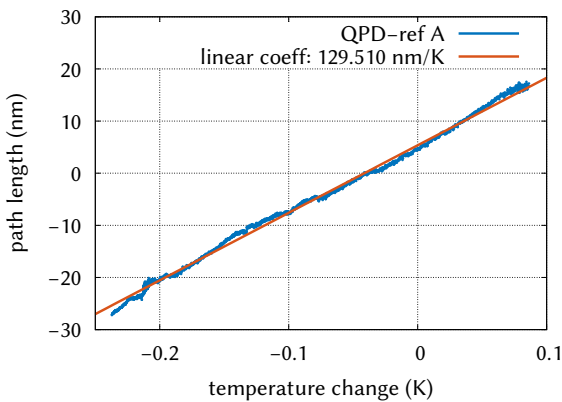
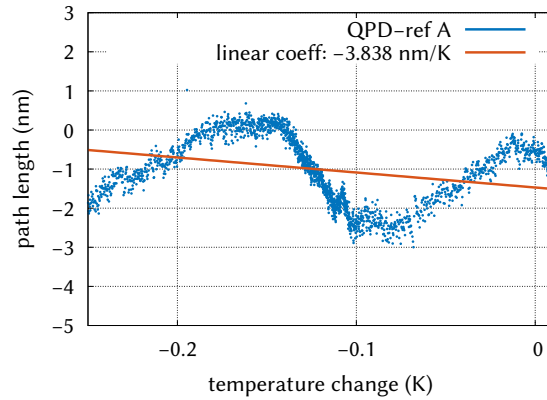


Figure 5.12: Path length change plotted over the temperature change of a longterm measurement with adjustment screws attached to the mounting feet. The linear relation between temperature and path length changes indicates a strong correlation. The data is the same as in Figure 5.10a in the time between Tuesday 5 pm and Thursday midnight (for ≈ 55 h).

to half of this optical path length change. This measurement is compatible with the thermal expansion of 3 mm stainless steel ($10.17 \cdot 10^{-6}/\text{K}$), 10 mm Invar ($2 \cdot 10^{-6}/\text{K}$), and 120 mm Zerodur[®] ($2 \cdot 10^{-8}/\text{K}$) – this is comparable with the composition of the tip-tilt mount.

Figure 5.13 shows no linear behavior, the path length change seems to be not temperature driven anymore. When the adjustment screws are attached, the height of the TS changes with temperature due to the expansion of the adjustment screws. When the adjustment screws are retracted, the change in the height of the TS is much smaller since the used Zerodur[®] has a much smaller coefficient of thermal expansion. However, the height of the TS is still not stable. Possibly the friction between feet and TS is not strong enough which leads to creep.

Figure 5.13: Path length change plotted over the temperature change of a longterm measurement with adjustment screws retracted from the mounting feet. No linear behavior is observable. However, the pattern is not random but looks like a sinusoidal. The data is the same as in Figure 5.10b in the time between Tuesday 5 pm and Friday 5 pm (for ≈ 72 h)



5.3.2. Telescope simulator height variation removal

The height of the TS is measured in two phase signals, in signal A between TX and RX and in signal B between LO and TX. Since the phase B measures the phase relation between two stable beams, it is a good measurement of the height variation of the TS. In the following we will use the phase signal of the B phase to correct for the height variations of the TS in the A phase. Thus, we are not sensitive to TS movement in the z axis anymore and we can and will use the TS with the adjustment screws attached to the mounting feet. Figure 5.14 shows a comparison between only A phase and A+B phase for the LOB2D imaging system. In the only A phase scenario a drift (hysteresis) can be observed which is caused by a height change of the TS. If the B phases is added, the drift disappears and the measured curve is not affected by the height variations anymore – no hysteresis.

5.3.3. The effect of an additional RX-clip

The RX-clip defines the interface between OB and TS. Per design, the RX-clip is the limiting aperture of the testbed. Limiting aperture means, that it is the smallest aperture in the science interferometer with respect to the corresponding beam size. On an actual LISA satellite, multiple apertures clip the received beam. E.g. the wavefront is clipped first by the entrance pupil of the telescope, a small fraction of a large wavefront is cut out. This wavefront is propagated to the interface between OB and TS, where the RX-clip cuts out the clean center part. This new wavefront is again propagated to the science interferometer diodes, which might be slightly smaller than the beam and clip again, to only detect the clean center region. In this scenario, the diodes are the defining aperture, since they are the smallest. If the

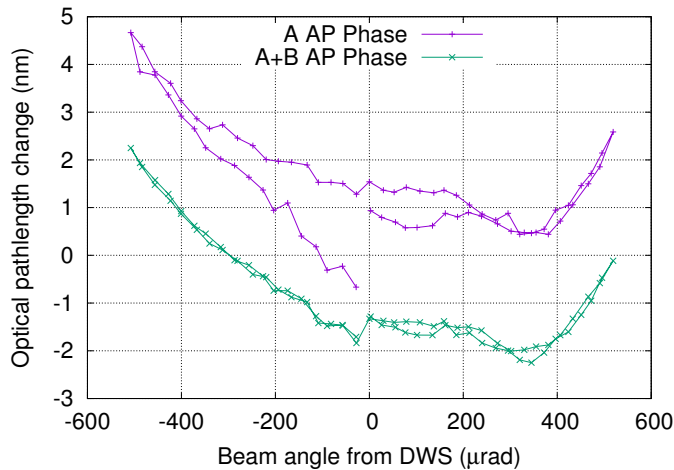


Figure 5.14.: Path length change plotted over the beam angle for a comparison between A phase and A+B phase. The angle moved from zero to +500 μrad , then to -500 μrad and back to zero. The hysteresis, visible in the A phase, can be suppressed by adding the B phase.

RX-clip happen to be smaller than the diodes, all light arriving at the diodes would be detected, and the RX-clip would be the defining aperture. In the end, only one aperture can be the defining one, and by choosing the right one, the performance might be improved.

Per design, the RX-clip is the limiting aperture in the science interferometer. The image of the RX-clip on the science interferometer photo diodes is slightly smaller than the diode itself. This ensures a clean definition of the amount of light used in the interferometer. If the RX-clip would be larger, the diode itself would be the limiting aperture. Making either of the two apertures defining, has advantages and disadvantages, in the following the two options are compared. On the one hand, the boundary of the diode is not well defined, variations in manufacturing and additional features like wires on the edges of the diode might change its behavior near the edges, on the other hand, the alignment of the diodes to the beam center might be much better than the alignment of the RX-clip. The improved alignment of the defining aperture might increase the performance.

Measurements show that without RX-clip in place the performance in the science interferometer can be improved as shown in Figure 5.15. The RX-clip is affecting the A and the C phase differently. In the A phase the RX-clip is causing an additional quadratic coupling that just meets the requirement. The performance can be improved by not using an RX-clip. In the C phase the effect is larger.

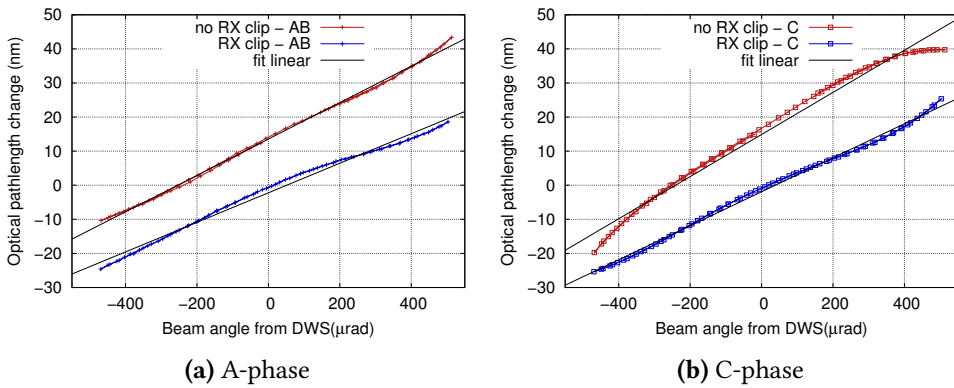


Figure 5.15.: A comparison of a scenario with RX clip and a scenario without RX clip with the LOB4C imaging system in place. An additional nonlinear contribution in the A phase signal can be observed when the RX clip is used.

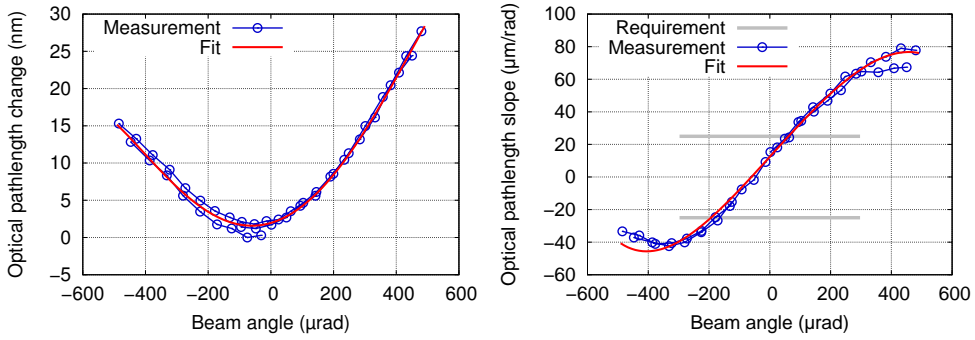
The reason for this behavior is assumed to be a small misalignment of the TS and therefore also of the LO. Probably the RX-clip is slightly clipping the LO beam which causes the quadratic coupling. This effect was suppressed by removing the RX-clip in the measurements. This was found to not influence the quality or representativity of the test campaign since the important phase signal is the A phase which is not affected by the RX clip significantly.

5.4. Two-lens imaging system measurement results – LOB2D

In this section the results of the measurement campaign, testing the LOB2D imaging system presented in Section 4.3.10, is shown. The best possible performance with RX Gaussian and RX flat-top is shown as well as a tolerance analysis for different misalignment parameters.

5.4.1. Nominal performance

In this section we will show the best possible performance of both LOB2D imaging systems for both RX beams (flat-top and Gaussian) separately. In this context, the “best possible” performance is achieved with an as ideal as possible aligned imaging system and a QPD shifted longitudinally from its design position in order to minimize the remaining TTL coupling.



(a) Path length change vs. beam angle. (b) Slope of path length change vs. beam angle.

Figure 5.16.: LOB2D imaging system: best possible performance with Gaussian RX beam. The required $\pm 25 \mu\text{m}/\text{rad}$ cannot be achieved.

Gaussian RX beam

Figure 5.16 shows the best possible performance of the LOB2D imaging system placed in front of SciQPD 1 when the Gaussian RX beam was used. Figure 5.16a shows the path length change between SciQPD 1 and the reference pinhole versus beam angle between RX and TX beam, Figure 5.16b shows the slope of the path length change versus beam angle. In both cases, the beam angle was determined from the calibrated DWS signal of the reference QPD on the telescope simulator. The slope of the path length change in this and all following plots was computed as the average of the pair-wise differences of five neighboring data points.

The remaining TTL coupling does not fulfill the requirement, presumably due to the beam parameter mismatch of RX and TX beam. The relation between beam parameters and TTL coupling is discussed in the following.

Special beam parameters Numerical simulations suggested, that the beam parameters of the RX Gaussian beam are very unfavorable. The remaining TTL coupling due to beam parameter mismatch should be much smaller except for a few unique setups with very special parameters.

An example of this behavior can be seen in Figure 5.17. Here, a perfectly aligned imaging system is assumed, it is not part of the simulation. A direct rotation around the center of the QPD at its nominal position is modeled. The angular range is larger than usual, because the angular range behind an imaging system scales with the inverse of the magnification factor. The simulation parameters are: RX– waist position 50.6 mm in front of QPD, waist radius $25 \mu\text{m}$. TX– waist position 51.6 mm in front of QPD, waist radius $25 \mu\text{m}$. The QPD radius is 0.45 mm with a slid width of $20 \mu\text{m}$. The only change to a nominal LOB2D system is a change of the RX waist position from 51.6 mm to 50.6 mm.

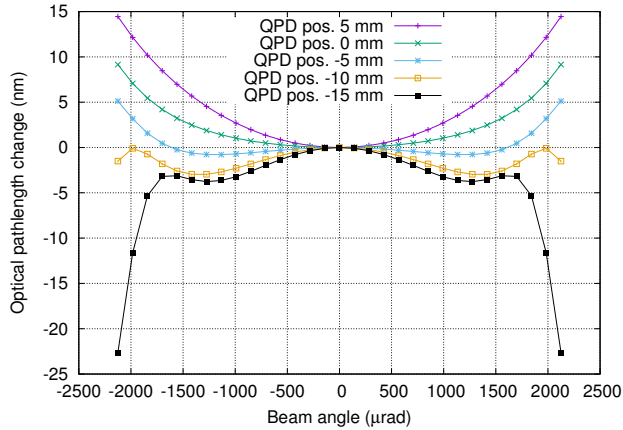
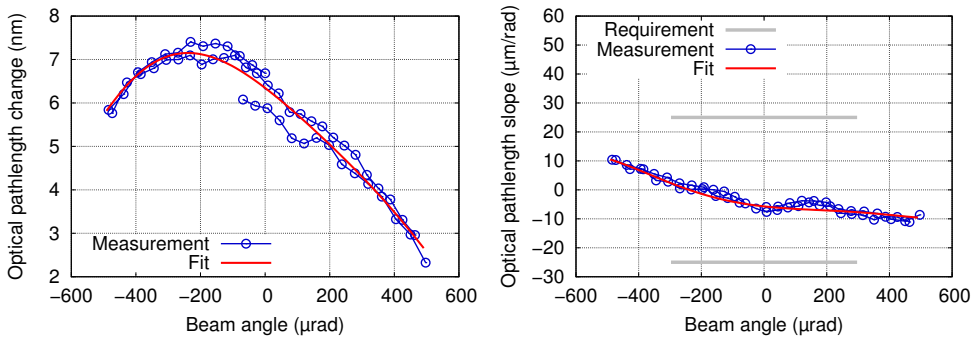


Figure 5.17.: In this simulated data the additional TTL coupling of unfavorable beam parameter combinations are shown. The TTL coupling for different QPD positions is shown in order to demonstrate that the residual coupling cannot be reduced with an adjustment of the QPD. Further details on this effect can be found in Chapter 6. The tilt angle is larger than for the measurement since the magnification of the angle due to the imaging system was neglected here. With a magnification factor of 0.4 in mind, a beam angle of 2000 μrad behind an imaging system corresponds to an angle of 800 μrad in front of the system.

The TTL coupling for different QPD positions is shown in order to demonstrate that the residual coupling cannot be reduced with an adjustment of the QPD. Usually, with nominal beam parameters, the parabola shape becomes flat at one QPD position. With the beam parameters chosen here this never happens – before the TTL coupling becomes flat, higher order polynomials appear.

The simulation here shows qualitatively the behavior we observed in the experiment. The beam parameters in the simulation are chosen without experimental evidence, they are solely used to reproduce the experiment’s behavior. Since it was not possible to determine the exact situation and measure the waist positions and sizes after the imaging system with the required accuracy, we decided to change the beam parameters of the RX beam in any direction in order to obtain a system that does not show this special behavior. Therefore, the RX beam was altered with an additional lens, not to match TX and RX beam, but only to get rid of these unfortunate parameter combination.

We chose lenses with a large focal length in order to minimize the variations of the beam parameters. We tested two lenses (1 m and 0.5 m focal length). Other lenses with a larger focal length were not at hand at that time.



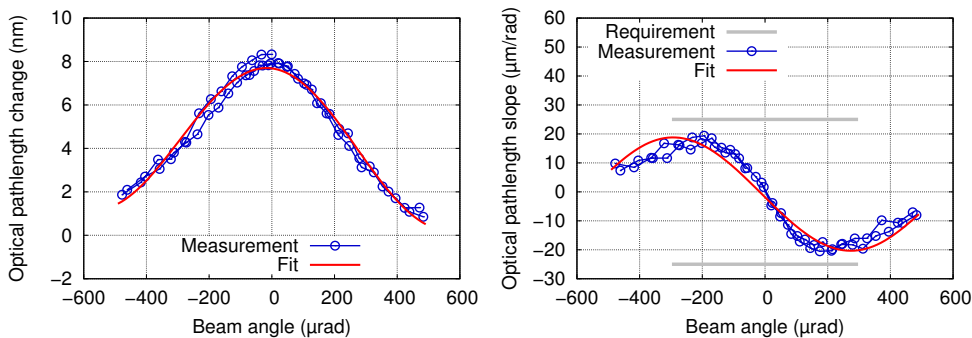
(a) Pathlength change vs. beam angle. (b) Slope of path length change vs. beam angle.

Figure 5.18.: LOB2D imaging system: best possible performance with Gaussian RX beam and 500 mm focal length lens in front of RX FIOS on telescope simulator. The optical path length fit parameters are shown in Appendix C.4 in Table C.3.

Figure 5.18 shows the best possible performance of the LOB2D imaging system placed in front of SciQPD 1 when the Gaussian RX beam was used with an additional 500 mm focal length lens in front of the RX FIOS. Figure 5.18a shows the path length change between SciQPD 1 and the reference pinhole versus beam angle between RX and TX beam, Figure 5.18b shows the slope of the path length change versus beam angle. Due to the modified RX beam the DWS signal calibration used for Figure 5.16 is no longer valid here. The calibration was scaled so that the RX beam angle range covered the same range as in Figure 5.16. The optical path length fit parameters are shown in Appendix C.4 in Table C.3.

Similarly, Figure 5.19 shows the best possible performance of the LOB2D imaging system placed in front of SciQPD 1 when the Gaussian RX beam was used with an additional 1 m focal length lens in front of the RX FIOS. Figure 5.19a shows the path length change between SciQPD 1 and the reference pinhole, and Figure 5.19b shows the slope of the path length change versus beam angle. Again, due to the modified RX beam the DWS signal calibration used for Figure 5.16 is no longer valid here. The calibration was scaled so that the RX beam angle range covered the same range as in Figure 5.16. The optical path length fit parameters are shown in Appendix C.4 in Table C.3.

With the additional lens the remaining TTL coupling is reduced and now fulfills the requirement. Unequal beam parameters are in principle not a problem, but we observed that some special combinations generate additional TTL coupling that disturbs the measurement significantly. In Chapter 6 further investigations on this topic are shown.



(a) Path length change vs. beam angle. (b) Slope of path length change vs. beam angle.

Figure 5.19.: LOB2D imaging system: best possible performance with Gaussian RX beam and 1 m focal length lens in front of RX FIOS on telescope simulator. The optical path length fit parameters are shown in Appendix C.4 in Table C.3.

Flat-top RX beam

Figure 5.20 shows the best possible performance of the LOB2D imaging systems placed in front of the science QPDs when the flat-top RX beam was used. Figure 5.20a shows the path length change versus beam angle, Figure 5.20b shows the slope of the path length change versus beam angle. In both cases, the beam angle was determined from the calibrated DWS signal of the reference QPD on the telescope simulator. The remaining TTL coupling fulfills the requirement for both imaging systems. The path length plot of SciQPD 1 is slightly tilted with respect to SciQPD 2. This indicates a residual lateral alignment. However, since the lateral misalignment is sufficiently small, the requirement was fulfilled.

The optical path length fit parameters for SciQPD 1 and SciQPD 2 are shown in Appendix C.4 in Table C.5.

The required level of residual TTL coupling can be achieved with both, the RX Gaussian and the RX flat-top beam. In order to do so with the Gaussian RX, an additional lens is required to change the beam parameters. The measurements with different weak lenses (0.5 m and 1.0 m focal length) as well as numerical simulations suggest that it is not necessary to match the beam parameters of RX Gaussian and LO, but to avoid certain special beam parameter combinations, which lead to a huge amount of residual TTL coupling.

The circumstances that lead to the measured amount of additional TTL coupling is discussed separately in Chapter 6. With the RX flat-top no additional lenses are required. Therefore, since the flat-top is the more representative one for the LISA science interferometer, we will proceed with the measurements using the RX flat-top.

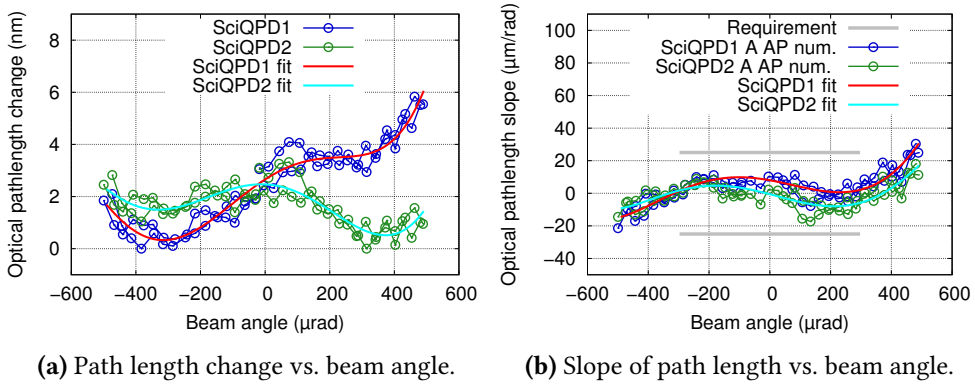


Figure 5.20.: LOB2D imaging systems: best possible performance with RX flat-top beam. The optical path length fit parameters for SciQPD 1 and SciQPD 2 are shown in Appendix C.4 in Table C.5.

5.4.2. Sensitivity to misalignments

In this section the remaining TTL coupling behind an imaging system is shown in the presence of intentional misalignments within the imaging system. Furthermore, the behavior of the TTL coupling in response to misalignments of different parameters is compared with optical simulations performed in IfoCAD. In all following simulations, the imaging system is aligned and set up as designed, the TX beam is simulated as a pure fundamental Gaussian beam with a waist radius of 1 mm and a waist position 550 mm in front of the RX aperture. The RX flat-top beam is simulated as a pure fundamental Gaussian beam with a waist radius of 100 mm and a waist position at the RX aperture. This is an approximation for a flat-top beam that is cut out in the RX-clip, providing a perfectly flat phase front and a nearly flat intensity front. Using a better model of the flat-top beam used in the measurements was not necessary since, even with this primitive model, a sufficient match between measurements and simulation was achieved.

Lateral QPD shift

Lateral QPD displacement is an offset of the QPD in Z direction (according to Figure 4.7). For a vertical beam tilt, as used in this measurement, this is the most critical degree of freedom for the QPD. According to Chapter 3, a lateral offset between the QPD and the point of rotation generates, besides other effects, a geometrical coupling of

$$\Delta s = \sin \alpha \cdot d_{\text{off}} \quad . \quad (5.5)$$

Here Δs is the path length change, α the beam angle on the QPD d_{off} the offset or misalignment.

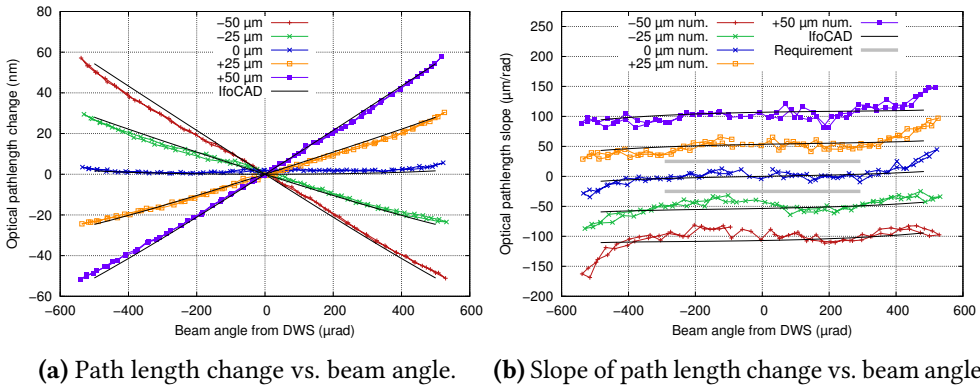


Figure 5.21.: LOB2D imaging system: sensitivity to lateral QPD displacement in vertical direction.

Figure 5.21 shows the sensitivity of the LOB2D imaging system to lateral QPD displacements in vertical direction. Figure 5.21a shows path length change versus beam angle, Figure 5.21b shows the slope of the path length change versus beam angle.

The measurements show that a lateral misalignment of $\pm 25 \mu\text{m}$ result in an additional TTL coupling of $\approx \pm 50 \mu\text{m}/\text{rad}$. With a nominal magnification factor (m) of 0.4 for the imaging system in mind, these results match very well with the expected geometrical TTL coupling of the path length slope

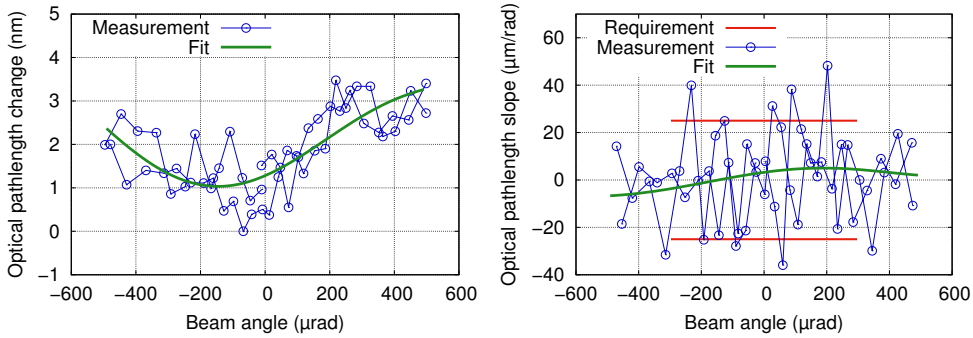
$$\frac{\partial \Delta s}{\partial \alpha} \approx \frac{1}{m} d_{\text{off}} = 62.5 \frac{\mu\text{m}}{\text{rad}}. \quad (5.6)$$

In this scenario the entire TTL coupling can be explained by a geometric effect, since the tilting beam can be approximated by a plane wave (flat-top). The residual mismatch between measured and estimated TTL coupling can be explained by the residual mismatch between the RX flat-top beam and a perfect plane-wave.

The same result can be obtained from numerical simulations, which match the measurements very well, too. The slight mismatch between the two can be explained by the uncertainty of the alignment screw which was used to adjust the QPD position. This screw has a resolution of $200 \mu\text{m}$ per turn. Therefore, the misalignment of $\pm 25 \mu\text{m}$ is affected by an uncertainty of at least a few micrometer.

Lateral imaging system shift

Figure 5.22 shows the sensitivity of the LOB2D imaging system to lateral displacement of the entire imaging system. The direction of the shift here is horizontal, parallel to the OB baseplate and perpendicular to the tilt direction of the RX beam. Since the misalignment is not in the sensitive axis of the experiment, a horizontal shift



(a) Path length change vs. beam angle. (b) Slope of path length change vs. beam angle.

Figure 5.22.: LOB2D imaging system: sensitivity to lateral displacement of the entire imaging system in horizontal direction (perpendicular to the tilt direction) by $\approx 25 \mu\text{m}$.

should not affect the TTL coupling in the vertical axis. Figure 5.22a shows path length change versus beam angle, Figure 5.22b shows the slope of the path length change versus beam angle. Due to minor difficulties in the experiment, a higher noise level is present in the shown measurement. However, since the TTL coupling can still be determined sufficiently, this measurement was not repeated. As expected, a horizontal shift of the two lenses is not visible in the TTL coupling for a vertical beam tilt. Even with the shift of $\approx 25 \mu\text{m}$, the requirement can be fulfilled.

Numerical simulations suggest that the same is true for a shift of the photo diode in the same direction. This means that the alignment of the photo diode is not critical in the horizontal direction for measurements with a vertical tilt. However, imaging systems, as the ones tested here, are designed to suppress TTL coupling originating from an unintended tilt (TM or spacecraft) which do not feature a special tilt axis. A tilt in an arbitrary axis is expected, which means that imaging systems and photo diodes on a LISA satellite do not have a passive axis. Therefore, misalignments in the passive axis were not investigated further.

Longitudinal QPD shift

The longitudinal QPD position is expected to be less critical than the lateral position. A longitudinal offset has the effect that the beam walk is not zero any more, since the QPD is not placed at the pivot but slightly before or after it. However, the generated beam walk is very small, for a longitudinal offset in the range of mm, the expected beam walk for 0 to $500 \mu\text{rad}$ is in the range of nanometers. Therefore, a large longitudinal offset is required to significantly change the TTL coupling.

Figure 5.23 shows the sensitivity of the LOB2D imaging system to a longitudinal QPD displacement. Figure 5.23a shows path length change versus beam angle, Figure 5.23b shows the slope of the path length change versus beam angle.

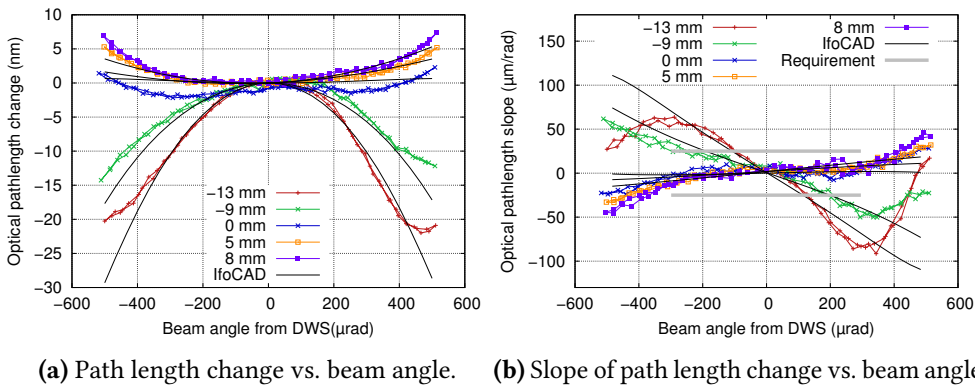


Figure 5.23.: LOB2D imaging system: sensitivity to longitudinal displacement of the QPD.

The longitudinal misalignment is resulting in a higher order polynomial TTL coupling that depends on the direction of the photo diode offset and is not symmetrical for both directions. The chosen offsets are larger in the negative direction - which is closer to the imaging system - because in the positive direction the tie down for the photo diode is not allowing a position further away.

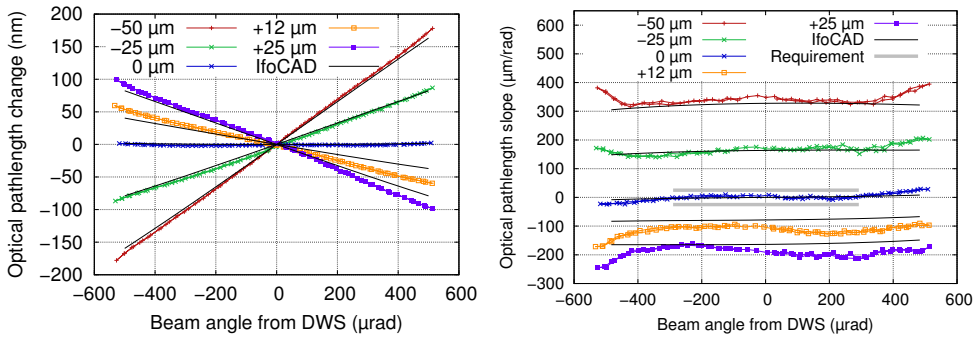
The IfoCAD simulations are matching the measurements well but not perfectly. The reason for the mismatch is the uncertainty of the precise parameters of the experiment. Besides the beam walk, the TTL coupling, generated by longitudinally shifting the photo diode, strongly depends on the beam parameters, which are not precisely known. Furthermore, the QPD shift is measured with respect to its optimal position, which cannot be accurately measured in the experiment. Therefore, the relative shifts in simulation and experiment are with respect to different positions, in the simulation this position is the nominal one, while in the experiment it is the position where the “best possible” performance was measured.

With all unknown parameters in mind, the match between simulation and measurement has to be rated as reasonable.

Lateral shift of lens 1

Lens 1, the first lens the beam interacts with, was misaligned laterally in the vertical axis. This parameter is assumed to be more critical than the longitudinal offset of the QPD and the horizontal offset of the entire imaging system, and similarly critical as the vertical offset of the QPD.

Figure 5.24 shows the sensitivity of the LOB2D imaging system to lateral displacement of lens 1 in vertical direction. Figure 5.24a shows path length change versus beam angle, Figure 5.24b shows the slope of the path length change versus beam angle. The measurements show that a lateral misalignment of $\pm 25 \mu\text{m}$ result in an



(a) Path length change vs. beam angle. (b) Slope of path length change vs. beam angle.

Figure 5.24.: LOB2D imaging system: sensitivity to lateral displacement of lens 1 in vertical direction.

additional TTL coupling of $\approx \pm 170$ $\mu\text{m}/\text{rad}$. This is more than three times as much as a similar QPD misalignment is causing. The effect of misaligning the first lens must be amplified by the following lens, resulting in a large effective offset between point of rotation and QPD in the end.

For this measurement in one direction smaller step sizes are chosen 12 μm and 25 μm instead of 25 μm and 50 μm . But the uncertainty how much the lens actually moved is getting relatively larger for smaller step sizes, due to the play of the Allen key and the difficulty to turn the screw by a certain amount. With this uncertainty, it can be explained why the simulation for the +12 μm has the largest deviation from the measurement and it was chosen to take the 25 μm as step size for the following measurements.

Lateral shift of lens 2

Lens 2 is expected to show results similar to lens 1. Figure 5.25 shows the sensitivity of the LOB2D imaging system to lateral displacement of lens 2 in vertical direction. Figure 5.25a shows path length change versus beam angle, Figure 5.25b shows the slope of the path length change versus beam angle.

The measurements show that a lateral misalignment of ± 25 μm result in an additional TTL coupling of $\approx \pm 100$ $\mu\text{m}/\text{rad}$. This means that the alignment of the lens 2 is a little bit less critical than the alignment of lens 1.

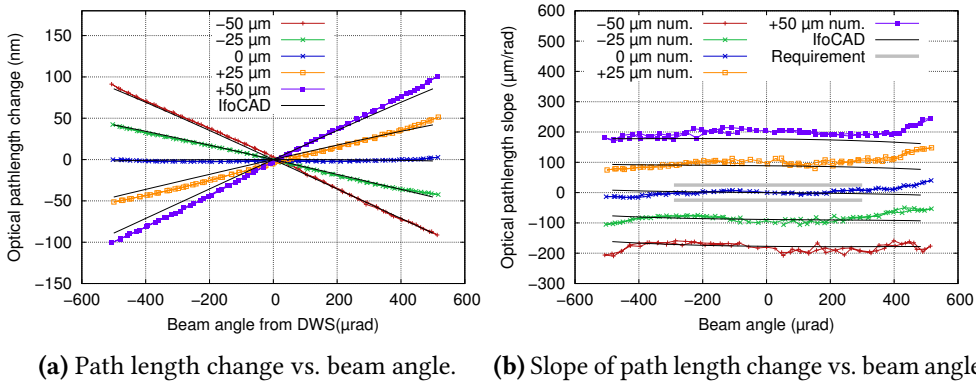


Figure 5.25.: LOB2D imaging system: sensitivity to lateral displacement of lens 2 in vertical direction.

5.4.3. Compensation by photo diode alignment

As shown before, misalignment of lenses and photo diodes generate similar TTL coupling contributions. With a variation of the longitudinal and the lateral position of the QPD a linear and a parabola TTL coupling contribution can be generated. In this section it is shown that these TTL contributions generated via misalignment of the QPD can be used to compensate any TTL coupling (up to axiomatically second order) that remains after the imaging system, as previously mentioned in Section 3.4.

To demonstrate this effect, a scenario was generated where a significant amount of TTL coupling is measurable behind the imaging system. This behavior was generated on purpose by shifting the second lens by 50 μm , which lead to a large linear coupling if the photo diode is at the nominal position, as shown in measurement in Figure 5.26a.

The first iteration in compensating this TTL coupling was to shift the QPD out of its nominal position to the center of the, now misaligned, LO beam. The resulting path length and slope measurements are shown in Figure 5.26c and Figure 5.26d. The TTL coupling is significantly reduced, even with this simple realignment step. To improve the performance even further, the QPD was carefully misaligned to the LO beam, with the corresponding measurement shown in Figure 5.27. The position of the photo diode was further optimized to minimize the TTL coupling. Since the imaging system is not aligned perfectly the point of minimal coupling is not at zero DPS.

In this section a dedicated measurement with a deliberate misalignment of the imaging system was shown, to illustrate the mechanism of compensating residual TTL coupling with an intentional misalignment of the QPD and to demonstrate that this compensation works. This method of compensation was already used to optimize performance of the imaging systems in Section 5.4.1. The best possible performance shown, is the resulting TTL coupling after optimizing the QPD position

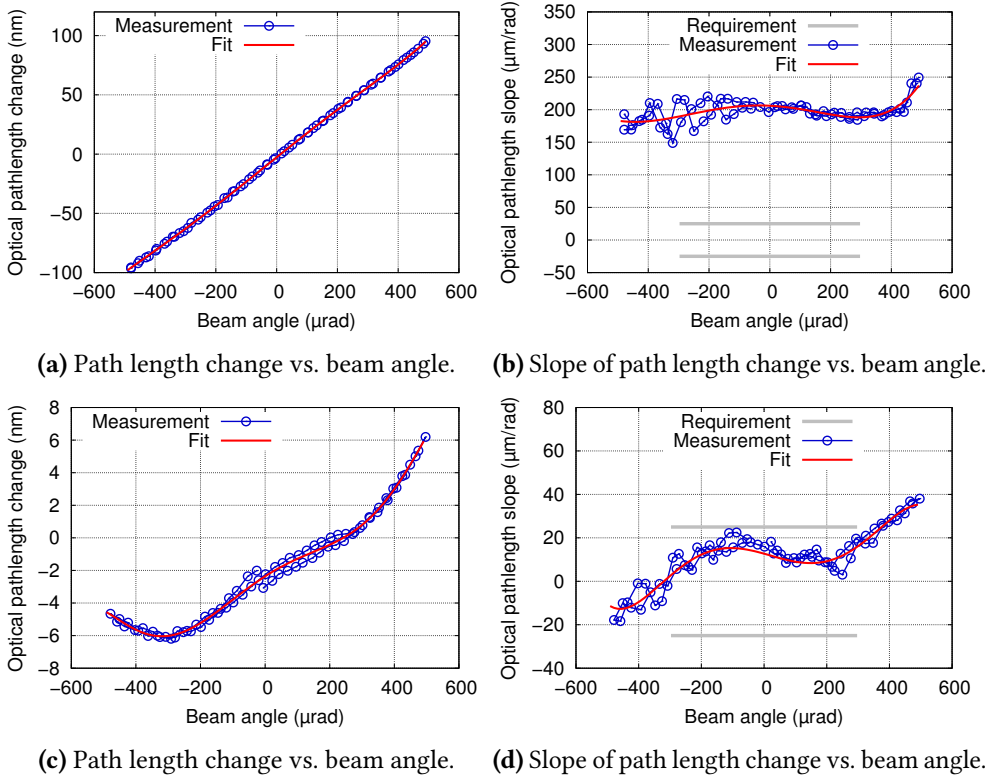


Figure 5.26.: Linear TTL coupling generated by a 50 μm lateral misalignment of lens 2 and the result after aligning the photo diode to DPS = 0.

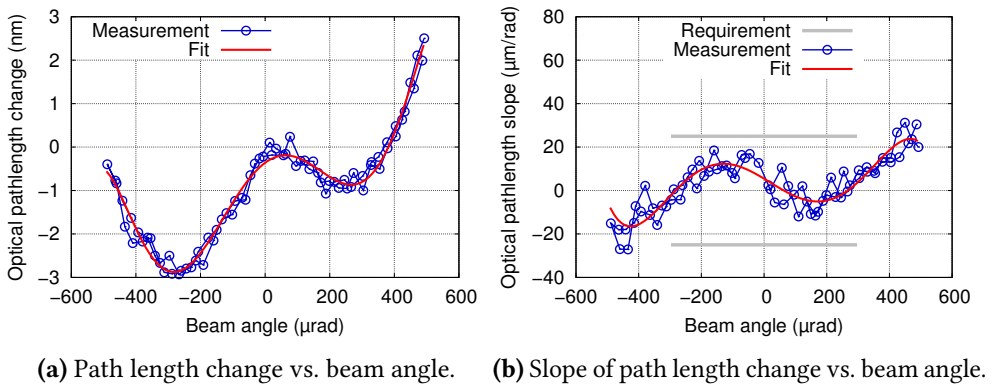


Figure 5.27.: Result after realigning the photo diode to an optimized position to get the smallest TTL coupling.

for minimal TTL coupling. This optimization step was necessary in order to reach the required TTL coupling below $\pm 25 \mu\text{m}/\text{rad}$. With the initial – nominal – alignment (without optimizing the QPD), the residual misalignments within the imaging system, prevent the setup from reaching the performance requirement. The initial alignment was done with an external setup to align the lenses with regard to each other and minimize the beam walk. In this setup it was not possible to control the beam height and beam angle perfectly. Unfortunately, the alignment was done with a slightly different beam than the beam on the OB which let to a height deviation of the lenses from the nominal height. However, as shown in this section and the previously shown optimal performance, small deviations can be compensated by adjusting the photo diode position.

5.5. Four-lens imaging system measurement results – LOB4C

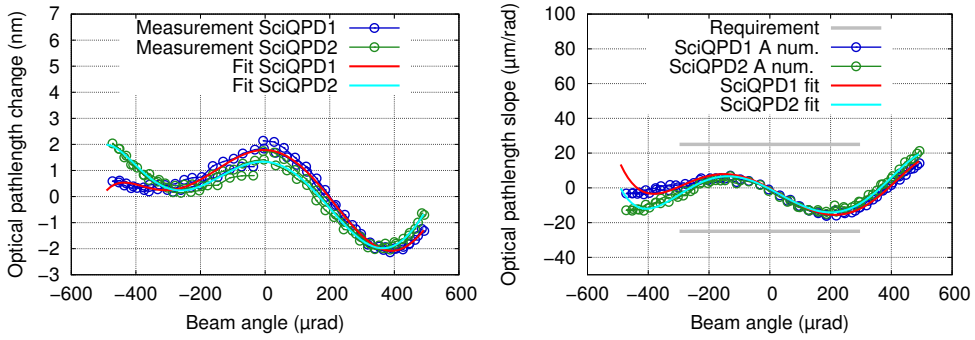
The measurements performed with the LOB2D imaging system were repeated with the LOB4C imaging system and shown in this section. All parameters, the design and further details of the LOB4C imaging system used here, can be found in Section 4.3.9.

5.5.1. Nominal performance

Figure 5.28 shows the optimal possible performance of the LOB4C imaging system placed in front of SciQPD 1 when the flat-top RX beam was used. Figure 5.28a shows the path length change between SciQPD 1 and the reference pinhole versus beam angle, Figure 5.28b shows the slope of the path length change versus beam angle. In both cases, the beam angle was determined from the calibrated DWS signal of the reference QPD on the telescope simulator. Both LOB4C imaging systems show similar results. The TTL coupling is well below the required level of $\pm 25 \mu\text{m}/\text{rad}$. The path length signal show a small linear component which was not removed since the requirement was already fulfilled. The residual linear coupling is assumed to originate from lateral misalignment of the imaging system or the QPD, with reasonable effort, it should be correctable. The optical path length fit parameters for SciQPD 1 and SciQPD 2 are shown in Appendix C.4 in Table C.7.

5.5.2. Sensitivity to misalignments

In the following sections the remaining TTL coupling behind an imaging system in the presence of intentional misalignments is shown. We will systematically show the behavior of the TTL coupling in response to single misalignments of different parameters and compare the results with optical simulations performed in IfoCAD. In all following simulations, the imaging system is aligned and set up as designed, the TX beam is simulated as a pure fundamental Gaussian beam with waist radius



(a) Path length change vs. beam angle. (b) Slope of path length change vs. beam angle.

Figure 5.28.: LOB4C imaging system: nominal performance with RX flat-top beam. Path length change on the left and TTL slope on the right. Both imaging systems shown here fulfill the requirement of $\pm 25 \mu\text{m}/\text{rad}$. The corresponding optical path length fit parameters for SciQPD 1 and SciQPD 2 are shown in Appendix C.4 in Table C.7.

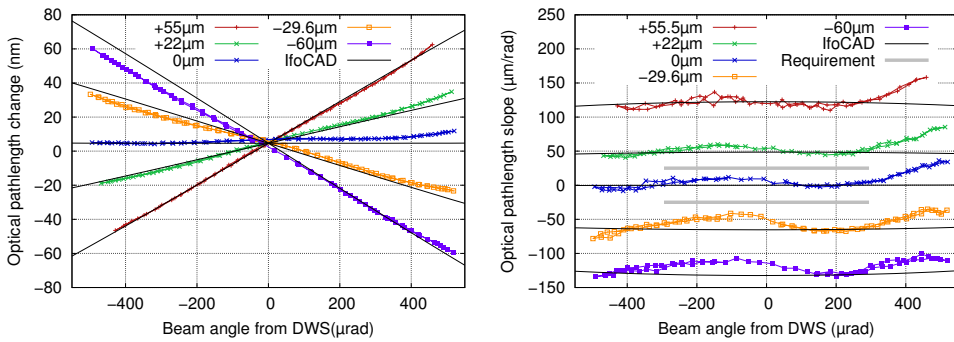
of 1 mm and a waist position 550 mm in front of the RX aperture. The RX flat-top beam is simulated as a pure fundamental Gaussian beam with a waist size of 100 mm and a waist position at the RX aperture, which should represent a top-hat beam with nearly flat phase and intensity profile within a few millimeters at the RX-clip.

Lateral QPD shift

Figure 5.29 shows the sensitivity of the LOB4C imaging system to lateral QPD displacements in vertical direction (active axis). Figure 5.29a shows path length change versus beam angle, Figure 5.29b shows the slope of the path length change versus beam angle.

The measurements show that a lateral misalignment of $\approx \pm 25 \mu\text{m}$ results in additional TTL couplings of $\approx \pm 50 \mu\text{m}/\text{rad}$. With a nominal magnification factor of 0.4 for the imaging system in mind, these results match very well with the expected performance. Here, a strong match between measurement and simulation can be observed. Both, the quality and quantity of the TTL coupling could be reproduced very well. The residual mismatch between simulation and experiment can be explained with the uncertainty in the QPD displacement estimation.

The QPD displacements were measured using the DPS signal of the LO beam. This was necessary since the alignment screws did not adjust the diode positions reliably. The DPS signals were calibrated using its analytical expression [16] for the DPS signal and the nominal beam parameters and magnification factors. Therefore, the resulting QPD displacements have a quite large uncertainty, a change of the LO waist radius



(a) Path length change vs. beam angle. (b) Slope of path length change vs. beam angle.

Figure 5.29.: LOB4C imaging system: sensitivity to lateral QPD displacement in vertical direction. On the left, the path length change is shown, compared to numerical simulations. The path length slope is shown on the right, again against simulated results.

of 100 μm will alter the resulting offsets by $\approx 20\%$. For this reason, this method for the displacement estimation is only used in this measurement, where the alignment screws were not good enough to directly adjust the displacements (the alignment screws in the lens mounts are significantly better).

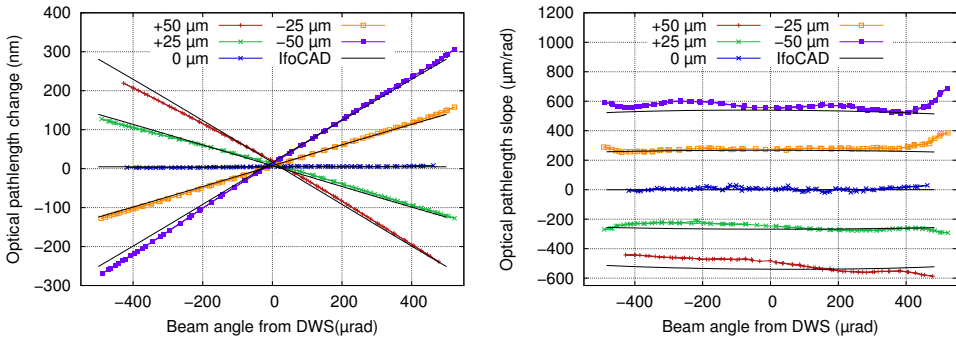
Lateral shift of lens 1

Figure 5.30 shows the sensitivity of the LOB4C imaging system to lateral displacement of lens 1 in vertical direction. Figure 5.30a shows path length change versus beam angle, Figure 5.30b shows the slope of the path length change versus beam angle.

The TTL coupling depends linearly on the lens shift. For $\pm 25 \mu\text{m}$ shift we measured an additional TTL coupling of $\approx \mp 250 \mu\text{m}/\text{rad}$. For a shift of $\pm 50 \mu\text{m}$ the TTL coupling becomes $\approx \mp 530 \mu\text{m}/\text{rad}$. Again, the simulation matches the measured results very well. Only small differences can be observed, which can be explained with the inaccurate measurement of the lens offset.

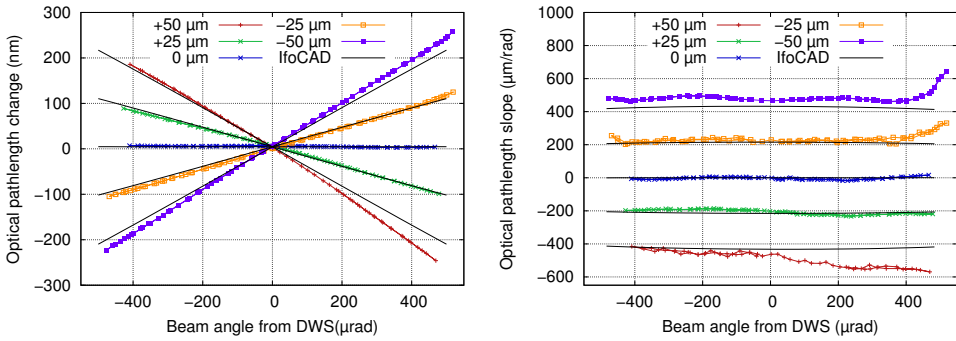
Lateral shift of lens 2

Figure 5.31 shows the sensitivity of the LOB4C imaging system to lateral displacement of lens 2 in vertical direction. Figure 5.31a shows path length change versus beam angle, Figure 5.31b shows the slope of the path length change versus beam angle. For lens 2 for a $\pm 25 \mu\text{m}$ shift we measured an additional TTL coupling of $\approx \mp 200 \mu\text{m}/\text{rad}$. So the additional coupling is a little bit less than for lens 1 for the same shift.



(a) Path length change vs. beam angle. (b) Slope of path length change vs. beam angle.

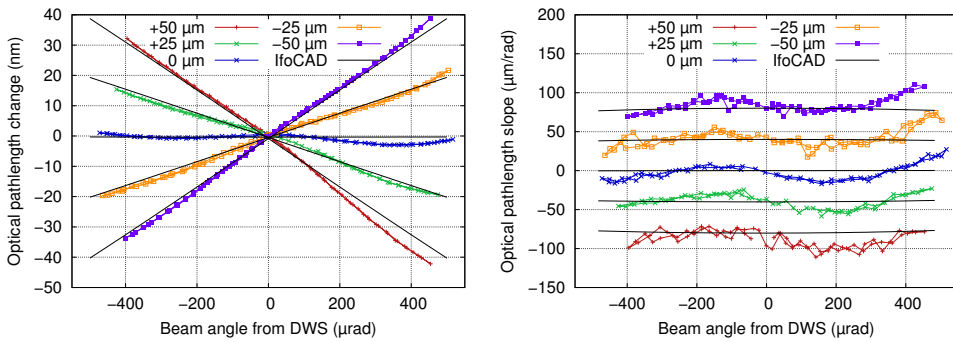
Figure 5.30.: LOB4C imaging system: sensitivity to lateral displacement in vertical direction of lens 1. The path length signal on the left and the path length slope on the right. Both compared to numerically simulated results.



(a) Path length change vs. beam angle. (b) Slope of path length change vs. beam angle.

Figure 5.31.: LOB4C imaging system: sensitivity to lateral displacement in vertical direction of lens 2.

The measurements are fitting the simulations quite well. Except for some small deviations for the larger lens shifts, especially for a displacement of +50 μm . Here, the mechanics of the lens mount was limiting the match between simulation and measurement. For +50 μm , the mount was not actuating smoothly anymore, therefore the final lens position was not based on a certain turn angle of the screw, but on a DPS signal, opposite to the -50 μm displacement. As observable in the measurement, this method provides a large error in the displacement estimation.



(a) Path length change vs. beam angle. (b) Slope of path length change vs. beam angle.

Figure 5.32.: LOB4C imaging system: sensitivity to lateral displacement in vertical direction of lens 3. Path length signal on the left and path length slope on the right, both compared to numerical simulations.

Lateral shift of lens 3

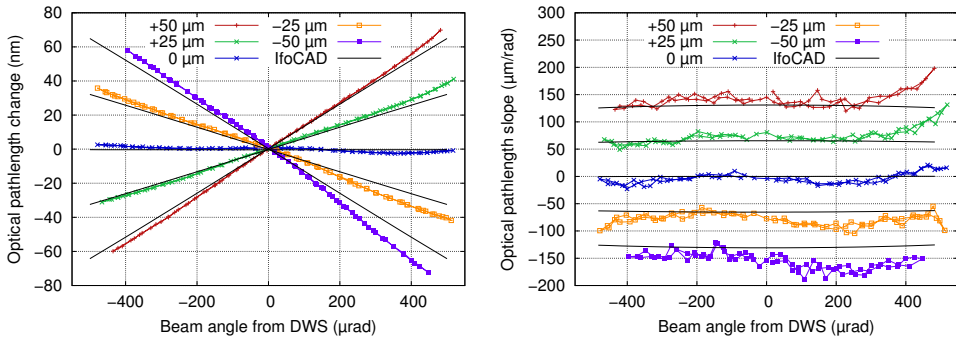
Figure 5.32 shows the sensitivity of the LOB4C imaging system to lateral displacement of lens 3 in vertical direction. Figure 5.32a shows path length change versus beam angle, Figure 5.32b shows the slope of the path length change versus beam angle.

For lens 3 we measured an additional TTL coupling of $\approx \mp 50 \mu\text{m}/\text{rad}$ for a $\pm 25 \mu\text{m}$ shift. This is significantly less than for lens 1 and lens 2. Lens 3 is less critical to misalignment in the active axis (tilt axis). The same result can be obtained from the simulated data which match the measurement very well.

Lateral shift of lens 4

Figure 5.33 shows the sensitivity of the LOB4C imaging system to lateral displacement of lens 4 in vertical direction. Figure 5.33a shows path length change versus beam angle, Figure 5.33b shows the slope of the path length change versus beam angle.

For lens 4 we measured an additional TTL coupling of $\approx \mp 60 \mu\text{m}/\text{rad}$ for a $\pm 25 \mu\text{m}$ shift. This is a little bit more than for lens 3 but still less than for the first two lenses. Therefore, the alignment of the first two lenses is more critical than for the second pair. Again, the measured behavior of the system could be simulated very well. Both quality and quantity of the simulated TTL coupling matches the measurements. A more detailed discussion of the results and a comparison between the LOB4C and the LOB2D system can be found in Section 5.6.



(a) Path length change vs. beam angle. (b) Slope of path length change vs. beam angle.

Figure 5.33.: LOB4C imaging system: sensitivity to lateral displacement in vertical direction of lens 4. Path length signal on the left and path length slope on the right. Both compared to numerical simulations.

5.5.3. Compensation by photo diode alignment

In this section it is shown that a misalignment of the imaging system can be compensated by realigning the photo diode. Here the first lens is shifted intentionally by $25\ \mu\text{m}$ in the vertical axis, which leads to a larger linear coupling if the photo diode is at the nominal position as shown in Figure 5.34a.

To compensate for this TTL coupling the QPD can be realigned. For the first iteration, as shown in Figure 5.34c and Figure 5.34d, the photo diode was aligned to the center of the LO beam (which is misaligned as a result of the misalignment of lens 1), corresponding to a DPS signal close to zero (to the same value as for the nominal performance). Since the imaging system is not aligned perfectly the point of minimal coupling is not at zero DPS. Although the lens is still in the shifted position the TTL coupling is reduced significantly and lays within the requirement. The additional TTL coupling induces for example by a misalignment of one lens can be suppressed by intentionally shifting the QPD from its nominal position.

5.5.4. The effect of the field stop

In imaging system one a field stop was placed in the pupil plane between the lens pairs during the alignment of the imaging system. This was foreseen in the design as described in [TD3]. However, on the optical bench it was not possible to align the imaging system in a way that there was no clipping at the field stop (it has a diameter of $150\ \mu\text{m}$ at a nominal position where the nominal beam diameter is just slightly smaller). Since it is difficult to distinguish between clipping at the photo diode and clipping at the field stop (both result in a change of the DPS signal) a WinCam (CCD based beam profiler) was used. The photo diode was removed and the WinCam was placed next to the optical bench to monitor the beam. No position of the imaging

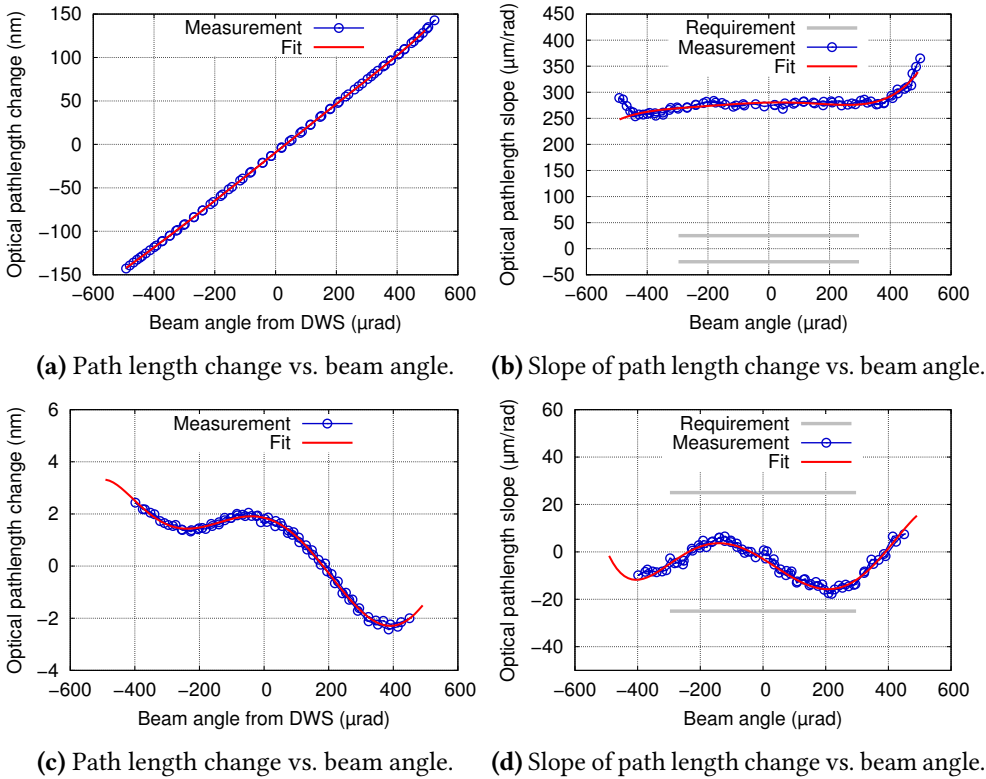


Figure 5.34.: Linear TTL coupling caused by a $25\ \mu\text{m}$ lateral misalignment of lens 1 and the result after realigning the photo diode. In Figure 5.34a and Figure 5.34b path length change and slope are shown for the QPD in its nominal position. Accordingly, in Figure 5.34c and Figure 5.34d path length change and slope for a realigned QPD are shown. Without realignment, the requirement is breached, with a realigned QPD the required performance can be achieved.

system could be found where no clipping was visible over the whole angular range. The clipping was clearly visible by diffraction patterns on the beam profile. An exemplary measurement of the diffraction pattern in one field stop position is shown in Figure 5.35. In the end, the field stop was removed for all following measurements.

In Figure 5.36 a measurement with and without the field stop is shown. For the measurement with the field stop the position was optimized with the help of the WinCam and the clipping could not be minimized further. The clipping is causing a large change in the measured path length, because of the signal loss and it was not possible to meet the requirement with the field stop in place. In the alignment process of imaging system two the field stop was left out from the beginning.

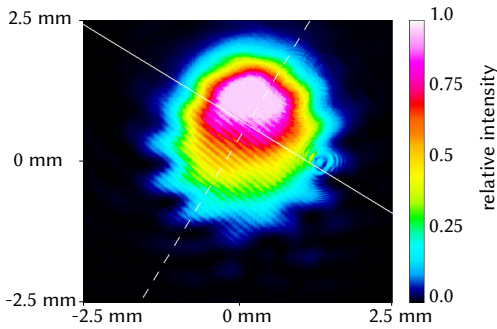


Figure 5.35: Diffraction pattern behind the field stop in the LOB4C imaging system, measured with the WinCam. The measured relative intensity is measured on the CCD detector. The non-Gaussian diffraction pattern indicates that the field-stop is not aligned with respect to the beam. If the two were perfectly aligned a concentric diffraction pattern could be observed.

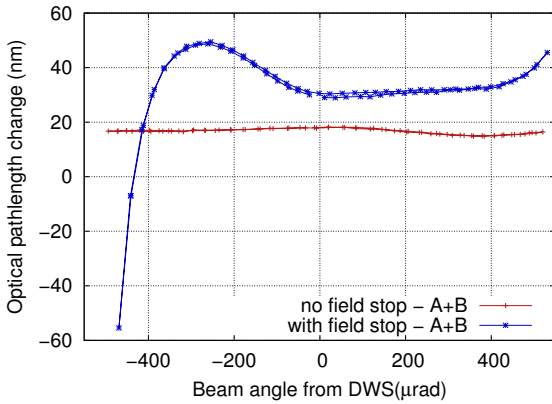


Figure 5.36: Comparison of a scenario with field stop and a scenario without – path length change of the phase A+B plotted over the beam angle.

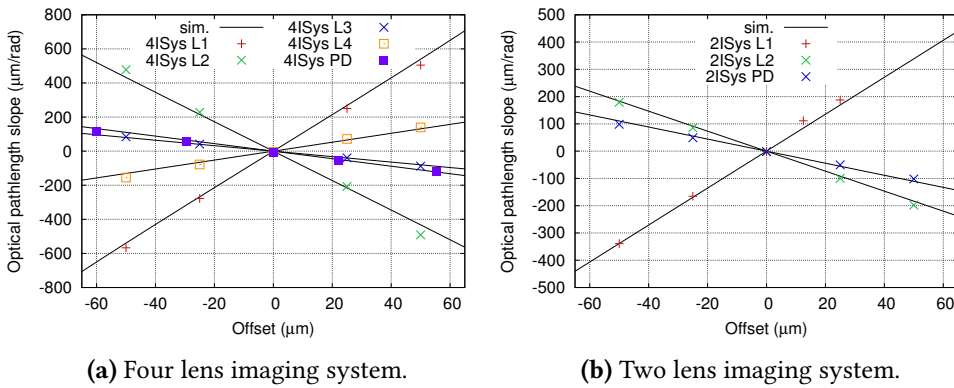
The purpose of the field stop is to suppress stray light and ghost beams. In all measurements taken, the performance was not limited by the former named effects, therefore an additional field stop within the imaging systems seems to be not required.

5.6. Results of the tolerance analysis

To compare the two different imaging system designs, all misalignment measurements were combined and are shown in Figures 5.37. Here, the resulting TTL coupling is plotted over the corresponding misalignment for the different parameters.

For each misalignment parameter the measured TTL coupling is compared with the expected results that were obtained from simulations. The different lenses as well as the photo diode were misaligned in the range of $\pm 50 \mu\text{m}$. The resulting TTL coupling depends on the specific parameters.

For the LOB4C system (see Figure 5.37a), the more critical parameters – lens 1 (L1) and lens 2 (L2) – show a TTL coupling in the range of $\pm 700 \mu\text{m}/\text{rad}$. The less critical parameters – lens 3 (L3), lens 4 (L4) and the photo diode (PD) – show a TTL coupling of less than $\pm 200 \mu\text{m}/\text{rad}$. A sensitivity for the alignment of the field stop is not provided since the requirements were not met with the field stop. The corresponding plot for the LOB2D imaging system is shown in Figure 5.37b. Here,



(a) Four lens imaging system.

(b) Two lens imaging system.

Figure 5.37.: Sensitivity of the different misalignment parameters for both imaging systems, compared to simulated data. 4ISys describes the LOB4C system and 2ISys describes the LOB2D system.

the sensitivity to misalignments are in the range of $-450 \mu\text{m}/\text{rad}$ for L1, $250 \mu\text{m}/\text{rad}$ for L2 and $150 \mu\text{m}/\text{rad}$ for the photo diode. Based on the motto a chain is as strong as its weakest link, the alignment of the LOB2D imaging system is less demanding than the alignment of the LOB4C imaging system.

5.7. Summary of the LISA telescope simulator project

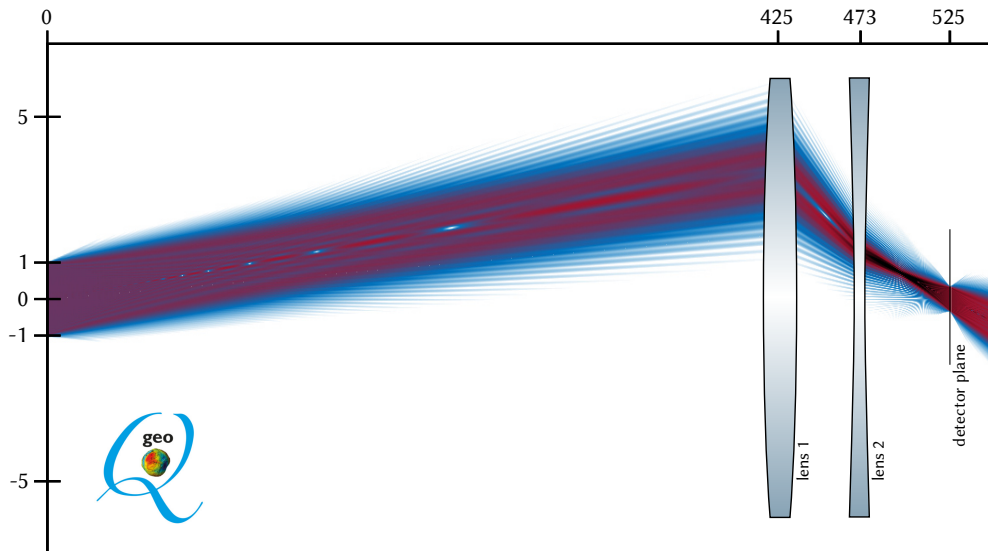
Tilt-to-length coupling tests were successfully performed within the frame of the LISA optical bench development project. It was experimentally demonstrated in a representative setup that imaging systems are capable of reducing tilt-to-length coupling to a level compatible with LISA. The setup, developed within this project, consisted of an ultra stable optical bench and a telescope simulator on a separate baseplate to operate the science interferometer on the optical bench. To our knowledge it is the first time precision interferometry with two separate ultra stable optical benches sitting on top of each other was demonstrated. For disentangling the tilt-to-length contributions from the telescope simulator and the optical bench a reference pinhole photo diode was used. This reference photo diode was aligned using an identical photo diode, temporarily centered in the RX-clip. The reference photo diode alignment was verified by rotating the telescope simulator by 180° (“flipping”) and again measuring tilt-to-length coupling.

Two types of imaging systems with different design approaches were investigated (LOB2D and LOB4C). For both, tilt-to-length coupling was measured within the requirement of $\pm 25 \mu\text{m}/\text{rad}$ for beam angles from $-300 \mu\text{rad}$ to $+300 \mu\text{rad}$ using the RX flat-top beam. The LOB2D imaging systems were also operated with a Gaussian RX beam. Three different Gaussian beams were used. A dependency of tilt-to-length coupling on the beam parameters of the Gaussian RX beam was found. This dependency was reproduced in a numerical simulation.

For a sensitivity analysis of the imaging systems their mechanical mounts allowed for misalignments of individual components (lenses or photo diode). The measured tilt-to-length coupling for misalignments of single elements was in good agreement with simulations. The tilt-to-length coupling due to lens misalignment within the LOB4C imaging system is a factor of 1.5 stronger than for the LOB2D imaging system. The LOB2D imaging systems require less space and were easier to align than the LOB4C imaging systems. Both the two- and LOB4C imaging systems were shown to be fully capable of suppressing TTL coupling to a level which is compatible with an LISA-like instrument. The LISA optical bench project was successfully ended in 2016. However, some issues were found which merit consideration in future development stages of the OB in selecting which imaging system would be most suitable. The main issue, Gaussian beam parameter dependency of the TTL coupling, will be addressed in the next chapter.

Part III

Optical simulations – imaging systems and diffraction



6

Parameter sensitivity of imaging systems

Within this chapter, numerical simulations are used to investigate the beam parameter dependencies of the two imaging systems tested before for LISA. As a result, additional requirements for future imaging systems designs are formulated. With the new requirements a new imaging system design algorithm is developed and two exemplary imaging systems are designed and compared to the old systems.

In the previous chapter, imaging systems were tested and the performance towards misalignment was investigated. Most of the time, the performance of the imaging systems matched the expected one. However, in certain scenarios an unexpected behavior of the LOB2D system was observed. In the measurements with the Gaussian RX and without additional lenses, the coupling behind the LOB2D imaging systems could not be reduced by longitudinally shifting the QPD. In the same setup, the LOB4C system behaved as expected, the TTL coupling was reduced by shifting the QPD. Furthermore, after changing the beam parameters of the RX with different lenses, the LOB2D system behaved as expected too. The TTL coupling could be reduced by adapting the longitudinal QPD position. These observations suggest a so far unnoticed interaction between beam parameters and the LOB2D system. This might be either a special feature of the LOB2D system, or an effect that can affect both designs, provided the respective beam parameters are present. In any case, the mechanism behind this effect needs to be investigated in order to ensure an appropriate TTL performance in any scenario conceivable for future interferometers in space.

In the following sections a simulation is described that was used to investigate the relation between TTL coupling and beam parameters in imaging systems. The aim of this investigation is to understand why the imaging system in the LISA-OB-TS experiment behaved as it did and to find design criteria that can be used for future imaging systems that are robust against beam parameters.

6.1. Beam parameter sensitivity simulator

In the first step, the beam parameter dependencies of the LOB2D and LOB4C imaging systems were simulated to reproduce the measured behavior in the previous experiment.

The goal of this simulation is to show the best possible TTL coupling behind an imaging system (best possible: optimal QPD position for minimal coupling) as a function of the beam parameters – RX and TX waist size and position – to find correlations between the different properties. In detail, the simulation follows the algorithm shown here:

1. The simulation assumes a perfectly aligned imaging system, the point of rotation (RX-clip) is at position zero and all lenses and the QPD are at nominal position.
2. The TTL coupling for given beam parameters of the TX and RX beam is computed in the range of $0 \mu\text{rad}$ to $500 \mu\text{rad}$. The maximal slope of the TTL coupling in this range is called c_{TTL} .
3. The QPD is longitudinally shifted in both directions (position: d_{tmp}) in order to reduce the maximal TTL coupling c_{TTL} (cf. Section 5.5.3 and 5.4.3). The optimal position is called d_{QPD} and the TTL coupling c_{TTL} at this optimized QPD location is called c_{opt} .
4. Next, the beam parameters of the RX beam (waist radius and waist position) are varied and the optimized couplings c_{opt} and the optimal QPD positions d_{QPD} are computed for all combinations in the range of $\omega_0 = 0.8 \text{ mm}$ to 1.2 mm and $z_0 = -2 \text{ m}$ to 2 m . The results are plotted in a heat map, where the x axis is the waist radius of the RX beam, the y axis is the waist position of the RX beam and the color identifies the optimal coupling c_{opt} in $\mu\text{m}/\text{rad}$ (e.g. one subplot of Figure 6.1).
5. Finally, the beam parameters of the TX beam (waist radius and waist position) are varied in the same ranges $\omega_0 = 0.8 \text{ mm}$ to 1.2 mm and $z_0 = -2 \text{ m}$ to 2 m . For multiple combinations of TX beam parameters a heat map of RX beam parameters and the resulting TTL coupling c_{opt} is computed. The results are arranged in a multi-plot. On the y axis of the overall plot, the TX waist position is varied between the sub plots, on the x axis, the TX waist position is varied between the sub plots. In each sub plot the TX parameters are constant, but the RX parameters are varied over the x and y axis, and the color indicated the optimal TTL coupling c_{opt} .

Besides the optimized TTL coupling (c_{opt}) also plots showing the optimal QPD position d_{QPD} and the curvature slope over the longitudinal QPD position are computed. Here, the curvature slope ρ_s is defined as

$$\rho_s = \left. \frac{d(\rho_{\text{RX}} - \rho_{\text{TX}})}{dd_{\text{tmp}}} \right|_{d_{\text{tmp}}=d_{\text{QPD}}}, \quad (6.1)$$

with ρ_{RX} and ρ_{TX} being the curvatures of the RX and the TX wavefront respectively, d_{tmp} is the longitudinal position of the QPD and d_{QPD} is the optimal position of the QPD with minimal TTL coupling. The curvature slope describes how strong the curvature difference between the two interfering beams vary over the QPD position. A small curvature slope (e.g. zero) indicates that a longitudinal shift of the QPD will no alter the curvature difference of the two beams on the QPD. A large curvature slope indicates for example that before the shift the curvature slope is small and after the longitudinal shift the curvature slope on the QPD is large.

The idea behind this simulation is to identify certain beam parameter combinations that prevent sufficient performance and relate this to other parameters, like QPD position and curvature slope. This simulation was computed for both, the LOB2D and the LOB4C imaging system. The results are shown and discussed in the following sections.

6.1.1. Results for the two-lens imaging system

Figure 6.1 shows the multi-plot for the TTL slope c_{opt} behind the two-lens imaging system. In each subplot the waist position and waist radius of the RX beam are varied. In the overall scheme waist radius and position of the TX beam are varied. The color indicates the residual TTL coupling. Similarly, Figure 6.2 shows the curvature difference slope over the QPD position. In Figure 6.3 the optimal QPD position for the two-lens imaging system is shown, again as a function of the TX and RX parameters.

Each point in Figure 6.1 shows the optimized TTL coupling for different beam parameters, the resulting TTL coupling cannot be reduced further by alignment. The colored areas indicating high TTL coupling therefore indicate, that for the given choice of beam parameters, the imaging system generates poor quality of TTL suppression. To find the reason for this behavior, the plots showing the different parameters are compared to each other, Figure 6.4 shows one subplot of each parameter (TTL coupling, curvature slope and QPD position) for an exemplary TX waist of 1 mm radius at -2 m. The same area that show a high TTL coupling, the upper right corner, shows a larger curvature slope. Only the area with a curvature slope that is significantly below $0.5 \cdot 10^{-3} \text{ mm}^{-2}$ features negligible residual TTL coupling. This suggests a strong relationship between the observed non reducible TTL coupling and the fact that the curvature difference between RX and TX beam changes with the QPD position.

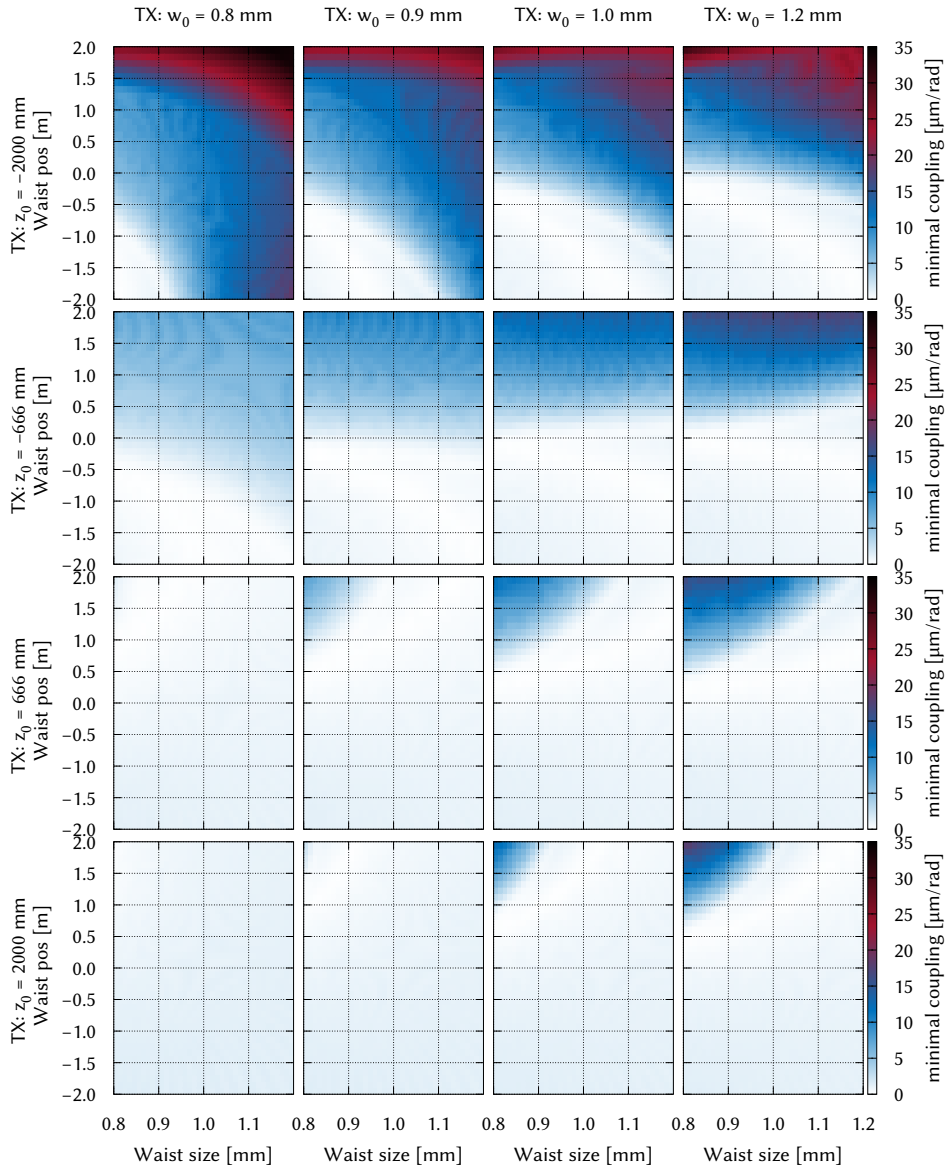


Figure 6.1.: Beam parameter sensitivity simulator results for the TTL slope of the two-lens imaging system. In each subplot the waist position and waist radius of the RX beam are varied. In the overall scheme waist radius and position of the TX beam are varied. The color indicates the maximum of the residual TTL coupling in an angular range of $\pm 500 \mu\text{rad}$.

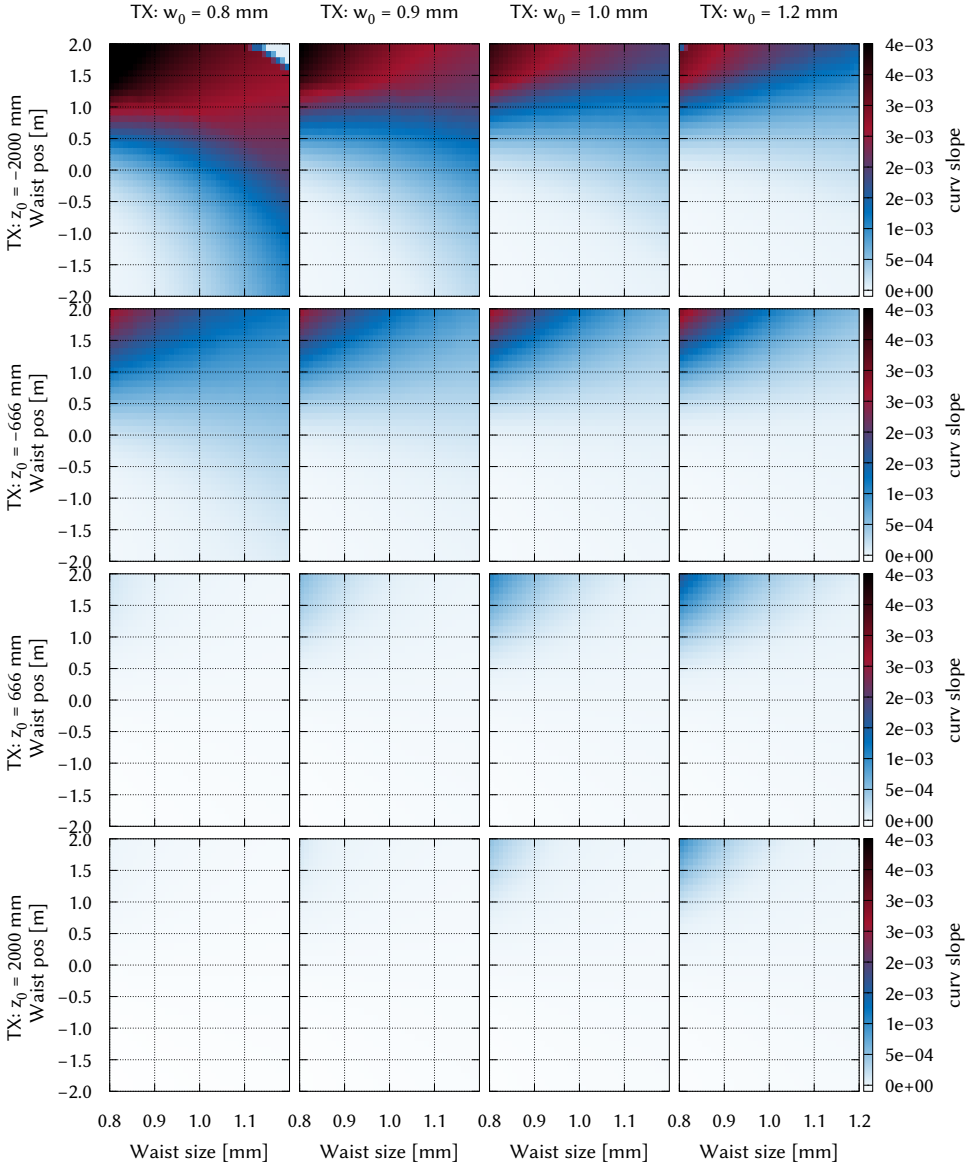


Figure 6.2.: Beam parameter sensitivity simulator results for the beam curvature difference slope of the LOB2D imaging system. In each subplot the waist position and waist radius of the RX beam are varied. In the overall scheme waist radius and position of the TX beam are varied. The color indicates the beam curvature difference slope with respect to the QPD position.

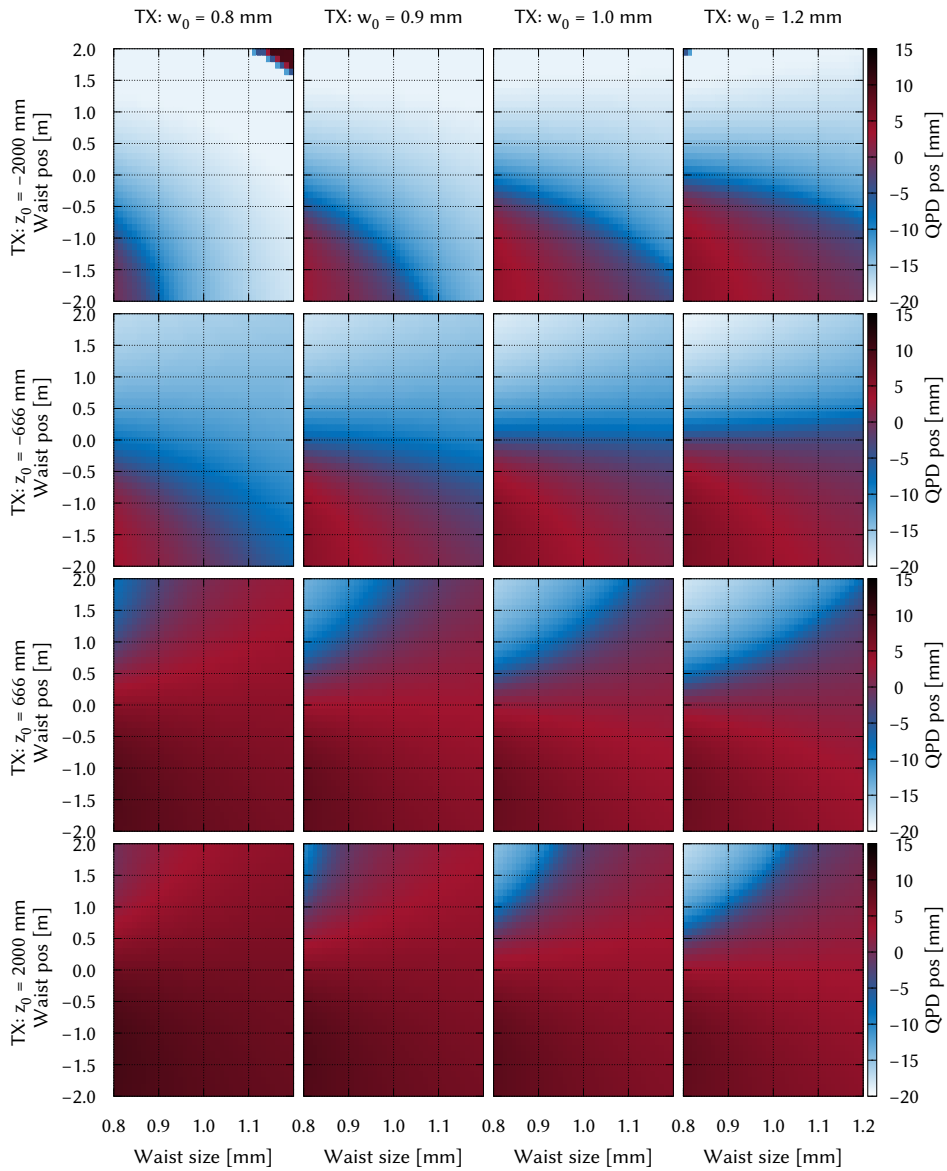


Figure 6.3.: Beam parameter sensitivity simulator results for the optimal QPD position of the LOB2D imaging system. In each subplot the waist position and waist radius of the RX beam are varied. In the overall scheme waist radius and position of the TX beam are varied. The color indicates the optimal QPD position at which the minimal TTL coupling is achieved.

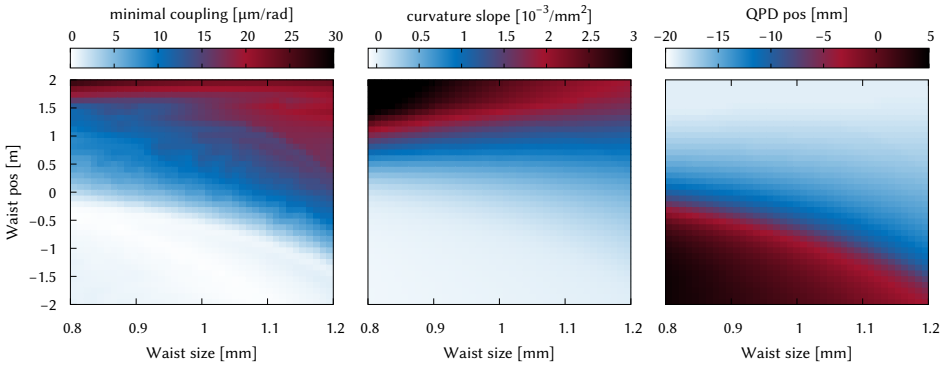


Figure 6.4.: Beam parameter sensitivity simulator results for the LOB2D imaging system. Comparison of residual TTL coupling, curvature difference slope and the optimal QPD position. – TX waist position = -2 m, TX waist radius = 1 mm.

Due to the small waist in front of the QPD in the LOB2D imaging system, certain beam parameters generate a high slope of the curvature difference between the beams over the QPD position. If the QPD is shifted to reduce a quadratic TTL contribution, the curvature slope will generate a changing quadratic coupling too. At certain combinations of parameters, the two quadratic parts will cancel each other and no change in TTL coupling due to QPD shifts can be observed. This becomes a real problem, if the TTL coupling of the two effect contain higher order contributions. This effects might not cancel each other and the residual TTL coupling does not match the requirements.

Furthermore, in Figure 6.4 it can be observed that the area, where the optimal position is closer to the lens than the nominal position, matches the area where the TTL coupling is too high. If the QPD is shifted in this direction, the beam curvature difference slope will generate a TTL coupling that is stronger than the one, which should be removed by shifting in the first place.

In the top left subplot of Figure 6.3, a sharp edge in the QPD position is visible. This behavior is also present in the curvature slope and indicates a scenario where the optimal QPD position is closer to the last lens than allowed – free space in front of the QPD is required for alignment and additional optics, like polarizers (cf. Table 6.1). Therefore, the best QPD position switches from close to the lens to far away. Without limitations in the QPD position, the edge can be removed. However, very close to the lens, the resulting magnification of the imaging system is not sufficient anymore.

6.1.2. Results for the LOB4C imaging system

The same simulation as for the LOB2D system, was repeated with the LOB4C system. A comparison with one subplot of each parameter is shown in Figure 6.5. The detailed multiplots of the individual parameters can be found in Appendix D, Figure D.1 on page 198 shows the TTL coupling slope for the LOB4C imaging system. In Figure D.2 on page 199 the slope of the curvature difference is shown. The plot of the optimal QPD position is shown on page 200 in Figure D.3. To allow a comparison with the LOB2D system, the multiplots in Appendix D have the same scaling for each imaging system. The x-axis and the y-axis in Figure 6.4 and Figure 6.5 use the same scaling, but the color scale has been adapted to improve the visibility.

The overall TTL coupling is smaller than $10 \mu\text{m}/\text{rad}$ for the entire range of beam parameters. In comparison, for the LOB2D system the TTL coupling reached up to $35 \mu\text{m}/\text{rad}$. In terms of LISA, the LOB4C system is well within the requirements over the entire beam parameter range, while the LOB2D system does not fulfill the requirements with certain beam parameter combinations. For the LOB4C system, in the entire spectrum of beam parameters the TTL coupling is below the LISA requirement, however the TTL coupling is not constant and still beam parameter dependent. The residual TTL coupling can be reduced even more by choosing the right beam parameters.

The LOB4C system provides a collimated output beam, thus the wavefront curvatures of the beams after the imaging system are more stable than for the LOB2D system and the curvature difference slope is expected to be much smaller. The simulations show that curvature slopes indeed have a different behavior than for the LOB2D system. Instead of the same pattern as the TTL coupling, here the curvature slope shows a pattern that is more than three orders of magnitude smaller than for the LOB2D system. This explains on the one hand why the strong beam parameter dependent TTL coupling of the LOB2D system does not appear for the LOB4C system and on the other hand demonstrates the advantage of the LOB4C system to image a collimated beam into a collimated beam. The change in the beam parameter due to shifting of the QPD is as small as possible and thus, the system is much more robust. A quadratic coupling can simply be removed by moving the QPD longitudinally, since the beam parameters change less over the photo diode position.

The property of imaging a collimated beam into a collimated beam was considered of secondary importance in the process of finding a suitable two-lens imaging system (see Section 4.3.10). For the original two-lens systems it seemed to be not important to have a collimated beam on the QPD and it was necessary to reduce the requirements to find a two-lens system consisting of off-the-shelf lenses.

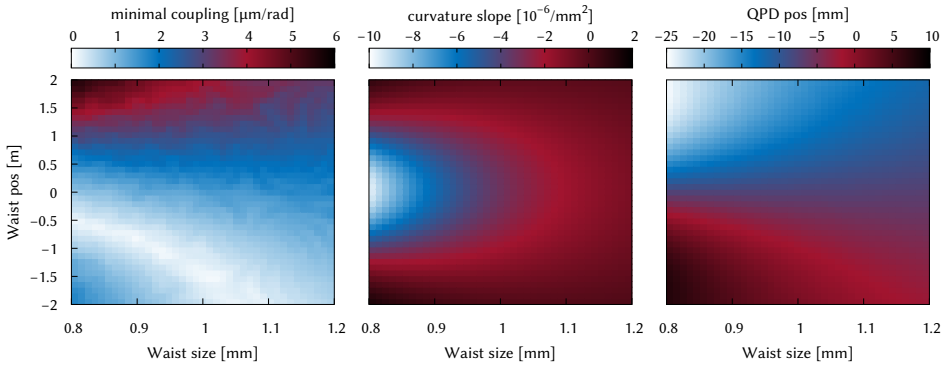


Figure 6.5.: Beam parameter sensitivity simulator results for the LOB4C imaging system. Comparison of residual TTL coupling, curvature difference slope and the optimal QPD position. – TX waist position = -2 m, TX waist radius = 1 mm.

6.1.3. Consequences from the beam parameter investigations

The LOB2D system suffers from beam parameter dependencies. This is a crucial disadvantage, since with the current alignment and manufacturing methods the beam parameters cannot be controlled very well. With the monolithic FIOS design planned for LISA, it is not possible to adjust the beam parameters after assembly, therefore the final parameters depend on the manufacturing tolerances. In the LISA testbed FIOSs have been used that should nominally produce similar beams, but as the measurements show, this was not sufficient for the LOB2D imaging system.

With the current manufacturing tolerances for FIOSs it cannot be ruled out that the required TTL coupling on an actual optical bench cannot be achieved with the current LOB2D system and no additional measures, which leads to the following options:

1. Use the LOB4C imaging system with four lenses that requires more alignment effort.
2. Define new requirements for the beam parameters on the optical bench to exclude the scenarios where the requirements cannot be matched. E.g. RX beam waist radius of 1 mm positioned at the point of rotation and TX beam waist radius of 0.8 mm positioned 2 m in front of the point of rotation.
3. Design new imaging systems which provide a collimated beam to the QPD and are less critical in alignment than the LOB4C system.

Option 1. requires a deeper investigation in the alignment of the LOB4C imaging system, especially of the field stop. So far it was not possible to align it sufficiently. Furthermore, the amount of stray light and ghost beams with the additional lenses and without the field stop has to be investigated.

Option 2. depends on the capabilities to produce fiber injectors that generate beams with the right parameters. The higher the uncertainties in the beam parameters are, the higher is the risk of an excessive amount of TTL coupling.

Option 3. requires a new version of the algorithm which was used to design the first LOB2D imaging system. The requirement of imaging a collimated beam into a collimated beam has to be included in some suitable form.

6.2. Two-lens imaging system – GIS2C

The original two-lens imaging system design algorithm used off-the-shelf lenses to find a system that can suppress beam walk and provides the required magnification factor. Now an additional requirement is included to provide a collimated beam, thus at least one of the former properties cannot be maintained anymore. The only requirements which can be ruled out easily are the use of off-the-shelf lenses and the number of lenses.

In a first step, the number of lenses remains two, but the new imaging system will be designed using custom spherical lenses with arbitrary curvatures and thickness, which was the case for the LOB4C imaging system from the beginning. With the lack of an actual mission design, the imaging system is designed with dummy requirements which should be roughly suitable for a test mass interferometer of future geodesy missions (cf. Section 2.1.2), but should also be suitable for LISA like missions (cf. Section 2.1.1). A complete list of requirements used to design the new imaging system can be found in Table 6.1. These requirements are the same as in the LISA-OB testbed (cf. Chapter 4) with two minor changes. The first is an increase of the maximal envelope from 154 mm to 160 mm and the second is an additional limitation of the overall envelope (entrance pupil – exit pupil) of 800 mm. These two requirements were adapted to match the available space on the minimal optical bench. With these requirements the algorithm searches for imaging system by varying the parameters of each lens as well as the lens and photo diode positions. The functional principle as well as further details of the algorithm are described in the following section.

6.2.1. Second generation design algorithm

The imaging system design algorithm is implemented as a nonlinear minimization. A list of the fitting parameters, describing the entire imaging system, can be found in Table 6.2 containing essentially the position, thickness and curvatures of the two lenses as well as the QPD position. However, to simplify the fitting process, the lens and QPD positions are not fitted directly, but abstract auxiliary parameters are fitted instead which are later used to compute the final lens and QPD positions. Together

Table 6.1.: Requirements for the new imaging system design.

Description	Unit	Requirement
Minimal Entrance Distance: Entrance Pupil – First Lens Surface	mm	350
Minimum Exit Distance: Last Lens Surface – Exit Pupil (d_{exit})	mm	30
Maximum Envelope: First Lens Surface – Exit Pupil (m_{env})	mm	160
Maximal size: Entrance Pupil – Exit Pupil	mm	800
Magnification	a.u.	0.4
Photo diode active area radius	mm	0.45
Photo diode slit width	μm	20

Table 6.2.: Fit parameters of the evolved imaging system design algorithm. The first lens is called L1, accordingly the second one is L2 and the photo diode is called PD.

Name		Lower Limit	Upper Limit	Description
L1 position	L_{1p}	350	800	from minimum entrance distance to maximal size in mm
Scale for imaging system size	d_{total}	0	1	Limiting the amount of total space available for the entire system size
Scale L1 - L2 distance	d_{L1L2}	0	1	Amount of available additional distance between L1 and L2
L1 thickness	L_{1t}	1 mm	20 mm	Additional thickness to the minimal required thickness due to curvature
L2 thickness	L_{2t}	1 mm	20 mm	Additional thickness to the minimal required thickness due to curvature
L1 primary curvature	ρ_{11}	$-\frac{1}{15}$	$\frac{1}{15}$	Primary surface curvature of L1 in $\frac{1}{\text{mm}}$
L1 secondary curvature	ρ_{12}	$-\frac{1}{15}$	$\frac{1}{15}$	Secondary surface curvature of L1 in $\frac{1}{\text{mm}}$
L2 primary curvature	ρ_{21}	$-\frac{1}{15}$	$\frac{1}{15}$	Primary surface curvature of L2 in $\frac{1}{\text{mm}}$
L2 secondary curvature	ρ_{22}	$-\frac{1}{15}$	$\frac{1}{15}$	Secondary surface curvature of L2 in $\frac{1}{\text{mm}}$

with the fitting parameters and the values from the requirements in Table 6.1, d_{exit} the minimal exit distance and m_{env} the maximal size of the entire imaging system, the target function (figure of merit – called F) can be computed with the following features of performance:

- Zero beam walk on the QPD
- Magnification factor as required
- Outgoing beam as collimated as possible

To compute F , first the minimal thickness of the two lenses (i) are computed for the given curvatures (ρ_{ij}) and an assumed size of 5 mm radius (R). Here the index j indicates the two surfaces, $j = 1$ is the primary surface and $j = 2$ is the secondary surface. With the required thickness for each concave curvature the minimal required thickness (t_i^L) becomes

$$t_i^L = \sum_j \frac{1}{\rho_{ij}} - \sqrt{\rho_{ij}^{-2} - R^2}. \quad (6.2)$$

Here, L_1 is placed at its fitted position L_{1p} , therefore L_2 needs to be placed at the position

$$L_{2p} = L_{1p} + t_1^L + L_{1t} + d_1, \quad (6.3)$$

with the parameters

$$d_{\text{env}} = m_{\text{env}} * d_{\text{total}} - t_1^L - t_2^L - L_{1t} - L_{2t} - d_{\text{exit}} \quad (6.4)$$

$$d_1 = d_{\text{env}} * d_{L_1L_2} \quad (6.5)$$

$$d_2 = d_{\text{env}} - d_1. \quad (6.6)$$

The photo diode is placed at

$$\text{PD}_p = L_{1p} + t_1^L + t_2^L + L_{1t} + L_{2t} + d_1 + d_2 + d_{\text{exit}}, \quad (6.7)$$

with the condition $d_{\text{env}} \geq 0$ all size requirements are fulfilled and the imaging system is set up.

Next, a test beam is generated, with a waist radius of 1 mm positioned at 0 mm (in the point of rotation). This beam is traced through L_1 and L_2 and to the surface of the photo diode under the test angle of $300 \mu\text{rad}$. At the photo diode position the lateral offset of the tilted test beam (x_{off}), the spot radius on the diode (ω_{spot}) and the waist radius (ω_0) behind L_2 are computed. The required spot size on the photo diode (ω_{req}) is given by the original beam radius and the magnification: $1 \text{ mm} * 0.4 = 0.4 \text{ mm}$. In the end, the F is computed as

$$F = 10^4 x_{\text{off}}^2 + 5(\omega_0 - \omega_{\text{req}})^2 + 10^3(\omega_{\text{spot}} - \omega_{\text{req}})^2. \quad (6.8)$$

Table 6.3.: Specifications of the second generation imaging system GIS2C.

		Lens 1	Lens 2	QPD
Position	mm	351.008	452.087	506.208
Primary Curvature	mm ⁻¹	-0.0653129	0.0611418	
Secondary Curvature	mm ⁻¹	-0.0686662	0.0797959	
Center Thickness	mm	22.0431	22.9211	
Substrate Radius	mm	5	5	
Refraction Index	1	1.44963	1.44963	
QPD Aperture Diameter	mm			0.9
QPD Slit Diameter	μm			20

Here, the different terms represent the different features of performance: $x_{\text{off}}^2 = 0$ represents zero beam walk, $(\omega_{\text{spot}} - \omega_{\text{req}})^2 = 0$ represents the right magnification, $(\omega_0 - \omega_{\text{req}})^2 = 0$ represents a perfectly collimated beam.

The different terms are weighted in order to get an optimized result. The actual values of these magic numbers were optimized by hand. For example, the property to reduce beam walk is much more important than the property to produce a collimated beam.

6.2.2. Imaging system design

With the algorithm described above, a new imaging system was designed. All relevant parameters can be found in Table 6.3. In contrast to the old design, the lenses are much thicker, and the imaging system provides a nearly collimated beam. Instead of a waist in the range of a few tens of micro meter, the new design provides a waist radius close to 0.4 mm. A sketch of the new design is shown in Figure 6.6. This design is called GIS2C– generic two-lens imaging system featuring a collimated output beam.

The nominal performance with perfectly aligned system and perfect Gaussian beams is shown in Figure 6.7. The remaining TTL coupling is comparable to the former imaging systems in the optimal scenario and orders of magnitude below the required level.

More important is of course the performance under the effect of changing beam parameters. To compare the GIS2C system with the LOB2D and the LOB4C system, the same beam parameter variation simulations that were shown in Section 6.1.1 and Section 6.1.2 were performed for the new imaging system design. The comparison between the different parameters for one subplot is shown in Figure 6.8. Again,

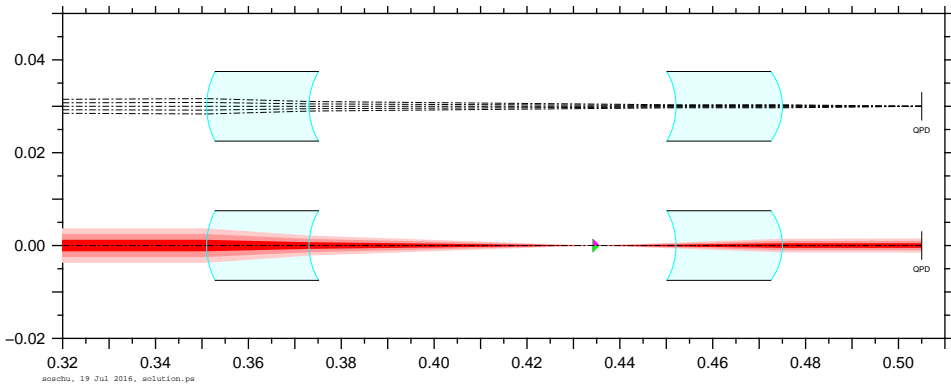


Figure 6.6.: Optical model of the GIS2C imaging system. The point of rotation is located at position 0 mm. The first plot shows the propagation of different base rays, which start under different angles at the point of rotation and end up in the center of the QPD (demonstrating zero beam walk). The second plot is showing the propagation of a Gaussian beam. The triangles indicate the waist position (tangential and sagittal plane). Furthermore, the magnification factor can be seen. The large 1 mm waist Gaussian beam is compressed and becomes 0.4 mm on the QPD.

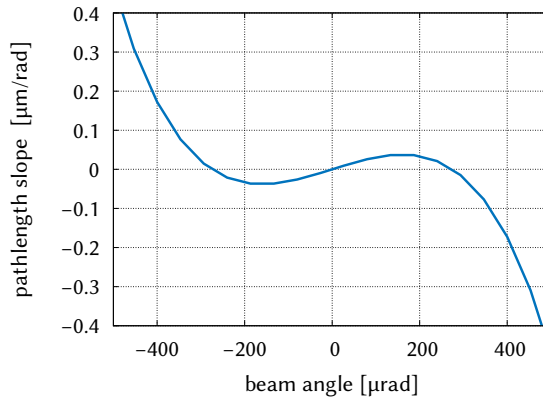


Figure 6.7.: GIS2C imaging system: nominal performance with Gaussian beams. Waist radius of 1 mm each, located at the point of rotation. The slope of the path length signal is plotted over the beam angle.

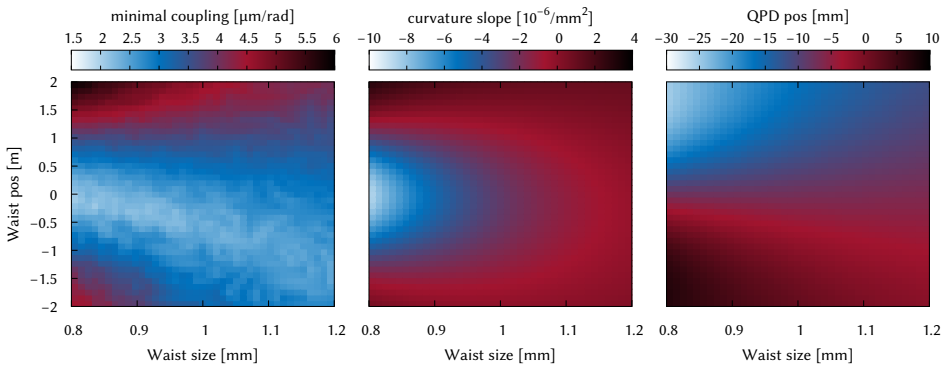


Figure 6.8.: Beam parameter sensitivity simulator results for the GIS2C imaging system. Comparison of residual TTL coupling, curvature difference slope and the optimal QPD position. – TX waist position = -2 m, TX waist radius = 1 mm.

the detailed multiplots of the individual parameters can be found in Appendix D, Figure D.4 on page 201 shows the multi-plot of the path length slope. Figure D.5 on page 202 shows the slope of the curvature difference and on page 203 in Figure D.6 the optimal QPD position in relation to the beam parameters is shown.

The performance over the entire range of beam parameters is well within the requirements. The critical behavior of the LOB2D system cannot be observed. The curvature slope is similar to the one of the LOB4C system. More importantly, the magnitude is three orders below the one of the LOB2D system, comparable to the LOB4C system. Therefore, the wavefront curvature difference slope does not have an influence to the path length signal slope. The optimal photo diode position shows the same result as for the LOB4C system.

6.2.3. Results of the GIS2C imaging system investigation

The shown simulation suggests, that with the new imaging system design algorithm, we can design imaging systems that combine the advantages of the LOB4C and the LOB2D imaging system – less components and less beam parameter dependent. With the use of custom lenses (instead of off-the-shelf components) it is possible to design a two-lens system that provides a collimated beam at the output. The result is a simple system of only two lenses, that provide the required TTL reduction and is robust against beam parameter mismatches.

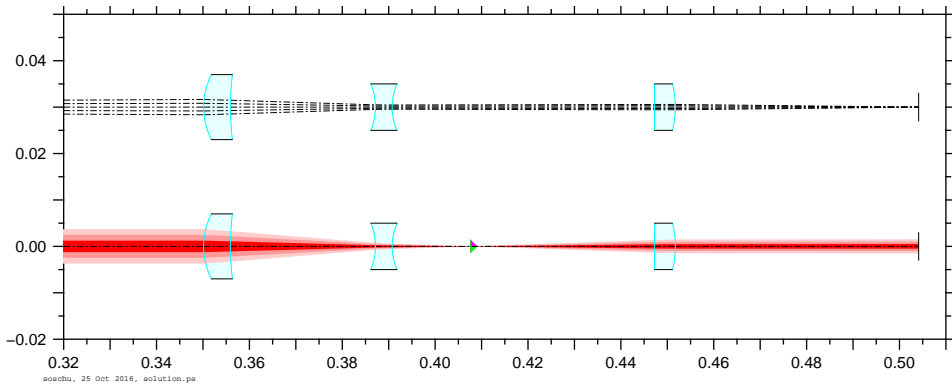


Figure 6.9.: Optical model of the GIS3C imaging system. The point of rotation is located at position 0 mm. The first plot shows the propagation of different base rays, which start under different angles at the point of rotation and end up in the center of the QPD (demonstrating zero beam walk). The second plot is showing the propagation of a Gaussian beam. The triangles indicate the waist position (tangential and sagittal plane). Furthermore, the magnification factor can be seen. The large 1 mm waist Gaussian beam is compressed and becomes 0.4 mm on the QPD.

6.3. Three-lens imaging system – GIS3C

The GIS2C imaging system fulfills all requirements and shows great performance. However, it has one major drawback, which lies in the required thickness of the lenses. With the given requirements a center thickness of more than 22 mm is needed. Usually, transmitting through large amounts of material is avoided to suppress the effect of thermal-elastic noise, which is the combined effect of the coefficient of thermal expansion and the change in refractive index with temperature [51]. However, the imaging systems are used in a common mode path for both interfering beams and therefore no additional noise is expected. Nonetheless, an alternative design with less transmitting material is presented in the following section. For this second new design, the thickness of the lenses is limited to be less than 6 mm. To compensate for this additional requirement, a third lens had to be added to the imaging system.

Optical design The design algorithm was adapted to handle three instead of two lenses. Additionally the limits for the lens thickness was reduced to 6 mm. The resulting design can be seen in Figure 6.9. All relevant parameters are listed in Table 6.4. This design features three thin lenses, compared to the 22 mm of the GIS2C system, and provides a collimated output beam. It is named GIS3C– generic three lens imaging system with three lenses, featuring a collimated output beam. Again, the beam parameter dependency of the design is computed.

Table 6.4.: Specifications of the three lens imaging system.

		Lens 1	Lens 2	Lens 3	QPD
Position	mm	350.129	387.149	447.235	504.129
Primary Curvature	mm ⁻¹	0.0647504	-0.0778622	0.00109276	
Secondary Curvature	mm ⁻¹	-0.0178643	-0.0812156	0.0499057	
Center Thickness	mm	5.77614	3.5947	4.51577	
Substrate Radius	mm	7	5	5	
Refraction Index	1	1.44963	1.44963	1.44963	
QPD Aperture Diameter	mm				0.9
QPD Slit Diameter	μm				20

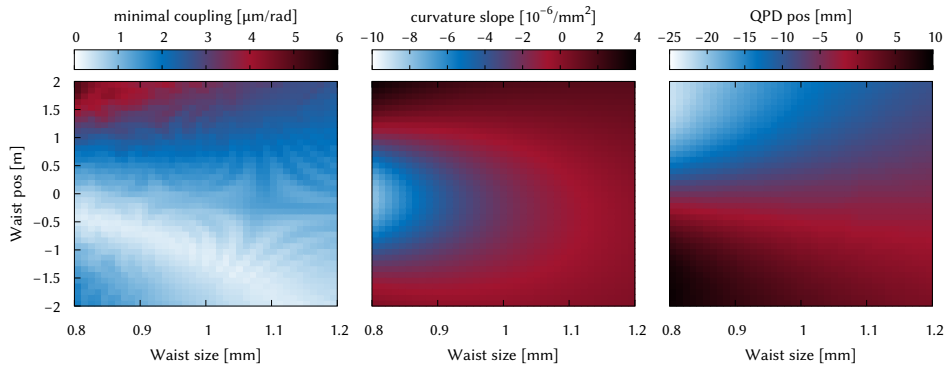


Figure 6.10.: Beam parameter sensitivity simulator results for the GIS3C imaging system. Comparison of residual TTL coupling, curvature difference slope and the optimal QPD position. – TX waist position = -2 m, TX waist radius = 1 mm.

The comparison between the different parameters for one subplot is shown in Figure 6.10. Again, the detailed multiplots of the individual parameters can be found in Appendix D, Figure D.7 on page 204 shows the multi-plot of the path length slope. Figure D.8 on page 205 shows the slope of the curvature difference and Figure D.9 on page 206 shows the optimal QPD position.

The performance over the entire range of beam parameters is below $10 \mu\text{m}/\text{rad}$ and thus, this design would match the LISA requirement of $25 \mu\text{m}/\text{rad}$. The curvature slope pattern is similar to the one of the LOB4C system and the GIS2C system. The optimal photo diode position, shown in Figure D.9 shows the same result as for the LOB4C system. Overall, the GIS3C system shows the same performance and robustness regarding beam parameter variations as the GIS2C and the LOB4C design.

6.4. Misalignment sensitivity comparison to old imaging systems

A tolerance analysis, similar to the one in the LISA telescope simulator experiment, were simulated with the GIS2C system and the GIS3C system. Since the tolerance analysis of the LOB2D and LOB4C system shown in Section 5.4.2 and 5.5.2 showed a good match to the corresponding simulations, the simulations of the new systems provide a good impression of how critical the alignment of the new systems is. Both, TX and RX beam, are represented by a 1 mm radius Gaussian beam with the waist positioned in the RX-clip. Results of all individual measurements are shown in Appendix D.2.

Here, only an overview of the responses towards the different parameters is shown. Figure 6.11 shows the sensitivity to lateral misalignments of the lenses and the detectors for the GIS2C imaging system and the GIS3C imaging system compared to the LOB2D and the LOB4C system.

The sensitivity towards misalignment of the QPD is equal for all systems, which is expected, since this behavior is mostly influenced by the spot size at the detector. Due to the given magnification this is equal for all imaging systems tested here.

The most critical parameter of the LOB2D system is the alignment of L1 with $6.8 \mu\text{m}/\text{rad}$ per μm misalignment, the most critical one for the LOB4C system is L1 with $10.9 \mu\text{m}/\text{rad}$ per μm offset, for the GIS2C system it is L1 with $2.4 \mu\text{m}/\text{rad}$ per μm and for the GIS3C system again L1 with $5.5 \mu\text{m}/\text{rad}$ per μm . Based on the motto “a chain is as strong as its weakest link”, the new two lens system is more than a factor of two less critical than the LOB2D system and the GIS3C system, and more than a factor of 4 better than the LOB4C system. The new GIS3C system is comparable with the LOB2D system.

An overview over the performance of all imaging systems in the different simulations is shown in Table 6.5. The criticality of the alignment, the residual TTL coupling due to beam parameter variations, the number of components and the propagation path length in material is color-coded from green to red. Green indicates the best performance, yellow stands for: not optimal but probably tolerable, and red means: not tolerable without additional measures.

From this list, it can be derived that the GIS2C system shows great performance in all aspects, except the propagation length in material. It cannot be ruled out that the thermo elastic noise (cf. Section 6.3) in 45 mm glass lead to problems in the future. In order to use this or a similar design it needs to be ensured, that this feature will not lead to additional noise in the measurement. The LOB4C and the GIS3C system show slightly less good results for the number of components and the alignment criticality. However, since the propagation path in glass is much smaller than for the GIS2C system, these two designs are favorable here. The LOB2D system shows a residual

Table 6.5.: Comparison of the different imaging systems, results of the different simulations – green: optimal performance, yellow: not optimal but still tolerable, red: needs further attention.

imaging system	alignment coupling μrad	residual TTL coupling $\mu\text{m}/\text{rad}$	number of components 1	path in material mm
LOB2D	6.8	35	2	7.3
LOB4C	10.9	<10	4	12.5
GIS2C	2.4	<10	2	45
GIS3C	5.5	<10	3	13.9

TTL coupling that exceeds the required level of $25 \mu\text{m}/\text{rad}$. In the scope of the LISA OB testbed, this imaging system does not provide a sufficient TTL suppression with the present beams. However, the limit $25 \mu\text{m}/\text{rad}$ is not a strict threshold, for a future LISA mission the LOB2D system might be sufficient.

One remaining difference between LOB4C and all other systems is the optional field stop, which can be used to suppress stray light. Since all other systems do not feature an internal pupil, it is not possible to insert a field stop. Estimations of the effect of a field stop towards stray light suppression were not investigated in this thesis. However, within the LISA OB experiment the alignment of a field stop in the LOB4C system proved to be complicated and after numerous unsuccessful tries the field stop was finally discarded, as shown in Section 5.5.4. The benefits and possible risks of a field stop needs to be further investigated.

The second generation imaging systems will be tested experimentally in the near future. Especially the relation between residual TTL coupling and beam parameter combinations is interesting to test in an experiment. To test this feature, not the LISA testbed but the ATA (cf. Section 4.4.4) will be used.

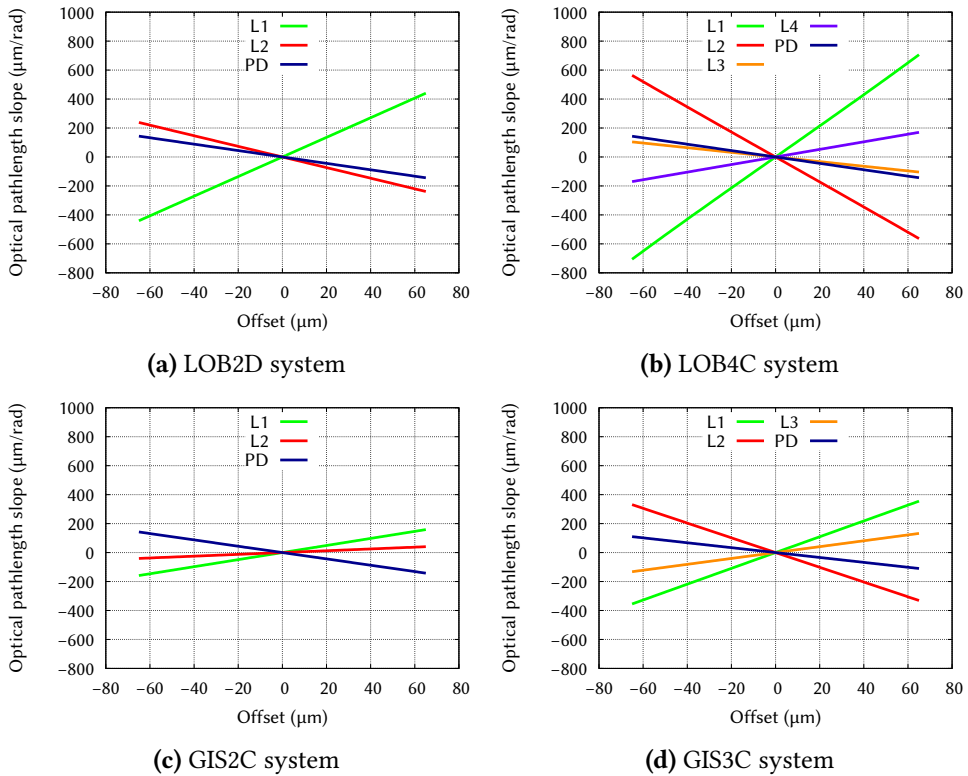


Figure 6.11.: Sensitivity of the different misalignment parameters for the LOB2D design, the LOB4C design, the GIS2C design and the GIS3C design. Each of the individual lenses and the diodes were moved laterally and the resulting TTL coupling was measured. The resulting relation between TTL coupling and corresponding misalignment is shown here.

7

Diffraction

In this chapter, a Gaussian beam decomposition method is developed and implemented into IfoCAD. This implementation is compared to other diffraction propagation methods and analytic solutions.

In most parts of this thesis so far, laser beams were modeled with fundamental Gaussian beams (Section 2.3.1). In some scenarios, this is a valid and accurate approach, for example in the proof-of-principle experiment (Appendix B), where an optical resonator was used to generate a nearly perfect Gaussian fundamental mode. In other situations however, the fundamental Gaussian beam is not sufficient anymore. In general, the propagation characteristic of an arbitrary wavefront is much more complicated and therefore not representable with a Gaussian beam. The example, most important for this thesis, is the LISA science interferometer, where a small fraction of a large wavefront is cut out. This scenario was reproduced in the LISA OB testbed in Chapter 4, where a large flat-top beam was used to operate a LISA like science interferometer. Similarly, the beam geometry in the receive path of the long arm interferometers of any future inter-satellite laser link will be top-hat like and therefore suffer from diffraction. Furthermore, even a locally generated beam from a FIOS is not a perfect fundamental Gaussian but a fiber mode [52]. Clipping of laser beams, intentional with a field-stop or unintentional due to misalignment or size constraints of optical components will lead to diffraction and disturbed wavefronts. It is of utmost importance to model, compute and simulate diffraction effects in order to design and understand this potential noise and TTL coupling sources.

In this chapter different approaches of diffraction modeling are shown. All simulations were performed with IfoCAD [P2, 23, P4], details about the methods and implementation of the FFT optics can be found in [53]. An explanation about the mode expansion method and its implementation is written in [52]. My contribution comprises the implementation of the Gaussian beam decomposition and the comparison between the different methods.

7.1. Reasons for diffraction

Usually laser beams are described as rays or Gaussian beams. In most scenarios this is sufficient to model an experimental setup and sufficiently estimated interferometric signals, as shown in Chapter 4. However, in certain situations the Gaussian beam model is not capable of modeling the real behavior of a system. In this section a few examples of non negligible diffraction effects are listed and explained.

Clipping in the telescope In LISA and GRACE-FO laser light is exchanged between satellites. Light from one satellite is emitted, propagates for hundreds or millions of kilometers and is detected at the second satellite. Since the wavefront after propagation is significantly large than the satellite, not the entire light can be gathered, but a small fraction of the arriving wavefront is cut out. Even if a perfect telescope is assumed (GRACE-FO features no telescope at all), which imprints no distortion to the wavefront, the local interferometer has to handle a flat intensity and phase front with sharp edges. Due to diffraction, the photo diodes without proper imaging systems would sense a concentric diffraction pattern instead of a homogeneous field.

Ghost beams and field stops A ghost beam is a laser beam which is unintentionally generated in an interferometer. For example, the secondary surface of a beam splitter is supposed to not reflect light. Any beam hitting this surface should only refract at it, but never reflect. Proper coating suppresses most of the reflected light but not all of it. There will always be a small portion of reflected light at any transmitting surface in an interferometer. These unintended reflections are called ghost beams (in addition unintended transmissions at e.g. mirrors are called ghost beams, too).

With sufficient knowledge of the optical components and coating, ghost beams can be computed and simulated with ease. But with an unintended reflection at e.g. the backside of a beam splitter, the corresponding ghost beam has to travel the beam splitter twice, generating a significant offset between nominal beam and the parallel ghost beam. With larger beams (e.g. the top hat beam in the LISA OB experiment) clipping of ghost beams at the edges of optical components might occur. Further propagation after clipping will lead to diffraction of the ghost beams, leading to ghost beam wavefronts on the photo diodes, featuring patterns that cannot be simulated easily.

The four lens imaging system used in Chapter 4 features a field stop suppressing the effect of ghost beams and stray light in general. The field stop is an aperture placed in the internal pupil of the system and absorbs any light that travels the system off axis. On the one hand, the effect of ghost beams should be reducible by the use of a field stop, on the other hand even slight misalignments of this aperture will lead to diffraction of the nominal beam, as experienced in the LISA OB experiment and shown in Section 5.5.4, especially in Figure 5.35.

Top-hat generators As mentioned above, the wavefront received on a LISA satellite is a cut out part of a large Gaussian beam, nearly flat in intensity and phase limited by sharp edges. One challenge is to simulate the behavior of this beam to understand the possible limitations and problems of the LISA OB. Another challenge is to build a device that can produce such a wavefront to experimentally test the performance of a LISA like interferometer in the lab.

In the second TTL experiment (LISA telescope simulator) a fancy hyper Gaussian aperture was used to provide a flat wavefront, as described in Section 4.3.6. This was sufficient to determine coupling factors and measure nanometers, however to demonstrate the performance of LISA with a much higher accuracy, more advanced flat-top generators have to be designed and build.

7.2. Simulation of diffraction

There are multiple methods to describe and compute diffraction. The most accurate and elegant method is the analytical solution of the diffraction integral (e.g. Rayleigh-Sommerfeld [54]). Unfortunately, there is no general solution, only solutions for special cases exist and in most other scenarios the diffraction integral is not solvable. Therefore, FFT based direct integration methods were developed to solve the Rayleigh-Sommerfeld diffraction integral [55, 56].

Another approach is to decompose the wavefront of which the diffraction has to be computed into a superposition of more simple, more fundamental wavefronts. Due to the superposition principle of electro magnetic waves it is possible to decompose an arbitrary wavefront into a set of other wavefronts and if the superposition matches the original wavefront in the beginning, the superposition of the propagated wavefronts at any other location will match the diffraction pattern of the original wavefront.

In the following sections, the most common methods to decompose a wavefront are explained.

7.2.1. Angular spectrum decomposition

The idea is to decompose the wavefront into an infinite number of plane waves. The different waves propagate in all possible directions and therefore form a basis in which an arbitrary wavefront can be decomposed. The propagation of a plane wave is simple and therefore, the superposition can be used to describe the propagation characteristics of the initial wavefront. Broadly speaking, the angular spectrum method works as follows: The initial wavefront is decomposed by applying an FFT. The result, the angular spectrum, can be propagated by multiplying it with a suitable propagation term, and the propagated wavefront can be found by applying the inverse FFT to the propagated angular spectrum. More details can be found in [57, 58]. One problem in the angular spectrum method is, how to handle curved surfaces, or in general, a surface that is not orthogonal to the propagation direction. Since the angular spectrum can only be propagated as a whole, it is difficult to propagate through curved or tilted components. Tricks and workarounds were developed to overcome this difficulty [53]. Another problem is that the window of the FFT algorithm has to cover the entire wavefront at any time. Without the use of rescaling windows sizes, which requires additional care, the initial window has to be sufficiently large to cover the entire wavefront after propagation. For near-field propagation this is not critical, most of the time, but for far-field propagation, like an inter-satellite laser link, finding a proper window size is quite challenging.

The last challenge mentioned here, is to handle large curvatures in wavefronts, which cannot be done with a simple approach like mentioned above, but like the tilted components, needs additional care [59]. All FFT based angular spectrum methods, used in this thesis were implemented in IfoCAD by Vitaly Müller, additional information about the implementation can be found in [53].

7.2.2. Mode expansion method

In the mode expansion method, the initial wavefront is decomposed into a superposition of higher order TEM modes, e.g. Hermite-Gaussian or Laguerre-Gaussian modes [34]. By choosing suitable parameters for the fundamental mode of the decomposition (position and waist size), power and phase of the different TEM modes can be computed via the mode-overlap between the initial wavefront and the different TEM modes. Since both the Hermite-Gaussian and the Laguerre-Gaussian modes represent an orthogonal basis, a perfect decomposition can be achieved with an infinite number of higher-order modes of either kind. The propagation of the individual modes is well known and can be computed efficiently by using the ABCD-matrix formalism.

Far-field propagation and complex local interferometry (lenses, curved surfaces and titled components) can be easily computed. Only the base ray and the q parameter have to be propagated through a system. From this two features, the electric fields of all TEM modes can be computed.

The main challenge with this method lays in the infinite number of TEM modes that is required for a perfect decomposition. With reasonable computational effort, only a small number of modes (in the order of a few hundred) can be computed. For an initial wavefront close to a Gaussian beam, or at least compact and smooth, the superposition of the small number of Gaussian modes generates a good representation of the initial wavefront, but for an initial wavefront with sharp edges, complicated pattern or high frequency variations in phase or intensity, the number of modes required for a decent decomposition exceeds the computation power available.

Details about mode expansion in general can be found in [60, 61]. The mode-expansion methods, used in this thesis were developed and implemented in IfoCAD by Christoph Mahrtdt, details about this implementation and the algorithms can be found in [52, 62].

7.2.3. Gaussian beam decomposition

The GBDC uses a grid of small fundamental Gaussian modes to decompose an arbitrary wavefront. The propagation of fundamental Gaussian modes is trivial and therefore is the propagation of the decomposed field. A basic description of this method can for example be found in [63].

Decomposition algorithm

We start with a wavefront that needs to be decomposed (W_{front}), such as a Gaussian beam that is clipped at an aperture, or any other wavefront. As an example a plane wave after a square aperture of 4 mm side length is shown in Figure 7.1a. A window area around this wavefront is defined, which is sufficiently large to cover the entire wavefront. Parts of the wavefront which do not lay in this window area are not considered in the decomposition and will cause additional diffraction. In the example, the window area is 6 mm times 6 mm large.

In the next step fundamental Gaussian beams b_i are placed all over the window area. The exact position of each beam can be chosen arbitrarily. Certain patterns might be preferable for respective initial wavefronts. A spiral shaped pattern (as shown in Figure 7.1b) is certainly more useful to describe a round wavefront, while a equidistant grid seems to be more suitable for a rectangular pattern as shown in Figure 7.1c. However, with a little effort, both pattern can be used for both types of wavefronts and in order to define an algorithm which can be used to decompose any wavefront, a fixed pattern – an equidistant grid – is set for the single fundamental Gaussian beams.

The next parameter is the overlap of the different fundamental modes. The spot sizes in relation to the grid sizes describes how large the overlap is. If the overlap is too large, as in Figure 7.1d, the single beams are too large and small structures cannot be replicated. Figure 7.1e shows a scenario where the overlap is too small, here the area between the single beams cannot be filled successfully. The optimal relation between grid size and waist diameter is around 1 to 1.5, with a little to no overlap as shown in Figure 7.1c.

After the positions of all fundamental modes are defined, the amplitudes of each beam can be adapted to form the initial wavefront in the superposition. To do that, a sample grid is generated, which might be more dense than the grid of the fundamental modes (The density of the sample grid is chosen in order to get a good compromise between accuracy and computational effort). At each sample point the complex amplitude of the initial wavefront is computed (w_i) and stored in the vector \vec{w} . The Power of each fundamental mode b_i is set in order to make the complex amplitude in the center of the corresponding beam become one. Next, the complex amplitude of each beam at each sample position is computed (u_i) and stored in the matrix \hat{U} . The superposition of all beams should be equal to the initial wavefront at each sample point. This is realized by searching for a suitable power and phase offset for each individual beam. A variation of the power and a constant phase offset can be expressed through a multiplication with a constant complex number. The individual power and phase combinations for each beam are called c_i and are stored in a vector \vec{b} . The idea is to minimize the difference between superposition and initial wavefront. This can be achieved via the least square solution of the over-determined linear equation system:

$$\vec{w} = \hat{U} \vec{b} \quad (7.1)$$

By solving this equation system, one gets the optimal decomposition of the initial wavefront. Multiple methods to efficiently solve this equation are known and available (e.g. QR decomposition). However, in most situations the size of the \vec{w} , \hat{U} and \vec{b} are challenging.

As an example, with 100×100 Gaussian fundamental modes ($10^4 b_i$) we get 500×500 sample points ($2.5 \cdot 10^5 s_i$). This means \vec{w} is a vector with $2.5 \cdot 10^5$ elements, \hat{U} is a matrix with the dimensions $2.5 \cdot 10^5 \times 10^4$ and \vec{b} contains 10^4 elements. Representing each entry (w_i , u_i and c_i) as a complex double (16 Bytes), the memory required to store the given equation system adds up to more than 37 gigabytes. The required memory for a QR decomposition would exceed this even more. In order to reduce the computational effort, all combinations of sample points and beam in \hat{U} are ignored where the distance between beam center and the sample point is larger than four times the spot size of the given beam, such that the remaining elements of \hat{U} can be

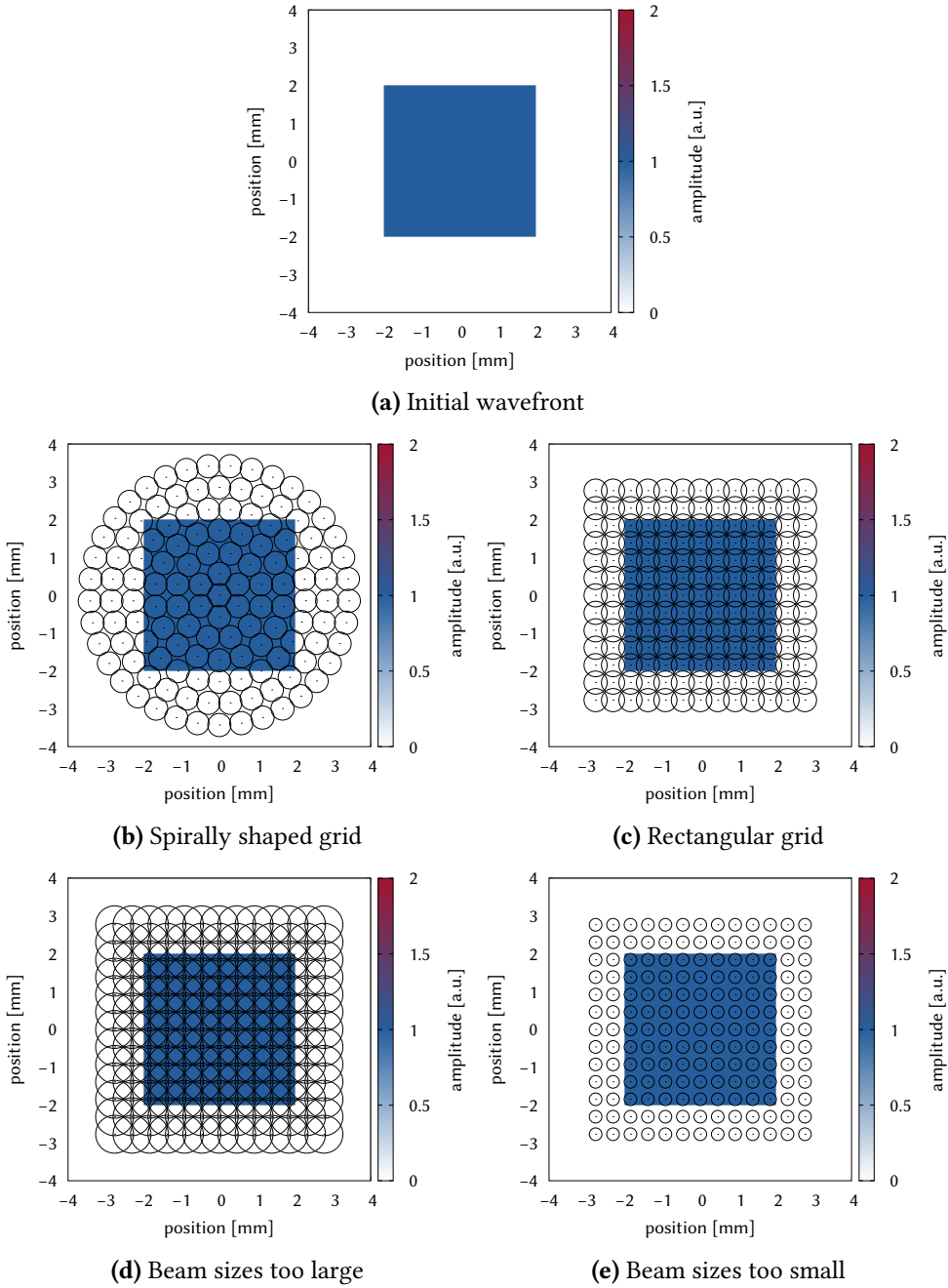


Figure 7.1.: Gaussian beam decomposition, relation between initial wavefront and grid of fundamental Gaussian beams.

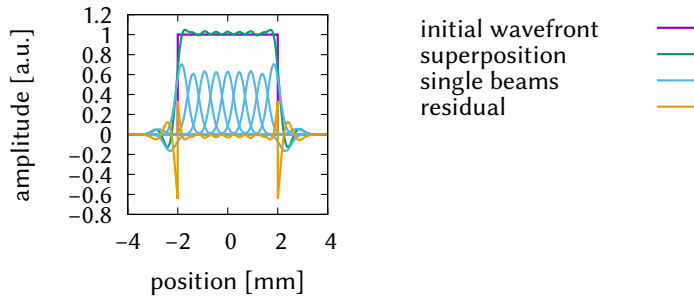


Figure 7.2.: Cross-section showing the initial wavefront together with the Gaussian beam decomposition and the single fundamental modes.

stored in a sparse matrix. Furthermore, the sampling grid is set equal to the Gaussian beam grid which results in a quadratic matrix \hat{U} that allows for efficient solving algorithms. With the memory consumption reduced to a manageable amount and a quadratic matrix \hat{U} , an iterative method [64] is used to find a solution of Equation (7.1).

A cross section of the example decomposition (square wavefront) is shown in Figure 7.2. The purple lines indicate the initial wavefront, the single fundamental modes with optimal power and phase are shown in blue, while the green line shows the superposition of all blue beams. The superposition matched the initial wavefront quite well considering the small number of fundamental beams used in this decomposition. Here, a negative amplitude means a phase offset of π . Due to the simplicity of the initial wave, only phase offsets 0 and π are necessary. Therefore, showing only the amplitude with positive and negative sign is sufficient to represent this decomposition.

A more complex example can be found in Figure 7.3. Here, the starting point is a fundamental Gaussian beam with a waist radius of 0.5 mm (Figure 7.3a). This beam is clipped by a circular aperture of 0.5 mm radius (Figure 7.3b). The resulting wavefront, the clipped Gaussian amplitude profile is the initial wavefront which is decomposed into a set of smaller fundamental Gaussian beams. The superposition of the 10×10 Gaussian beams can be found in Figure 7.3c, the residuum, the difference between decomposition and initial wavefront can be found in Figure 7.3d. The difference is quite large, especially the sharp edges of the aperture cannot be represented well. Furthermore, the rectangular grid of the Gaussian beams can be found in the residuum pattern. To improve the result more beams are needed for the decomposition. Figure 7.3e shows the same decomposition but with 75×75 beams instead of 10×10 . The residuum in Figure 7.3f is much smaller. However, the pattern of the circular aperture can still be observed and also the rectangular pattern of the Gaussian fundamental modes.

This example shows the limitations of the Gaussian beam decomposition. Sharp edges, as the ones of the aperture, can only be represented roughly. The more Gaussian beams are used, the smaller they can be and the sharper structures can be modeled. However, discontinuous forms like apertures can never be modeled perfectly with the use of Gaussian beams. By rising the number of Gaussian beams used in decomposition, the residuum becomes smaller and the pattern moves to higher frequencies, but the residuum will never become zero.

Fortunately, higher frequency pattern will become more and more irrelevant, as the decomposed wavefront propagates. Figure 7.4 shows the decomposed wavefront after propagation of 200 mm. The pattern became smoother and the high frequency disturbances disappeared.

7.3. Comparison of diffraction model techniques in free space

In this section, MEM, FFT and GBDC methods are used to simulate diffraction patterns in optical setups where it is possible to compute the diffraction pattern analytically. Therefore, a qualitative and quantitative comparison between the different methods is possible.

This chapter follows the structure of “Comparison of Mode Expansion Method to Analytical Equations - Truncated Gaussian beam in Fresnel and Fraunhofer regions” from Christoph Mahrtdt [62]. The optical setups and simulations described in this manuscript are repeated with the Gaussian beam decomposition and FFT methods. The algorithms to compute the analytic solutions in the Fresnel and Fraunhofer approximation were kindly provided by Christoph Mahrtdt [62].

In the scenarios shown here, a far field propagation is simulated in order to investigate laser beam propagation in inter-satellite laser links. FFT methods using a fixed window size usually struggle in this scenario as soon the beam size exceeds the FFT window. A compromised window size was chosen here to cover the near field. The far-field propagation is performed with a scaling window.

In both extreme regions (close to the aperture and far away) the limitations of the simple FFT method can be observed. Close to the aperture, the field shows the effects of under sampling due to the large grid width and in the far distance, additional diffraction due to the limited windows size can be observed.

7.3.1. Large Gaussian behind a circular aperture

In this scenario a large fundamental Gaussian beam with 10 mm waist radius is clipped at its waist position by an aperture with 1 mm diameter. The result wave front is decomposed using FFT with a grid 14 mm times 14 mm consisting of $2^{13} \times 2^{13}$ samples. This window is kept constant until the propagation exceeds 1000 mm. Af-

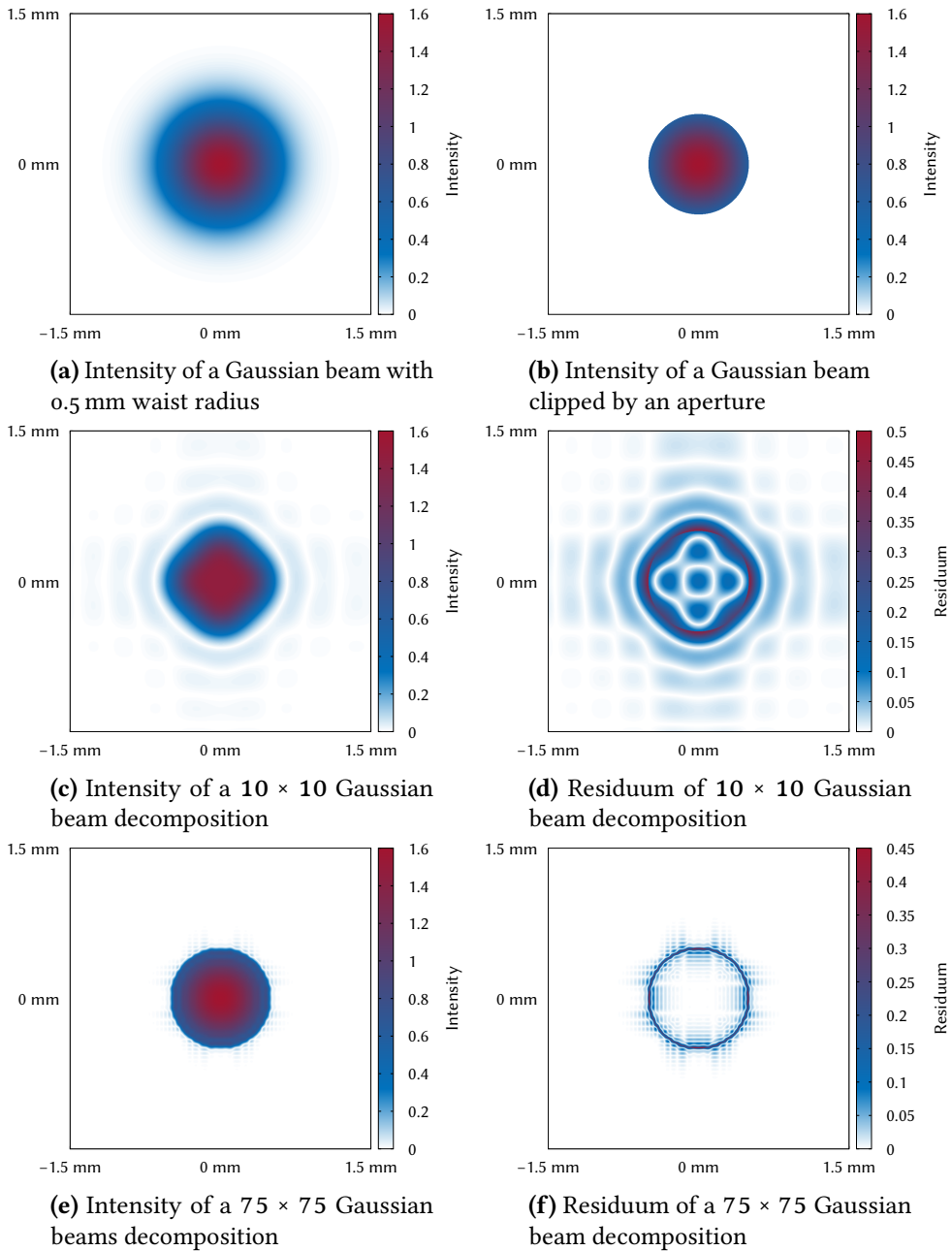


Figure 7.3.: Demonstration of the Gaussian beam decomposition. It is shown that with a higher number of Gaussian beams in the decomposition, the quality of the model rises.

are around 10^{-3} and the GBDC 1.5 orders of magnitude better around $5 * 10^{-5}$. The FFT shows first artifacts from the limited window size. The wavefront is cut off at the edges producing additional diffraction. With the fixed window size the FFT method is not able to accurately compute the wavefront at this distance.

Figure 7.6 show amplitude cross section and residuum for large distances compared to analytic results in the Fraunhofer region. Here, the FFT scales its window while propagating, which is a valid approximation in the far-field.

For a propagation distance of 2350 mm, the performance of the three methods is in the center region of the wavefront equal. In the outer parts the FFT methods show additional patters due to the still limited window size (the chosen window size is 280 mm). For 23500 mm distance the gets better compared to the results before, however the performance of the GBDC is significantly better (nearly two orders of magnitude). The FFT method shows even more diffraction in the outer areas of the beam. The effective window size of 1400 mm is only able to model the inner beam area without significant errors.

The results shown here were obtained with comparable computational cost. With more rescaling, a higher resolution, and more computational power the results can be improved. However, in order to compare the different methods, the their parameters were chosen in order to match the computation time between the different methods.

7.3.2. Small Gaussian behind a circular aperture out of waist

In the first scenario a top hat Gaussian beam with nearly flat amplitude and phase was simulated. In this second scenario a 1 mm radius Gaussian fundamental mode is clipped by a 0.5 mm radius aperture that is located in front of the waist at a distance equal to the Raleigh length of the beam. Therefore, neither the amplitude nor the phase in the aperture is homogeneous.

Figure 7.7 shows the amplitude and phase of the three simulation methods as well as the analytic solution next to the difference between them. At 5 mm distance, the expected Gaussian amplitude and the curved phase front is clearly modeled by all methods FFT, MEM and GBDC. Besides that, the overall behavior of all simulation methods is similar to the first scenario. Again, the highly oscillating component in the analytic solution in the near field behind the aperture (5 mm and 10 mm) can only be simulated correctly by the GBDC. The larger the distance between aperture and observation plane, the better the simulated interference patterns get. The FFT reaches its sweet-spot around 50 mm matching the GBDC performance. However, in all other distances the GBDC is much better than FFT and MEM.

The far field (Fraunhofer region) is shown in Figure 7.8. Here, the similar results as for the first scenario can be observed. MEM,FFT and GBDC show the same quality at 2350 mm. At 23500 mm the MEM is slightly better than the GBDC while the FFT in the center region shows similar performance. In the outer regions artifacts from the limited window can be observed.

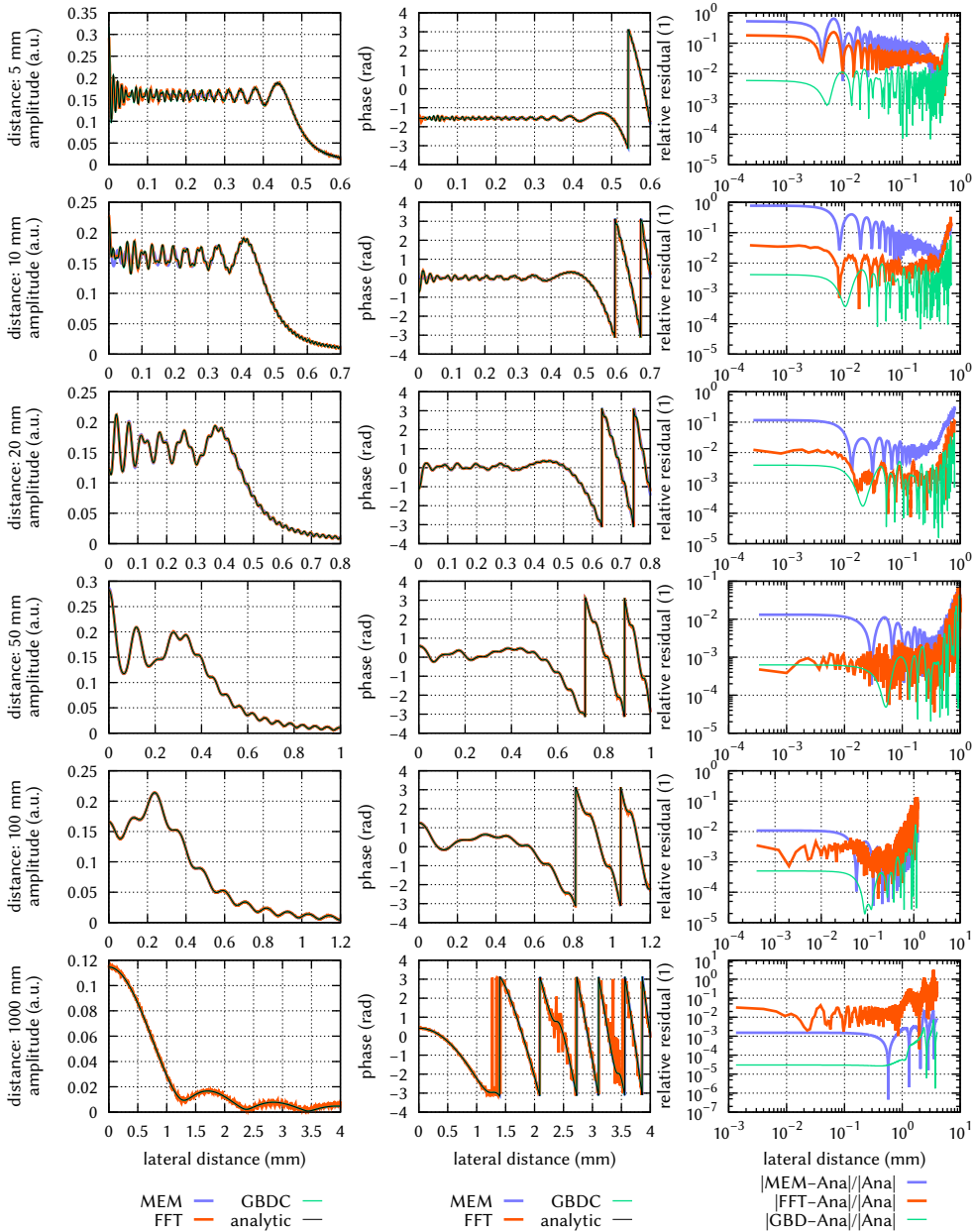


Figure 7.5.: Comparison between MEM, FFT, GBDC and analytical solutions of diffraction propagation. A Gaussian beam with 10 mm radius waist is clipped at a 1 mm circular aperture placed directly in the Gaussian beam waist. Amplitude- (left) and phase-cross-section (middle) is shown for the three different simulation methods and the Fresnel solution. On the right the residuum shows the difference between the simulation methods and the analytical approach. The results for different longitudinal distances to the circular aperture are shown.

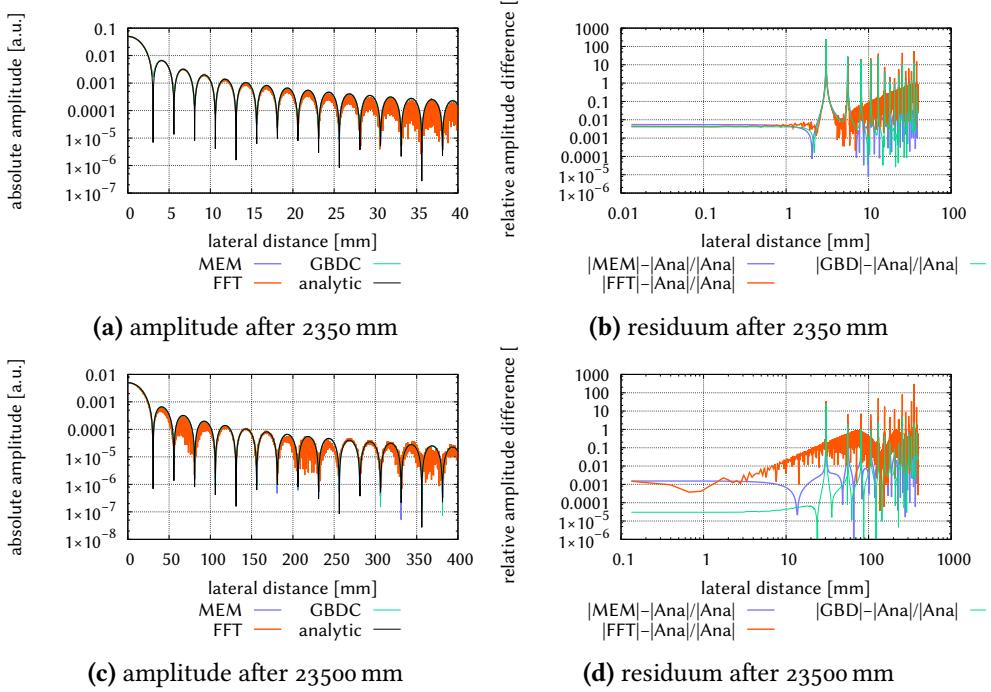


Figure 7.6.: Comparison between MEM, FFT, GBDC and analytical solutions of diffraction propagation. A Gaussian beam with 10 mm radius waists is clipped at a 1 mm circular aperture placed directly in the Gaussian beam waist. An amplitude-cross-section (left) is shown for the three different simulation methods and the Fraunhofer solution. On the right the residuum shows the difference between the simulation methods and the analytical approach. The results for different longitudinal distances to the circular aperture are shown.

7.3.3. Summary of the free space propagation comparison

In the two example scenarios, the highly oscillating component of the diffraction pattern, which was observed in the analytic solution could be simulated best by the GBDC. The FFT method was not capable of showing this fine structures as good as the GBDC due to the large window size, which was necessary to simulate the large wavefronts after propagation up to 1000 mm. The MEM was not able to show the fine pattern due to the limitation in the mode order. After further propagation, the highly oscillating pattern disappears and all methods show better performance. Most of the time the GBDC is significantly better than the MEM, especially in the near-field the MEM is not able to show similar results.

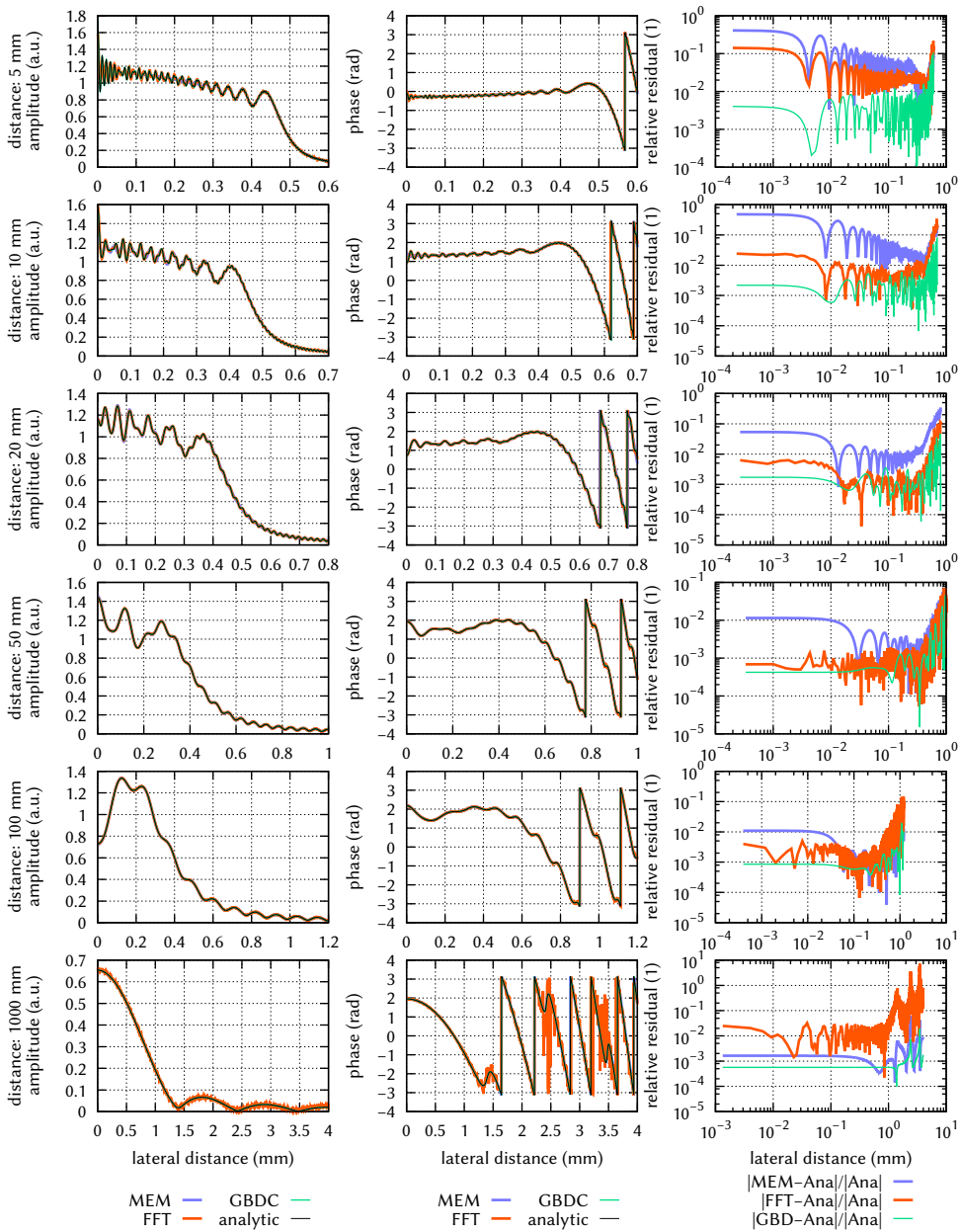


Figure 7.7.: Comparison between MEM, FFT, GBDC and analytical solutions of diffraction propagation. A Gaussian beam with 1 mm radius waist is clipped at a 1 mm diameter circular aperture placed in front of the waist in a distance equal to the Rayleigh length. An amplitude (left) and phase (middle) cross-section is shown for the three different simulation methods and the Fresnel solution. On the right the residuum shows the difference between the simulation methods and the analytical approach. The results for different longitudinal distances to the circular aperture are shown.

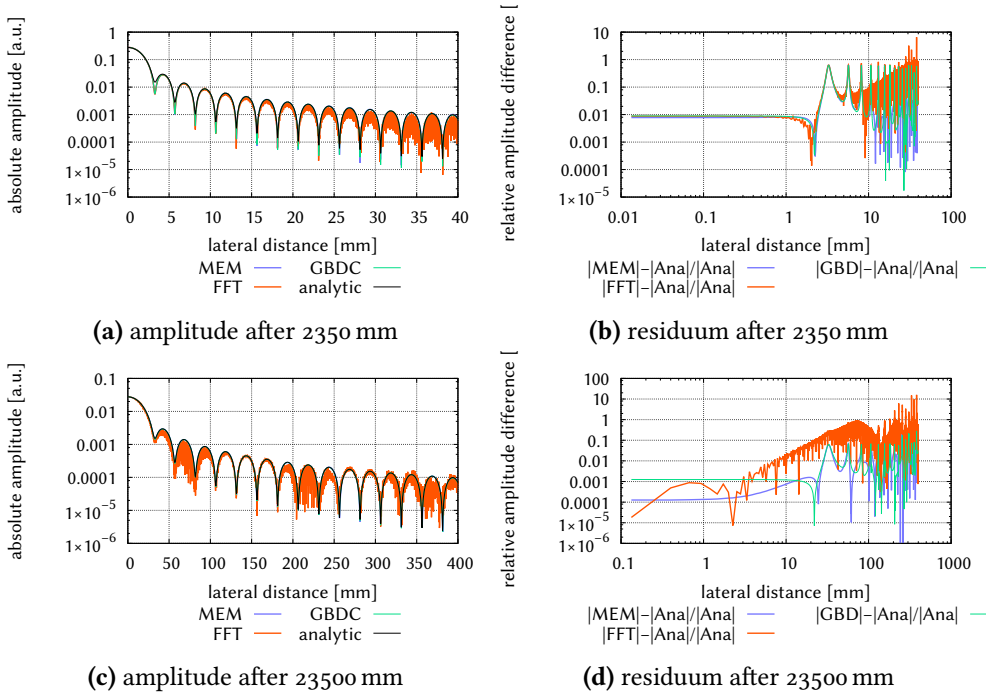


Figure 7.8.: Comparison between MEM, FFT, GBDC and analytical solutions of diffraction propagation. A Gaussian beam with 1 mm radius waist is clipped at a 1 mm diameter circular aperture placed in front of the waist in a distance equal to the Rayleigh length. An amplitude (left) cross-section is shown for the three different simulation methods and the Fraunhofer solution. On the right the residuum shows the difference between the simulation methods and the analytical approach. The results for different longitudinal distances to the circular aperture are shown.

In the far-field after 2350 mm all methods show the same performance. With the scaled window for the FFT the inner area of the beam can be modeled with all methods in the same quality. Further propagation to 23500 mm leads to problems with the FFT, the outer areas suffer from the limited window. In the first scenario the GBDC was slightly better than the MEM in this region. However, in the second scenario the MEM was slightly better. Overall both, MEM and GBDC show great performance in the far-field.

The MEM is a good method to simulate the far-field of a diffracted wavefront. The quality of the decomposition increases with the propagated distance. The quality in the near-field close behind the aperture is limited due to the mode order. Here, a maximal order of 120 was chosen. Increasing this number would only help if the entire computation would use higher numerical precision, which would increase the computational effort tremendously. Therefore, it is practically impossible to simulate the high frequency diffraction pattern close behind an aperture using the MEM.

The quality of the FFT methods in this scenarios is limited by the corresponding window size. In the near-field the window size is a compromise between the different distances. In the two extrema, close behind the aperture the high frequency diffraction pattern can be emulated with reasonable precision and in a distance of 1000 mm only small artifacts from the window size are visible. Only in the sweet-spot around 50 mm the quality of the decomposition is very good. The far-field can only be simulated with a scaling window size. However, only the inner area of the wavefront can be reconstructed accurately. The outer areas suffer from artifacts generated by the limited window. With additional care and adaption of the different methods, the performance of the FFT methods could be improved in all areas, but the aim of this section is a comparison with respect to the GBDC. Therefore, a simple approach and an FFT method that is applicable to most scenarios was chosen.

The GBDC showed in a scenarios the best performance (or comparable). The high frequency diffraction pattern was clearly visible in the decomposition and the difference between measurement and analytical solution was very small, less than 10^{-2} in all scenarios. The window size in the GBDC is only relevant in the decomposition. The possible propagation distance is not affected by the window size, in contrast to the FFT. The far-field quality of the GBDC is as good as the one from the MEM. Overall, the GBDC shows by far the best performance in this comparison.

Summary

Tilt-to-length (TTL) coupling is the unintended cross correlation between beam jitter and the path length readout. It is a major entry in the noise budget of space based interferometers like in LISA, GRACE-FO or future geodesy missions that use laser interferometers. Fundamental understanding and modeling of this effect is the essential precondition to find solutions which suppress TTL coupling in order to reach the required performance. In order to do so, it was shown that imaging systems can suppress TTL coupling below the requirement of $\pm 25 \mu\text{m}/\text{rad}$ in a distinguished setup which is representative for LISA. This performance was shown for two different imaging systems in two different scenarios. The first imaging system (LOB4C) is a classical pupil plane imaging system with four lenses. The second one (LOB2D) is a two-lens imaging system which was obtained from numerical optimization and does not feature all classical properties of a pupil plane imaging system, since it does not provide a collimated output beam. The two scenarios were on the one hand a test mass interferometer setup with two Gaussian beams and on the other hand a science interferometer setup with a stable Gaussian and a tilting flat-top beam.

For both imaging systems a tolerance analysis was performed. The most critical parameter of the LOB2D imaging system is the lateral alignment of the first lens with a resulting TTL coupling of $-450 \mu\text{m}/\text{rad}$ for an offset of approximately $60 \mu\text{m}$, while the most critical parameters of the LOB4C system are the alignment of lens one and two with $\pm 700 \mu\text{m}/\text{rad}$ for an offset of approximately $60 \mu\text{m}$, each. Therefore, the allowed misalignment in the LOB2D system is approximately $3.3 \mu\text{m}$ while in the LOB4C system only around $2.1 \mu\text{m}$ are allowed to reach the requirement. Overall, the alignment of the LOB2D system was found to be less critical.

Besides the higher robustness against misalignment it was found that the residual TTL coupling behind the LOB2D system strongly depends on the beam parameters. The LOB2D system produces a non collimated beam with a small waist between second lens and the photo detector. This leads to a strong coupling between the beam parameters in front of the imaging system and the longitudinal curvature change of the wavefronts around the detector. Thus, additional TTL coupling contributions are present which cannot be reduced by adapting the longitudinal detector position. To overcome this behavior a new guideline for the design process of imaging systems

was developed. In addition to the properties of the LOB2D system the waist size behind the second lens is required to be of similar size as the spot on the detector. This ensures a nearly collimated beam that features a much more stable wavefront curvature. With this property an exemplary new two-lens imaging system (GIS2C) and a three-lens imaging system (GIS3C) were designed and tolerance analyses were simulated. The outcome promises similar TTL coupling reduction as the old imaging systems and robustness against beam parameter variations.

All measurements regarding imaging systems were additionally simulated with the numerical tool IfoCAD. IfoCAD can be used to trace Gaussian beams through interferometric setups and simulate the detection of interference patterns as well as the phase readout scheme as implemented in a phase meter. In all scenarios the simulated results matched the measured data, which on the one hand indicates that the measured results are not compromised by additional effects, not covered by the simulation, and on the other hand promises to hopefully reach comparable accuracies in simulations concerning experimental setups which are not yet built.

In the last part of this thesis diffraction simulations were investigated. Therefore, a method called Gaussian beam decomposition (GBDC) was implemented in IfoCAD. In the GBDC an initial wavefront is decomposed into a superposition of spatially divided fundamental Gaussian beams. By propagating all fundamental Gaussian beams and computing the superposition of them at an arbitrary point, the diffracted propagation pattern of the initial wavefront can be simulated. GBDC was compared with other diffraction simulation methods, namely the mode-expansion-method (MEM) and angular spectrum methods (Fourier optics – FFT). The FFT methods provide accurate results with small computational effort only in certain situations. In general the outcome strongly depends on the used algorithms, which lack accuracy especially in the presence of tilted or strongly curved surfaces. The MEM yields good results, however the computational effort is larger than for the other methods and, in practice, the accuracy is limited due to the enhanced computational accuracy required for mode orders higher than approximately 120. Overall, the outcome shows that GBDC provides the most accurate results with manageable computational effort.

Appendix

A

Vanishing tilt-to-length coupling for a singular case in two-beam laser interferometers with Gaussian beams

The content of this section was formerly published in [6, P5]. The special behavior of the system shown here was described by Gerhard Heinzel.

In this section a special situation is shown and explained in which multiple TTL coupling contributions (compare to Section 3) appear and happen to cancel each other. In the end, a system without TTL coupling remains. In Section 3.1.1 the analytic expression of the geometric lever arm TTL coupling was computed (cf. Equation (3.1))

$$\Delta s_{\text{lever}} \approx \frac{\alpha^2}{2} d_{\text{pivot}} + O(\alpha^4). \quad (\text{A.1})$$

One would expect that this geometric path length change always appears in the measured s_{LPS} . This section shows that this is indeed true for plane waves, but not for Gaussian beams.

A.1. Plane waves

In this section, the relation between the geometrical path length change and the s_{LPS} is discussed for the case of two plane waves. The electric field for an infinite plane wave is given by

$$E_{\text{plane}}(x, y, z) = A \exp(-i\omega t - ikz + i\Phi), \quad (\text{A.2})$$

if the plane wave propagates in the z direction, where $k = 2\pi/\lambda$ is the wave number, ω the frequency, A is the amplitude and Φ is the initial phase. This expression is used for the reference beam $E_{\text{ref}}(x, y, z) = E_{\text{plane}}(x, y, z)$, and a rotated version is used for the tilted measurement beam. We denote the coordinate system of E_{ref} by \vec{r}_{ref} , the location of the pivot by \vec{p}_{pivot} , the rotation matrix for a rotation around the y -axis is \hat{m}_{rot} , and the resulting coordinate system of the second electric field E_{meas} is called \vec{r}_{meas} :

$$\vec{r}_{\text{ref}} = \begin{pmatrix} x \\ y \\ z \end{pmatrix}, \quad \vec{p}_{\text{pivot}} = \begin{pmatrix} 0 \\ 0 \\ -d_{\text{pivot}} \end{pmatrix},$$

$$\hat{m}_{\text{rot}} = \begin{pmatrix} \cos \alpha & 0 & -\sin \alpha \\ 0 & 1 & 0 \\ \sin \alpha & 0 & \cos \alpha \end{pmatrix} \quad (\text{A.3})$$

$$\vec{r}_{\text{meas}} = \hat{m}_{\text{rot}}^{-1} \cdot (\vec{r}_{\text{ref}} - \vec{p}_{\text{pivot}}) + \vec{p}_{\text{pivot}}. \quad (\text{A.4})$$

A more detailed explanation of this transformation can be found in [33]. The tilted electric field is now defined similar to E_{ref} , but with new coordinates:

$$E_{\text{meas}}(x, y, z) = E_{\text{plane}}(\vec{r}_{\text{meas}}(x, y, z)). \quad (\text{A.5})$$

Since the z position of the photo diode plane is arbitrary, it can be set to zero. The path length difference between the two beams is encoded in the intensity of the superposition between the two beams and also in the complex argument, as shown in Section 2.2.2. We prefer to extract the phase from the complex overlap term instead of from the power variation as this reduces the computational effort, which leads to the following equation

$$\arg \left(\int_{\text{pd}} E_{\text{meas}} E_{\text{ref}}^* \text{d}r^2 \right) = k s_{\text{LPS}}. \quad (\text{A.6})$$

Since the s_{LPS} does not change in time and we are only interested in the variation of the phase difference between the two beams, we can set $t = 0$ and the initial total phase $\Phi = 0$. An integration of the overlap term over a square detector at position $z = 0$ (side length $2r_{\text{pd}}$) gives the overlap integral for plane waves O_{ovi}^P , which corresponds to the complex amplitude in [P2]

$$O_{\text{ovi}}^P = A_{\text{ref}} A_{\text{meas}} \frac{4r_{\text{pd}} \sin(kd_{\text{pivot}} \sin \alpha)}{k \sin \alpha} \cdot \left\{ \cos [kd_{\text{pivot}} (-1 + \cos \alpha)] - i \sin(-kd_{\text{pivot}} + kd_{\text{pivot}} \cos \alpha) \right\}. \quad (\text{A.7})$$

The complex phase of this integral describes the phase difference between the two plane waves. This phase difference can be translated to the s_{LPS} using the wave number k :

$$s_{\text{LPS}} = \frac{\arg(O_{\text{ovi}}^P)}{k} \approx \frac{\alpha^2}{2} d_{\text{pivot}} + O(\alpha^4) \approx \Delta s_{\text{lever}}. \quad (\text{A.8})$$

Thus, two plane waves on a detector show approximately the geometrical coupling Δs_{lever} , confirming the intuitive results from Equation (A.1).

A.2. Gaussian beams

We start with the special case of two identical fundamental Gaussian beams and an infinite detector (i.e., both beams are completely detected without any clipping). A full description of a Gaussian mode can be found in Section 2.3.1. Here, a simplified version is used, the amplitude of the electric field is irrelevant for the path length signal and is therefore set to unity. The Gouy phase is also ignored, since its offset is negligible in the case of equal beams. The electric field shown in Equation (2.33) can then be simplified

$$E_{\text{Gauss}}(x, y, z) = \exp\left(-i\omega t - ik\frac{x^2 + y^2}{2q} - ik(z - z_0)\right). \quad (\text{A.9})$$

The z_0 is a constant phase shift, therefore the term $-ik(z - z_0)$ can be set to $-ikz$ since. The expression in Equation (A.9) is used for the reference beam $E_{\text{ref}}(x, y, z)$, and a rotated version is used for the tilted measurement beam. The coordinate system of the tilted beam is computed analogously to Equation (A.4). The real part of the q parameter changes only by propagation in beam direction. For the reference beam, the propagation corresponds to an increase in z . For the measurement beam, the change in direction of propagation corresponds to an increase in z but also a change of x (Equation (A.4)). This x dependence makes the 2D integration in the detector plane much harder. For convenience, z is set to zero, which makes the real part of the q parameter $z - z_0$ become the constant value $-z_0$. The changes in z due to the coordinate transformation over the detector surface are very small and cause a negligible change (therefore the error produced by a z -independent q parameter becomes also very small and is neglected). Furthermore, an infinite detector is assumed, which in practice means any single element photo diode (SEPD) that is larger than three times the beam size. The integral of the overlap term over an infinite detector at position $z = 0$ yields

$$O_{\text{ovi}}^G = \frac{2\pi(z_0^2 + z_r^2)}{k\sqrt{z_r[-iz_0 + 3z_r + (z_r + iz_0)\cos 2\alpha]}} \\ * \exp\left[\frac{2ik\xi\sin(\alpha/2)^2}{-z_0 - 3iz_r + (z_0 - iz_r)\cos(2\alpha)}\right]$$

with:

$$\xi = (z_0 + d_{\text{pivot}})^2 + 2id_{\text{pivot}}z_r + z_r^2 + [(z_0 + d_{\text{pivot}})^2 - 2id_{\text{pivot}}z_r + z_r^2] \cos \alpha.$$

This leads to the resulting path length change:

$$s_{\text{LPS}} = \frac{\arg(O_{\text{ovi}}^G)}{k} \approx \frac{\alpha^2 z_0}{4z_r k} + O(\alpha^4) \approx 0. \quad (\text{A.10})$$

This result matches the expressions in [33] for the special case of equal beams. For two plane waves the resulting coupling (Equation (A.8)) has the same form (proportional to α^2) with a proportionality factor given by $d_{\text{pivot}}/2$, which usually is a macroscopic quantity of magnitude between centimeters and meters. For two Gaussian beams, this factor becomes $z_0/(4z_r k)$, which is of the same order of magnitude as the wavelength, i.e., nanometers to micrometers for visible or infrared light. For typical parameters and beam angles, ≈ 1 mrad, the resulting length change is significantly below pico meter scale and thus below the sensitivity of most interferometers.

All results in this section were confirmed by numerical simulations computed with IfoCAD, compare to Section 2.3. Example results for the actual setup of two Gaussian beams on a large detector are shown in Figure A.1 for a wavelength of 1064 nm, waist radii of 1 mm, 30 mm photo diode diameter and the pivot and waists located 100 mm in front of the photo diode.

In the remaining part of this section, we will show that the reason for the vanishing coupling for two Gaussian beams is an additional coupling effect that is caused by an angle-dependent offset. A beam tilt generates, besides the geometric change of the path length, two other effects. The first one is a relative angle between the two beams on the photo diode and the other is an offset between them, as described in Section 3.2.1. Since infinite plane waves have no uniquely defined center, any shift orthogonal to their direction of propagation maps the wave upon itself and therefore causes no effect. This is different for Gaussian beams. Due to the Gaussian intensity profile, there is a uniquely defined center. To investigate the effect of the generated offset in the case of Gaussian beams, the initial setup (Figure 3.1) is changed to create a situation with an angle-invariant offset and no lever arm: we place the pivot directly on the detector. Furthermore, the measurement beam is placed with a transversal offset and tilted around its center on the SEPD (Figure 3.6). According

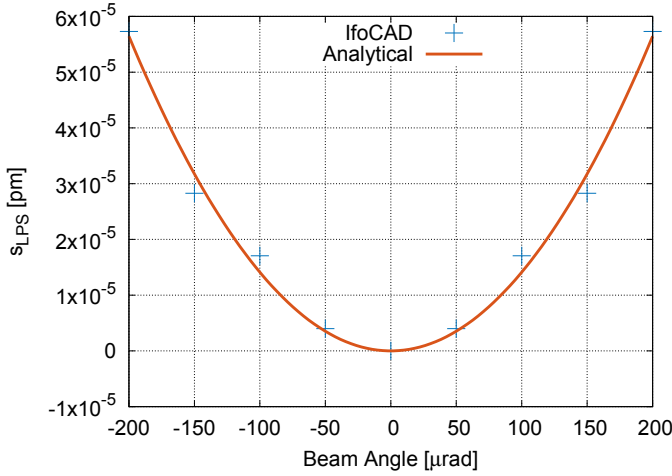


Figure A.1.: Numerically/Analytically computed s_{LPS} (second-order approximation) for Gaussian beams. The differences are due to numerical errors.

to Equation (A.1) there is no coupling for plane waves ($d_{pivot} = 0$), and only the effect of the static offset remains. For the analytical computation, we assume that the initial transversal offset changes the stationary reference beam $E_{ref}(x + d_{offset}, y, z)$ instead of the measurement beam, since it is unimportant which beam is moved, and the transformation of the measurement beam would be more complicated with an additional offset. The distance between pivot and SEPD is set to zero ($d_{pivot} = 0$) and the measurement beam E_{meas} is rotated around zero [see Equation (A.4)]. The expressions for the beams are the same as in Equation (A.9). The resulting overlap integral O_{ovi}^{GO} for Gaussian beams with initial offset becomes

$$O_{ovi}^{GO} = \frac{\exp\left(-\frac{k\{-id_{offset}^2 \cos^2 \alpha + (z_r - iz_0) \sin \alpha [2d_{offset} + (z_0 - iz_r) \sin \alpha]\}}{-z_0 - 3iz_r + (z_0 - iz_r) \cos(2\alpha)}\right) 2\pi (z_0^2 + z_r^2)}{k\sqrt{z_r[-iz_0 + 3z_r + (iz_0 + z_r) \cos(2\alpha)]}}. \quad (A.11)$$

This leads to the path length change,

$$s_{LPS} \approx \frac{-\alpha d_{offset}}{2} + O(\alpha^2). \quad (A.12)$$

This coupling is a result of a static offset. To compute the effect of the dynamic (angle depending) offset in the initial case (as shown in Figure 3.1), the offset itself (d_{offset}) has to be replaced by its geometric expression,

$$d_{offset} = \tan(\alpha) d_{pivot} \approx \alpha d_{pivot}. \quad (A.13)$$

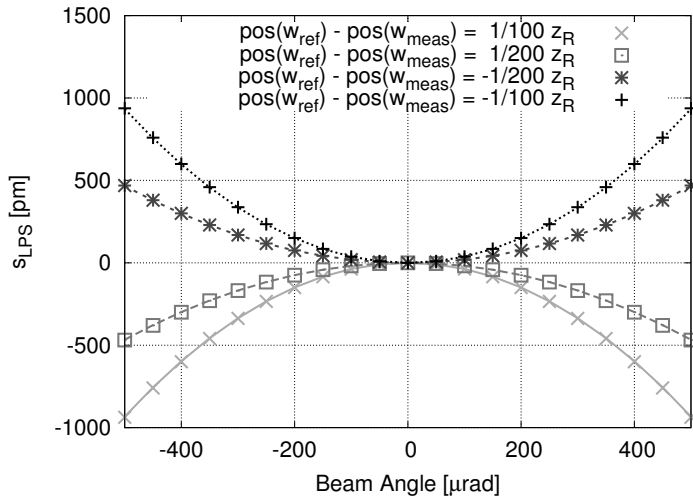


Figure A.2.: Numerically and analytically [33] computed s_{LPS} for two Gaussian beams on an SEPD with differences in the waist position. The numeric values are marked with symbols, while the analytical expressions are lines. (The simulated setup is described in Section A.2.)

By combining Equation (A.12) and (A.13) the coupling caused by the offset in the initial setup becomes

$$s_{\text{LPS}} \approx \frac{-\alpha d_{\text{offset}}}{2} = \frac{-\alpha^2}{2} d_{\text{pivot}}. \quad (\text{A.14})$$

Therefore, the negligible tilt-to- s_{LPS} coupling of Equation (A.10), is the result of two effects. The first one is an obvious geometric effect [Equation (A.8)], which is the geometrical distance-change between the pivot (beam origin) and the photo diode. The second one results from the offset between the two beams, which is also caused by the beam tilt. The two effects generate the same amount of coupling, but with different sign. In the special case of two identical Gaussian beams on an infinite single-element diode, the resulting coupling between beam tilt and measured path length becomes negligible.

For unequal beam parameters Equation (34) in [33] shows that additional coupling terms appear that disturb the balance between the two effects and lead to significant residual coupling. As an example, Figure A.2 shows numerical simulations and analytical expressions of the coupling for the same situation as in Sec. A.2 but with slightly different waist positions for the measurement and reference beams. Similarly, incomplete detection, non-fundamental Gaussian beams and misalignment cause non-negligible tilt-to-length coupling, as we have observed in numerical simulations and more complex analytic computations.

Therefore, the effect described in this section appears only under very specific circumstances. However, it can be used in various situations, for example to stabilize an interferometer and investigate additional coupling effects. In Appendix B an experiment that make use of this effect to measure the tilt-to-length coupling caused by a quadrant photo diode is shown.

Another well-known way to explain this effect for very small tilt angles is to express the tilt as an excitation of the Hermite-Gaussian (HG) 0_1 mode as explained in [65]. Due to the orthogonality of the HG modes this excitation will not change the path length readout when the entire interference pattern is detected. However, this is an approximation that is valid only for very small angles (much smaller than the far field divergence [65]). The angles in the present examples exceed this limitation such that the field cannot be suitably expressed by an excitation of only the HG 0_1 mode.

When comparing the tilt-to-length coupling for plane waves Equation (A.8) to that of Gaussian beams Equation (A.10) or Equation (A.12), it should be pointed out that Equation (A.8) is not a special case of Equation (A.10) or Equation (A.12). Due to the assumed complete detection (infinite integration limits) the Gaussian beams cannot be approximated by a plane wave.

B

Tilt-to-length coupling suppression by a two-lens imaging system

The content of this chapter covers the results from my master thesis [6] and was afterwards published by myself in [P1].

The relation between TTL coupling and the use of imaging systems was only present in simulations so far. It could be shown that the amount of TTL coupling can be suppressed. But only under the assumption of a well aligned system and well defined beams. In a hardware realization both is not true, or at least not guaranteed. In an build up interferometer small misalignments are inevitable and the achievable TTL coupling is different from the theoretical possible. One way to get information about the expectable performance are tolerance analysis and investigations on the build quality of interferometers. However, to be absolutely sure that a technology is capable to do what it is designed for, one needs to test it in hardware. In this chapter the first successful TTL coupling measurement with an imaging system is shown. Former experiments could already demonstrate, that the TTL coupling can be reduced by using an imaging system, but due to the presence of additional noise and TTL coupling sources, a quantitative match with simulations was not possible. [TD2] The experiment here is based on the LISA TM interferometer. The imaging system design fits to the original LISA requirements [TD6]. However, the results should be representable for an arbitrary TM interferometer.

As explained in former chapters, to suppress coupling between tilt angle and measurement of the longitudinal position, the beam walk on the photo diode, originating from the tilt angle, must be suppressed. In this experiment a two-lens imaging system called Doo3 [16] was tested (Figure B.1). It was designed without the need to provide a collimated beam at the photo diode (similar to the imaging system presented in Section 4.3.10). It features suppression of the beam walk on the photo diode and a magnification factor of 3:1. This magnification is required because in the LISA TM interferometer the nominal waist radius is 1 mm while the QPD radius is only 0.5 mm. By compressing the beam size with an imaging system, more light power can be used

Table B.1.: Specifications of the Doo3 imaging system. The point of rotation is assumed to be on axis at longitudinal position 0.0 mm. The QPD slit width indicates the width of the insensitive area between the QPD segments. The magnification is 3:1.

	Unit	Lens 1	Lens 2	QPD
Position	mm	425.00	472.89	525.24
Nominal Focal Length	mm	60.00	-50.00	
Primary Curvature	$\frac{1}{m}$	31.39	-19.80	
Secondary Curvature	$\frac{1}{m}$	0.00	-19.80	
Center Thickness	mm	4.00	1.50	
Substrate Radius	mm	11.20	11.20	
Refractive Index	1	1.51	1.45	
QPD Diameter	mm			1.00
QPD Slit Width	μm			20.00

in detection and stray light originating from the QPD borders can be suppressed [16]. The imaging system is defined as the positions and parameters of the lenses as well as the position and the properties of the photo diode. A list of these parameters can be found in Table B.1.

With the help of numerical simulations (IfoCAD [P₂, P₄]) it could be shown that this kind of imaging system should be able to reduce the TTL coupling significantly. The simulated TTL coupling with and without the Doo3 imaging system for a typical LISA-like TM-interferometer and a perfectly aligned system is shown in Figure B.2. The left-hand graph shows the path length change plotted over the beam angle in the scenario without imaging system, a tilt of one laser beam by a few hundred micro radian results in an unwanted longitudinal path length change in the readout of a few tens of nanometers. In contrast, the graph on the right (Figure B.2) shows the TTL coupling in the same interferometer with an additional imaging system, the amount of path length change is reduced below 0.05 nm.

B.1. Mechanisms of tilt-to-length coupling

The Doo3-performance simulations in the previous section assumed a perfectly aligned setup under ideal conditions. However, this does not apply to any experimental realization. Small misalignments like lateral or longitudinal positioning offsets of the lenses or variations of the focal lengths are unavoidable. Any of those imperfections are a possible source of additional TTL coupling. These need to be controlled carefully in the experiment in order to allow a comparison to the simulations. In the following, the different relevant TTL coupling sources are discussed.

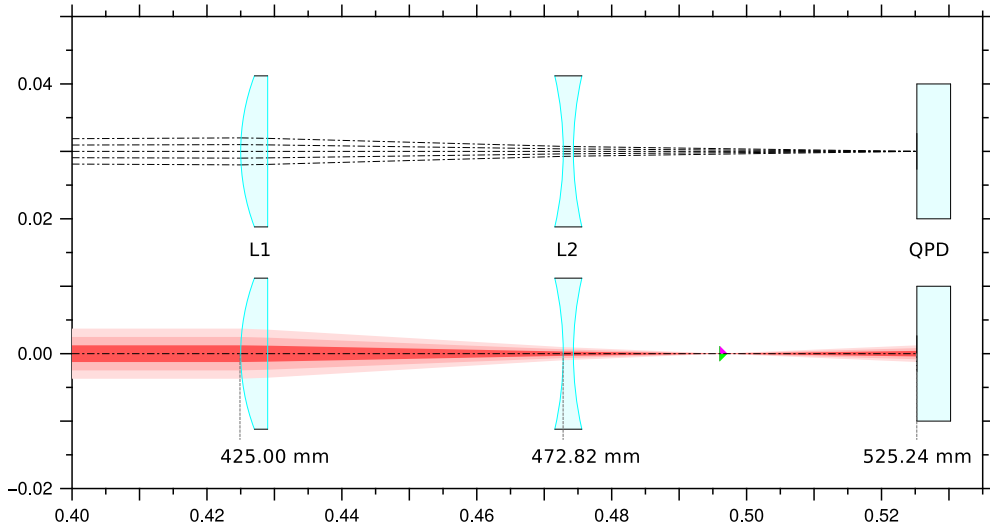


Figure B.1.: Doo3 imaging system design. The longitudinal positions of the centers of the front surfaces of the lenses and the QPD are marked, while the point of rotation (TM) is located at position 0 mm. The first plot shows the propagation of different base rays, which start under different angles at the point of rotation and end up in the center of the QPD (demonstrating zero beam walk). The second plot is showing the propagation of a Gaussian beam. The triangle indicates the waist position. Furthermore, the magnification factor can be seen. The large 1 mm waist Gaussian beam is compressed and becomes much smaller on the QPD.

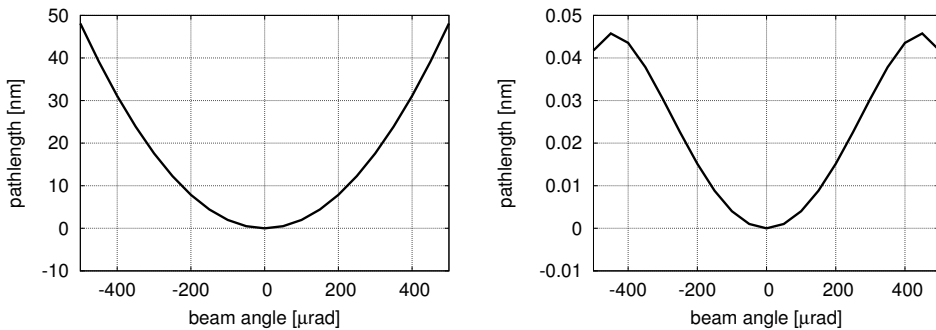


Figure B.2.: Simulated TTL coupling in the LISA TM interferometer without (left) and with (right) the Doo3 imaging system and a perfectly aligned setup. With the help of the imaging system Doo3 the TTL coupling can be reduced significantly.

B.1.1. Parasitic longitudinal movement of the tilt actuator

To realize a tilting beam in an experiment, usually a tilt-actuator is used. The main challenge is that the mirror mounted to the actuator often does not tilt around a fixed pivot in the center of the mirror's surface. The real pivot is located with an offset and might slightly move during one tilt-cycle. With a smart driver that controls fine adjusted linear combinations of three piezos, for example, it is possible to reduce this noise source, but since the longitudinal movement couples directly in the measurement, it has to be reduced significantly below the interferometer sensitivity. To remove the TTL coupling caused by the longitudinal movement of the tilt-actuator in our setup, we measure the interference pattern with a large single element photo diode (SEPD). As shown in Chapter A, a large SEPD is not affected by TTL coupling in the case of equal beam shapes and no lateral offset between the beams and the pivot.

B.1.2. Wavefront curvature mismatch

We use a homodyne equal arm-length Mach-Zehnder interferometer in order to match the beam parameters perfectly, to allow the SEPD to sense solely the longitudinal motion of the actuator. Since unequal beam parameter generate additional TTL coupling as explained in Section 3.2.2.

B.1.3. Higher order Gaussian modes

Higher order Gaussian modes of odd order generate in general an asymmetric amplitude profile (compare to Section. 3.2.4), which disturbs the phase readout, since the phases at the different detector positions are weighted with the product of the electric fields amplitudes. We get rid of higher order modes with the use of an optical resonator.

B.2. Experimental setup

A sketch of a TM interferometer is shown in Figure B.3. The red measurement beam is reflected towards the TMs surface and afterwards interfered with the blue reference beam and imaged to the detector. The key components are numbered to give an orientation for the schematic of the experimental setup, which is shown in Figure B.4. To ensure that both beams in the experiment are equal and have the same wavefront curvature at the detector (to suppress unequal beams, compare to Sec. B.1.2), a homodyne equal arm-length Mach-Zehnder interferometer with only one light source is used. The path length is measured with multiple different detectors which will be described subsequently.

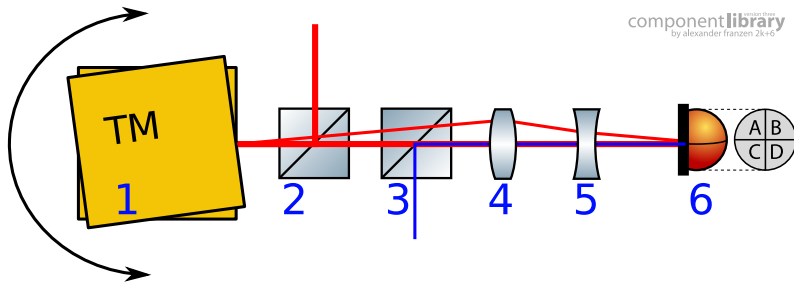


Figure B.3.: Working principle of a test mass interferometer with imaging system. The measurement beam (red) is reflected at the TM (yellow) and interfered with the reference beam (blue). The TM angle is measured by using DWS [20], the longitudinal TM movement corresponds to the phase change in the interferometer. The imaging system images the point of reflection from the TM to the photo diode and therefore suppresses beam walk on the diode. All components in this sketch are labeled in order to make them easily visible in later schematics. 1 test mass, 2 polarizing beam splitter, 3 recombining beam splitter, 4 lens one, 5 lens two, 6 quadrant photo diode.

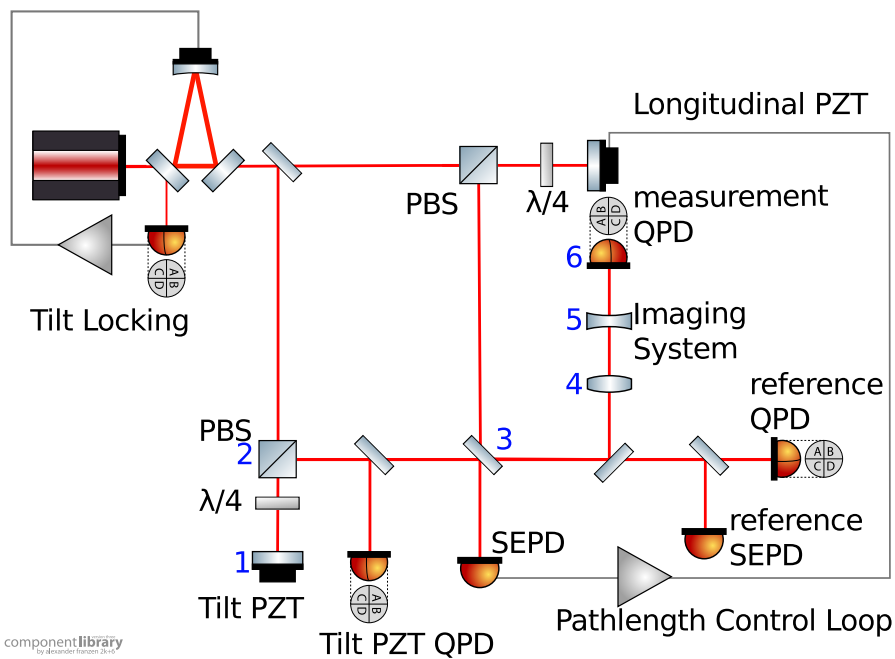


Figure B.4.: Draft of the experimental setup, with: polarizing beam splitter (PBS), quarter waveplate ($\lambda/4$), quadrant photo diode (QPD), single element photo diode (SEPD), piezo driven actuator (PZT). The key components from Figure B.3 are labeled in blue.

The optical resonator (called mode cleaner [66]) in front of the experiment produces a purely fundamental Gaussian beam to suppress higher order modes (compare to Sec. B.1.3). The resonator comprises two plane mirrors and one concave mirror with a radius of curvature of 1 m. The resonator round-trip length measures 416 mm. The eigenmode has a waist radius of 370 μm located between the two plane mirrors. After the resonator a telescope magnifies the eigenmode to a waist radius of 1 mm located roughly at the tilt mirror, which is representative for LISA. The resonator was used with p-polarized light and has a finesse of 360. The cavity round-trip length can be actuated by a piezo crystal attached to the concave mirror. It is stabilized using the tilt-lock technique [67]. The control loop has a unity gain frequency of ≈ 15 kHz and a phase margin of $\approx 40^\circ$.

The tilting of the beam is performed by a commercial piezo driven tilt-actuator and an additional QPD is placed behind the tilt-actuator in order to monitor the actual tilt angle. This tilt-QPD measures the difference of the power between its sides (differential power sensing signal - DPS) [P2]. By tilting the beam, its center moves over the photo diode's surface and the DPS signal varies.

To remove the TTL coupling caused by the longitudinal movement of the tilt-actuator (compare to Sec. B.1.1), the interference pattern is measured with a large SEPD. The SEPD will only detect the longitudinal movement of the tilt-actuator in the interference pattern. As shown in Section chap: vanishing TTL and [P5], a large SEPD is not affected by TTL coupling in the case of equal beams and no lateral offset between the beams and the pivot. Due to the resonator and the equal arm-length Mach-Zehnder design, this is guaranteed here.

This movement is minimized by a control loop and a linear actuator in the second arm. This control loop also ensures a stable midfringe lock. A unity gain frequency of ≈ 195 Hz and a phase margin of $\approx 25^\circ$ were measured. This path length control loop uses the photo current of an SEPD as a sensor. Only if the interferometer is perfectly locked to midfringe, the SEPD power theoretically does not change with the beam angle. At any other operating point, the beam tilt couples into the power detected by the SEPD. To avoid additional coupling which appears by a mismatch between operating point and midfringe and to suppress the angular dependency of the midfringe level, the interference pattern was measured with an additional SEPD (reference SEPD). The residual coupling, measured with this reference SEPD, was in the end subtracted from the TTL coupling, measured behind the imaging system.

Besides the reference-SEPD, a measurement-QPD measured the TTL coupling behind an imaging system and a reference-QPD measured the TTL coupling without an imaging system.

B.3. Photo diode calibration

In a homodyne interferometer a photo diode can only detect power (P). If the phase difference between the two beams is equal to an even multiple of π they interfere constructively and the power is P_{\max} . If the phase difference is equal to an uneven multiple of π they interfere destructively and the power is P_{\min} . By comparing the measured power to P_{\max} and P_{\min} it is possible to compute the phase relation between the two beams. The minimal and maximal power depend, besides the beam geometry and alignment, also on the beam angle. Therefore, the two power extrema have to be measured for any beam angle and every specific photo diode. In Figure B.5, P_{\min} and P_{\max} are plotted over the DPS signal of the tilt-QPD (which we use as measure for the beam angle) for the measurement-QPD, the reference-QPD and the reference-SEPD. These measurements were obtained by applying a slow sinusoidal waveform to the tilt piezo and a fast sinusoidal waveform to the longitudinal piezo while monitoring the power on all diodes.

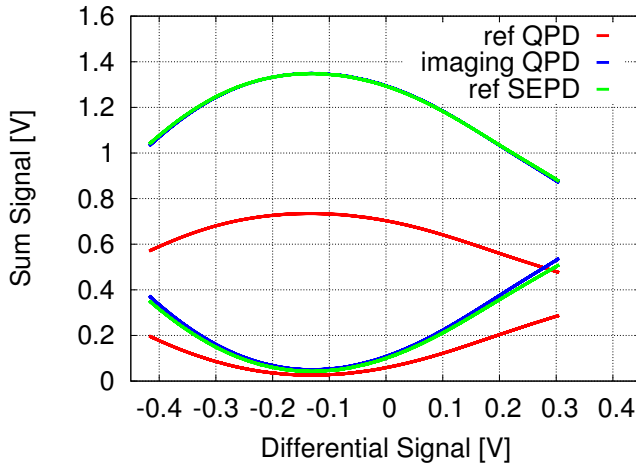


Figure B.5.: Angle dependent maximal and minimal power on the different photo diodes (sum signal \propto power, differential signal \propto DPS).

The power P on a QPD can be expressed as a function of the phase-difference $\Delta\varphi$ between the two beams

$$P := \bar{P} [1 + c \sin(\Delta\varphi)] . \quad (\text{B.1})$$

Here, the contrast c is

$$c := \frac{P_{\max} - P_{\min}}{P_{\max} + P_{\min}} , \quad (\text{B.2})$$

and the mean power \bar{P} is

$$\bar{P} := \frac{P_{\max} + P_{\min}}{2} . \quad (\text{B.3})$$

Therefore, the phase-difference becomes

$$\Delta\varphi := \arcsin \left[\frac{2P - (P_{\max} + P_{\min})}{P_{\max} - P_{\min}} \right], \quad (\text{B.4})$$

and the related longitudinal path length signal (LPS) gets

$$s_{\text{LPS}} := \frac{\lambda}{2\pi} \Delta\varphi. \quad (\text{B.5})$$

Since P_{\max} and P_{\min} are a function of the beam angle, the LPS signal depends on the beam power and the beam angle, too.

B.4. Coherent filtering

Often, high precision experiments are built on highly temperature stable glass base-plates (compare to Section 4) and are operated in vacuum to suppress the influence of pressure, air fluctuations, and temperature (e.g. the optical bench of LISA pathfinder [17]). The present experiment is built as a table top experiment on a steel breadboard and is operated in air.

To suppress the mentioned noise sources anyway, a filter technique that we call coherent filtering is used. The idea is to apply a modulation to the tilt actuator, measure many cycles of the resulting interferometric signals and perform a fast Fourier transformation (FFT). Any signal frequency which is unequal to the modulation frequency or higher harmonics cannot be caused by the actuator and therefore must be noise. By computing the inverse transformation of only those bins, which correspond to the modulation frequency and higher harmonics, only the beam tilt dependent parts of the signals are left.

In order to use coherent filtering, some technical conditions have to be fulfilled. The sampling frequency of the signal readout system must be an exact integer multiple of the tilt piezos modulation frequency. Therefore, a strict phase-lock between the tilt piezos function generator and the signal readout is required. Furthermore, the measurement length for the coherent filtering must be an integer multiple of the piezos modulation period.

In the presented experiment the sampling frequency is 20 kHz, the tilt piezos modulation frequency is 0.2 Hz and the measurement time is 90 s.

B.5. Post-processing

In a measurement, the tilt actuator is tilted sinusoidally. The power signal of the reference-QPD, the measurement-QPD, the reference-SEPD and the DPS signal of the tilt-QPD are measured over several tilt cycles. All signals are coherently filtered. The different power signals are transformed to the corresponding LPS signals via

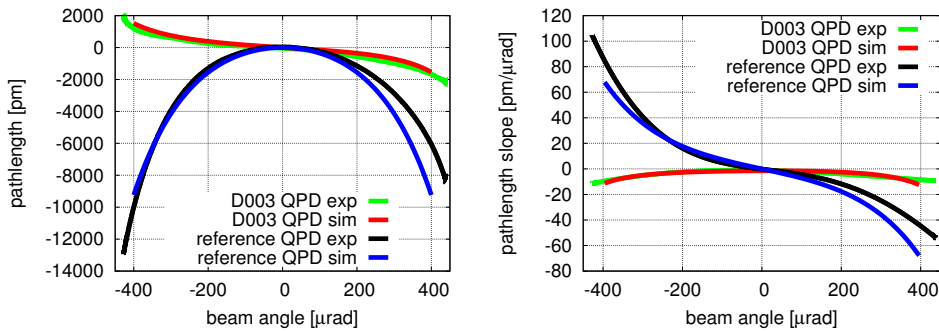


Figure B.6.: LPS signals and slope of the measurement-QPD (behind the Doo3 imaging system) and reference-QPD compared to a numerical simulation.

the calibration of the different photo diodes. The TM-tilt DPS signal is transformed to the real beam angle via the tilt actuator-QPD calibration. Afterwards, the LPS signal of the reference-SEPD is subtracted from both, the measurement-QPD and the reference-QPD. In the end, the two QPD signals are plotted against the beam angle and the related signal slopes are computed.

B.6. Measurement results

Figure B.6 shows the LPS signal and its slope as measured in the experiment for the measurement-QPD with imaging system and the reference-QPD without imaging system, compared to numerical simulations which were performed with IfoCAD [P2, P4]. The measured and the simulated TTL coupling on the reference-QPD match very well. Both, amount and shape of the TTL coupling appear similar.

To provide a proper comparison between simulation and measurement the residual misalignment in the experiment has to be considered in the simulation. It is impossible to determine which parameter is misaligned, since many of the possible misalignments produce TTL coupling of the same shape and we cannot measure all misalignment parameters with the required precision. Therefore, the set of misalignment parameters was chosen, which can explain the measured coupling with the most simple combination of misalignments. The misaligned parameter is a transversal misalignment of the first lens of $0.7 \mu\text{m}$. This misalignment was applied to the simulation. The assumed combination of misaligned parameters is one possibility to explain the measured TTL coupling. Nevertheless, it can be concluded that within the experimental alignment accuracy, the measured performance of the imaging system matches the simulated results.

Without imaging system, the measured TTL coupling rises up to $100\ \mu\text{m}/\text{rad}$. By using the imaging system, the TTL coupling could be reduced in the complete angular range below $\pm 15\ \mu\text{m}/\text{rad}$. Moreover, in the small angular tilt range of $\pm 100\ \mu\text{rad}$, the slope could even be reduced to less than $2\ \mu\text{m}/\text{rad}$. The imaging system design Doo3 is able to suppress the TTL coupling significantly and behaves as expected from the numerical simulations. The residual coupling which is higher than the theoretical possible performance can be explained with a residual misalignment. Therefore, this type of two lens imaging system is a possible solution to suppress TTL coupling.

With the knowledge of the performance of an isolated imaging system further investigations become possible that will show the performance of individual imaging systems under more realistic conditions. The shown performance of an imaging system was achieved in a homodyne Mach-Zehnder interferometer with equal beams without higher-order modes. The baseline concept for LISA foresees heterodyne interferometry instead of a homodyne readout [4, Sec. 4.1.1]. However, the TTL coupling should not depend on the readout scheme. Unequal beams and the presence of higher-order modes affect the TTL coupling. The coupling strongly depends on the specific beam parameter mismatch and higher-order mode content and hence the specific mission design.

Miscellaneous information

C.1. The difference between intensity and irradiance

Intensity and irradiance are used with different meanings in different fields of physics. Even in the same field, different people and groups use these two words with different definitions. To clarify the meaning of the word “intensity” in this thesis, I will list the most common definitions and point out which of these is used.

1. Radiant intensity, measured in watts per steradian (W/sr) describes the power per solid angle – used mostly in radiometry and radio engineering, where it is called radiation intensity.
2. Luminous intensity, measured in lumen per steradian (lm/sr) or candela (cd), describes the emitted power per solid angle, here the different wavelengths are weighted by their visibility in the human eye – used mostly in photometry for applications related to the human eye.
3. Intensity, measured in watts per meter squared (W/m^2), describes the emitted power per unit area – used in most fields of physics
4. Irradiance, measured in watts per meter squared (W/m^2), describes the emitted power per unit area and therefore the same value as intensity – mostly used in radiometry to avoid confusion with radiant intensity
5. Radiance, measured in watts per solid angle per unit area ($\text{W}/(\text{sr}\cdot\text{m})$), describes the emitted power of an object that is received by an observing optical system – mostly used in astronomy to describe the effective brightness of astrophysical objects in telescopes.

Within this thesis I use definition 3, the intensity describes the light power per unit area.

C.2. Phase extraction

To extract the phase $\Delta\varphi$ from the measured signal on a photo detector in a heterodyne interferometer, the power

$$\begin{aligned} P &= \int_S d^2r J \\ &= \bar{P} \cdot [1 + c \cdot \cos(\Omega_{\text{het}} \cdot t - \Delta\varphi)] \end{aligned} \quad (\text{C.1})$$

is multiplied by a cosine or sine, respectively and then integrated over a period of $\Omega_{\text{het}} \cdot t$

$$\begin{aligned} \text{int}_1 &= \frac{1}{\pi} \int_0^{2\pi} d(\Omega_{\text{het}} t) \sin(\Omega_{\text{het}} t) \cdot P(\Omega_{\text{het}} t) \quad (\text{C.2}) \\ &= \frac{1}{\pi} \int_0^{2\pi} d(\Omega_{\text{het}} t) \sin(\Omega_{\text{het}} t) \cdot \bar{P}(1 + \cos(\Omega_{\text{het}} t - \Delta\varphi)) \\ &= \frac{1}{\pi} \int_0^{2\pi} d(\Omega_{\text{het}} t) \bar{P} \sin(\Omega_{\text{het}} t) + \frac{1}{\pi} \int_0^{2\pi} d(\Omega_{\text{het}} t) \sin(\Omega_{\text{het}} t) \cdot \bar{P} \cos(\Omega_{\text{het}} t - \Delta\varphi). \end{aligned} \quad (\text{C.3})$$

Afterwards, the $\cos(\Omega_{\text{het}} t - \Delta\varphi)$ is replaced by a $\sin\left(\Omega_{\text{het}} t + \frac{\pi}{2} - \Delta\varphi\right)$, the additionally added $\pi/2$ defines a new phase $\Delta\varphi^* := \frac{\pi}{2} - \Delta\varphi$. The result is a product of two sine functions

$$\text{int}_1 = \frac{\bar{P}c}{\pi} \int_0^{2\pi} d(\Omega_{\text{het}} t) \sin(\Omega_{\text{het}} t) \cdot \sin(\Omega_{\text{het}} t + \Delta\varphi^*). \quad (\text{C.4})$$

The phase can be placed in both sine functions, because of the periodicity of the sine which leads to

$$\text{int}_1 = \frac{\bar{P}c}{\pi} \int_0^{2\pi} d(\Omega_{\text{het}} t) \sin(\Omega_{\text{het}} t - \Delta\varphi^*/2) \cdot \sin(\Omega_{\text{het}} t + \Delta\varphi^*/2). \quad (\text{C.5})$$

By using the trigonometric identity $\sin(x + y) \cdot \sin(x - y) = \cos^2(y) - \cos^2(x)$ int_1 gains the following form

$$\begin{aligned} \text{int}_1 &= \frac{\bar{P}c}{\pi} \int_0^{2\pi} d(\Omega_{\text{het}} t) (\cos^2(\Delta\varphi^*/2) - \cos^2(\Omega_{\text{het}} t)) \\ &= \frac{\bar{P}c}{\pi} \int_0^{2\pi} d(\Omega_{\text{het}} t) \underbrace{\cos^2(\Delta\varphi^*/2)}_{=\frac{1+\cos\Delta\varphi^*}{2}} - \underbrace{\frac{\bar{P}c}{\pi} \int_0^{2\pi} d(\Omega_{\text{het}} t) \cos^2(\Omega_{\text{het}} t)}_{=\pi} \\ &= \bar{P}c + \bar{P}c \cos \Delta\varphi^* - \bar{P}c = \bar{P}c \cos\left(-\Delta\varphi + \frac{\pi}{2}\right) \\ \text{int}_1 &= \underline{\underline{\bar{P}c \sin \Delta\varphi}}. \end{aligned} \quad (\text{C.6})$$

The integration with an additional cosine is performed in analogously

$$\text{int}_2 = \frac{1}{\pi} \int_0^{2\pi} d(\Omega_{\text{het}} t) \cos(\Omega_{\text{het}} t) \cdot P(\Omega_{\text{het}} t) \quad (\text{C.7})$$

$$\begin{aligned} &= \frac{1}{\pi} \int_0^{2\pi} d(\Omega_{\text{het}} t) \cos(\Omega_{\text{het}} t) \cdot \bar{P} [1 + \cos(\Omega_{\text{het}} t - \Delta\varphi)] \\ &= \frac{1}{\pi} \int_0^{2\pi} d(\Omega_{\text{het}} t) \bar{P} \cos(\Omega_{\text{het}} t) + \frac{1}{\pi} \int_0^{2\pi} d(\Omega_{\text{het}} t) \cos(\Omega_{\text{het}} t) \cdot \bar{P} \cos(\Omega_{\text{het}} t - \Delta\varphi). \end{aligned} \quad (\text{C.8})$$

The cosine is periodic, therefore it is possible to split the phase and place it in both cosines

$$\text{int}_2 = \frac{\bar{P}_C}{\pi} \int_0^{2\pi} d(\Omega_{\text{het}} t) \cos(\Omega_{\text{het}} t - \Delta\varphi/2) \cdot \cos(\Omega_{\text{het}} t + \Delta\varphi/2). \quad (\text{C.9})$$

With the trigonometric identity $\cos(x+y) \cdot \cos(x-y) = \cos^2(y) + \cos^2(x) - 1$, the equation gets

$$\begin{aligned} \text{int}_2 &= \frac{\bar{P}_C}{\pi} \int_0^{2\pi} d(\Omega_{\text{het}} t) (\cos^2(\Delta\varphi/2) + \cos^2(\Omega_{\text{het}} t) - 1) \\ &= \frac{\bar{P}_C}{\pi} \int_0^{2\pi} d(\Omega_{\text{het}} t) \underbrace{\cos^2(\Delta\varphi/2)}_{=\frac{1+\cos\Delta\varphi}{2}} + \underbrace{\frac{\bar{P}_C}{\pi} \int_0^{2\pi} d(\Omega_{\text{het}} t) \cos^2(\Omega_{\text{het}} t)}_{=\pi} - \frac{\bar{P}_C}{\pi} \int_0^{2\pi} d(\Omega_{\text{het}} t) \cdot 1 \\ &= \bar{P}_C + \bar{P}_C \cos \Delta\varphi + \bar{P}_C - \bar{P}_C \cdot 2 \\ \text{int}_2 &= \underline{\underline{\bar{P}_C \cos(\Delta\varphi)}}. \end{aligned} \quad (\text{C.10})$$

The phase $\Delta\varphi$ is therefore computed via int_1 and int_2 by

$$\Delta\varphi = \arctan\left(\frac{\text{int}_2}{\text{int}_1}\right). \quad (\text{C.11})$$

For convenience, the phase equations and the two integrals are often expressed as a complex amplitude

$$a := \text{int}_1 + i \cdot \text{int}_2. \quad (\text{C.12})$$

Therefore the phase signal is defined by

$$\Delta\varphi = \arg(a). \quad (\text{C.13})$$

The shown derivation of the phase readout is computed via integrations (cf. Equations (C.2) and (C.7)). In reality the integration is carried out as a summation over single phase-points, the detected power needs to be sampled with multiple sample points per heterodyne period. The summation is an approximation of the integration by using the formalism of Surrel [68]. The entire derivation of the phase readout according to Surrel is shown in [16].

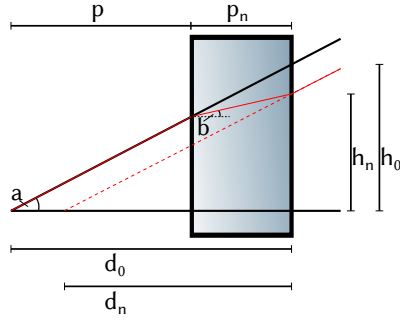
To simplify the subsequent equations, the phase difference $\Delta\varphi$ is substituted by the phase φ :

$$\Delta\varphi \Rightarrow \varphi. \tag{C.14}$$

Since in a heterodyne interferometer the phase relation between two beam varies in time (beat note) a measured phase only contains useful information when it is compared with a reference phase. Therefore, any system operating with a heterodyne interferometer (e.g. TM interferometer in LISA) requires a reference interferometer which provides a stable reference phase for the two interfering beams.

More information about the equations shown here can be found in [16][6, P2].

Figure C.1: In this simplified figure, the propagation characteristic of a pivot is demonstrated. Without the optical component, the crossing black lines define the original pivot. With the component, the red lines define the propagation of a tilted ray. The dashed red line indicates the position of the pivot as it looks like from behind the component.



C.3. Propagation characteristic of a pivot

In Figure C.1 the characteristic of a pivot is illustrated. Compared is the visual pivot, as seen from the right, for a scenario with and without a component. The different distances to the pivot (d_0 and d_n) can be computed.

$$d_0 = p + p_n \quad (\text{C.15})$$

$$\frac{d_n}{h_n} = \frac{d_0}{h_0} \Rightarrow d_n = \frac{d_0}{h_0} h_n \quad (\text{C.16})$$

$$h_n = h_0 - (\tan a - \tan b) p_n \quad (\text{C.17})$$

$$\Rightarrow d_n = \frac{d_0}{h_0} [h_0 - (\tan a - \tan b) p_n] \quad (\text{C.18})$$

$$h_0 = \tan a \cdot d_0 \quad (\text{C.19})$$

$$\Rightarrow d_n = \frac{d_0}{\tan a \cdot d_0} [\tan a d_0 - (\tan a - \tan b) p_n] \quad (\text{C.20})$$

$$\Rightarrow d_n = d_0 - p_n + \frac{\tan b}{\tan a} p_n \quad (\text{C.21})$$

$$\sin a = n \sin b \Rightarrow d_n \approx p + \frac{1}{n} p_n \quad (\text{C.22})$$

Thus the distance to a pivot can be computed similarly to the distance of a Gaussian waist position, it computes as $1/n \cdot d$, where n is the refractive index and d the physical distance.

C.4. Auxiliary information regarding the LISA OB TS testbed

This chapter contains fit parameters of TTL coupling measurements previously shown in the context of the LISA OB testbed (Chapter 4 and Chapter 5). The reason for the sixth order fit is the previously assumed first order dominance of the TTL coupling. With the parameters of the fitted higher order polynomial shown here, it can be reviewed if the TTL coupling is really dominated by the first order.

Table C.1.: The optical path length fit parameters for the difference between reference and temporary pinhole featuring the Gaussian RX. Here, α is the beam angle after DWS calibration in μrad and s is the optical path length change in nm. The units of the different parameters are $\text{nm}/\mu\text{rad}^x$ where x is the order of the corresponding monomial.

$$s(\alpha) = P_6 * \alpha^6 + P_5 * \alpha^5 + P_4 * \alpha^4 + P_3 * \alpha^3 + P_2 * \alpha^2 + P_1 * \alpha + P_0$$

before flipping			after flipping		
$P_6 =$	$9.80343e^{-18}$	$\pm 5.469e^{-17}$	$P_6 =$	$1.34011e^{-16}$	$\pm 7.509e^{-17}$
$P_5 =$	$3.40637e^{-15}$	$\pm 1.363e^{-14}$	$P_5 =$	$-9.36037e^{-15}$	$\pm 1.903e^{-14}$
$P_4 =$	$4.50675e^{-12}$	$\pm 1.843e^{-11}$	$P_4 =$	$-5.11721e^{-11}$	$\pm 2.502e^{-11}$
$P_3 =$	$-1.02854e^{-8}$	$\pm 3.803e^{-9}$	$P_3 =$	$-3.71808e^{-9}$	$\pm 5.148e^{-9}$
$P_2 =$	$-9.02929e^{-6}$	$\pm 1.631e^{-6}$	$P_2 =$	$-1.58142e^{-6}$	$\pm 2.174e^{-6}$
$P_1 =$	$4.11571e^{-3}$	$\pm 2.368e^{-4}$	$P_1 =$	$5.24915e^{-2}$	$\pm 3.085e^{-4}$
$P_0 =$	11.6792	± 0.03271	$P_0 =$	3.91332	± 0.04056
after realignment					
$P_6 =$	$1.96273e^{-16}$	$\pm 5.851e^{-17}$			
$P_5 =$	$-3.81639e^{-14}$	$\pm 1.544e^{-14}$			
$P_4 =$	$-7.88892e^{-11}$	$\pm 1.886e^{-11}$			
$P_3 =$	$8.6141e^{-9}$	$\pm 3.985e^{-9}$			
$P_2 =$	$1.25892e^{-6}$	$\pm 1.603e^{-6}$			
$P_1 =$	$-2.38406e^{-3}$	$\pm 2.284e^{-4}$			
$P_0 =$	6.60691	± 0.02996			

Table C.3.: The optical path length fit parameters for SciQPD 1 and SciQPD 2 in the nominal performance of the two-lens imaging system featuring the Gaussian RX beam with different lenses. Here, α is the beam angle after DWS calibration in μrad and s is the optical path length change in nm. The units of the different parameters are $\text{nm}/\mu\text{rad}^x$ where x is the order of the corresponding monomial.

$$s(\alpha) = P_6 * \alpha^6 + P_5 * \alpha^5 + P_4 * \alpha^4 + P_3 * \alpha^3 + P_2 * \alpha^2 + P_1 * \alpha + P_0$$

500 mm focal length		1000 mm focal length	
$P_6 =$	$2.34609e^{-17} \pm 6.465e^{-18}$	$P_6 =$	$-1.00079e^{-16} \pm 7.732e^{-18}$
$P_5 =$	$-1.1167e^{-14} \pm 2.648e^{-15}$	$P_5 =$	$-7.34276e^{-15} \pm 3.428e^{-15}$
$P_4 =$	$-1.74478e^{-11} \pm 5.325e^{-12}$	$P_4 =$	$1.31165e^{-10} \pm 6.758e^{-12}$
$P_3 =$	$1.30072e^{-8} \pm 1.771e^{-9}$	$P_3 =$	$5.41373e^{-9} \pm 2.383e^{-9}$
$P_2 =$	$-5.90038e^{-6} \pm 1.14e^{-6}$	$P_2 =$	$-5.36058e^{-5} \pm 1.52e^{-6}$
$P_1 =$	$-5.70566e^{-3} \pm 2.615e^{-4}$	$P_1 =$	$-1.83862e^{-3} \pm 3.614e^{-4}$
$P_0 =$	6.34587 ± 0.05282	$P_0 =$	7.68327 ± 0.0689

Table C.5.: The optical path length fit parameters for SciQPD 1 and SciQPD 2 in the nominal performance of the two-lens imaging system (RX- flat top). Here, α is the beam angle after DWS calibration in μrad and s is the optical path length change in nm. The units of the different parameters are $\text{nm}/\mu\text{rad}^x$ where x is the order of the corresponding monomial.

$$s(\alpha) = P_6 * \alpha^6 + P_5 * \alpha^5 + P_4 * \alpha^4 + P_3 * \alpha^3 + P_2 * \alpha^2 + P_1 * \alpha + P_0$$

SciQPD 1		SciQPD 2	
$P_6 =$	$-6.50963e^{-17} \pm 8.743e^{-17}$	$P_6 =$	$-1.02597e^{-16} \pm 8.925e^{-17}$
$P_5 =$	$9.20724e^{-14} \pm 2.421e^{-14}$	$P_5 =$	$4.64967e^{-14} \pm 2.471e^{-14}$
$P_4 =$	$1.05916e^{-10} \pm 3.68e^{-11}$	$P_4 =$	$1.15679e^{-10} \pm 3.757e^{-11}$
$P_3 =$	$-3.6902e^{-8} \pm 8.398e^{-9}$	$P_3 =$	$-1.24886e^{-8} \pm 8.573e^{-9}$
$P_2 =$	$-1.66948e^{-5} \pm 4.087e^{-6}$	$P_2 =$	$-2.44289e^{-5} \pm 4.172e^{-6}$
$P_1 =$	$7.99239e^{-3} \pm 6.527e^{-4}$	$P_1 =$	$-5.51974e^{-4} \pm 6.663e^{-4}$
$P_0 =$	2.65489 ± 0.1014	$P_0 =$	2.46846 ± 0.1035

Table C.7.: The optical path length fit parameters for SciQPD 1 and SciQPD 2 in the nominal performance of the four-lens imaging system. Here, α is the beam angle after DWS calibration in μrad and s is the optical path length change in nm. The units of the different parameters are $\text{nm}/\mu\text{rad}^x$ where x is the order of the corresponding monomial.

$$s(\alpha) = P_6 * \alpha^6 + P_5 * \alpha^5 + P_4 * \alpha^4 + P_3 * \alpha^3 + P_2 * \alpha^2 + P_1 * \alpha + P_0$$

SciQPD 1		SciQPD 2	
$P_6 =$	$-4.64372e^{-16} \pm 6.431e^{-17}$	$P_6 =$	$-5.07448e^{-16} \pm 6.315e^{-17}$
$P_5 =$	$1.59141e^{-13} \pm 1.847e^{-14}$	$P_5 =$	$1.41098e^{-13} \pm 1.814e^{-14}$
$P_4 =$	$2.67592e^{-10} \pm 2.211e^{-11}$	$P_4 =$	$2.97993e^{-10} \pm 2.172e^{-11}$
$P_3 =$	$-4.37196e^{-8} \pm 5.048e^{-9}$	$P_3 =$	$-4.26386e^{-8} \pm 4.957e^{-9}$
$P_2 =$	$-4.71248e^{-5} \pm 2.069e^{-6}$	$P_2 =$	$-4.51644e^{-5} \pm 2.032e^{-6}$
$P_1 =$	$-2.57056e^{-4} \pm 3.165e^{-4}$	$P_1 =$	$-6.35278e^{-4} \pm 3.108e^{-4}$
$P_0 =$	1.78522 ± 0.04643	$P_0 =$	1.33535 ± 0.0456

C.5. Numerical trouble spot in IfoCAD: GA_GBeam

According to [69], the electric field of a general astigmatic Gaussian beam follows the equation

$$E(x, y, z) = E_0(z) \exp \left\{ -i\Phi_{ac} + i\eta(z) - \frac{k}{2} \left[\left(\frac{\cos^2 \Theta}{q_1(z)} + \frac{\sin^2 \Theta}{q_2(z)} \right) x^2 + \left(\frac{\sin^2 \Theta}{q_1(z)} + \frac{\cos^2 \Theta}{q_2(z)} \right) y^2 + \sin 2\Theta \left(\frac{1}{q_1(z)} - \frac{1}{q_2(z)} \right) xy \right] \right\}. \quad (\text{C.23})$$

Featuring the curvature tensor Q

$$Q = \begin{pmatrix} \frac{\cos^2 \Theta}{q_1(z)} + \frac{\sin^2 \Theta}{q_2(z)} & \frac{1}{2} \sin 2\Theta \left(\frac{1}{q_1(z)} - \frac{1}{q_2(z)} \right) \\ \frac{1}{2} \sin 2\Theta \left(\frac{1}{q_1(z)} - \frac{1}{q_2(z)} \right) & \frac{\sin^2 \Theta}{q_1(z)} + \frac{\cos^2 \Theta}{q_2(z)} \end{pmatrix} \quad (\text{C.24})$$

the electric field, with the complex angle Θ , becomes

$$E(r, z) = E_0(z) \exp \left\{ -i\Phi_{ac} + i\eta(z) - ir^T Q(z) r \right\}. \quad (\text{C.25})$$

In the paper mentioned before this complex angle was derived from the Q tensor with the equation

$$\tan 2\Theta = \frac{Q_{12} + Q_{21}}{Q_{11} - Q_{22}}. \quad (\text{C.26})$$

Therefore, Equation (C.23) can be written as

$$E(x, y, z) = E_0(z) \exp \left\{ -i\Phi_{ac} + i\eta(z) - i\frac{k}{2} \left[Q_{11}x^2 + Q_{22}y^2 + \tan 2\theta(Q_{11} - Q_{22})xy \right] \right\}. \quad (C.27)$$

I will show this derivation in more detail and will explain why this term leads to numerical problems and should be avoided in numerical implementations. Using $\cos^2 \theta - \sin^2 \theta = \cos 2\theta$ Equation (C.26) becomes

$$\tan 2\theta(Q_{11} - Q_{22}) \stackrel{!}{=} \sin 2\theta \left(\frac{1}{q_1(z)} - \frac{1}{q_2(z)} \right) \quad (C.28)$$

$$\stackrel{!}{=} \sin 2\theta \left(\frac{1}{q_1(z)} - \frac{1}{q_2(z)} \right) \frac{\cos 2\theta}{\cos 2\theta} \quad (C.29)$$

$$\stackrel{!}{=} \frac{\sin 2\theta}{\cos 2\theta} \left(\frac{\cos 2\theta}{q_1(z)} - \frac{\cos 2\theta}{q_2(z)} \right) \quad (C.30)$$

$$\stackrel{!}{=} \tan 2\theta \left(\frac{\cos^2 \theta - \sin^2 \theta}{q_1(z)} - \frac{\cos^2 \theta - \sin^2 \theta}{q_2(z)} \right) \quad (C.31)$$

$$\stackrel{!}{=} \tan 2\theta \left[\left(\frac{\cos^2 \theta}{q_1(z)} + \frac{\sin^2 \theta}{q_2(z)} \right) - \left(\frac{\sin^2 \theta}{q_1(z)} + \frac{\cos^2 \theta}{q_2(z)} \right) \right] \quad (C.32)$$

$$\stackrel{!}{=} \tan 2\theta(Q_{11} - Q_{22}). \quad (C.33)$$

The problem appears in Eq. C.29. When expanding the term with $\cos 2\theta$ the right side becomes $Q_{11} - Q_{22}$ and the left side becomes $\tan 2\theta$. However, the $\cos 2\theta$ is zero at $\theta = \pi/4$. Close to this angle the $\tan 2\theta$ tends to infinity and $(Q_{11} - Q_{22})$ tends to zero. In the analytic expression this is not a problem since the two effects cancel each other. But in a numerical implementation infinity is a tricky thing and the result of infinite $\tan 2\theta$ times $(Q_{11} - Q_{22})$ close to zero depends strongly on the numeric precision used in computation.

Therefore, the substitution:

$$\sin 2\theta \left(\frac{1}{q_1(z)} - \frac{1}{q_2(z)} \right) \Rightarrow \tan 2\theta(Q_{11} - Q_{22}) \quad (C.34)$$

should be avoided in any implementation.

D

Auxiliary optical simulations

D.1. Beam parameter sensitivity simulations

In this section the results for the beam parameter sensitivity simulations, discussed in Chapter 6, are shown.

Figure D.1 shows the multi-plot for the TTL slope behind the LOB4C imaging system. In each subplot the waist position and waist radius of the RX beam are varied. In the overall scheme waist radius and position of the TX beam are varied. The color indicates the residual TTL coupling. Similarly, Figure D.2 shows the curvature difference slope over the QPD position. In Figure D.3 on page 200 the optimal QPD position for the LOB4C imaging system is shown, again as a function of the TX and RX parameters.

Figure D.4 shows the multi-plot of the path length slope for the GIS2C system. Similarly, Figure D.5 shows the slope of the curvature difference and in Figure D.6 the optimal QPD position in relation to the beam parameters is shown.

For the GIS3C system, Figure D.7 shows the multi-plot of the path length slope. Figure D.8 shows the slope of the curvature difference and Figure D.9 shows the optimal QPD position.

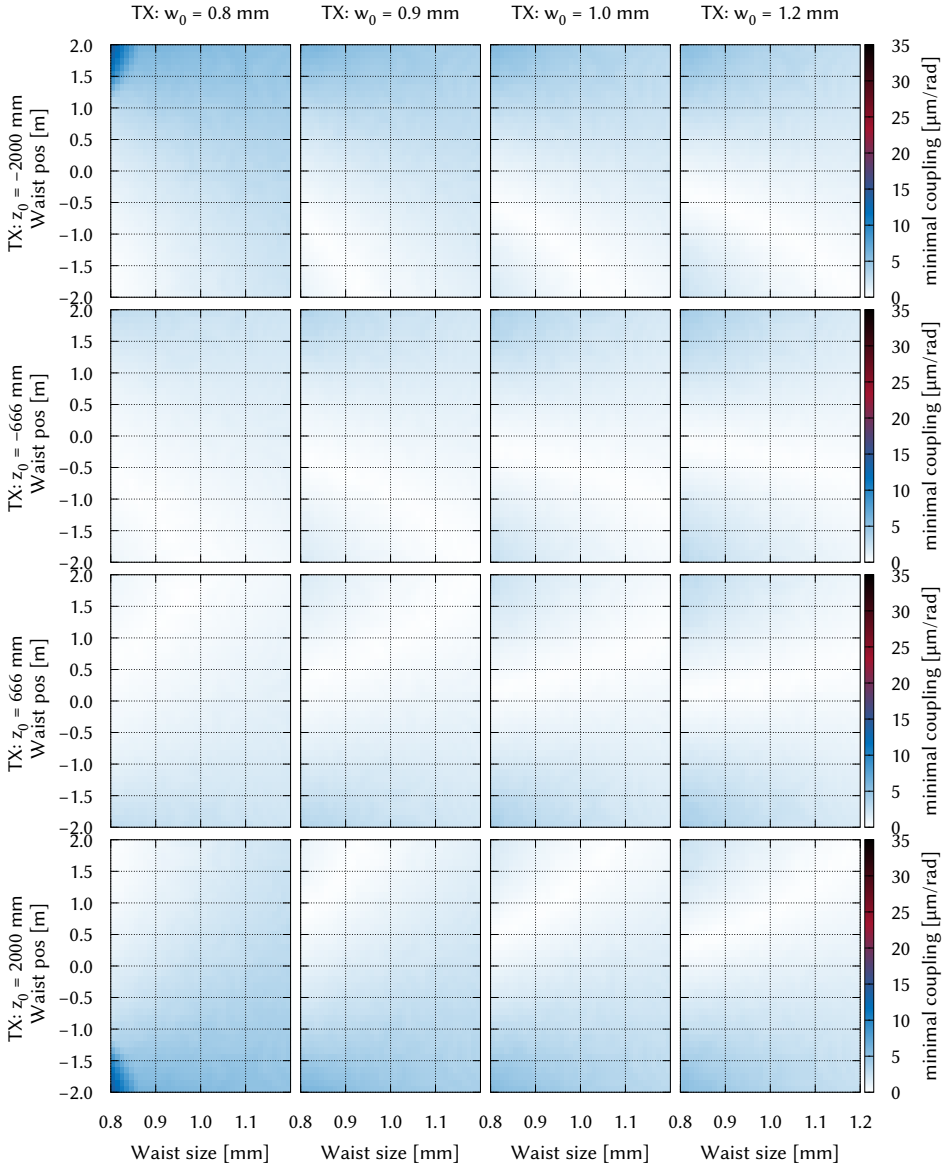


Figure D.1.: Beam parameter sensitivity simulator results for the TTL slope of the LOB4C imaging system. In each subplot the waist position and waist radius of the RX beam are varied. In the overall scheme waist radius and position of the TX beam are varied. The color indicates the residual TTL coupling.

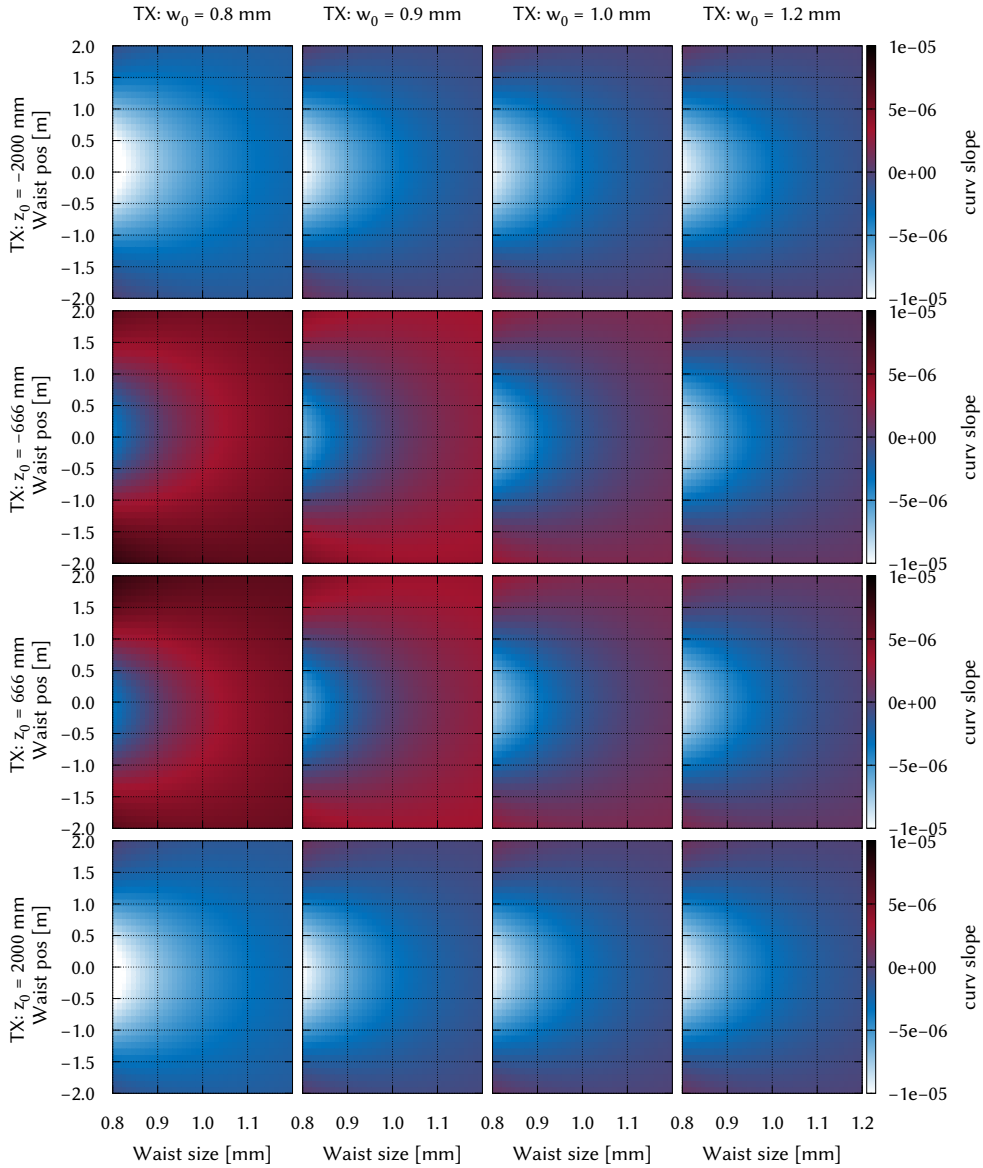


Figure D.2.: Beam parameter sensitivity simulator results for the beam curvature difference slope of the LOB4C imaging system. In each subplot the waist position and waist radius of the RX beam are varied. In the overall scheme waist radius and position of the TX beam are varied. The color indicates the beam curvature difference slope with respect to the QPD position.

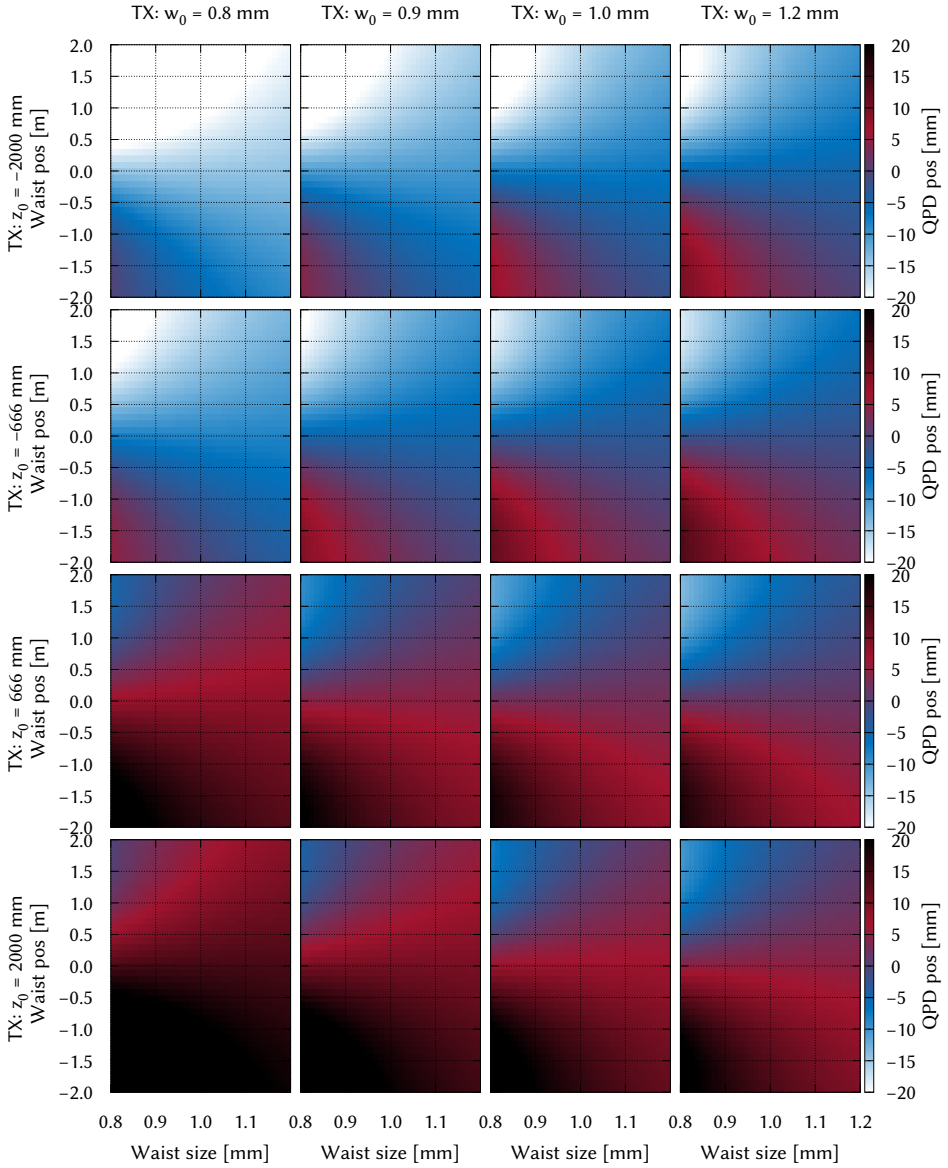


Figure D.3.: Beam parameter sensitivity simulator results for the optimal QPD position of the LOB4C imaging system. In each subplot the waist position and waist radius of the RX beam are varied. In the overall scheme waist radius and position of the TX beam are varied. The color indicates the optimal QPD position at which the minimal TTL coupling is achieved.

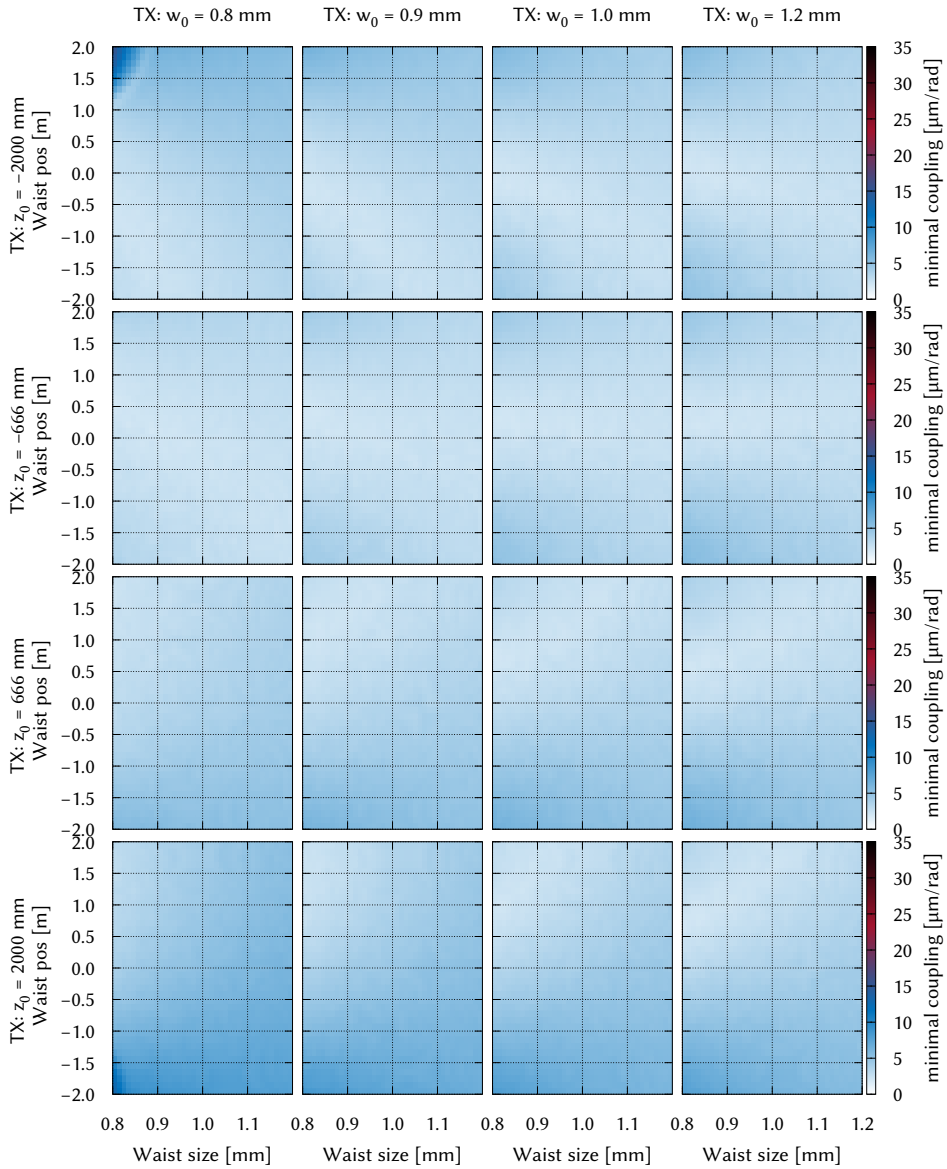


Figure D.4.: Beam parameter sensitivity simulator results for the TTL slope of the GIS2C imaging system. In each subplot the waist position and waist radius of the RX beam are varied. In the overall scheme waist radius and position of the TX beam are varied. The color indicates the residual TTL coupling.

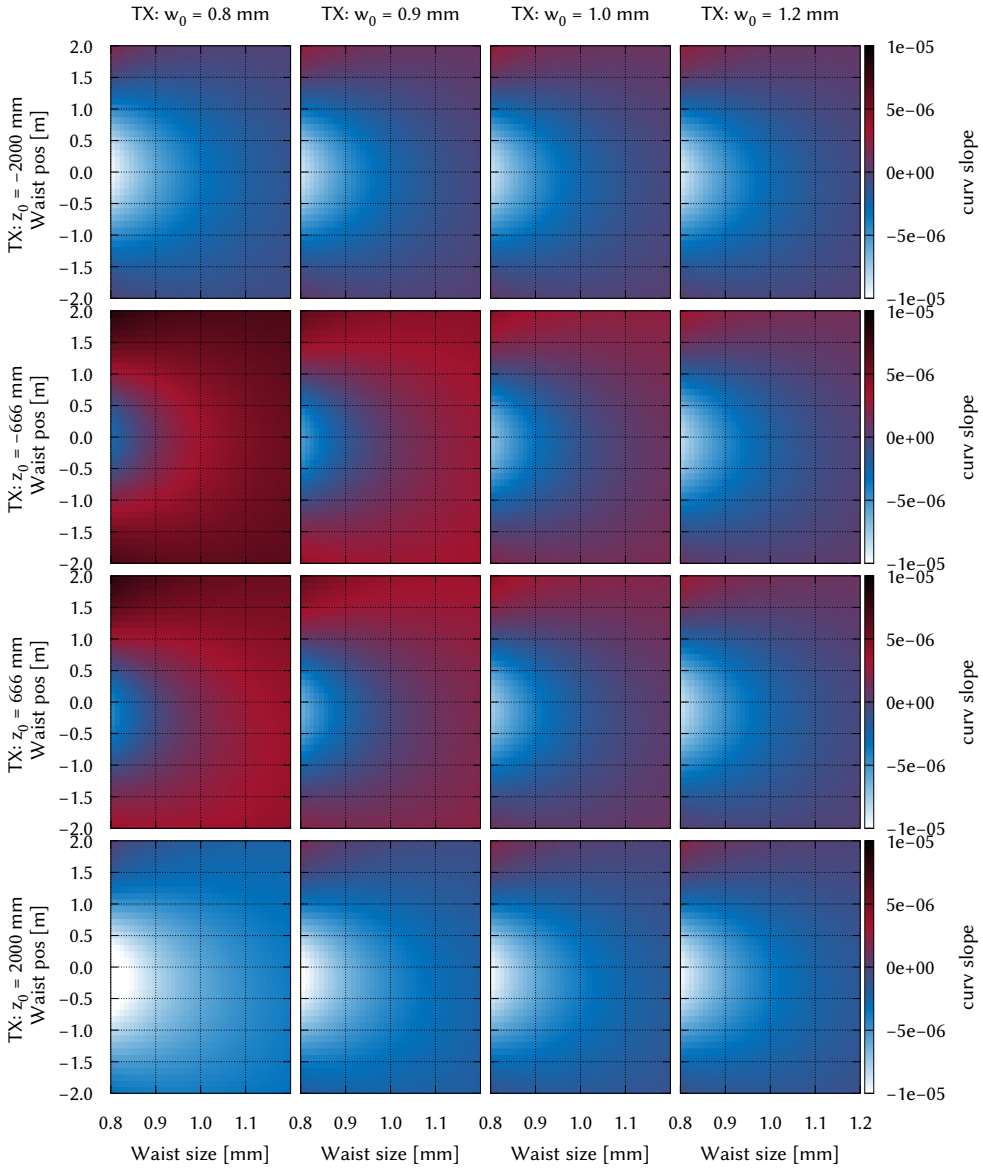


Figure D.5.: Beam parameter sensitivity simulator results for the beam curvature difference slope of the GIS2C imaging system. In each subplot the waist position and waist radius of the RX beam are varied. In the overall scheme waist radius and position of the TX beam are varied. The color indicates the beam curvature difference slope with respect to the QPD position.

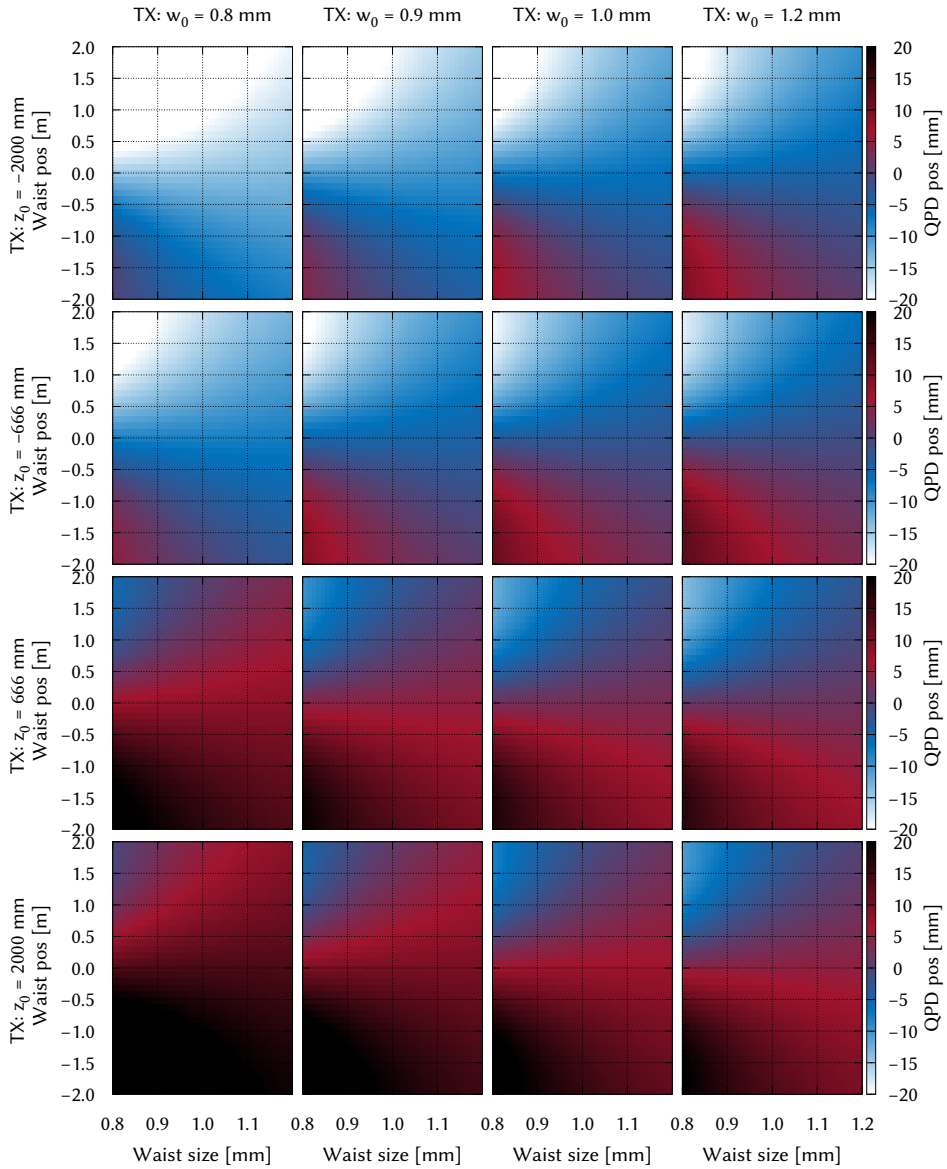


Figure D.6.: Beam parameter sensitivity simulator results for the optimal QPD position of the GIS2C imaging system. In each subplot the waist position and waist radius of the RX beam are varied. In the overall scheme waist radius and position of the TX beam are varied. The color indicates the optimal QPD position at which the minimal TTL coupling is achieved.

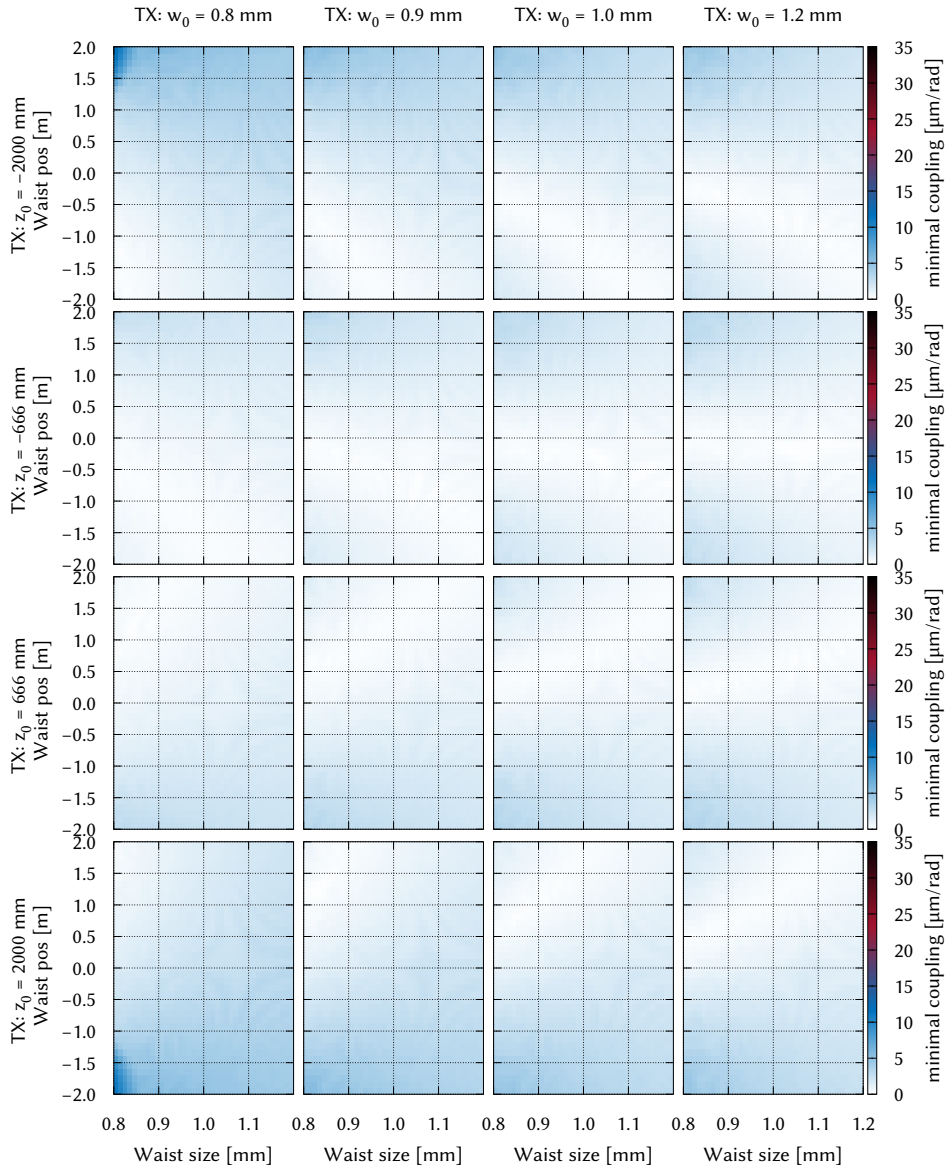


Figure D.7.: Beam parameter sensitivity simulator results for the TTL slope of the GIS3C imaging system. In each subplot the waist position and waist radius of the RX beam are varied. In the overall scheme waist radius and position of the TX beam are varied. The color indicates the residual TTL coupling.

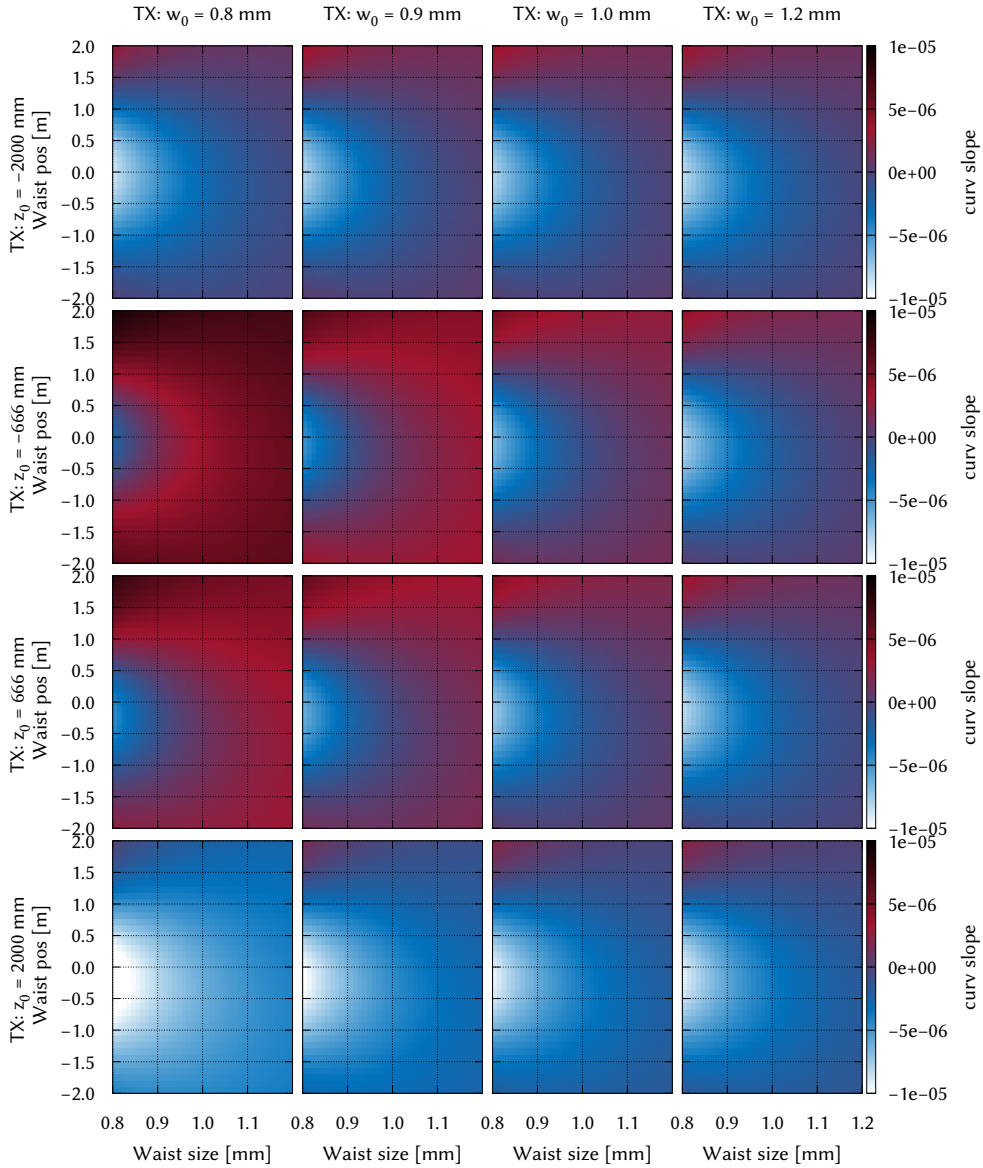


Figure D.8.: Beam parameter sensitivity simulator results for the beam curvature difference slope of the GIS3C imaging system. In each subplot the waist position and waist radius of the RX beam are varied. In the overall scheme waist radius and position of the TX beam are varied. The color indicates the beam curvature difference slope with respect to the QPD position.

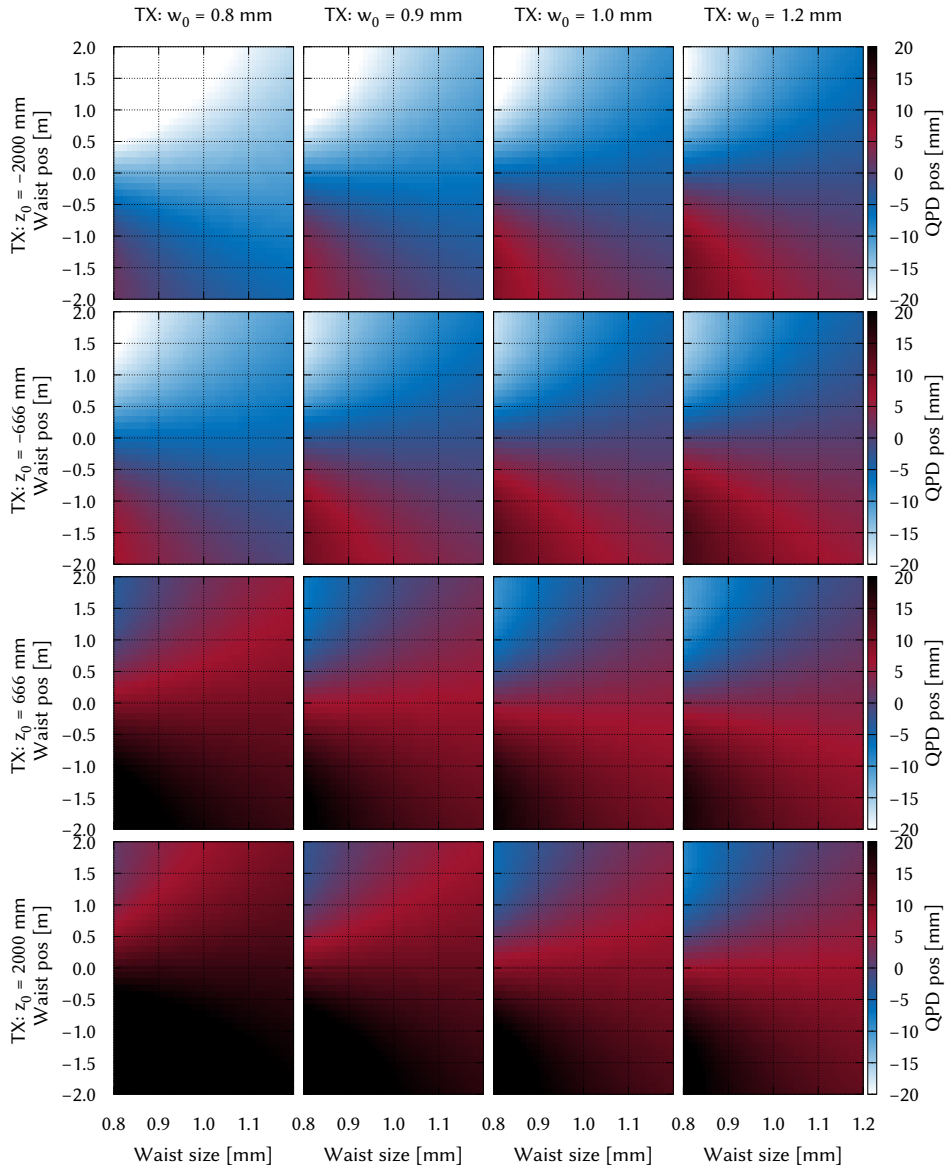


Figure D.9.: Beam parameter sensitivity simulator results for the optimal QPD position of the GIS3C imaging system. In each subplot the waist position and waist radius of the RX beam are varied. In the overall scheme waist radius and position of the TX beam are varied. The color indicates the optimal QPD position at which the minimal TTL coupling is achieved.

D.2. Alignment test of the new imaging systems

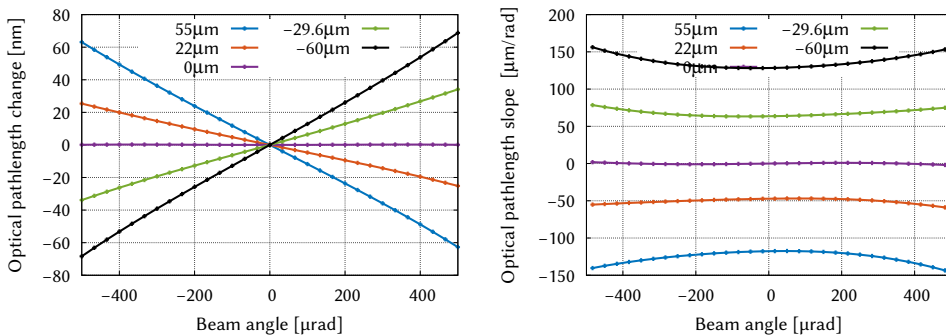
In this section, the misalignment measurements from the LISA telescope simulator experiment were simulated with the new GIS2C system and the GIS3C system. The measurements of the LOB2D and LOB4C system showed a good match to the corresponding simulations. Therefore, the simulations of the new systems provide a good impression of how critical the alignment for the new systems is. The TX and RX beam have the same beam parameters as for the simulations computed for the LISA TS experiment. The TX beam has a 1 mm waist 550 mm in front of the RX-clip, while the RX beam is a flat-top beam represented via a 100 mm waist radius Gaussian with the waist at the RX-clip.

D.2.1. GIS2C system

Lateral QPD shift Figure D.10 shows the sensitivity of the GIS2C imaging system to lateral QPD displacements in vertical direction. Figure D.10a shows path length change versus beam angle, Figure D.10b shows the slope of the path length change versus beam angle. All data points are obtained from numerical simulations.

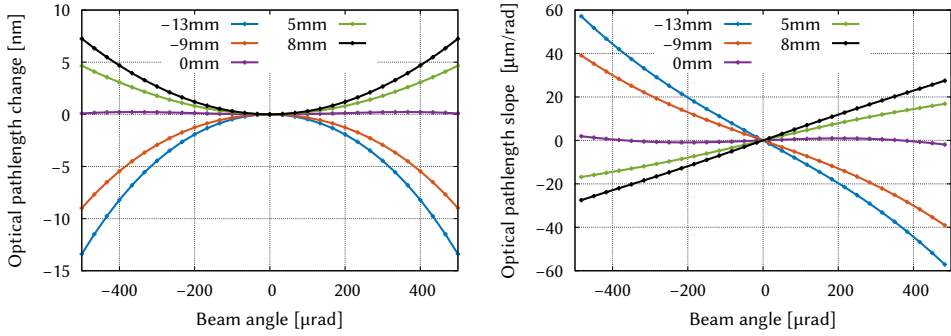
The simulation shows that a lateral misalignment of $\pm 22 \mu\text{m}$ results in an additional TTL coupling of $\approx \pm 50 \mu\text{m}/\text{rad}$.

Longitudinal QPD shift Figure D.11 shows the sensitivity of the GIS2C imaging system to longitudinal QPD displacement. Figure D.11a shows path length change versus beam angle, Figure D.11b shows the slope of the path length change versus beam angle. The longitudinal misalignment is resulting in a higher order coupling that is dependent on the direction of the photo diode offset and not symmetrical for both directions to match the data from the LOB2D system.



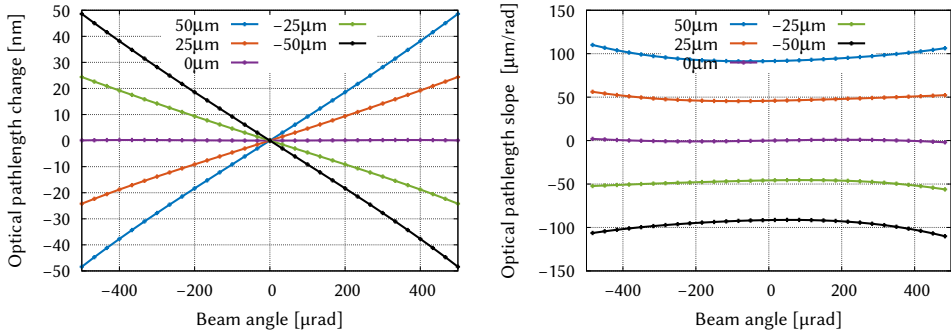
(a) Path length change vs. beam angle. (b) Slope of path length change vs. beam angle.

Figure D.10.: GIS2C imaging system: sensitivity to lateral QPD displacement in vertical direction.



(a) Path length change vs. beam angle. (b) Slope of path length change vs. beam angle.

Figure D.11.: GIS2C imaging system: sensitivity to longitudinal displacement of the QPD.

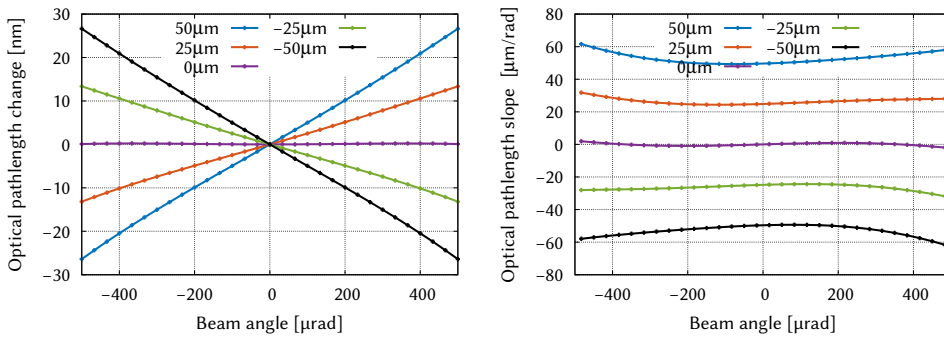


(a) Path length change vs. beam angle. (b) Slope of path length change vs. beam angle.

Figure D.12.: GIS2C imaging system: sensitivity to lateral displacement of lens 1 in vertical direction.

In contrast to lateral misalignments, the actual shapes of simulations featuring longitudinal displacements strongly depend on the beam parameters used, as previously explained in Section 5.4.2. The beam parameters used for this simulation are the ones estimated for the LISA OB testbed. If this simulation will be realized in an experiment with different parameters, the simulation has to be recomputed accordingly with new beam parameters. However, qualitatively this results show the general behavior of the new imaging system towards photo diode displacement.

Lateral shift of lens one Figure D.12 shows the sensitivity of the GIS2C imaging system to lateral displacement of lens one in vertical direction. Figure D.12a shows path length change versus beam angle, Figure D.12b shows the slope of the path length change versus beam angle. The simulation show that a lateral misalignment of ± 25 μm results in an additional TTL coupling of $\approx \pm 65$ $\mu\text{m}/\text{rad}$.



(a) Path length change vs. beam angle. (b) Slope of path length change vs. beam angle.

Figure D.13.: GIS2C imaging system: sensitivity to lateral displacement of lens 2 in vertical direction.

Lateral shift of lens two Figure D.13 shows the sensitivity of the GIS2C imaging system to lateral displacement of lens two in vertical direction. Figure D.13a shows path length change versus beam angle, Figure D.13b shows the slope of the path length change versus beam angle.

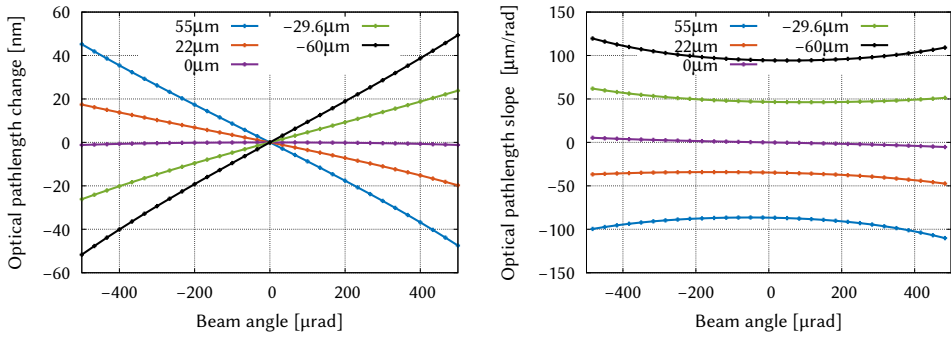
The measurements show that a lateral misalignment of $\pm 25 \mu\text{m}$ results in an additional TTL coupling of $\approx \pm 15 \mu\text{m}/\text{rad}$. This means that the alignment of the lens two is a little bit less critical than the alignment of lens one.

D.2.2. GIS3C system

Lateral QPD shift Figure D.14 shows the sensitivity of the GIS3C imaging system to lateral QPD displacements in vertical direction. Figure D.14a shows path length change versus beam angle, Figure D.14b shows the slope of the path length change versus beam angle. All data points are obtained from numerical simulations.

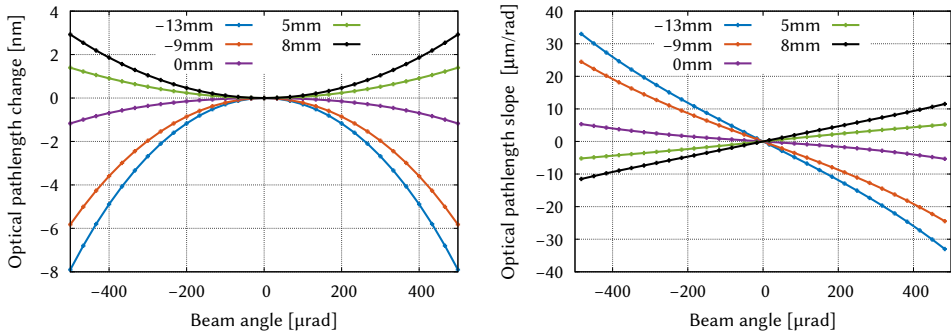
The simulation shows that a lateral misalignment of $\pm 22 \mu\text{m}$ results in an additional TTL coupling of $\approx \pm 40 \mu\text{m}/\text{rad}$.

Longitudinal QPD shift Figure D.15 shows the sensitivity of the GIS3C imaging system to longitudinal QPD displacement. Figure D.15a shows path length change versus beam angle, Figure D.15b shows the slope of the path length change versus beam angle. The longitudinal misalignment is resulting in a higher order coupling that is dependent on the direction of the photo diode offset and not symmetrical for both directions to match the data from the LOB2D system.



(a) Path length change vs. beam angle. (b) Slope of path length change vs. beam angle.

Figure D.14.: GIS3C imaging system: sensitivity to lateral QPD displacement in vertical direction.

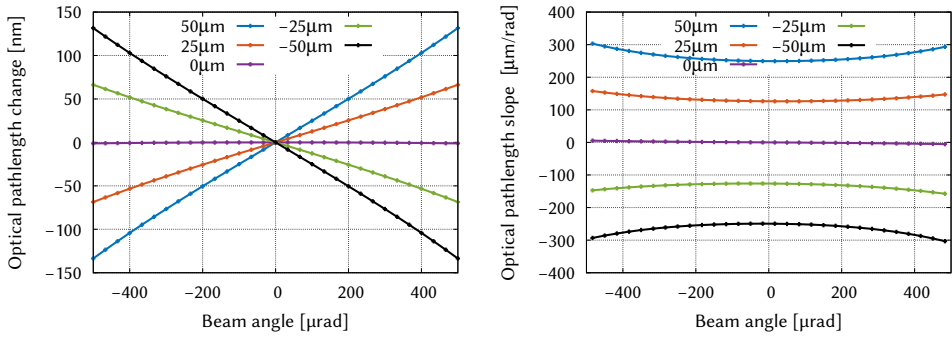


(a) Path length change vs. beam angle. (b) Slope of path length change vs. beam angle.

Figure D.15.: GIS3C imaging system: sensitivity to longitudinal displacement of the QPD.

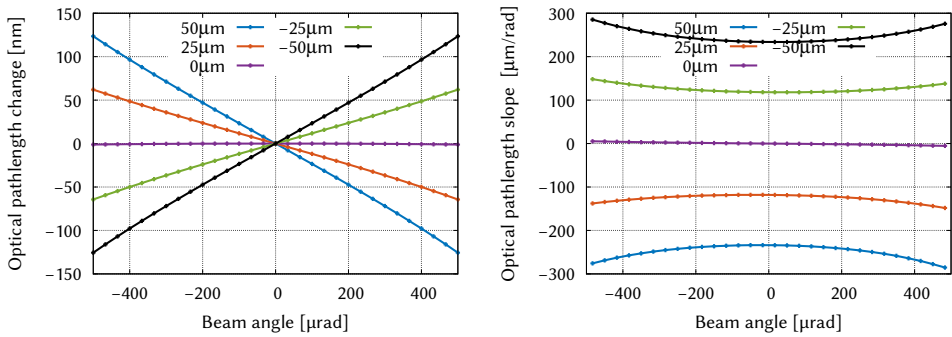
In contrast to lateral misalignments, the actual shapes of simulations featuring longitudinal displacements strongly depend on the beam parameters used, as previously explained in Section 5.4.2. The beam parameters used for this simulation are the ones estimated for the LISA OB testbed. If this simulation will be realized in an experiment with different parameters, the simulation has to be recomputed accordingly with new beam parameters. However, qualitatively this results show the general behavior of the new imaging system towards photo diode displacement.

Lateral shift of lens one Figure D.16 shows the sensitivity of the GIS3C imaging system to lateral displacement of lens one in vertical direction. Figure D.16a shows path length change versus beam angle, Figure D.16b shows the slope of the path length change versus beam angle. The simulation show that a lateral misalignment of $\pm 25 \mu\text{m}$ results in an additional TTL coupling of $\approx \pm 110 \mu\text{m/rad}$.



(a) Path length change vs. beam angle. (b) Slope of path length change vs. beam angle.

Figure D.16.: GIS3C imaging system: sensitivity to lateral displacement of lens 1 in vertical direction.



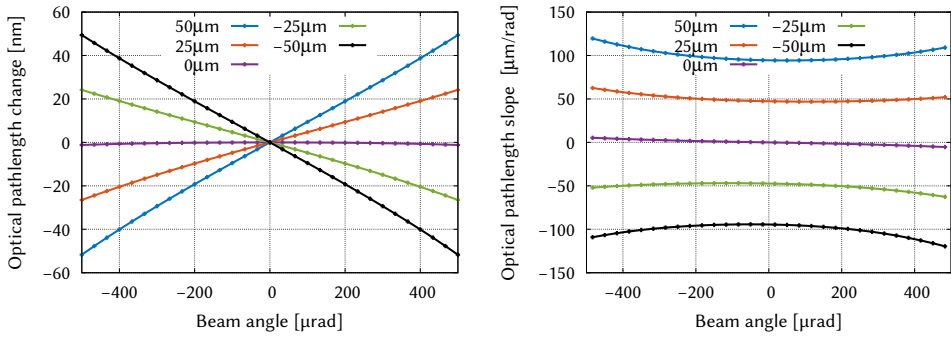
(a) Path length change vs. beam angle. (b) Slope of path length change vs. beam angle.

Figure D.17.: GIS3C imaging system: sensitivity to lateral displacement of lens 2 in vertical direction.

Lateral shift of lens two Figure D.17 shows the sensitivity of the GIS3C imaging system to lateral displacement of lens two in vertical direction. Figure D.17a shows path length change versus beam angle, Figure D.17b shows the slope of the path length change versus beam angle.

The measurements show that a lateral misalignment of $\pm 25 \mu\text{m}$ results in an additional TTL coupling of $\approx \pm 110 \mu\text{m/rad}$.

Lateral shift of lens three Figure D.18 shows the sensitivity of the GIS3C imaging system to lateral displacement of lens two in vertical direction. Figure D.18a shows path length change versus beam angle, Figure D.18b shows the slope of the path length change versus beam angle.



(a) Path length change vs. beam angle. (b) Slope of path length change vs. beam angle.

Figure D.18.: GIS3C imaging system: sensitivity to lateral displacement of lens 3 in vertical direction.

The measurements show that a lateral misalignment of $\pm 25 \mu\text{m}$ results in an additional TTL coupling of $\approx \pm 50 \mu\text{m}/\text{rad}$. This means that the alignment of the lens three is a little bit less critical than the alignment of lens one and two.

Glossary

A	amplitude
E_0	electric field amplitude
F	figure of merit
J	intensity
O_{ovi}	overlap integral between two beams
P	power
Q	general astigmatic curvature tensor
R	radius of curvature
$\Delta\varphi$	phase difference
Δs	path length difference
Δs_{LPS}	TTL coupling due to the path length signal definition
Δs_{WFE}	TTL coupling due to wavefront errors
$\Delta s_{\text{beam parameter}}$	TTL coupling due to beam parameter mismatch
$\Delta s_{\text{const. offset}}$	TTL coupling due to a constant beam offset
$\Delta s_{\text{detector}}$	TTL coupling due to the detector geometry
$\Delta s_{\text{dyn. offset}}$	TTL coupling due to a dynamic beam offset – beam walk
Δs_{lever}	lever arm TTL coupling
Δs_{piston}	piston TTL coupling
Ω	electro magnetic frequency
Ω_{het}	heterodyne frequency
Θ	general astigmatism – complex angle
α	beam tilt angle
\bar{J}	mean intensity
\bar{P}	mean power
β	angle of incidence – angle between TM and beam
η_h	horizontal DWS angle
η_v	vertical DWS angle
\hat{U}	Gaussian beam decomposition – transfer matrix between individual beams and all sample points

Glossary

\hat{M}	matrix
λ	wavelength
DPS_h	differential power sensing signal – horizontal
DPS_v	differential power sensing signal – vertical
DWS^{AP}	differential wavefront sensing signal – average phase definition
DWS^{LPF}	differential wavefront sensing signal – LISA Pathfinder definition
DWS_h	differential wavefront sensing signal – horizontal
DWS_v	differential wavefront sensing signal – vertical
$\omega(z)$	Gaussian spot size
ω_0	Gaussian waist radius
ϕ	phase offset
ρ	curvature
d_{exit}	minimal exit distance
m_{env}	maximum envelope
\vec{b}	Gaussian beam decomposition – vector of beams
\vec{v}	vector
\vec{w}	Gaussian beam decomposition – vector sample points
ξ	substitution variable
ζ	Gouy phase
a	complex amplitude
b	individual beam
c	contrast
c_{OB}	flipping procedure – TTL coupling of the OB
c_{TS}	flipping procedure – TTL coupling of the TS
d_{QPD}	distance to the QPD
d_{ap}	four-hole aperture parameter – distance between neighboring holes
d_{pivot}	distance between point of rotation and detector
f	focal length of a lens
k	wave number
k_h^{DWS}	horizontal DWS coupling factor
k_v^{DWS}	vertical DWS coupling factor
m	magnification
n	refractive index

p_{long}	longitudinal movement due to the piston effect
q	Gaussian q -parameter
r	radial distance
r_{ap}	four-hole aperture parameter – radius of the individual holes
s_{LPS}	longitudinal path length signal
$s_{\text{LPS}}^{\text{AP}}$	longitudinal path length signal on a QPD with the average phase definition
$s_{\text{LPS}}^{\text{LFP}}$	longitudinal path length signal on a QPD with the LISA Pathfinder definition
t	time
t_1	flipping procedure – TTL coupling in orientation 1
t_2	flipping procedure – TTL coupling in orientation 2
x, y, z	Cartesian coordinates
z_0	Gaussian waist position
z_R	Rayleigh length
GIS2C	generic two-lens imaging system – providing a collimated beam
GIS3C	generic three-lens imaging system – providing a collimated beam
LOB2D	LISA optical bench two-lens imaging system – providing a divergent beam
LOB4C	LISA optical bench four-lens imaging system – providing a collimated beam
IfoCAD	simulation tool for 3D interferometer design
ABCD	ray transfer matrix method
AOM	acousto-optical modulator
AP	averaged path length signal
ATA	advanced tilt actuator
CCD	charge-coupled device
CMM	coordinate measurement machine
CQP	calibrated photo diode pair
DC	direct current
DPS	differential power sensing
DUT	device under test
DWS	differential wavefront sensing
EBB	elegant bread board

Glossary

FFT	fast Fourier transformation
FIOS	fibre injector optical subassembly
GBDC	Gaussian beam decomposition
GRACE	gravity recovery and climate experiment
GRACE-FO	GRACE follow on mission
L_{np}	position of lens number n
L_{nt}	additional thickness of lens number n
LISA	laser interferometer space antenna
LO	local oscillator
LPF	LISA pathfinder
MEM	mode expansion method
OB	optical bench
OGSE	optical ground support equipment
OPD	optical path difference
PBS	polarizing beam splitter
QPD	quadrant photo diode
RSS	residual sum of squares
RX	received (e.g. beam)
RX-clip	RX aperture
SciQPD	science interferometer quadrant photo diode
SEPD	single element photo diode
T	Period time
t_i^L	minimal lens thickness – derived from radius and curvature
TIA	trans-impedance amplifiers
TM	test mass
TS	telescope simulator
TTL	tilt-to-length coupling
TX	transmitted (e.g. beam)
WinCam	beam profiler from DataRay Inc. http://www.dataray.com
Zerodur®	glass ceramic with ultra low coefficient of thermal expansion

Bibliography

- [1] BP Abbott, Richard Abbott, TD Abbott, MR Abernathy, Fausto Acernese, Kendall Ackley, Carl Adams, Thomas Adams, Paolo Addesso, RX Adhikari, et al. “Observation of gravitational waves from a binary black hole merger”. In: *Physical review letters* 116.6 (2016), p. 061102.
- [2] BP Abbott, R Abbott, TD Abbott, MR Abernathy, F Acernese, K Ackley, C Adams, T Adams, P Addesso, RX Adhikari, et al. “GW151226: Observation of gravitational waves from a 22-solar-mass binary black hole coalescence”. In: *Physical Review Letters* 116.24 (2016), p. 241103.
- [3] M Sallusti, P Gath, D Weise, M Berger, and HR Schulte. “LISA system design highlights”. In: *Classical and Quantum Gravity* 26.9 (2009), p. 094015.
- [4] Karsten Danzmann, T Prince, and the LISA international science team. *LISA ASSESSMENT STUDY REPORT (YELLOW BOOK)*. Tech. rep. ESA, 2011.
- [5] CJ Hogan. “Gravitational Wave Sources from New Physics”. In: *AIP Conf. Proc.* Vol. 873. 2006, pp. 30–40.
- [6] Sönke Schuster. *Investigation of the coupling between beam tilt and longitudinal pathlength signal in laser interferometers*. Master Thesis. University of Hannover. 2013.
- [7] Sönke Schuster. *Numerical comparison of different quadrant photodiode orientations relating to the signal readout of laser interferometer*. Bachelor Thesis. University of Hannover. 2011.
- [8] David Adam. “Gravity measurement: amazing GRACE”. In: *Nature* 416.6876 (2002), pp. 10–11.
- [9] Byron D Tapley, S Bettadpur, M Watkins, and Ch Reigber. “The gravity recovery and climate experiment: Mission overview and early results”. In: *Geophysical Research Letters* 31.9 (2004).
- [10] VM Tiwari, J Wahr, and S Swenson. “Dwindling groundwater resources in northern India, from satellite gravity observations”. In: *Geophysical Research Letters* 36.18 (2009).
- [11] I Velicogna, TC Sutterley, and MR Van Den Broeke. “Regional acceleration in ice mass loss from Greenland and Antarctica using GRACE time-variable gravity data”. In: *Geophysical Research Letters* 41.22 (2014), pp. 8130–8137.

- [12] Shin-Chan Han, CK Shum, Michael Bevis, Chen Ji, and Chung-Yen Kuo. “Crustal dilatation observed by GRACE after the 2004 Sumatra-Andaman earthquake”. In: *Science* 313.5787 (2006), pp. 658–662.
- [13] Frank Flechtner, Phil Morton, Mike Watkins, and Frank Webb. “Status of the GRACE follow-on mission”. In: *Gravity, Geoid and Height Systems*. Springer, 2014, pp. 117–121.
- [14] BS Sheard, Gerhard Heinzel, Karsten Danzmann, DA Shaddock, WM Klipstein, and WM Folkner. “Intersatellite laser ranging instrument for the GRACE follow-on mission”. In: *Journal of Geodesy* 86.12 (2012), pp. 1083–1095.
- [15] Brian J Meers. “Recycling in laser-interferometric gravitational-wave detectors”. In: *Physical Review D* 38.8 (1988), p. 2317.
- [16] Gudrun Wanner. “Complex optical systems in space : numerical modelling of the heterodyne interferometry of LISA Pathfinder and LISA”. PhD thesis. Leibniz Universität Hannover, 2010.
- [17] F Antonucci, M Armano, H Audley, G Auger, M Benedetti, P Binetruy, C Boatella, J Bogenstahl, D Bortoluzzi, P Bosetti, et al. “LISA Pathfinder: mission and status”. In: *Classical and Quantum Gravity* 28.9 (2011), p. 094001.
- [18] Gerhard Heinzel, Claus Braxmaier, Roland Schilling, Albrecht Rüdiger, David Robertson, M Te Plate, Vinzenz Wand, K Arai, Ulrich Johann, and Karsten Danzmann. “Interferometry for the LISA technology package (LTP) aboard SMART-2”. In: *Classical and Quantum Gravity* 20.10 (2003), S153.
- [19] G Wanner, G Heinzel, E Kochkina, C Mahrtdt, B Sheard, S Schuster, and K Danzmann. “Methods for simulating the readout of lengths and angles in laser interferometers with Gaussian beams”. In: *Optics Communications* 285 (2012).
- [20] E Morrison, B Meers, D Robertson, and H Ward. “Automatic alignment of optical interferometers”. In: *Applied Optics* 33.22 (1994).
- [21] E Morrison, B Meers, D Robertson, and H Ward. “Experimental demonstration of an automatic alignment system for optical interferometers”. In: *Applied Optics* 33.22 (1994).
- [22] G Hechenblaikner. “Measurement of the absolute wavefront curvature radius in a heterodyne interferometer”. In: *J. Opt. Soc. Am. A* 27.9 (2010).
- [23] Gerhard Heinzel. *Ifocad: A framework of C subroutines to plan and optimize laser interferometers*. 2012.
- [24] John A Nelder and Roger Mead. “A simplex method for function minimization”. In: *The computer journal* 7.4 (1965), pp. 308–313.

- [25] Russ C Eberhart, James Kennedy, et al. “A new optimizer using particle swarm theory”. In: *Proceedings of the sixth international symposium on micro machine and human science*. Vol. 1. New York, NY. 1995, pp. 39–43.
- [26] DI Robertson, ED Fitzsimons, CJ Killow, M Perreur-Lloyd, H Ward, J Bryant, AM Cruise, G Dixon, D Hoyland, D Smith, et al. “Construction and testing of the optical bench for LISA Pathfinder”. In: *Classical and Quantum Gravity* 30.8 (2013), p. 085006.
- [27] Christian J Killow, Ewan D Fitzsimons, James Hough, Michael Perreur-Lloyd, David I Robertson, Sheila Rowan, and Henry Ward. “Construction of rugged, ultrastable optical assemblies with optical component alignment at the few microradian level”. In: *Applied optics* 52.2 (2013), pp. 177–181.
- [28] Javier Alda. “Laser and Gaussian beam propagation and transformation”. In: *Encyclopedia of Optical Engineering* 2013 (2003), pp. 999–1013.
- [29] Jacques A Arnaud and Herwig Kogelnik. “Gaussian light beams with general astigmatism”. In: *Applied Optics* 8.8 (1969), pp. 1687–1693.
- [30] Evgenia Kochkina. “Stigmatic and Astigmatic Gaussian Beams in Fundamental Mode – Impact of Beam Model Choice on Interferometric Pathlength Signal Estimates”. PhD thesis. Leibniz Universität Hannover, 2013.
- [31] Amnon Yariv. “Quantum electronics, 3rd”. In: *Edn. (John Wiley & Sons, New York, 1988) p 389* (1989).
- [32] Bahaa E Saleh and Malvin Carl Teich. *Fundamentals of photonics*. Vol. 22. Wiley New York, 1991.
- [33] Gudrun Wanner and Gerhard Heinzl. “Analytical description of interference between two misaligned and mismatched complete Gaussian beams”. In: *Applied optics* 53.14 (2014), pp. 3043–3048.
- [34] A.E. Siegman. *Lasers*. University Science Books, Sausalito, CA, 1986.
- [35] Orazio Svelto and David C Hanna. *Principles of lasers*. Springer, 1976.
- [36] Anthony Gerrard and James M Burch. *Introduction to matrix methods in optics*. Courier Corporation, 2012.
- [37] GA Massey and AE Siegman. “Reflection and refraction of Gaussian light beams at tilted ellipsoidal surfaces”. In: *Applied optics* 8.5 (1969), pp. 975–978.
- [38] F Arellano and C Speake. “Mirror tilt immunity interferometry with a cat’s eye retroreflector”. In: *Applied Optics* 50.7 (2011).
- [39] Germán Fernández Barranco, Michael Tröbs, Vitali Müller, Oliver Gerberding, Frank Seifert, and Gerhard Heinzl. “Spatially resolved photodiode response for simulating precise interferometers”. In: *Applied Optics* 55.24 (2016), pp. 6688–6693.

- [40] M Armano, H Audley, G Auger, JT Baird, M Bassan, P Binetruy, M Born, D Bortoluzzi, N Brandt, M Caleno, et al. “Sub-Femto-g Free Fall for Space-Based Gravitational Wave Observatories: LISA Pathfinder Results”. In: *Physical Review Letters* 116.23 (2016), p. 231101.
- [41] L. d’Arcio, J. Bogenstahl, M. Dehne, C. Diekmann, E. D. Fitzsimons, R. Fleddermann, E. Granova, G. Heinzl, H. Hogenhuis, C. J. Killow, M. Perreur-Lloyd, J. Pijenburg, D. I. Robertson, A. Shoda, A. Sohmer, A. Taylor, M. Tröbs, G. Wanner, H. Ward, and D. Weise. “OPTICAL BENCH DEVELOPMENT FOR LISA”. In: *Proc. of the International Conference on Space Optics*. (2010).
- [42] Maike Lieser. “LISA optical bench development – Experimental investigation of tilt-to-length coupling for a spaceborne gravitational wave detector”. to appear. PhD thesis. Leibniz Universität Hannover, 2017.
- [43] Luigi d’Arcio, Johanna Bogenstahl, Christian Diekmann, Ewan D Fitzsimons, Gerhard Heinzl, Harm Hogenhuis, Christian J Killow, Maike Lieser, Susanne Nikolov, Michael Perreur-Lloyd, et al. “An Elegant Breadboard of the Optical Bench for eLISA/NGO”. In: *Proceedings of ICSO* 116 (2012), p. 2012.
- [44] A Taylor, L d’Arcio, J Bogenstahl, K Danzmann, C Diekmann, ED Fitzsimons, O Gerberding, G Heinzl, JS Hennig, H Hogenhuis, et al. “Optical bench interferometer – from LISA Pathfinder to NGO/eLISA”. In: *9th LISA Symposium*. Vol. 467. Astronomical Society of the Pacific. 2013, pp. 311–315.
- [45] J Bogenstahl, L Cunningham, ED Fitzsimons, J Hough, CJ Killow, M Perreur-Lloyd, D Robertson, S Rowan, and H Ward. “LTP fibre injector qualification and status”. In: *Journal of Physics: Conference Series*. Vol. 154. 1. IOP Publishing. 2009, p. 012011.
- [46] Ewan D Fitzsimons, Johanna Bogenstahl, James Hough, Christian J Killow, Michael Perreur-Lloyd, David I Robertson, and Henry Ward. “Precision absolute positional measurement of laser beams”. In: *Applied optics* 52.12 (2013), pp. 2527–2530.
- [47] G. Heinzl, V. Wand, A. Garcia, O. Jennrich, C. Braxmaier, D. Robertson, K. Middleton, D. Hoyland, A. Rüdiger, R. Schilling, U. Johann, and K. Danzmann. “The LTP interferometer and phasemeter”. In: *Class. Quantum Grav.* 21 (2004), S581–S587.
- [48] M. Tröbs, L. d’Arcio, S. Barke, J. Bogenstahl, I. Bykov, M. Dehne, C. Diekmann, E. D. Fitzsimons, R. Fleddermann, O. Gerberding, J.-S. Hennig, F. G. Hey, H. Hogenhuis, C. J. Killow, E. Kochkina, J. Kullmann, M. Lieser, S. Lucarelli, M. Perreur-Lloyd, J. Pijenburg, D. I. Robertson, A. Shoda, A. Sohmer, A. Taylor, G. Wanner, H. Ward, D. Weise, G. Heinzl, and K. Danzmann. “Testing the LISA optical bench”. In: *Proc. of the International Conference on Space Optics*. 2012.

- [49] Gerhard Heinzel. *IfoCAD – compressor search*. 2011. URL: www.geo600.uni-hannover.de/ifocad.
- [50] Brigitte Kaune. “Kontrolle und Charakterisierung von piezobetriebenen Kipp- und Linearaktuatoren für die optische Bank von LISA”. Bachelor’s thesis. Leibniz Universität Hannover, Hannover, 2011.
- [51] M Tröbs, L d’Arcio, S Barke, J Bogenstahl, I Bykov, M Dehne, C Diekmann, ED Fitzsimons, R Fleddermann, O Gerberding, et al. “Testing the LISA optical bench”. In: *Proceedings of the 9th International Conference on Space Optics, Ajaccio*. 2012.
- [52] Christoph Mahrtdt. “Laser Link Acquisition for the GRACE Follow-On Laser Ranging Interferometer”. PhD thesis. Leibniz Universität Hannover, 2014.
- [53] Vitali Müller. to appear. PhD thesis. Leibniz Universität Hannover, 2017.
- [54] Arnold Sommerfeld. “Mathematische theorie der diffraction”. In: *Mathematische Annalen* 47.2 (1896), pp. 317–374.
- [55] Fabian Shen and Anbo Wang. “Fast-Fourier-transform based numerical integration method for the Rayleigh-Sommerfeld diffraction formula”. In: *Applied optics* 45.6 (2006), pp. 1102–1110.
- [56] Victor Nascov and Petre Cătălin Logofătu. “Fast computation algorithm for the Rayleigh-Sommerfeld diffraction formula using a type of scaled convolution”. In: *Applied optics* 48.22 (2009), pp. 4310–4319.
- [57] N Delen and B Hooker. “Free-space beam propagation between arbitrarily oriented planes based on full diffraction theory: a fast Fourier transform approach”. In: *JOSA A* 15.4 (1998), pp. 857–867.
- [58] Nuri Delen and Brian Hooker. “Verification and comparison of a fast Fourier transform-based full diffraction method for tilted and offset planes”. In: *Applied optics* 40.21 (2001), pp. 3525–3531.
- [59] Satoru Odate, Chiaki Koike, Hidemitsu Toba, Tetsuya Koike, Ayako Sugaya, Katsumi Sugisaki, Katsura Otaki, and Kiyoshi Uchikawa. “Angular spectrum calculations for arbitrary focal length with a scaled convolution”. In: *Optics express* 19.15 (2011), pp. 14268–14276.
- [60] Andreas Freise and Kenneth Strain. “Interferometer Techniques for Gravitational-Wave Detection”. In: *Living Rev. Relativity* 13.1 (2010).
- [61] Novak S Petrovic and Aleksandar D Rakic. “Modeling diffraction and imaging of laser beams by the mode-expansion method”. In: *JOSA B* 22.3 (2005), pp. 556–566.
- [62] Christoph Mahrtdt. *GEOQ-TN-001 – Comparison of Mode Expansion Method to Analytical Equations - Truncated Gaussian beam in Fresnel and Fraunhofer regions*. Tech. rep. AEI Hannover, 2016.

- [63] Alan W. Greynolds. *Propagation Of Generally Astigmatic Gaussian Beams Along Skew Ray Paths*. 1986.
- [64] Henk A Van der Vorst. “Bi-CGSTAB: A fast and smoothly converging variant of Bi-CG for the solution of nonsymmetric linear systems”. In: *SIAM Journal on scientific and Statistical Computing* 13.2 (1992), pp. 631–644.
- [65] Dana Z Anderson. “Alignment of resonant optical cavities”. In: *Applied Optics* 23.17 (1984), pp. 2944–2949.
- [66] B Willke, N Uehara, EK Gustafson, RL Byer, PJ King, SU Seel, and RL Savage. “Spatial and temporal filtering of a 10-W Nd: YAG laser with a Fabry–Perot ring-cavity premode cleaner”. In: *Optics letters* 23.21 (1998), pp. 1704–1706.
- [67] DA Shaddock, MB Gray, and DE McClelland. “Frequency locking a laser to an optical cavity by use of spatial mode interference”. In: *Optics letters* 24.21 (1999), pp. 1499–1501.
- [68] Yves Surrel. “Fringe analysis”. In: *Photomechanics*. Springer, 2000, pp. 55–102.
- [69] Evgenia Kochkina, Gudrun Wanner, Dennis Schmelzer, Michael Tröbs, and Gerhard Heinzl. “Modeling of the general astigmatic Gaussian beam and its propagation through 3D optical systems”. In: *Applied optics* 52.24 (2013), pp. 6030–6040.

Project Documents

- [TD1] Jeff Livas. *LISA-MSE-TN-0001 – Laser Interferometer Space Antenna (LISA) Measurement Requirements Flowdown Guide*. Tech. rep. European Space Agency, 2009.
- [TD2] Michael Tröbs, Johanna Bogenstahl, Marina Dehne, Christian Diekmann, Evgenia Granova, Ayaka Shoda, Gudrun Wanner, and Gerhard Heinzl. *LOB-AEI-TN-005.1 – Test of interferometry concept*. Tech. rep. AEI Hannover, 2011.
- [TD3] Ewan Fitzsimons, Michael Perreur-Lloyd, Michael Tröbs, Sönke Schuster, and Germán Fernández Barranco. *LOB-TN-14-01-ASD – Detailed Design of Tilt-to-Piston Investigation*. Tech. rep. Airbus Defence and Space, University of Glasgow, AEI Hannover, 2015.
- [TD4] Maike Lieser, Sönke Schuster, and Michael Tröbs. *LOB-AEI-TN-15 – Test of interferometry concept*. Tech. rep. AEI Hannover, 2015.
- [TD5] Ewan Fitzsimons, Maike Lieser, Michael Perreur-Lloyd, Sönke Schuster, and Michael Tröbs. *LOB-AEI-TN-16 – Testing Interferometric Imaging for eLISA - LISA Optical Bench Development - Test Report and Final Report*. Tech. rep. UK Astronomy Technology Centre, University of Glasgow, AEI Hannover, 2016.
- [TD6] Dennis Weise. *LOB-TN-006-02-ASD – OB Requirements Specification and Justification*. Tech. rep. Airbus Defence and Space, 2010.
- [TD7] Michael Perreur-Lloyd, Christian Killow, Ewan Fitzsimons, David Robertson, Harry Ward, and Alasdair Taylor. *LOB-TN-8.2-14-UGL – Optical Bench EBB Design Definition File - Opto-Mechanical Design*. Tech. rep. UK Astronomy Technology Centre, University of Glasgow, AEI Hannover, 2011.
- [TD8] Ewan Fitzsimons. *eLISA-TN-002.2-ASD – Metrology System Architecture Analysis and Optimisation*. Tech. rep. Airbus Defence and Space, 2016.
- [TD9] Jess Köhler, Daniel Kochems, Dennis Weise, and Michael Wiesmayer. *LISA-ASD-TN-3032 – OGSE Architecture and Concept of Operations*. Tech. rep. Airbus Defence and Space, 2010.

Complete list of publications

- [P1] Sönke Schuster, Michael Tröbs, Gudrun Wanner, and Gerhard Heinzel. “Experimental demonstration of reduced tilt-to-length coupling by a two-lens imaging system”. In: *Optics Express* 24.10 (2016), pp. 10466–10475.
- [P2] Gudrun Wanner, Gerhard Heinzel, Evgenia Kochkina, Christoph Mahrddt, Benjamin Sheard, Sönke Schuster, and Karsten Danzmann. “Methods for simulating the readout of lengths and angles in laser interferometers with Gaussian beams”. In: *Optics communications* 285.24 (2012), pp. 4831–4839.
- [P3] Gudrun Wanner, Sönke Schuster, Michael Tröbs, and Gerhard Heinzel. “A brief comparison of optical pathlength difference and various definitions for the interferometric phase”. In: *Journal of Physics: Conference Series* 610 (2015), p. 012043.
- [P4] Evgenia Kochkina, Gerhard Heinzel, Gudrun Wanner, Vitali Müller, Christoph Mahrddt, Benjamin Sheard, Sönke Schuster, and Karsten Danzmann. “Simulating and optimizing laser interferometers”. In: *9th LISA Symposium* (2013), pp. 291–292.
- [P5] Sönke Schuster, Gudrun Wanner, Michael Tröbs, and Gerhard Heinzel. “Vanishing tilt-to-length coupling for a singular case in two-beam laser interferometers with Gaussian beams”. In: *Applied optics* 54.5 (2015), pp. 1010–1014.
- [P6] Michael Chwalla, Karsten Danzmann, Germán Fernández Barranco, Ewan Fitzsimons, Oliver Gerberding, Gerhard Heinzel, Christian J Killow, Maike Lieser, Michael Perreure-Lloyd, David I Robertson, Sönke Schuster, Thomas Schwarze, Michael Tröbs, Harry Ward, and Max Zwetz. “Design and construction of an optical test bed for LISA imaging systems and tilt-to-length coupling”. In: *Classical and Quantum Gravity* 33.24 (2016), p. 245015.
- [P7] Michael Perreure-Lloyd, Karsten Danzmann, Ewan D Fitzsimons, Gerhard Heinzel, Jan-Simon Hennig, Christian J Killow, Maike Lieser, David I Robertson, Sönke Schuster, Alasdair Taylor, et al. “Sub-system mechanical design for an eLISA optical bench”. In: *Journal of Physics: Conference Series* 610 (2015), p. 012032.

- [P8] Maike Lieser, Ewan Fitzsimons, Katharina Sophie Isleif, Christian Killow, Michael Perreur-Lloyd, David Robertson, Sönke Schuster, Michael Tröbs, Sonja Veith, Harry Ward, et al. “Construction of an optical test-bed for eLISA”. In: *Journal of Physics: Conference Series* 716 (2016), p. 012029.

Acknowledgements

First of all, I would like to thank Karsten Danzmann for giving me the opportunity to work at the Albert Einstein Institute. It is an honor and a pleasure to learn, study and work in a thriving environment like this. Equally, I would like to thank Gerhard Heinzl, not only for supervising me but also for having an answer to every question I challenged him with over the years. Furthermore, I want to thank him for developing a variety of tools and programs which build the backbone of all simulations and work I did. I would like to thank Guido Müller, who agreed to be my referee.

Next in line are Gudrun Wanner and Michael Tröbs - I am indebted to you for sharing knowledge and time, your advice and guidance were essential for my education. My gratitude goes to Maike Lieser and all those who participated in the LISA optical bench development project. It was a pleasure to work with you on both, challenging and reasonably trivial tasks. A huge thanks to Nils Brause, without whose comprehensive knowledge I would certainly still be stuck, producing only segmentation faults and kernel panics.

I am much obliged to the lovely “Promo-Drachen” – I truly believe the book “Einfach promovieren mit Frau Ohlendorf” will be a great success. I am also grateful to the current residents of the “Diplomanden Zimmer” and anyone who spent time there in the past years. It was and is always a pleasure to have such nice colleagues. Equally, I want to thank the entire space interferometry group for the excellent working atmosphere and wonderful hours spent in the mensa and elsewhere.

At this point I want to especially thank those people who are important enough to not be mentioned – I deliberately did not include you in this acknowledgement to accompany those I forgot.

Finally, I would like to extend my thanks to my family and especially to my wife, for continued support in the past.

I would like to acknowledge Alexander Franzen for developing the component library and Roland Schilling for developing OptoCad. Stating the obvious, any errors that remain are my sole responsibility.

Curriculum Vitae

Personal Details

Name	Sönke Schuster
Date of Birth	August 19, 1988
Place of Birth	Hannover
Marital Status	married
Nationality	German

Education

2001–2008	Geschwister-School-Gymnasium Berenbostel graduated with Abitur
2008–2011	Leibniz Universität Hannover graduated with Bachelor of Science
2011–2013	Leibniz Universität Hannover graduated with Master of Science
since 2013	Ph.D. student at Albert-Einstein-Institute in Hannover

